



THE HONG KONG
POLYTECHNIC UNIVERSITY

香港理工大學

Pao Yue-kong Library

包玉剛圖書館

Copyright Undertaking

This thesis is protected by copyright, with all rights reserved.

By reading and using the thesis, the reader understands and agrees to the following terms:

1. The reader will abide by the rules and legal ordinances governing copyright regarding the use of the thesis.
2. The reader will use the thesis for the purpose of research or private study only and not for distribution or further reproduction or any other purpose.
3. The reader agrees to indemnify and hold the University harmless from and against any loss, damage, cost, liability or expenses arising from copyright infringement or unauthorized usage.

IMPORTANT

If you have reasons to believe that any materials in this thesis are deemed not suitable to be distributed in this form, or a copyright owner having difficulty with the material being included in our database, please contact lbsys@polyu.edu.hk providing details. The Library will look into your claim and consider taking remedial action upon receipt of the written requests.

**MULTI-SCALE STRUCTURAL DAMAGE DETECTION
USING WAVELET FINITE ELEMENT METHOD**

HE WENYU

Ph.D

The Hong Kong Polytechnic University

2015



THE HONG KONG POLYTECHNIC UNIVERSITY

Department of Civil and Environmental Engineering

**Multi-scale Structural Damage Detection Using
Wavelet Finite Element Method**

He Wenyu

A thesis submitted in partial fulfillment of the requirements for the degree
of Doctor of Philosophy

January 2015

CERTIFICATE OF ORIGINALITY

I hereby declare that this thesis is my own work and that, to the best of my knowledge and belief, it reproduces no material previously published or written, nor material that has been accepted for the award of any other degree or diploma, except where due acknowledgement has been made in the text.

_____ (Signed)

Wenyu He (Name of student)

To my family

Abstract

Damage detection of civil infrastructures will be essential in future decision making on structural maintenance and hazard mitigation. Damage-induced changes in dynamic characteristics and responses are commonly utilized to locate and quantify structural damages. Common vibration-based damage detection methods can be categorized into two groups, namely, frequency- and time-domain methods. This thesis focuses on developing multi-scale structural damage detection strategies in both frequency- and time-domain with the use of wavelet finite element models (WFEM). Such multi-scale strategies would optimize structural modeling in accordance with damage scenarios and external load conditions. These strategies are very efficient in terms of the number of degree-of-freedom (DOFs) of structural models, number of sensors, and computation effort.

Multi-scale dynamic formulations and corresponding lifting schemes were derived for beam and thin plate structures individually through the use of the cubic Hermite WFEM. In particular, the multi-scale formulation of beam structures under moving load excitation was derived. Such a formulation lays the theoretical foundation of multi-scale damage detection in a progressive manner.

In frequency-domain, multi-scale damage detection methods to progressively detect sub-element damage in beam and plate structures were proposed based on modal strain energy and model updating technique in the context of WFEM. The structural modelling resolutions did not only spatially vary but also changed dynamically according to actual requirements. A coarse WFEM was utilized to identify the likely damaged regions first. Meanwhile, gradually lifted WFEMs with local refinement were utilized to estimate the exact damage location and severity. Numerical and experimental examples were conducted to demonstrate the high efficiency of the proposed methods in

terms of the number of DOFs, number of sensors, and computation effort.

In time-domain, the closed-form solution of the dynamic response of a simply supported damaged beam under a moving force was derived based on modal perturbation and modal superposition methods. With this solution, the damage effect on different components of the dynamic response was investigated. A simple and efficient damage localization approach that employs discrete wavelet transform (DWT) was then proposed. Numerical examples were utilized to validate the accuracy of the response computation algorithm and demonstrate the effectiveness of the damage localization approach. Subsequently, an adaptive-scale analysis strategy for beam structures subjected to moving loads was developed with WFEM. In this strategy, the wavelet element scales were dynamically changed to remain compatible with the moving load position. A two-phase damage detection method for beam structures under moving load was then proposed by combining the adaptive-scale analysis strategy, DWT-based damage localization, and progressive WFEM updating in time-domain. The scale of the wavelet elements were adaptively enhanced or reduced not only according to the moving load–beam contact position but also to the progressively identified damage locations. Such a method can effectively minimize the number of modelling DOFs and updating parameters during optimization. A laboratory experiment was conducted to examine the feasibility and efficiency of the two-phase damage detection method.

Publications

Journal Papers:

He, W.Y., and Zhu, S., (2013), “Progressive damage detection based on multi-scale wavelet finite element model: numerical study”, *Computers & Structures*, 125: 177-186

He, W.Y., Zhu, S., and Ren, W.X., (2014), “A wavelet finite element-based adaptive-scale damage detection strategy”, *Smart Structures and Systems*, 14(3): 285- 305

Zhu, S., He, W.Y., and Ren, W.X., (2014), “Adaptive-scale damage detection for frame structures using beam-type wavelet finite element: experimental validation”, *Journal of Earthquake and Tsunami*, 7(3): 1350024

He, W.Y., and Zhu, S., (2015), “Adaptive-scale damage detection strategy for plate structures based on wavelet finite element model”, *Structural Engineering and Mechanics*, 54(2): 239-256

He, W.Y., and Zhu, S., (2015), “Moving load-induced response of damaged beam and its application in damage localization”, *Journal of Vibration and Control* (in press, DOI: 10.1177/1077546314564587)

Conference Papers:

Zhu, S., He, W.Y., and Ren, W.X., (2012), “A bio-inspired damage detection approach based on multi-scale wavelet finite element”, *Proceedings of the 12th International Symposium on Structural Engineering*, 17-29, November, Wuhan, China, 1596-1602
(Best Paper Award)

He, W.Y., and Zhu, S., (2013), “Damage detection of beam structures under moving vehicle using wavelet finite model”, *Proceedings of the 6th International Conference on Structural Health Monitoring of Intelligent Infrastructure*, 9-11, December, Hong Kong, (CD-ROM)

He, W.Y., and Zhu, S., (2014), “Multi-scale finite element modeling and model updating using wavelet technique”, *Proceedings of the 6th World Conference on Structural Control and Monitoring*, 15-17, July, Barcelona, Spain, (CD-ROM)

He, W.Y., and Zhu, S., (2014), “Damage localization of simply-supported beam under moving force”, *Proceedings of the 13th International Symposium on Structural Engineering*, 24-27, October, Hefei, China, 1797-1805

Acknowledgments

I would like to express my sincere gratitude to my chief supervisor, Dr. Songye Zhu, for providing me the unique opportunity to pursue my Ph.D. degree and for helping me find an area that fits my research background and interests perfectly. I sincerely appreciate Dr. Zhu's expert guidance, constant encouragement, and extensive discussions throughout my stay at PolyU. I would also like to thank my co-supervisor, Prof. You-lin Xu, for giving me valuable academic guidance and encouragement. I would like to express my gratitude to my master supervisor, Prof. Wei-Xin Ren at Hefei University of Technology, for recommending me to study at PolyU and for providing me plenty of helpful advice.

I am grateful to Dr. Yong Xia at PolyU for providing the modal testing data of a steel frame and to Dr. Zhongqing Su and Dr. Hao Xu at PolyU for helping in the plate vibration testing. Moreover, I am grateful to Mr. C.F. Cheung, Mr. T.T. Wai, Mr. M.C. Ng, Mr. Y.H. Yiu, and Mr. K.H. Wong for their very professional and useful suggestions and help in my laboratory experiments. Gratitude is also extended to former FYP student, Mr. Y.S. Chan, for his generous assistance throughout the moving vehicle testing.

I would also like to thank my fellows Dr. Xiao-hua Zhang, Dr. Wen-ai Shen, Mr. Can-xing Qiu, Mr. Zhi-lu Lai, Mr. Xiang Shi, Mr. Jing-yang Li, Mr. Quan Liu, Dr. Zhiwei Chen, Dr. Xiang Xiao, Mr. Shen Zhan, Dr. Bing Wang, Mr. Yue Zheng, Dr. Qing Zhu, Mr. Chao-dong Zhang, Mr. Jian-fu Lin, Miss. Yi-xin Peng, Mr. Rong-pang Hu, Mr. Peng Zhang, Mr. Jia-zhang Su, Mr. Hai-quan Jing, Mr. Wei-li Luo, and Mr. Ping-he Ni for their discussions and constructive comments.

Lastly, I wish to thank all my family members and friends for their love and endless support.

Contents

CERTIFICATE OF ORIGINALITY	i
Abstract	v
Publications.....	vii
Acknowledgments.....	ix
Contents	xi
List of Figures	xv
List of Tables	xix
List of Abbreviation.....	xxi
Chapter 1 Introduction	1
1.1 Research Background and Motivation.....	1
1.2 Literature Review	4
1.2.1 Vibration-Based Damage Detection Methods	4
1.2.1.1 Frequency-Domain Damage Detection Methods.....	4
1.2.1.2 Time-Domain Damage Detection Methods.....	8
1.2.1.3 Multi-Scale FEM in SHM.....	13
1.2.2 Application of Wavelet in Structural Engineering.....	14
1.2.2.1 Multi-Resolution Wavelet Analysis.....	14
1.2.2.2 Multi-Scale Wavelet-Based Signal Processing	16
1.2.2.3 Multi-Scale Wavelet-Based Finite Element Modeling.....	17
1.2.3 Remarks.....	22
1.2.3.1 Challenges in FEM during Damage Detection	22
1.2.3.2 Challenges in Moving Load-Based Damage Detection.....	23
1.3 Research Objectives.....	24
1.4 Thesis Outline	25
Chapter 2 Multi-Scale WFEM.....	28
2.1 Introduction.....	28
2.2 Cubic Hermite Multi-Scale Wavelet.....	28
2.3 Dynamic Formulation of Multi-Scale WFEM for Beam Structures.....	34

2.4 Dynamic Formulation of Multi-Scale WFEM for Plate Structures.....	40
2.5 Summary.....	43
Chapter 3 Progressive Damage Detection Based on Modal Strain Energy.....	44
3.1 Introduction.....	44
3.2 Progressive Damage Detection.....	44
3.2.1 Beam Structure.....	45
3.2.1.1 Damage Localization.....	45
3.2.1.2 Damage Quantification.....	46
3.2.2 Plate Structure.....	48
3.2.2.1 Damage Localization.....	49
3.2.2.2 Damage Quantification.....	49
3.2.3 Damage Detection Procedure.....	54
3.3 Numerical Study.....	55
3.3.1 Beam Structure.....	56
3.3.2 Plate Structure.....	65
3.3.3 Noise Effects.....	74
3.4 Summary.....	78
Chapter 4 Progressive Damage Detection Based on Model Updating.....	80
4.1 Introduction.....	80
4.2 Progressive Updating of WFEM.....	80
4.2.1 WFEM Updating.....	81
4.2.2 Damage Detection Procedure.....	82
4.2.3 Effect of Sub-Element Damage.....	84
4.3 Numerical Study.....	85
4.3.1 Beam Structure.....	86
4.3.2 Plate Structure.....	90
4.4 Experimental Verification.....	99
4.4.1 Frame Structure.....	99
4.4.1.1 Experimental Description.....	99
4.4.1.2 Damage Detection Process and Results.....	101

4.4.2 Plate Structure	105
4.4.2.1 Experimental Description.....	105
4.4.2.2 Damage Detection Process and Results	109
4.5 Summary.....	116
Chapter 5 Moving Load-Induced Response of a Damaged Simply Supported Beam and Its Application in Damage Localization	117
5.1 Introduction.....	117
5.2 Moving Load-Induced Response of a Simply Supported Beam	118
5.2.1 Undamaged Beam	118
5.2.2 Damaged Beam	120
5.2.3 Algorithm Verification.....	123
5.2.4 Discussion on the Undamaged Beam.....	126
5.2.5 Discussion on the Damaged Beam.....	130
5.3 Wavelet-Based Damage Localization.....	135
5.3.1 Localization Procedure.....	135
5.3.2 Numerical Study.....	136
5.3.3 Discussion.....	139
5.4 Summary.....	146
Chapter 6 Two-Phase Damage Detection of Beam Structures Subjected to a Moving Vehicle	148
6.1 Introduction.....	148
6.2 WFEM-Based Modeling Strategy	149
6.2.1 Adaptive-Scale Analysis Strategy.....	149
6.2.2 Numerical Study.....	150
6.2.3 Discussion.....	154
6.3 Two-Phase Damage Detection Method	155
6.3.1 Damage Localization.....	156
6.3.2 Damage Quantification.....	156
6.4 Experimental Verification	158
6.4.1 Experiment Description.....	158

6.4.2 Damage Detection	166
6.4.2.1 Single Damage	166
6.4.2.2 Double Damages	173
6.4.3 Discussion	178
6.5 Summary.....	179
Chapter 7 Conclusions and Recommendations.....	181
7.1 Conclusions.....	181
7.2 Recommendations for future work	185
References	187

List of Figures

Figure 1.1.	Local refinement in traditional plate elements	3
Figure 1.2.	Wavelet decomposition of a signal	17
Figure 2.1.	The refinement relation for cubic Hermite scaling functions.....	32
Figure 2.2.	2D tensor products of cubic Hermite functions.....	34
Figure 2.3.	Simply-supported beam subjected to a moving force/vehicle.....	37
Figure 2.4.	Plane beam-type wavelet finite element.....	40
Figure 2.5.	Rectangular elastic thin plate.....	41
Figure 3.1.	Flowchart of the adaptive-scale damage detection scheme.....	55
Figure 3.2.	Model refinement process for Case B-1	57
Figure 3.3.	Adaptive-scale damage identification results for Case B-1.....	59
Figure 3.4.	Model refinement process for Case B-2.....	62
Figure 3.5.	Model refinement process for Case B-3	64
Figure 3.6.	Thin plate in numerical study	65
Figure 3.7.	Model refinement process for Case P-1	66
Figure 3.8.	Adaptive-scale damage identification results for Case P-1	69
Figure 3.9.	Model refinement process for Case P-2	70
Figure 3.10.	Adaptive-scale damage identification results for Case P-2.....	73
Figure 3.11.	Damage detection results under different noise levels in Stage 4 of Case B-3.....	76
Figure 3.12.	COV of the estimated damage localization index in Case B-1	77
Figure 3.13.	COV of the estimated damage severity index in Case B-3	77
Figure 3.14.	COV of the estimated damage localization index in Case P-1.....	78
Figure 3.15.	COV of the estimated damage severity index in Case P-1.....	78
Figure 4.1.	Diagram of the multi-scale WFEM updating scheme	83
Figure 4.2.	Local damage in a wavelet beam element.....	85
Figure 4.3.	Model refinement process in Case B1	86

Figure 4.4.	Progressive damage identification results in Case B1	88
Figure 4.5.	Model refinement process in Case B2	89
Figure 4.6.	Progressive damage identification results in Case B2	89
Figure 4.7.	Thin plate in the numerical study	90
Figure 4.8.	Model refinement process in Case P1	92
Figure 4.9.	Progressive damage identification results in Case P1	94
Figure 4.10.	Model refinement process in Case P2	96
Figure 4.11.	Progressive damage identification results in Case P2	98
Figure 4.12.	Configuration of the frame specimen	100
Figure 4.13.	Experimental mode shapes of the undamaged frame	101
Figure 4.14.	Model refinement process	103
Figure 4.15.	Progressive damage identification results	104
Figure 4.16.	Setup of the plate experiment	106
Figure 4.17.	Damage zone on the plate.....	106
Figure 4.18.	Vibration exciter	107
Figure 4.19.	Vibration test on the plate with 49×49 measurement points	108
Figure 4.20.	Experimental mode shapes of the damaged plate.....	109
Figure 4.21.	Thin plate in the experimental study	110
Figure 4.22.	Model refinement process of the experiment	113
Figure 4.23.	Progressive damage identification results of the plate experiment	115
Figure 5.1.	Simply supported beam subjected to moving load.....	118
Figure 5.2.	Displacement response of the damaged beam at mid-span calculated with the presented algorithm.....	125
Figure 5.3.	Variation in dimensionless moving velocity S_1 with the maximum span of highway bridges L_{max}	127
Figure 5.4.	Moving load-induced displacement response of the undamaged beam ($S_1 = 0.1$).....	128
Figure 5.5.	Effect of moving velocity on the displacement amplitude on the undamaged beam ($x = L/2$)	129
Figure 5.6.	Damage-induced change in normalized displacement response at	

	mid-span.....	132
Figure 5.7.	Damage-induced change in normalized displacement response at mid-span for difference damping ratios ($S_1 = 0.05$).....	133
Figure 5.8.	Acceleration response at mid-span after damage ($S_1 = 0.025$)	135
Figure 5.9.	Damage-induced total displacement change at mid-span in Case 1 with and without noise ($S_1 = 0.025$)	138
Figure 5.10.	DWT results of displacement change with 5% noise in Case 1	139
Figure 5.11.	DWT results of displacement change under different change under different noise levels in Case 1 ($S_1 = 0.1$)	140
Figure 5.12.	DWT results of displacement change with 5% noise in Case 2	141
Figure 5.13.	DWT results of displacement change with 5% noise in Case 3	141
Figure 5.14.	Velocity time history of the force before and after damage	142
Figure 5.15.	DWT results of the displacement change under varying velocity.....	143
Figure 5.16.	Moving vehicle model.....	144
Figure 5.17.	Comparison of the results calculated using different models (Case 1) .	146
Figure 6.1.	Adaptive-scale analysis strategy.....	150
Figure 6.2.	Adaptive wavelet element scale strategy during the moving process ...	151
Figure 6.3.	The accurate displacement time history	152
Figure 6.4.	Displacement error calculated by different models.....	153
Figure 6.5.	Damage-induced displacement change of the beam.....	153
Figure 6.6.	Effects of RL	154
Figure 6.7.	Diagram of multi-scale damage detection	155
Figure 6.8.	Experimental arrangement and configuration of the beam	161
Figure 6.9.	Moving vehicle	162
Figure 6.10.	Electric motor	162
Figure 6.11.	Displacement transducers	163
Figure 6.12.	Beam damages	164
Figure 6.13.	Typical displacement time history of the undamaged beam.....	165
Figure 6.14.	Typical velocity information of the moving vehicle	166
Figure 6.15.	Damage localization results for Case 1	169

Figure 6.16.	Finite element mesh of the beam.....	170
Figure 6.17.	Adaptive wavelet element scale strategy during the quantification process in Case 1.....	170
Figure 6.18.	Damage quantification results for Case 1.....	172
Figure 6.19.	Damage localization results for Case 2.....	174
Figure 6.20.	Adaptive wavelet element scale strategy during the quantification process in Case 2.....	175
Figure 6. 21.	Damage quantification results for Case 2.....	177

List of Tables

Table 2.1.	Comparison of different wavelet elements.....	29
Table 3.1.	Damage scenarios considered in the numerical simulations of the beam...	56
Table 3.2.	Adaptive-scale location and quantification of damage using WFEM.....	63
Table 3.3.	Damage scenarios considered in the numerical simulations of the plate....	66
Table 3.4.	Damage severity quantification results	71
Table 4.1.	Damage scenarios considered in the numerical simulations of the beam...	87
Table 4.2.	Damage scenarios considered in the numerical simulations of the plate....	91
Table 4.3.	Modal frequencies of the tested frames (Hz)	100
Table 4.4.	Frequency of the plate in the experimental study (Hz)	107
Table 5.1.	Damage scenarios of the simply supported beam	137
Table 6.1.	Damage scenarios of the simply supported beam	159
Table 6.2.	Velocity parameters	165

List of Abbreviation

COMAC	coordinate modal assurance criterion
COV	coefficient of variance
DOF	degree-of-freedom
DWT	discrete wavelet transform
EMD	empirical mode decomposition
FEM	finite element model
IF	interaction force
MAC	modal assurance criterion
MSE	modal strain energy
RL	refinement length
SHM	structural health monitoring
SGW	second generation wavelets
TFEM	traditional finite element model
WFEM	wavelet finite element model
WT	wavelet transform

Chapter 1 Introduction

1.1 Research Background and Motivation

Damage detection of civil infrastructures will be essential in future decision making on structural maintenance and hazard mitigation. This subject has been gaining worldwide popularity in the past 20 years. Damage-induced changes in the dynamic characteristics and responses of structures have been extensively utilized to localize and quantify structural damages (Doebbling et al. 1996; Salawu 1997; Sohn et al. 2004; Carden and Fanning 2004; Yan et al. 2007; Wang and Chan 2009; Fan and Qiao 2011; Brownjohn et al. 2011). Vibration-based damage detection methods can generally be categorized into two groups, namely, (1) frequency-domain methods based on natural frequencies, mode shapes, and their derivatives and (2) time-domain methods, such as moving load-based methods.

From the perspective of structure modeling, these methods can be classified into model-free and model-based types. Given that no structural finite element model (FEM) is required, the former is regarded as more appealing and efficient than the latter by several scholars (Rucka and Wilde 2006; Fan and Qiao 2009; Beheshti-Aval et al. 2011). However, some inherent limitations of model-free methods, such as the inability to estimate damage severity and the need for a dense network of sensors to accurately locate damage, prevent the extensive application these methods (Antonio and Erin 2014). Thus, model-based types, particularly FEM-based methods, have been eliciting widespread attention. The quality of FEM affects not only the accuracy but also the efficiency of damage detection. A dilemma exists in FEM-based methods. On one hand, a delicate FEM with fine details is required to obtain high-resolution structural dynamic properties and enable the identification of minor or localized damages; on the other

hand, an excessively dense meshed FEM is often impractical, if not impossible, in the damage detection of large-scale civil structures because a large number of degree-of-freedom (DOFs) does not only increase the computation cost but also tends to make solutions ill-conditioned and non-unique in inverse problems. Moreover, owing to sensor noise and other testing constraints, only low frequencies and mode shapes can be obtained through with *in situ* test data on damage detection. In this situation, a coarse FEM may be preferred considering the complexity and efficiency involved in the computation. Therefore, a multi-scale FEM with a resolution compatible with damage scenarios, that is, using a dense mesh in suspected damage regions and a coarse mesh in other regions, would be attractive. A practical challenge arises from the fact that probable damage locations and the required modeling resolutions are often unpredictable; thus, a priori finite element meshing based on analytical simulations or empirical estimates may be incorrect. An ideal damage detection strategy should be based on an adaptive-scale modeling technique that enables us to examine a structure in its entirety, detect suspected regions by using a low-resolution model, and identify the accurate location and severity of the damage with localized refinement in the suspected regions only. With such a model, an appropriate tradeoff between modeling details and entirety and between computation accuracy and efficiency can be achieved.

In popular moving load-based damage detection problems (Majumder and Manohar 2002; Li and Zhao 2006; Bu et al. 2006; Lu and Law 2007a; 2007b; Lu and Liu 2011; Li and Law 2012), the geometric discretization employed in FEM is even more critical. A uniform discretization, either fine or coarse, in the entire domain may be inadvisable in consideration of both computation cost and accuracy. An ideal option is to utilize multi-scale mesh generation with a dense mesh in regions near the load–structure contact position and a coarse mesh in other regions (Rieker et al. 1996). Consequently, the regions with fine mesh resolution should be continually and adaptively changed according to the contact position when the load moves over time. Sufficient modeling accuracy and reduced number of DOFs can then be simultaneously achieved.

However, the implementation of a multi-scale model and mesh generation in the context of traditional FEM (TFEM) is difficult. Re-meshing a local region requires reconstructing stiffness and mass matrices and repeating the entire computation process; these procedures consequently lead to a large amount of computation. Re-meshing is even more complicated for plate structures. Figure 1.1 shows a plate with a damaged region, which is represented by the red area. The plate is initially divided into nine elements. If the center element (ABCD) is identified as a suspected damage region, such element is subsequently divided into four equal elements. During refinement, a node (N_0) inside the element and four hanging nodes on the elemental edges (N_1 to N_4) are introduced. These hanging nodes should meet special compatibility conditions and may cause numerical computation difficulties (Becker and Braack 2000; Biboulet et al. 2013). The recently developed wavelet FEM (WFEM) that employs wavelets and scaling functions as element shape functions may provide a more convenient alternative to solve these problems because the resolution of the model can be changed conveniently according to actual damage scenarios and load conditions (Ko et al. 1995; Chen and Wu 1995; Sudarshan et al. 2003; Han et al. 2005; Amaratunga and Sudarshan 2006; He et al. 2012; He and Ren 2012).

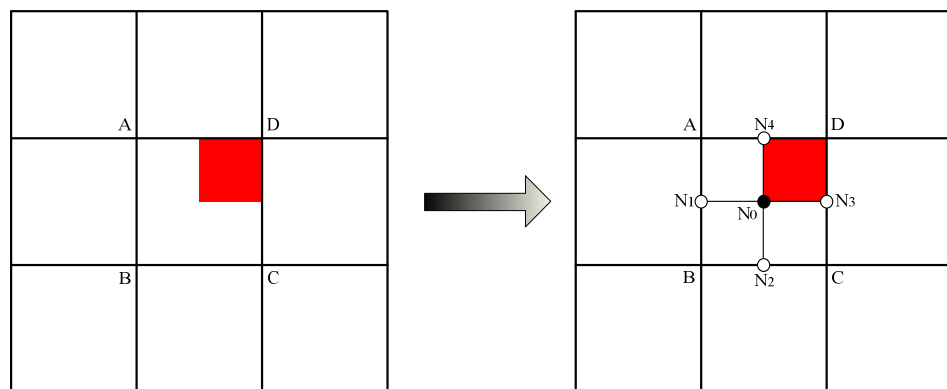


Figure 1.1. Local refinement in traditional plate elements

Another fundamental problem that has received insufficient attention in moving load-based damage detection methods is how local damages affect the moving load-induced structural dynamic response. Yang and Lin (2005) stated that the dynamic response of a

simply supported beam under moving load consists of two components, namely, the moving-frequency component corresponding to the moving load and the natural-frequency component of the beam structure. Investigating the local damage effect on these two different components and separating them via a multi-scale signal processing technique are essential in developing a simple and efficient moving load-based damage localization approach.

1.2 Literature Review

1.2.1 Vibration-Based Damage Detection Methods

Structural damage detection has elicited an increasing amount of attention in the engineering community because unanticipated structural damage may cause catastrophic failure and substantial economic and human life loss. Extensive research has focused on vibration-based damage detection by considering that damage induces a change in structural dynamic characteristics or responses. As explained in Section 1.1, most vibration-based damage detection methods can be categorized into two groups, namely, frequency- and time-domain methods.

1.2.1.1 Frequency-Domain Damage Detection Methods

Frequency-domain damage detection methods have been widely studied in terms of damage-induced changes in frequencies (Cawley and Adams 1979; Stubbs and Osegueda 1990; Friswell et al. 1994; Koh et al. 1995; Salawu 1997), mode shapes (Fox 1992; Ratcliffe 1997; Shi et al. 2000a; Parloo et al. 2003), mode shape curvature/strain (Pandey et al. 1991; Wahab and De Roeck 1999; Shi et al. 2000b), measured flexibility matrix (Pandey et al. 1994; Peterson et al. 1995; Bernal 2006), modal strain energy (MSE) (Stubbs et al. 1995; Shi and Law 1998; Shi et al. 2002; Au et al. 2003; Yan et al. 2010), frequency response functions (Ni et al. 2006; Huang et al. 2012), residual modal force vectors (Kosmatka and Ricles 1999), and so on. Comprehensive reviews on damage detection from structural dynamic characteristics and their derivatives have

been conducted by Salawu (1997), Doebling et al. (1996; 1998), Sohn et al. (2004), Carden and Fanning (2004), and Fan and Qiao (2011).

Researchers have conducted comparative studies on the effectiveness of various frequency-domain damage detection methods. For example, Farrar and Jauregui (1998a; 1998b) compared five damage detection methods in terms of MSE, mode shape curvature, flexibility and stiffness coefficients, and curvature of the uniform load surface by using experimental data on the Interstate-40 Bridge. The authors concluded that frequencies and mode shapes are not good damage indices. Ndambi et al. (2002) examined different damage detection methods in terms of frequencies, modal assurance criterion (MAC), coordinate MAC (COMAC), flexibility matrices, and MSE by conducting laboratory tests on two cracked reinforced concrete beams. The results showed the following: (1) frequency variations can reflect the damage severity but not the crack location; (2) MAC factors are less sensitive to crack damage than frequencies; (3) COMAC factors can detect and locate damage but experiences difficulty quantifying the severity and extent of the damage; (4) changes in flexibility matrices can detect but not locate crack damage; and (5) MSE-based methods appear to be more accurate than others in damage localization; however difficulty arises when the damage is spread out over a certain length. Huth et al. (2005) applied several damage detection techniques on a progressively damaged concrete bridge. Only minor changes were found in the natural frequencies and mode shapes even though the bridge was severely cracked. However, changes in the flexibility matrix provided better results than using natural frequencies or mode shapes alone. Zhou et al. (2007) compared the performance of three curvature-based damage detection methods (i.e., mode shape curvature, strain energy, and flexibility curvature) and that of two other methods (i.e., mode shape and flexibility) through an experiment and FEM of a simply supported bridge. The curvature-based methods predicted the damage location at the measurement point. The mode shape and flexibility-based methods performed better than the curvature methods with the FEM data but performed similarly as the curvature methods with the experimental data. The authors also found that increasing the number of measurement points improved the

localization resolution of the three curvature-based methods; meanwhile, increasing the number of modes considered did not improve performance. Fan and Qiao (2011) comprehensively reviewed four major categories of damage detection methods, namely, natural frequency-based, mode shape-based, mode shape curvature-based, and mode shape plus frequency-based methods, for beam structures. The authors explored the pros and cons of these methods under different damage scenarios (e.g., single and multiple damages) and measurement conditions (e.g., noise and sensor spacing effects) through numerical simulations.

MSE-Based Damage Detection

Given that MSE-based damage detection is adopted in this thesis, a particular introduction to MSE-based damage detection is presented herein.

Stubbs et al. (1995) proposed a damage index based on MSE change. The index assumes that if damage is primarily located in a single sub-region, the fractional strain energy would remain relatively constant in the other sub-regions. For an Euler–Bernoulli beam, MSE can be computed by integrating the product of flexural rigidity and modal shape curvature along the length of the beam. Later on, Stubbs and Kim (1996) defined damage index as the ratio of the normalized MSE of the structure in undamaged and damaged states. The authors applied this index to the numerical model of a continuous beam, and the results indicated that the index can provide accurate information about the damage location. The index was further extended by Cornwell et al. (1999) to plate structures, where the calculation involved double integration of modal curvature along two coordinate axes. Law et al. (1998) utilized MSE to localize damage with incomplete and noisy measured modal data. The complete analysis procedure was evaluated through a case study on the European Space Agency Structure and a laboratory experiment on a plane frame structure. Shi and Law (1998) discussed the sensitivity of elemental MSE change in structural damage localization and verified its effectiveness through both numerical and experimental examples in consideration of

the effects of measurement noise and incompleteness of the measured modes. Shi et al. (2000b; 2002) analytically derived the sensitivity of MSE with respect to local damage and utilized this index not only to detect the structural damage location but also to quantify the damage severity for beam structures. Damage quantification was found to be more sensitive to noise than damage localization. Au et al. (2003) adopted a similar approach but utilized a micro-genetic algorithm instead of the traditional iterative algorithm together with incomplete and noisy modal data from the tests in the damage quantification stage. Guan and Karbhari (2008) formulated an improved damage index that does not rely on numerical differentiation so that the index can enhance the performance of the modal strain method under sparse and noisy measurement. By taking advantage of the recent advancement in moving scanning technology, Hu and Wu (2009) established a scanning damage index related to MSE by moving indices acquired from a local area throughout the entire structure; the authors used the index to localize and quantify damage in a plate. Yan et al. (2010) derived a closed-form sensitivity of elemental MSE, in which only one eigenvector with sufficient accuracy is required and used for damage detection. A statistic structural damage detection approach that employs ambient vibration measurements was proposed by Yan and Ren (2012). Fang and Qiao (2012) presented a plate damage identification method that combines two factors derived from elemental MSE, that is, damage location factor matrix and damage severity correction factor. This method consists of three steps: sensitive mode selection, damage localization, and damage quantification. Wang (2013) presented an iterative MSE method to estimate damage severity with lower modal frequencies that can be easily acquired and are more reliable than the commonly used mode shapes of the damaged structure. Grande and Imbimbo (2014) adopted a data-fusion technique to improve the performance of MSE-based damage localization and quantification method in the presence of noise and multiple damages. Entezami and Shariatmadar (2014) introduced a correlation of MSE in damage localization to overcome limitations, such as spatially incomplete modes and simplifications in structural modeling, and utilized the Tikhonov regularization method to enhance the robustness of damage quantification. Feasibility and effectiveness were verified through

numerical studies on a planar truss and portal frame. Liu et al. (2014) defined a series of stiffness-correction factors to calculate the measured MSE and then applied these factors to locate damages in both numerical and experimental jacket-type offshore wind turbines. Guo and Li (2014) deduced an energy equivalence equation that forms an accurate expression of MSE before and after damage. The four roots of the equation were utilized to formulate a damage index to identify multi-damage locations and extents.

1.2.1.2 Time-Domain Damage Detection Methods

Although frequency-domain damage detection methods have been extensively explored, several limitations have also been identified. For example, frequencies are often insensitive to local damages but extremely sensitive to temperature and other environmental changes. Frequency changes induced by damage are generally quite small (<5%); changes of 5% to 10% caused by temperature and other environmental conditions are common. Moreover, different cases of damage may result in a similar frequency change (Salawu 1997). Damage detection methods based on mode shapes require measurements at sufficient locations and thus have limited applicability in actual implementations. Hence, another type of detection methods called time-domain damage detection methods has been receiving an increasing amount of interest.

Early studies directly utilized time histories of acceleration, velocity, and displacement responses to detect structural damage (e.g., Li and Mau 1991; Ghanem and Shinozuka 1995). Cattarius and Inman (1997) compared displacement and velocity response time histories induced by a simple harmonic input to reveal the existence of damage in cases when the measured frequency shifts of structures are minimal. This method is independent of modal parameters and analytical models. Choi and Stubbs (2004) expanded the measured response in the time-domain over the structure and used the mean strain energy for a specified time interval for each element to localize and quantify damages. Xu and Chen (2004) conducted an experiment on the applicability of empirical mode decomposition (EMD) identifying damage caused by sudden changes in

structural stiffness. The results showed that the time instances when damage occurs can be accurately detected by observing spikes extracted directly from the measurement data; the damage location can be determined by the spatial distribution of the spikes along the structure. Chen and Xu (2007) proposed a corresponding damage index to estimate damage severity. Kang et al. (2005) presented a time-domain algorithm to estimate structural parameters by minimizing a function defined by the time integral of the least-squared error between the measured and calculated responses. The validity of this algorithm was demonstrated by conducting a numerical study on a two-span truss bridge and an experimental study on a three-story shear building model. Yang et al. (2006a; 2007a) proposed a sequential nonlinear least-squares approach to identify structural parameters and unmeasured excitations. The proposed approach was verified using the Phase I ASCE structural health monitoring (SHM) benchmark building. Then, an adaptive technique that can track the changes in system parameters was developed based on the extended Kalman filter approach (Yang et al. 2006b; Yang et al. 2007b). Lu and Law (2007a; 2007b) calculated dynamic response sensitivity under sinusoidal, impulsive, and random excitations with respect to a perturbation of structural parameters and provided a corresponding model updating method to identify both structural damage and input excitation force. Simulation studies and laboratory tests were performed to verify the effectiveness and accuracy of the method under measurement noise and initial model errors. Acceptable results could be obtained even with different types of model errors if a large amount of measured data is available. Meanwhile, Law et al. (2006) derived the sensitivity of the wavelet coefficient from structural responses with respect to system parameters to detect structural damage. The derived wavelet coefficients were found to be highly sensitive to structural response but are insensitive to different types of model errors in the initial model, including support stiffness, mass density, flexural rigidity, damping ratio, and excitation force. To reduce the effect of uncertainty in excitation at different testing states, unit impulse-induced response instead of dynamic response was considered by Law and Li (2007). Link and Weiland (2009) evaluated damage detection based on model updating in consideration of modal residuals (natural frequencies and mode shapes) and dynamic response time

history residuals via an experiment on a simple structure with high-resolution measurements. Fu et al. (2013) identified damages in plate structures through response sensitivity-based model updating in the time domain, in which only short time histories of a few measurement points are required. Jiang et al. (2014) developed multi-particle swarm coevolution optimization in the time domain to localize and quantify the damages in an experimental seven-story steel frame. The results revealed better noise tolerance than traditional genetic algorithm-based methods. Zhu et al. (2014) proposed a transmissibility concept-based approach to identify input force and structural damage simultaneously. Numerical and experimental examples of a cantilever beam indicated that this approach can detect damage locations and extent accurately. Based on the dynamic equations of undamaged and damaged structures, Chen and Maung (2014) established a relationship between damage-induced change in structural parameters and dynamic response and developed a corresponding damage detection approach directly from the measured dynamic response. The Tikhonov regularization method and L-curve criterion were employed to enhance the stability of the damage identification results.

Moving Load-Based Damage Detection

Damage detection based on moving load-induced structural response is often regarded as a type of time-domain damage detection method. This damage detection method is particularly interesting because moving loads are close to the actual conditions of vehicles passing on bridges; in addition, the method can excite structural vibrations with large amplitudes and high signal-to-noise ratios (Link and Weiland 2009). Furthermore, such a time-domain method requires relatively few sensors when applied in large-scale structures (Li and Zhao 2006). Majumder and Manohar (2002) proposed a damage detection scheme for local or distributed loss of stiffness in beam structures by using vibration data generated by a single moving oscillator. This scheme properly considers the time-varying structural matrices, structural nonlinearity, and spatial incompleteness of measurement data. Bu et al. (2006) proposed a parameter detection approach for a multi-span continuous beam with different moving vehicle models, namely, single-DOF,

two-DOF, and four-DOF systems; the vehicle parameters were assumed to be known when the dynamic response was calculated. For situations with unknown vehicle parameters, Lu and Liu (2011) presented a technique to identify both bridge damages and vehicle parameters simultaneously from the structural dynamic response time history and investigated the effects of measurement noise, vehicle model, and modeling error. Li and Law (2012) established a damage detection process for a sub-structure under moving vehicular excitation by using dynamic response reconstruction technique, which requires only the FEM of the intact concerned substructure and the measured dynamic acceleration responses of the concerned substructure in the damaged state. Kim and Kawatani (2008) developed a pseudo-static formulation from the equation of motion of vehicle–bridge coupled vibration system for damage detection in consideration of the effect of road surface roughness. Numerical examples revealed that vibration data obtained with vehicle speed, which are different from those used in updating the baseline model, have limited influences on damage detection accuracy. Subsequently, Chang et al. (2014) investigated the feasibility of this formulation as well as the effects of the dynamic parameters and running speed of a vehicle via a moving vehicle laboratory experiment. They found that adopting high vehicle speed and a vehicle with frequency close to that of the bridge increases the probability of damage identification. Cavadas et al. (2013) evaluated the performance of two data-driven methods, namely, moving principal component analysis and robust regression analysis, in detecting the occurrence and location of damage on a simple frame subjected to a point-load. They recommended combining the two methods in structural condition assessment. Li and Au (2014) presented a multistage damage localization strategy that employs the dynamic response of a vehicle moving over a bridge. Possible damage locations were estimated through an MSE-based method, and the exact locations were identified through a genetic algorithm-based global optimization method. The bridge frequencies extracted through EMD were utilized. Afterward, the authors proposed a method to simultaneously identify structural damage and road roughness profile (Li and Au 2015). Kong et al. (2014) examined the feasibility of using the dynamic response transmissibility of moving vehicles to detect bridge damages. Two approaches to

measure the transmissibility of vehicle responses were proposed, and the effects of measurement numbers, road roughness, and vehicle speed on the damage detection results were investigated.

Most of the aforementioned damage detection methods rely on the model updating technique, which often involves a time-consuming iterative optimization process. Several other methods exploit the idea that structural damages cause local singularity in response time history that may be visualized after special signal processing, such as wavelet transform (WT) and Hilbert–Huang transform (including EMD and Hilbert transform). An advantage of such methods is that a *priori* information about the response of the intact structure is not required. Zhu and Law (2006) performed continuous WT on the operational displacement response of a bridge subjected to a constant moving load and detected the crack from sudden changes in the spatial variation of the transformed response. The damage extent was estimated by a wavelet coefficient-based indicator. Based on this study, Hester and González (2012) utilized multiple scales instead of single scale wavelet to improve damage localization results and suggested the use of low vehicle speed and multiple sensor locations. Apart from the dynamic response of the bridge, the vertical response of a moving vehicle can also be utilized for damage detection. Nguyen and Tran (2010) applied WT on dynamic response measured directly from a sensor attached to a vehicle with low moving velocity to detect multi-cracks on beam structures. Zhang et al. (2012) extracted structural mode shape squares from the acceleration response induced by a passing tapping vehicle to detect damage in beam and plate structures. This method is time efficient and easy to implement because it does not require many preinstalled sensors. Zhang et al. (2013) extended this method to the situation where the mode shape squares in the damage state are available only by assuming that the intact structure is smooth and homogenous. Khorram et al. (2012) compared the performances of two wavelet-based damage detection approaches. A sensor was installed at the mid-span of the beam and on the moving load individually. The moving-sensor approach was found to be more effective than the fixed-sensor approach. Meredith et al. (2012) applied a moving

average filter and EMD together to the moving load-induced acceleration response of a beam to localize damage. They claimed that using a moving average filter prior to EMD improves sensitivity to damage. The influences of the number of measurement points and the distance of these points to the damaged sections on the accuracy of the predicted damage were also explored. Roveri and Carcaterra (2012) utilized Hilbert–Huang transform to identify the presence and location of damage along a bridge structure subjected to a moving load. The damage detection results were insensitive to crack depth and ambient noise but were significantly affected by damage location and speed of the moving load. Li and Au (2011) identified damage locations by applying continuous WT on the response of a vehicle moving on a damaged bridge with a smooth road surface. The authors extended their technique to locate damages on a bridge with a rough road surface by installing a sinusoidal exciter on a vehicle (Li and Au 2013).

1.2.1.3 Multi-Scale FEM in SHM

As explained in Section 1.1, a multi-scale FEM that can reduce the number of DOFs is appealing in the field of SHM in consideration of computation accuracy and efficiency. Chan et al. (2007) proposed a multi-scale model for Tsing Ma Bridge, a long-span suspension bridge in Hong Kong. This model successfully integrates detailed geometric models of the most vulnerable joints into a global model; thus, hot-spot stress can be directly analyzed to assess fatigue damage. Li et al. (2009) investigated the strategy of developing concurrent multi-scale FEM of civil infrastructures at different scales wherein a large-scale model is adopted for the global responses of structures with a linear behavior and a small-scale model is used for nonlinear damage analysis of the local welding. The final model was applied to the cable-stayed Runyang Bridge (Chan et al. 2009). Ding et al. (2010) developed a multi-scale FEM that combines a global-scale model for modal analysis of the entire bridge and local-scale models for local stress analysis of the concerned components for a long-span cable-stayed bridge. The model analysis results agreed well with the measured dynamic properties from ambient vibration tests and measured stress distributions of a steel box girder from moving

vehicle tests. Wang et al. (2013) provided a multi-objective optimization technique to update the concurrent multi-scale model of long-span bridges, with emphasis on forming an objective function, applying constraint conditions, and selecting an optimization algorithm. Field tests on a cable-stayed bridge were conducted to verify the technique on both global and local levels. Zhu et al. (2014) established a multi-scale FEM for a cable-stayed bridge. Shell elements were adopted to simulate the twin-box deck of the bridge, and beam or truss elements were used for the other components. Each segment of the girder was condensed into a super-element by using the sub-structuring method. This model can achieve balance between the modeling of detailed geometry and computation time. Furthermore, Xiao et al. (2014) updated the multi-scale model by minimizing an objective function that involves both dynamic response (modal frequencies) and static response (displacement and stress influence lines). The response surface method was adopted in the updating process to enhance computation efficiency.

The sub-structuring method has also been utilized to reduce the number of DOFs in FEM. Perera and Ruiz (2008) proposed a sub-structure method, in which a complete structure is divided into several sub-structures for multi-scale damage identification and analysis only focuses on one sub-structure with a small number of DOFs. Bakhary et al. (2010) employed a multi-stage artificial neural network model and progressive sub-structure zooming to establish a damage detection approach. The effectiveness of the approach was demonstrated by numerical studies on a two-span continuous concrete slab and a three-story portal frame. Kong et al. (2012) proposed a sub-structure method for a long-span bridge composed of steel and concrete segments. The entire structure with many sub-structures was modeled in detail, and all the sub-structures were condensed into super-elements except for the highly important steel–concrete joints.

1.2.2 Application of Wavelet in Structural Engineering

1.2.2.1 Multi-Resolution Wavelet Analysis

WT is a mathematical technique developed to convert a function or signal into another

form that makes certain features of the original function or signal clearer for further study or identification. Multi-resolution analysis is one of the most important characteristics of wavelets (Sweldens 1996; 1997; Mallat 1988; Chui 2009). A multi-resolution analysis R of L^2 is a sequence of closed sub-spaces $R = \{V_j \subset L^2 \mid j \in Z\}$, such that (Chui 2009)

- 1) $V_j \subset V_{j+1}$
- 2) $\bigcup_{j \in J} V_j$ is dense in L^2
- 3) for each $j \in J$, V_j has a Riesz basis given by scaling functions $\{\phi_{j,k} \mid k \in K(j)\}$, where j is the level of resolution, J is an integer index set associated with resolution levels, $K(j)$ is some index set associated with the scaling functions of level j , and V_j denotes the approximation spaces of level j . For each V_j , a complement of V_j exists in V_{j+1} , namely, W_j . Let spaces W_j be spanned by wavelets, $\psi_{j,m}(x)$ for every $m \in M(j)$, $M(j) = K(j+1) \setminus K(j)$, where $M(j)$ is the difference set of $K(j+1)$ and $K(j)$. Furthermore, let $l \in K(j+1)$ be the index at level $j+1$.

According to multi-resolution analysis theory, finite energy functions $f(x) \in L^2(R)$ can be approximated with different levels of precision in the corresponding space V_j , where the approximation space V_j is spanned by the scaling functions $\phi_{j,l}$.

$$\phi_{j,l}(x) = \phi[2^j(x-l)] \quad (1.1)$$

For example, function $f(x)$ can be approximated in V_0 as

$$f(x) \approx f^0(x) = \sum_l a_{0,l} \phi_{0,l} \quad (1.2)$$

where $\phi_{0,l}$ is the scaling function at scale 0 and $a_{0,l}$ represents the corresponding

wavelet coefficients.

$$a_{0,l} = \langle f(x), \phi_{0,l}(x) \rangle \quad (1.3)$$

Approximation accuracy can be improved by adding terms in wavelet space W_0 .

Therefore, the approximation in space V_1 is

$$f(x) \approx f^1(x) = \sum_l a_{0,l} \phi_{0,l} + \sum_m b_{0,m} \psi_{0,m} \quad (1.4)$$

where $\psi_{0,l}$ is the wavelet function at scale 0 and $b_{0,m}$ is the corresponding wavelet coefficients in space W_0 .

$$b_{0,m} = \langle f(x), \psi_{0,m}(x) \rangle \quad (1.5)$$

By further increasing the approximation order, the wavelet representation of the function approaches the exact function when $j \rightarrow \infty$.

$$f(x) \approx f^j(x) = \sum_l a_{0,l} \phi_{0,l} + \sum_j \sum_m b_{j,m} \psi_{j,m}, \quad f(x) = f^{j \rightarrow \infty}(x) \quad (1.6)$$

1.2.2.2 Multi-Scale Wavelet-Based Signal Processing

Discrete WT (DWT) is a commonly utilized mathematical tool in signal processing. Emphasized as the main merit of wavelet, the multi-scale (or multi-resolution) feature enables the analysis of signals at different scales in the time-frequency domain (Mallat 1988; 1989; 1998; Koc 1994; Strintzis 1996; Christian 2009). The signal is passed through a series of high-pass filters to analyze high frequencies and is passed through a series of low-pass filters to analyze low frequencies. As illustrated in Figure 1.2, DWT decomposes a signal into approximation part A_i and detail part D_i , where $i=1, 2, \dots, j$ denotes the decomposition level. Filtering at each level is associated with the decimation of data size by a factor of 2. The approximations correspond to the low-frequency part, whereas the details correspond to the high-frequency part (Christian 2009).

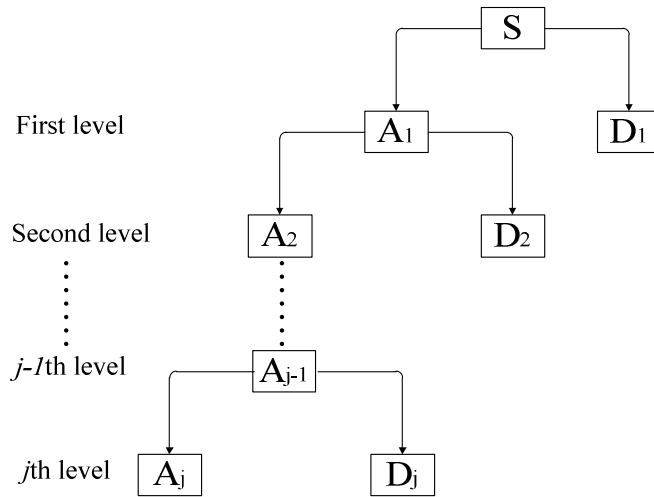


Figure 1.2. Wavelet decomposition of a signal

This salient feature of DWT has various applications in the field of signal processing related to system monitoring. He et al. (1996) decomposed signals into independent frequency bands via DWT, which contains much independent dynamic information because of the orthogonality of wavelet functions, for condition monitoring and fault diagnosis of machineries. Lee and Tarng (1999) applied DWT to monitor tool failure in milling operations. Experimental results showed that tool failure in milling operations can be clearly detected even under varying cutting conditions. Gaouda et al. (1999) employed DWT to monitor power quality problems generated by the dynamic performance of industrial plants. Results indicated that DWT can detect and localize transient events and classify power quality disturbances. Later on, Gaouda et al. (2000) decomposed signals into different resolution levels via DWT to detect, classify, and quantify short duration variations in an electrical distribution system.

1.2.2.3 Multi-Scale Wavelet-Based Finite Element Modeling

WFEM that employs wavelet functions or scale functions as elemental interpolating functions is an emerging numerical method developed in recent years. WFEM has attracted an increasing amount of attention in the field of numerical computation and structural analysis (Li and Chen 2014). The advantages of WFEM include its multi-resolution and localization properties. WFEM provides various basis functions for

structural problems with a high local gradient, such as material nonlinear, local damage, and cracking problems. Various wavelets have been utilized in WFEM. These wavelets include Daubechies wavelet (Ko et al. 1995; Cheng et al. 2006; Diaz et al. 2009), spline wavelet (Chen and Wu 1995; Cheng et al. 2010), trigonometric wavelet (He et al. 2012; He and Ren 2012; 2013a; 2013b), and Hermite wavelet (Xiang and Liang 2011; Wang et al. 2011; He et al. 2013). The types of elements include truss element (Wang et al. 2011), Timoshenko beam element (Wang et al. 2011; Wang and Wu 2013), Euler–Bernoulli beam element (Han et al. 2005; He and Ren 2012), plate element (Han et al. 2006), and solid element (Han et al. 2006).

Ko et al. (1995) constructed wavelet elements in a regular region via the orthogonal and compact Daubechies wavelet function and studied 1D and 2D Neumann problems. The resultant elements can be viewed as generalizations of the connection coefficients employed in the wavelet expansion of periodic differential operators. Chen and Wu (1995; 1996) solved the truss and membrane vibration problems by using elements constructed by a spline wavelet and derived the lifting algorithm that exploits the "two-scale relation" of wavelets. Patton and Marks (1996) utilized 1D finite element based on Daubechies wavelet to solve vibration and wave propagation problems and proved that the element can reduce the number of DOFs and the amount of computation time. Canuto et al. (1999; 2000) provided a globally continuous bi-orthogonal wavelet basis in the general domain by introducing appropriate matching conditions across inter-element boundaries and established the construction principle for 1D, 2D, and 3D WFEM. Luo and Zhang (2000) proposed a wavelet element construction method by using wavelet functions with compact support, with focus on large gradient problems. With this method, the additional DOF of a new interpolating pattern was eliminated via static condensation. Castro and Freitas (2001) deduced the hybrid-mixed finite element formation by adopting independent wavelet bases to approximate displacement and stress in the domain and on the boundary. Han et al. (2006) developed various typical elements, such as beam, triangular plane, rectangular plate, tetrahedral solid, and hexahedral solid elements, with high precision and fast convergence by selecting

appropriate spline wavelet scaling functions as the shape functions.

Given that wavelet coefficients have no definite physical meaning, dealing with boundary conditions and the connection between adjacent elements is generally difficult in structural analysis. Zhou et al. (1998; 1999) presented a modified Daubechies wavelet approximation for beam and plate analysis, in which boundary rotational DOFs were explicitly introduced as independent wavelet coefficients. This approximation can deal with both homogeneous and non-homogeneous boundary conditions. Ho et al. (2001) proposed a weak formulation of FEM, including a technique to deal with discontinuous derivatives and an approach to enforce essential boundary conditions using wavelet functions. The authors solved the wave guide problem. By introducing a transformation matrix that transforms the element deflection field represented by the coefficients of wavelet expansions from wavelet space to physical space, Ma et al. (2003) and Cheng et al. (2004) constructed the wavelet beam element based on Daubechies wavelet and B-spline wavelet, respectively. Xiang et al. (2007a), Cheng et al. (2010), and Zhang et al. (2010) constructed 2D wavelet plate finite elements using Daubechies and B-spline wavelets and performed an adaptive analysis on the corresponding structures. Han et al. (2005) deduced a multivariable wavelet finite element formulation and solved the bending problems of thick plates by selecting linear combinations of scaling functions that satisfy the given boundary conditions according to the Hellinger–Reissner generalized variational principle with two kinds of independent variables. Given that displacements and general forces are independent field functions, the method has higher precision and better convergence characteristics than other displacement-based approaches. He et al. (2012) employed trigonometric wavelet function with both good approximation characteristics of the trigonometric function and multi-resolution and localization characteristics of the wavelet to analyze beam structures. Boundary conditions can be processed conveniently as in TFEM owing to the interpolation feature of the trigonometric wavelet. Compared with polynomial interpolation functions that are utilized in TFEM, these elements have a natural advantage to perform vibration and buckling analysis because the trigonometric wavelet

itself has the "wave" property (He and Ren 2012; He and Ren 2013a; 2013b; 2013c). He et al. (2012) employed trigonometric WFEM to calculate the stress intensity factors of plane stress problems with cracks based on the displacement extrapolation technique and provided wavelet hierarchical and multi-resolution approaches to improve the calculation accuracy.

Second-generation wavelets (SGWs) are also adopted in the field of WFEM. Compared with traditional wavelets that rely on Fourier transform, SGWs are established through a lifting scheme that consists of split, predict, and update steps (Sweldens 1996; 1997). SGWs enable users to define a wavelet according to specific requirements by lifting the initial wavelet (Sweldens 1996; 1997). Amaratunga and his collaborators performed systematic work on multi-resolution WFEM based on SGWs (Sudarshan et al. 2003; Amaratunga and Sudarshan 2006). Based on their research, He et al. (2007a; 2007b) and Wang et al. (2011) discussed multi-resolution analysis for Lagrange and Hermite finite element space and constructed adaptive wavelet elements via the lifting scheme according to the operators of actual structural problems. SGWs possess an advantage that can be customized to make the finite element equation scale-decoupled for static analysis. In other words, a low-scale result can be obtained in a low-scale space, and a high-scale result with improved accuracy can be obtained by resolving it in the corresponding detail spaces independently (Li and Chen 2014).

WFEM has recently been applied in the field of structural damage detection. Li et al. (2005) proposed a methodology to detect the location and size of a crack in beam structures and exploited WFEM in the modal analysis of singularity problems. First, the relationship function between the first three natural frequencies and crack location and size was formulated through surface-fitting techniques and 3D plots. Second, crack location and size were identified through the intersection points of the three contour lines with the input of the measured frequencies of the damaged structure. Xiang et al. (2007b) utilized a similar procedure with B-spline wavelet based Rayleigh–Euler and Rayleigh–Timoshenko elements to estimate crack location and size in a rotor system.

Experimental results revealed the high performance of this technique in prognosis and quantitative diagnosis. Afterward, Dong et al. (2009) introduced EMD and Laplace wavelet to acquire modal parameters with high precision and help improve the accuracy of WFEM-based crack identification in a rotor system. Ye et al. (2010) presented a crack localization and size identification method based on the stress intensity factor and second-generation WFEM for a pipe structure. Numerical and experimental results validated the algorithm and revealed its advantages over TFEM. For inverse problems, back propagation neural networks were adopted by Xiang et al. (2009) to enhance the robustness and stability of the WFEM-based crack identification method. The genetic algorithm was employed by Wang et al. (2014) to reduce the computational cost. Xiang and Liang (2011) extended the detection method from single crack to multiple cracks with the root-mean-square of the differences between the measured and numerical frequencies as a search criterion in the inverse problem analysis. Considering that modal parameters obtained from testing are normally contaminated by noise, obtaining robust damage identification results with the abovementioned crack identification methods is difficult because these methods use natural frequencies only. Hence, Xiang et al. (2011; 2013a) and Xiang and Liang (2012) developed a two-step crack detection approach that combines natural frequency and mode shape. First, WT was applied to the modal shape to determine the crack location. Second, the relationship database between natural frequencies and crack depths constructed via WFEM was employed to estimate crack depth following the same procedure mentioned above. Numerical and experimental examples of beam, plate, and shell structures with single and double cracks were provided to examine the effectiveness of the two-step approach. The authors also recommended the use of interval wavelets to avoid the boundary distortion phenomenon in crack localization. By using operational deflection shape instead of mode shape, Xiang et al. (2013b) further extended the method to in-operation structures under harmonic force excitation.

1.2.3 Remarks

1.2.3.1 Challenges in FEM during Damage Detection

A multi-scale FEM whose resolution is compatible with damage scenarios and external load conditions would be promising and attractive because it would ensure both the accuracy and efficiency of damage detection. Such an FEM can reduce the number of DOFs in the structural model and the number of parameters to be optimized during model updating.

To reduce the number of updating parameters during damage detection through FEM updating, Teughels et al. (2002) proposed a parameterization method called damage function, which assumes that the correction factors of updating parameters vary continuously throughout FEM. The authors successfully applied this method to a reinforced concrete beam and to the Z24 Bridge in Switzerland modeled with 1D beam elements (Teughels and Roeck 2004). Fang et al. (2008) extended the 1D damage function to 2D structures to enhance the modeling capability. Perera and Ruiz (2008) developed a multi-stage damage detection scheme for large-scale structures. In the first stage, damage occurrence was detected with approximate locations. In the second stage, probable damaged areas were selected, and the exact locations and severities of the damaged members were estimated. Different objectives, identification algorithms, and spatial configurations of sensors were adopted in different stages. Although the aforementioned parameterization method reduces the number of updating parameters, the number of DOFs may still be large in a delicate FEM.

To reduce the number of DOFs, several researchers have explored the use of multi-scale FEM (Chan et al. 2007; Li et al. 2009; Chan et al. 2009; Ding et al. 2010; Wang et al. 2013; Zhu et al. 2014; Xiao et al. 2014) and sub-structure models (Perera and Ruiz 2008; Bakhary et al. 2010; Kong et al. 2012) in SHM. However, these models often depend on empirical judgment of critical zones and remain unchanged during the entire process, which may not fully satisfy the requirement of progressive damage detection. To

improve damage detection efficiency and accuracy, several multi-step damage detection processes, such as "location–quantification" (Shi et al. 2000b; 2002), "identify the general area of structural damage–locate a specific damaged structural component" (Kim and Bartkowicz 1997), "identify damage occurrence–classify damage type–locate and quantify damage" (Kim et al. 2010), have been presented.

The requirement to reconstruct stiffness and mass matrices and repeat the entire computation process makes realizing a multi-scale model in the context of TFEM challenging. WFEM, whose resolution can be modified conveniently, is particularly suitable for multi-scale structural analysis and damage detection. Several researchers have utilized WFEM to detect damage by establishing a database of the natural frequency–crack parameter relationship (Li et al. 2005; Xiang et al. 2007b; 2009; 2011; 2013a; 2013b; Dong et al. 2009; Ye et al. 2010; Xiang and Liang 2011; 2012; Wang et al. 2014). However, these forward problem-based damage detection methods only use WFEM to perform modal analysis and demonstrate the high computation efficiency of the method. The most important multi-resolution and localization features of WFEM, which are useful for adaptive-scale structural analysis, damage localization, and quantification, have not been studied. In addition, the applications of WFEM in civil engineering are largely limited by the fact that the previous studies only used frequency changes that are not sufficiently sensitive to structural local damages and because of the difficulty in establishing a comprehensive damage database for complicated structures.

1.2.3.2 Challenges in Moving Load-Based Damage Detection

In moving load-based damage detection, a feasible solution to reduce the number of updating parameters is to locate damages first and then select updating parameters in the damaged regions only. Previous studies applied special signal processing tools to the moving load-induced response to determine the damage locations (e.g., Zhu and Law 2006; Nguyen and Tran 2010; Hester and González 2012; Meredith et al. 2012; Roveri and Carcaterra 2012; Khorram et al. 2013; Zhang et al. 2012; 2013). However, a fundamental problem that has failed to elicit adequate attention is how local damages

affect the moving load-induced structural dynamic response. The answer to this issue is essential in developing a damage localization algorithm. Gonzalez and Hester (2013) divided the moving load-induced acceleration response into static, dynamic, and damage components and developed a damage detection algorithm that can make the damage component more consistent than the other two components. However, the authors did not provide a theoretical basis accordingly. Yang et al. (2004a) deduced the closed-form solution of the moving load-induced dynamic response of an undamaged simply supported beam. Yang and Lin (2005) stated that the dynamic response of a beam consists of two components, namely, the moving-frequency component that corresponds to the moving load and the natural-frequency component that corresponds to the natural frequencies of the beam. Investigating the closed-form solution of the dynamic response of a damaged simply supported beam subjected to moving load and examining the effects of local stiffness loss on these two components would provide deep insights into damage detection methods based on moving load-induced response.

1.3 Research Objectives

This work aims to develop multi-scale structural damage detection strategies in both frequency- and time-domain by utilizing the novel WFEM. Such strategies would achieve optimal matching among structural modeling resolution, damage scenarios, and external load conditions. In addition, such strategies are very efficient with regard to the number of DOFs in structural FEM, number of sensors, and computation cost. The main research objectives are summarized as follows.

- (1) To develop multi-scale WFEM-based damage detection methods in the frequency-domain for beam and thin plate structures. Sub-element damage can be detected in a progressive manner. The suspected damage region is initially identified with a low-scale structural model, and the more accurate damage location and severity can be estimated with a multi-scale model with local refinement. The model resolution

always remains compatible with actual damage scenarios during the progressive detection process.

(2) To develop a two-phase (i.e., localization and quantification) damage detection approach for beam structures under moving load with high efficiency and accuracy. In this approach, damages are located by separating the dynamic response via multi-scale DWT and quantified via multi-scale WFEM updating in a progressive manner. This approach includes the following two parts.

- To investigate local damage effects on moving- and natural-frequency components of the moving load-induced dynamic response of a simply supported beam and develop a corresponding simple and efficient damage localization algorithm.
- To present a multi-scale WFEM updating strategy with updating parameters limited to the localized damage regions alone to estimate the damage severity in a progressive manner. The elemental scales of WFEM change dynamically according to not only the time-varying moving load-structural contact position but also to the progressively identified damage scenarios.

1.4 Thesis Outline

This thesis comprises seven chapters.

Chapter 1 introduces the research background and motivation, literature review, research objectives, and thesis organization. The literature review focuses on two main parts: (1) vibration-based damage detection methods, with particular emphasis on MSE-based and moving load-based damage detection methods; and (2) application of multi-scale wavelet in structural engineering, including signal processing and structural modeling.

Chapter 2 derives multi-scale dynamic formulations and corresponding lifting schemes for beam and thin plate structures, including a particular case of multi-scale formulation of beam structures subjected to moving load excitation in the context of cubic Hermite WFEM. These formulations are the theoretical bases of progressive multi-scale damage detection. The advantages of using WFEM over TFEM are also discussed.

Chapter 3 presents a multi-scale damage detection method to detect sub-element damage in beam and plate structures progressively based on WFEM and MSE. A coarse WFEM is utilized to identify the likely damaged region, and gradually lifted WFEMs with local refinement are utilized to estimate the accurate location and severity of the damage. During damage detection, a limited number of sensors are added in the corresponding critical regions. Numerical examples with different damage scenarios indicate that the proposed strategy is very efficient in terms of the number of DOFs, number of sensors, and computation effort.

Chapter 4 presents a multi-scale damage detection method to detect sub-element damage in beam and plate structures progressively based on WFEM updating technique with an objective function that combines structural frequencies and MAC. The scales of the wavelet elements in the regions of concern are adaptively enhanced and reduced to remain compatible with the gradually identified damage regions. The test modal information remains the same, that is, no sensor replacement or addition is required. Numerical and experimental examples reveal that the proposed method can identify structural damage with satisfactory accuracy and reduced number of DOFs in the model and updating parameters during optimization. Finally, the advantages and disadvantages of the two methods presented in Chapters 3 and 4 are compared.

Chapter 5 firstly derives the closed-form solution of the dynamic response of a simply supported damaged beam under moving force. Then, the damage effect on the different components of the dynamic response is investigated, and a simple and efficient damage localization approach using DWT is presented. Numerical examples with single and multiple damages are utilized to validate the efficacy of the response computation

algorithm and demonstrate the effectiveness of the corresponding damage localization approach.

Chapter 6 presents the development of an adaptive-scale analysis strategy for beam structures under moving load using WFEM, in which the scales of wavelet elements are dynamically changed according to moving load–beam contact positions. A highly efficient and accurate two-phase damage detection approach that integrates DWT-based damage localization in Chapter 5, progressive damage detection in Chapter 4, and the adaptive-scale analysis strategy is then proposed. First, multi-scale DWT is adopted to decompose the change in the dynamic displacement response induced by moving load and localize damages. Second, WFEM updating, with updating parameters limited to the identified damage regions alone, is employed to estimate the accurate damage location and severity in a progressive manner. The elemental scales of WFEM change dynamically not only according to the moving load–structure contact positions but also to the damage scenarios. A laboratory experiment is conducted to examine the feasibility and effectiveness of the proposed two-phase method. The results indicate that the proposed method achieves optimal matching among structural modeling, damage scenarios, and load conditions, as well as between damage detection accuracy and efficiency.

Chapter 7 provides a summary of the main conclusions derived in this study and several recommendations for future research work related to the present one.

Chapter 2 Multi-Scale WFEM

2.1 Introduction

Multi-scale WFEM that employs wavelet functions or scale functions as elemental interpolating functions is the foundation of the multi-scale structural damage detection methods presented in this thesis. Various wavelets have been employed in WFEMs; these wavelets include Daubechies wavelet (Ko et al. 1995; Cheng et al. 2006; Diaz et al. 2009), spline wavelet (Chen and Wu 1995; Han et al. 2006; Cheng et al. 2010), trigonometric wavelet (He et al. 2012; He and Ren 2012; 2013a; 2013b; 2013c), and Hermite wavelet (Xiang and Liang 2011; Wang et al. 2011). Element type includes truss element (Wang et al. 2011), Timoshenko beam element (Wang et al. 2011; Wang and Wu 2013), Euler–Bernoulli beam element (Han et al. 2005; He and Ren 2012; 2013a), plate element (Han et al. 2006), and solid element (Han et al. 2006). The characteristics of multi-resolution and localization make WFEM a powerful tool to analyze fields with gradient changes or singularities, such as material nonlinearity, local damage, and cracks. This chapter presents the principles of selecting an appropriate wavelet element for multi-scale damage detection and the derivation of multi-scale dynamic formulations and corresponding lifting schemes for beam and plate structures. In particular, a multi-scale formulation under moving load excitation is presented for beam structures. The theoretical basis of multi-scale damage detection methods is established subsequently.

2.2 Cubic Hermite Multi-Scale Wavelet

The selection is made among WFEMs based on Daubechies wavelet, B-spline wavelet on the interval, trigonometric wavelet, and cubic Hermite wavelet, which have been

studied comprehensively and systematically. For the multi-scale damage detection method, wavelet elements with high computational efficiency, superior localization feature, and favorable compatibility with TFEM are preferred. Table 2.1 shows a comparison of different wavelet elements in terms of these aspects.

Table 2.1. Comparison of different wavelet elements

Wavelet Type	Computational Efficiency	Localization Feature	Compatibility with Traditional FEM
Daubechies Wavelet	poor	general	poor
B-spline Wavelet on the Interval	good	general	poor
Trigonometric Wavelet	general	general	good
Hermite Wavelet	good	good	good

(1) *Daubechies wavelet*. The disadvantage of this wavelet is that it has no explicit expression. This disadvantage makes traditional numerical integrals (e.g., Gaussian integrals) unable to provide desirable calculation precision (Li and Chen 2014). Furthermore, the transformation matrix utilized to deal with boundary conditions and adjacent element connections leads to complex formulation, time-consuming computation, and difficulties in realizing multi-scale analysis (He and Ren 2013c). Moreover, connecting the Daubechies wavelet to the traditional finite element is difficult.

(2) *B-spline wavelet on the interval*. The explicit expression of B-spline wavelet on the interval facilitates the calculation of the corresponding elemental matrices. However, faces the same problems in the aspects of transformation matrix and connection with the traditional finite element.

(3) *Trigonometric Hermite wavelet*. Given the Hermite interpolatory properties, boundary conditions and the connection between adjacent elements can be processed conveniently without the need for a transformation matrix. Trigonometric Hermite wavelet performs well in structural vibration analysis because of its "wave" properties; trigonometric wavelet composite beam element (He and Ren 2013c) can connect to the traditional finite element directly and conveniently. However, its disadvantages should not be ignored. These disadvantages include increasingly complicated and time-consuming integral operations involved in elemental matrices calculation than the polynomial integral in the traditional finite element (He and Ren 2012) and relatively poor local properties for structural damage localization (the support lengths of scaling and wavelet functions at different scales are the same, which is unsuitable for damage localization).

(4) *Cubic Hermite wavelet*. Although the computational efficiency in terms of the number of system DOFs of the FEM to achieve the same analysis accuracy is not as high as that of the B-spline wavelet on the interval and trigonometric wavelet elements, the computation of elemental matrices is very convenient and time efficient. The local property that enables progressive damage localization and the favourable compatible feature with the traditional finite element make this wavelet appropriate for multi-scale damage detection.

Given the abovementioned favorable characteristics, the second-generation cubic Hermite multi-wavelet (Averbuch et al. 2007; Wang et al. 2011) was adopted in this study. When defined within the interval $[-1, 1]$, the scaling functions of cubic Hermite multi-wavelet consist of two cubic Hermite splines as follows:

$$\phi_{0,0} = [\phi_{0,0}^1(x) \quad \phi_{0,0}^2(x)]^T \quad (2.1)$$

where

$$\phi_{0,0}^1(x) = \begin{cases} (x+1)^2(-2x+1) & x \in [-1,0] \\ (x-1)^2(2x+1) & x \in [0,1] \\ 0 & \text{otherwise} \end{cases} \quad (2.2a)$$

$$\phi_{0,0}^2(x) = \begin{cases} (x+1)^2 x & x \in [-1,0] \\ (x-1)^2 x & x \in [0,1] \\ 0 & \text{otherwise} \end{cases} \quad (2.2b)$$

The refinement relation of scaling functions at arbitrary vertices in two adjacent scales is

$$\mathbf{C}_{j+1} \begin{bmatrix} \mathbf{\Phi}_{j+1} \\ \mathbf{\Psi}_{j+1} \end{bmatrix} = \mathbf{\Phi}_j \quad (2.3)$$

where \mathbf{C}_{j+1} is the refinement coefficient matrix for level $j+1$ and $\mathbf{\Phi}_j = \{\phi_{j,k} : k \in K(j)\}$ and $\mathbf{\Psi}_j = \{\psi_{j,m} : m \in M(j)\}$ are the scaling and wavelet functions at the selected vertices, respectively. Given that Hermite scaling functions have a continuous first derivative at the nodes, the scaling functions have two DOFs at each node, that is, $\phi_{j,k} = [\phi_{j,k}^1(x) \ \phi_{j,k}^2(x)]^T = [\phi^1[2^j(x-k) \ \phi^2[2^j(x-k)]]^T$.

The refinement coefficients (\mathbf{C}_{j+1}) can be computed by solving the simultaneous equations shown in Equation (2.3) at random vertices. The refinement relation of the cubic Hermite scaling functions is

$$\phi_{j,k_2} = \phi_{j+1,k_2} + \begin{bmatrix} \frac{1}{2} & \frac{3}{2h} \\ h & -\frac{1}{4} \end{bmatrix} \phi_{j+1,m_1} + \begin{bmatrix} \frac{1}{2} & -\frac{3}{2h} \\ h & -\frac{1}{4} \end{bmatrix} \phi_{j+1,m_2} \quad (2.4)$$

where h is the length of an element. It corresponds to the following refinement matrix.

$$\mathbf{C}_{j+1} = \begin{bmatrix} 1 & 0 & \frac{1}{2} & \frac{3}{2h} & \frac{1}{2} & -\frac{3}{2h} \\ 0 & 1 & -\frac{h}{8} & -\frac{1}{4} & \frac{h}{8} & -\frac{1}{4} \end{bmatrix} \quad (2.5)$$

Figure 2.1 shows the refinement relation of the cubic Hermite scaling functions and wavelets defined in Equation (2.4) between two adjacent scales. The scaling function at scale j , ϕ_{j,k_2} , has compact support in $[k_1, k_3]$. The scaling function at scale $j+1$, ϕ_{j+1,k_2} , is supported in $[m_1, m_2]$, which is only a half interval of that at scale j .

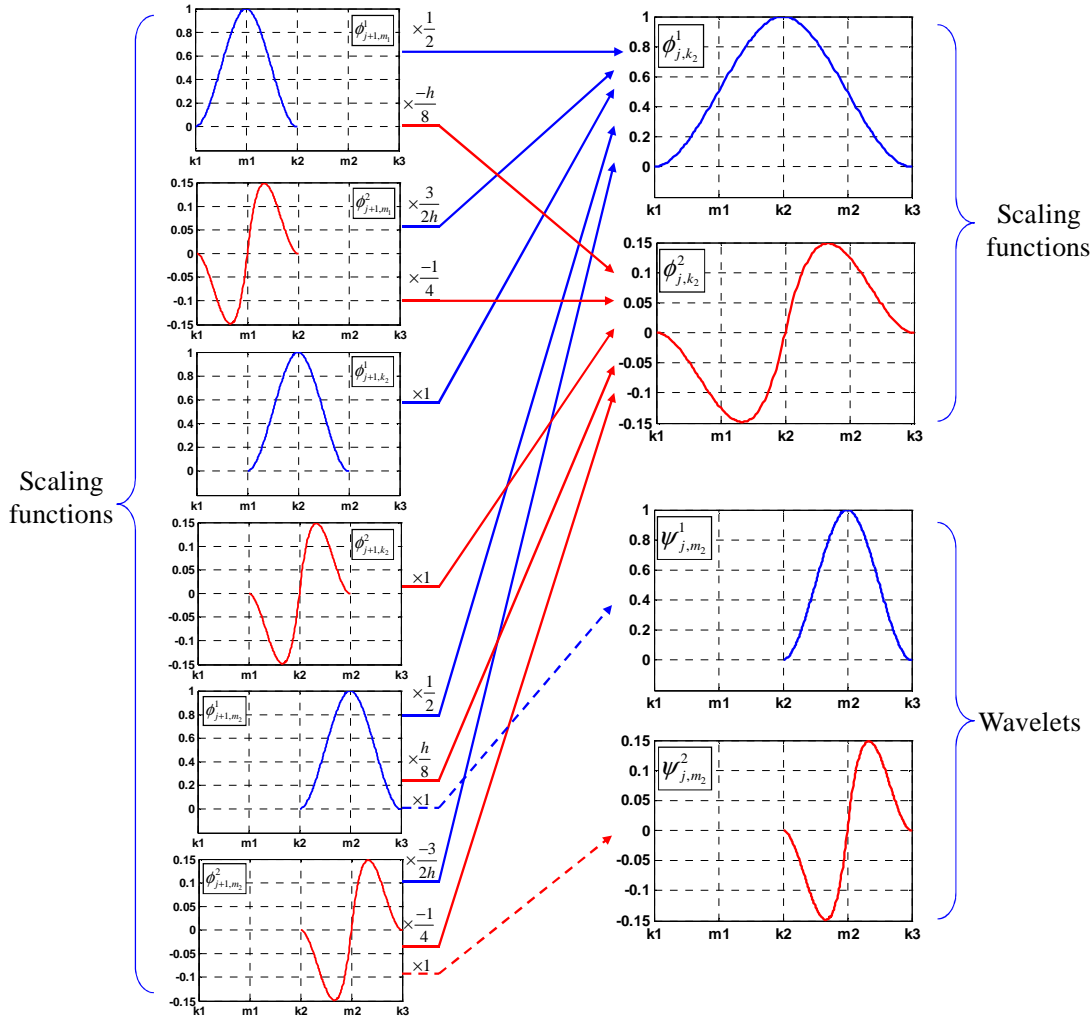


Figure 2.1. The refinement relation for cubic Hermite scaling functions

The wavelets corresponding to the cubic Hermite scaling functions are not unique. Several cubic Hermite wavelet functions have been derived previously (Sudarshan et al. 2003; Amaratunga and Sudarshan 2006; Averbuch et al. 2007; Wang et al. 2011). For example, Sudarshan et al. (2003) constructed cubic Hermite wavelets with four vanishing moments by using the lifting scheme proposed by Sweldens (1996). Another

simple form of cubic Hermite wavelets was constructed and used by Averbuch et al. (2007) and Wang et al. (2011).

$$\psi_{j,m_2} = \phi_{j+1,m_2} \quad (2.6)$$

These multi-wavelets are adopted in this study because of their simplicity and relatively short support length. The wavelets are compactly supported on the interval between two adjacent k -nodes, that is, $[k_2, k_3]$. The Hermite wavelet function also has two DOFs at each node.

The 2D cubic Hermite wavelets of scale j are constructed through the tensor products of 1D wavelets (Wang and Wu 2013; Quraishi and Sandeep 2013). The scaling function consists of four functions as follows:

$$\bar{\Phi}_j^1(x, y) = \Phi_j^1(x) \times \Phi_j^1(y) \quad (2.7a)$$

$$\bar{\Phi}_j^2(x, y) = \Phi_j^1(x) \times \Phi_j^2(y) \quad (2.7b)$$

$$\bar{\Phi}_j^3(x, y) = \Phi_j^2(x) \times \Phi_j^1(y) \quad (2.7c)$$

$$\bar{\Phi}_j^4(x, y) = \Phi_j^2(x) \times \Phi_j^2(y) \quad (2.7d)$$

These functions stand for displacement, y -direction difference, x -direction difference, and diagonal difference of the displacement field. Spanning of the scaling functions $\bar{\Phi}_j = \{\bar{\Phi}_j^1, \bar{\Phi}_j^2, \bar{\Phi}_j^3, \bar{\Phi}_j^4\}$ at scale j forms space F^j . These functions also have a multi-resolution property, $F^0 \subset F^1 \subset \dots \subset F^j$, $F^{j+1} = F^j \oplus G^j$, where G^j is spanned by the corresponding 2D wavelet functions $\bar{\Psi}_j$ of scale j .

$$\bar{\Psi}_j = \bar{\Phi}_{j+1} \quad (2.8)$$

The 2D wavelet at scale $j = 1$ is shown in Figure 2.2.

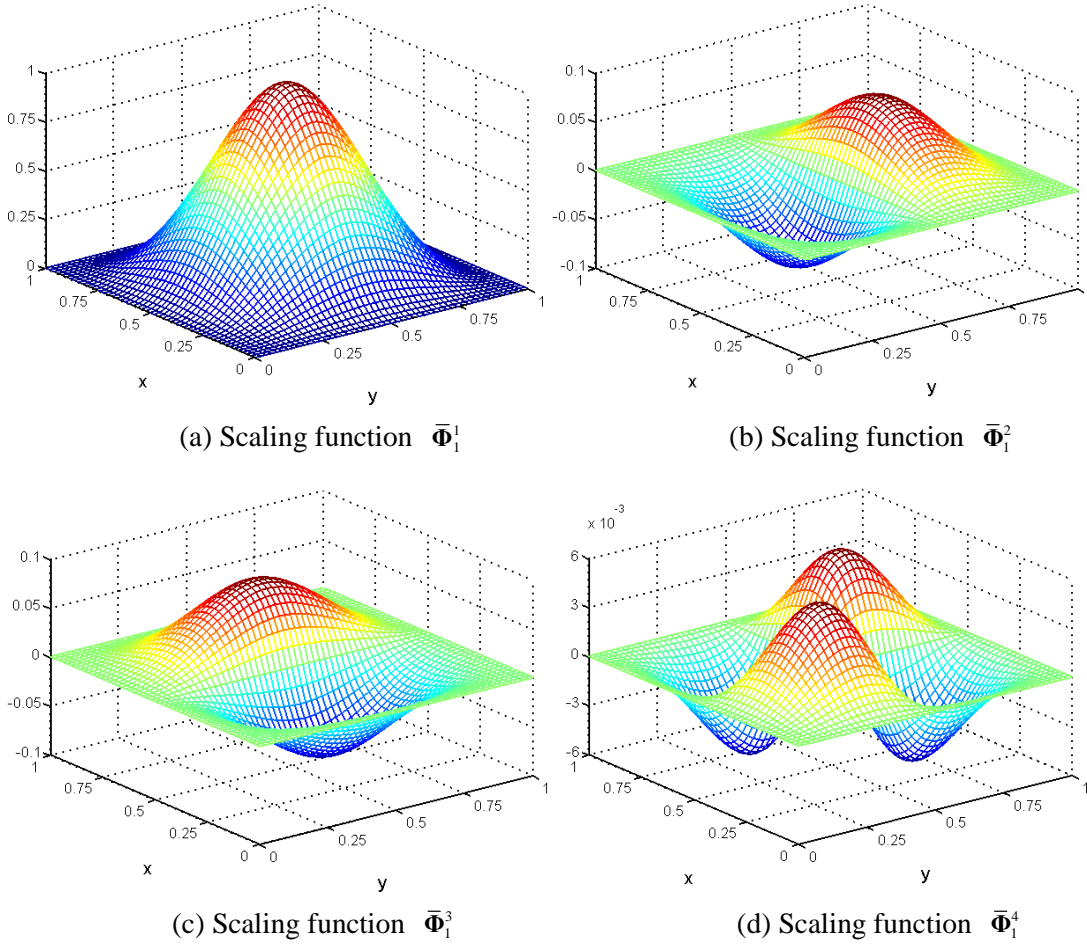


Figure 2.2. 2D tensor products of cubic Hermite functions

2.3 Dynamic Formulation of Multi-Scale WFEM for Beam Structures

Wang et al. (2011) presented a static equation and a corresponding lifting scheme for beam elements based on the cubic Hermite multi-scale wavelet. However, the dynamic parameters and response of structures are often of interest in vibration-based damage detection. Therefore, the dynamic equation for beam structures and the corresponding lifting scheme are formulated in the context of the aforementioned multi-scale WFEM. In particular, the multi-scale formulations of the beam-moving force and the beam-moving vehicle model are presented.

For the Euler–Bernoulli beam, the unknown field w can be approximated with the scaling and wavelet functions of cubic Hermite multiwavelets $\Phi_j = [\Phi_0, \Psi_0, \Psi_1 \cdots \Psi_{j-1}]$

$$w = \sum_k a_{0,k} \phi_{0,k} + \sum_{j=0}^N \sum_m b_{m,j} \psi_{m,j} = \Phi_0 \mathbf{a} + \Psi_0 \mathbf{b}_0 + \Psi_1 \mathbf{b}_1 \cdots + \Psi_{j-1} \mathbf{b}_{j-1} = \Phi_j \mathbf{q}_j \quad (2.9)$$

where Φ_0 represents the scaling functions at scale 0, Ψ_j represents the wavelet functions at scale j , and $\mathbf{q}_j = [\mathbf{a} \ \mathbf{b}_0 \ \mathbf{b}_1 \cdots \mathbf{b}_{j-1}]^T$ is the undetermined vector of wavelet coefficients, which can be regarded as generalized DOFs.

The application of WFEM to the dynamic problem yields the governing equation of motion.

$$\mathbf{M}_j \ddot{\mathbf{q}}_j + \mathbf{C}_j \dot{\mathbf{q}}_j + \mathbf{K}_j \mathbf{q}_j = \mathbf{P}_j \quad (2.10)$$

where \mathbf{M}_j , \mathbf{C}_j , \mathbf{K}_j , and \mathbf{P}_j are the mass matrix, damping matrix, stiffness matrix, and external load vector at scale j , respectively.

$$\mathbf{M}_j = \rho l \int_0^1 \Phi_j^T \Phi_j d\xi = \rho l \int_0^1 \begin{bmatrix} \Phi_0^T \Phi_0 & \Phi_0^T \Psi_0 & \cdots & \Phi_0^T \Psi_{j-1} \\ & \Psi_0^T \Psi_0 & \cdots & \Psi_0^T \Psi_{j-1} \\ & \text{sym} & \ddots & \vdots \\ & & & \Psi_{j-1}^T \Psi_{j-1} \end{bmatrix} d\xi \quad (2.11)$$

$$\mathbf{K}_j = \frac{EI}{l^3} \int_0^1 (\Phi_j'')^T \Phi_j'' d\xi = \frac{EI}{l^3} \int_0^1 \begin{bmatrix} (\Phi_0'')^T \Phi_0'' & (\Phi_0'')^T \Psi_0'' & \cdots & (\Phi_0'')^T \Psi_{j-1}'' \\ & (\Psi_0'')^T \Psi_0'' & \cdots & (\Psi_0'')^T \Psi_{j-1}'' \\ & \text{sym} & \ddots & \vdots \\ & & & (\Psi_{j-1}'')^T \Psi_{j-1}'' \end{bmatrix} d\xi \quad (2.12)$$

Considering the orthogonality of the cubic Hermite multiwavelet, the non-diagonal sub-matrices of \mathbf{K}_j become zero.

$$\mathbf{K}_j = \frac{EI}{l^3} \int_0^1 (\Phi_j'')^T \Phi_j'' d\xi = \frac{EI}{l^3} \int_0^1 \begin{bmatrix} (\Phi_0'')^T \Phi_0'' & & & \\ & (\Psi_0'')^T \Psi_0'' & & \\ & & \ddots & \\ & & & (\Psi_{j-1}'')^T \Psi_{j-1}'' \end{bmatrix} d\xi \quad (2.13)$$

Rayleigh damping can be assumed as $\mathbf{C}_j = a_1 \mathbf{M}_j + a_2 \mathbf{K}_j$, where a_1 and a_2 are two constants in this Rayleigh damping model, EI is flexural rigidity, ρ is the mass per unit length, and Φ_j'' and Ψ_j'' are the second derivatives of the functions Φ_j and Ψ_j with respect to the local coordinate ξ , respectively. The vectors \mathbf{q}_j , $\dot{\mathbf{q}}_j$, and $\ddot{\mathbf{q}}_j$ are the displacement, velocity, and acceleration vector at scale j in the wavelet subspaces, respectively; that is, they are expressed in accordance with the wavelet element. Measurements in dynamic tests are always expressed in general DOFs, but they can be easily converted to those in wavelet DOFs through the Hermite interpolation properties of the adopted multi-wavelets.

Modal characteristics, such as frequencies and mode shapes, can be obtained from the following free vibration formulations of scale j .

$$(\mathbf{K}_j - \lambda \mathbf{M}_j) \mathbf{q}_j = 0 \quad (2.14)$$

where λ is the eigenvalues and \mathbf{q}_j is the mode shapes that are expressed with regard to wavelet DOFs.

For the moving load problem discussed in Chapters 5 and 6, the beam-moving force model and the beam-moving vehicle model based on WFEM are derived in this section. Although only a single moving force/vehicle is presented, the method can be further extended to consider cases with multiple forces/vehicles via linear superposition.

(1) Beam-moving force model

When the mass of a moving vehicle is considerably smaller than that of a beam, the moving vehicle can be approximated by a moving force (Yang and Lin 2005). A simply supported beam model subjected to a moving concentrated force is shown in Figure 2.3. When the beam is modeled by cubic Hermite wavelet beam elements and a single moving force (F) is considered, the external load \mathbf{P}_j in Equation (2.10) becomes a time-varying load vector as follows:

$$\mathbf{P}_j(t) = \begin{bmatrix} \Phi_0^T(\xi(t)) \\ \Psi_0^T(\xi(t)) \\ \vdots \\ \Psi_{j-1}^T(\xi(t)) \end{bmatrix} \cdot F \quad (2.15)$$

where $\xi(t)$ is the local coordinate of the time-varying position and $\Psi_j(\xi(t)) = [\Phi_0^T(\xi(t)), \Psi_0^T(\xi(t)) \cdots \Psi_{j-1}^T(\xi(t))]^T$ is the value of the shape functions at the contact position. Consequently, the external load vector can be expressed as $\mathbf{P}_j = F[0 \ 0 \cdots \Phi_0, \Psi_0 \cdots \Psi_{j-1} \cdots 0]^T$, in which the entries are zero except for those DOFs corresponding to the element on which the moving force is acting upon. The number of DOFs for a single wavelet element depends on the present scale j . The numerical values of the wavelet functions (Ψ_j) and the external load vector (\mathbf{P}_j) change along with the moving force position.

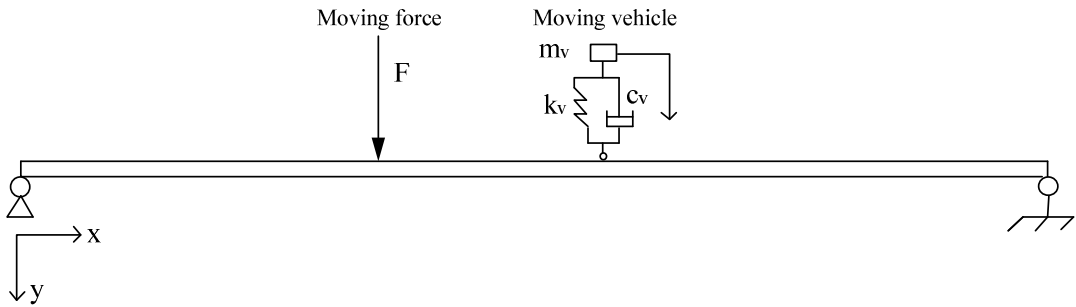


Figure 2.3. Simply-supported beam subjected to a moving force/vehicle

(2) Beam–moving vehicle model

To simulate the dynamics of a vehicle moving on a simply supported beam, the vehicle can be modeled by a single DOF system that comprises a mass connected to the beam through a dashpot and a spring, as shown in Figure 2.3. The single DOF vehicle model proposed by Lu and Liu (2011) involves three parameters: mass m_v , damping c_v , and stiffness k_v of the vehicle. Unlike the moving force model, the moving vehicle model

considers the dynamics of the moving vehicle and the interaction between the vehicle and the beam.

The equations of motion consist of two parts. The part corresponding to the beam structure is the same as the beam–moving force model. The other part for the moving vehicle can be expressed as (Lu and Liu 2011)

$$m_v \ddot{z} + c_v (\dot{z} - \dot{y}(x(t))) + k_v (z - y(x(t)) - r(x(t))) = 0 \quad (2.16)$$

where \ddot{z} , \dot{z} , and z are the vertical acceleration, velocity, and displacement response of the vehicle, respectively. $y(x(t))$ denotes the vertical displacement at the contact point $x(t)$ of the beam, and $r(x(t))$ denotes the road surface roughness at the location of the tire. Vehicle–beam interaction force $IF(t)$ can be expressed as

$$IF(t) = m_v g + c_v (\dot{z} - \dot{y}(x(t))) + k_v (z - y(x(t)) - r(x(t))) = m_v g - m_v \ddot{z} \quad (2.17)$$

where g is the acceleration of gravity.

The vehicle is assumed to maintain contact with the beam, and no separation occurs during the moving process. By combining Equations (2.10) and (2.17), the equations of motion for the vehicle–beam system can be expressed as

$$\begin{bmatrix} \mathbf{M}_j & \Psi_j m_v \\ 0 & m_v \end{bmatrix} \begin{Bmatrix} \dot{\mathbf{q}} \\ \dot{z} \end{Bmatrix} + \begin{bmatrix} \mathbf{C}_j & 0 \\ -\Psi_j^T c_v & m_v \end{bmatrix} \begin{Bmatrix} \mathbf{q} \\ z \end{Bmatrix} + \begin{bmatrix} \mathbf{K}_j & 0 \\ -\Psi_j^T k_v & k_v \end{bmatrix} \begin{Bmatrix} \mathbf{q} \\ z \end{Bmatrix} = \begin{Bmatrix} \Psi_j m_v g \\ k_v r(x(t)) \end{Bmatrix} \quad (2.18)$$

Define $\mathbf{M}_{s,j} = \begin{bmatrix} \mathbf{M}_j & \Psi_j m_v \\ 0 & m_v \end{bmatrix}$, $\mathbf{C}_{s,j} = \begin{bmatrix} \mathbf{C}_j & 0 \\ -\Psi_j^T c_v & m_v \end{bmatrix}$, $\mathbf{K}_{s,j} = \begin{bmatrix} \mathbf{K}_j & 0 \\ -\Psi_j^T k_v & k_v \end{bmatrix}$, $\mathbf{R}_{s,j} = \begin{Bmatrix} \mathbf{q}_j \\ z \end{Bmatrix}$, and

$\mathbf{P}_{s,j} = \begin{Bmatrix} \Psi_j m_v g \\ k_v r(x(t)) \end{Bmatrix}$. Equation (2.18) can be rewritten as

$$\mathbf{M}_{s,j} \ddot{\mathbf{R}}_{s,j} + \mathbf{C}_{s,j} \dot{\mathbf{R}}_{s,j} + \mathbf{K}_{s,j} \mathbf{R}_{s,j} = \mathbf{P}_{s,j} \quad (2.19)$$

Notably, $\mathbf{M}_{s,j}$, $\mathbf{C}_{s,j}$, $\mathbf{K}_{s,j}$, and $\mathbf{P}_{s,j}$ are time-varying and non-symmetric. The dynamic responses of the beam and vehicle can be computed through the time-domain

integration method.

As indicated in Chapter 1, the element scales of WFEM change dynamically not only according to the time-varying contact point between the moving vehicle and structure but also to the progressively identified damage scenarios; the convenient changes in scale are crucial in multi-scale damage detection. In the lifting or lowering procedure between scales, the sub matrices/vectors of the current scale can be retained, and only a few rows and columns need to be added or deleted. The procedure is analogous to the mesh refinement or roughening process in TFEM but is associated with much simpler operations because re-meshing the structures and reconstructing the matrices/vectors are not required. This merit of WFEM increases the efficiency of the computation in the refinement or roughening process and makes the multi-scale modeling technique more effective in multi-scale analyses and damage detection, where the desirable modeling scales are *a priori* unknown or need to be dynamically changed according to different external load conditions and damage scenarios. The new results after refinement can be quickly obtained via iteration, with the initial values equal to the results at the previous scale.

The plane beam-type wavelet finite element for frame structural analysis considers axial and flexural deformation. This element is constructed by the superposition of an axial rod element and an Euler–Bernoulli beam element (Figure 2.4). The traditional two-node rod element (Zienkiewicz and Taylor 1961) is adopted. Refining the rod element is usually unnecessary because axial deformation is relatively uniform in frame structures.

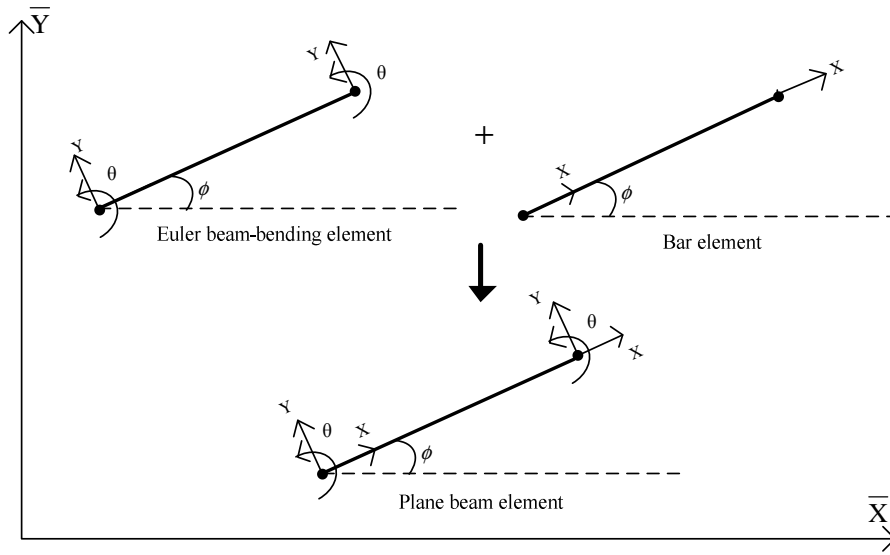


Figure 2.4. Plane beam-type wavelet finite element

2.4 Dynamic Formulation of Multi-Scale WFEM for Plate Structures

A rectangular elastic thin plate with dimensions $l_x \times l_y$ is shown in Figure 2.5. According to classical Kirchoff–Love plate theory, the generalized function of the potential energy of this rectangular elastic thin plate is (Zienkiewicz and Taylor 1961)

$$\Pi_p = \frac{1}{2} \iint_{\Omega} \boldsymbol{\kappa}^T \bar{\mathbf{D}} \boldsymbol{\kappa} dx dy - \frac{1}{2} \iint_{\Omega} \rho t \lambda w^2 dx dy \quad (2.20)$$

where Ω is the solving domain, λ is the vibration eigenvalue, w is the displacement field function, $\boldsymbol{\kappa}$ is the generalized strain matrix, D is the flexural rigidity, and $\bar{\mathbf{D}}$ is the plate elasticity matrix, which are defined as

$$\bar{\mathbf{D}} = D \begin{bmatrix} 1 & \mu & 0 \\ \mu & 1 & 0 \\ 0 & 0 & (1-\mu)/2 \end{bmatrix} \quad (2.21)$$

$$D = \frac{Et^3}{12(1-\mu^2)} \quad (2.22)$$

$$\kappa = \left[-\frac{\partial^2 w}{\partial x^2} \quad -\frac{\partial^2 w}{\partial y^2} \quad -\frac{\partial^2 w}{\partial x \partial y} \right]^T \quad (2.23)$$

where μ denotes the Poisson's ratio.

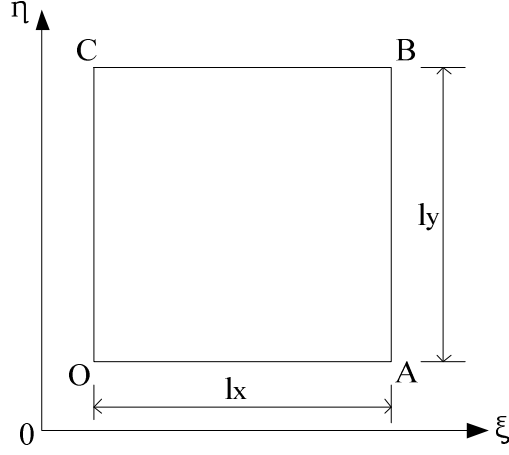


Figure 2.5. Rectangular elastic thin plate

By using the 2D multi-wavelets $\bar{\Phi}_j$ as the shape function and translating the corresponding coordinate into a standard solving domain, the unknown displacement field function $\bar{w}(\xi, \eta)$ can be expressed as

$$\bar{w}(\xi, \eta) = \bar{\Phi}_0 \mathbf{a}_0 + \sum_{n=0}^{j-1} \bar{\Psi}_n \mathbf{b}_n = \bar{\Phi}_j \bar{\mathbf{q}}_j \quad (2.24)$$

where ξ and η denote the local coordinates, $\bar{\Phi}_0$ represents the scaling functions at scale 0, $\bar{\Psi}_j = [\bar{\Phi}_0 \ \bar{\Psi}_0 \ \bar{\Psi}_1 \ \cdots \ \bar{\Psi}_{j-1}]$ represents the wavelet functions at scale j , and $\bar{\mathbf{q}}_j$ is the undetermined vector of the wavelet coefficients (i.e., coordinates corresponding to wavelet DOFs). The mode shapes obtained in the vibration test, which are expressed in the physical coordinate, can be conveniently converted into wavelet DOFs by exploiting the interpolation properties of the adopted multi-wavelets.

According to the principle minimum of potential energy, let $\delta \Pi_p = 0$, where δ is the variational operator and Π_p can be obtained by substituting Equation (2.24) into

Equation (2.20). The wavelet formulations for the modal analysis of elastic thin plates can be obtained as follows:

$$(\bar{\mathbf{K}}_j - \lambda \bar{\mathbf{M}}_j) \bar{\mathbf{q}}_j = 0 \quad (2.25)$$

where $\bar{\mathbf{K}}_j$ and $\bar{\mathbf{M}}_j$ are the element stiffness and mass matrices at scale j .

$$\bar{\mathbf{M}}_j = l_x l_y \rho t \Gamma_1^{j,0,0} \otimes \Gamma_2^{j,0,0} \quad (2.26)$$

$$\bar{\mathbf{K}}_j = D[\Gamma_1^{j,2,2} \otimes \Gamma_2^{j,0,0} + \mu \Gamma_1^{j,0,2} \otimes \Gamma_2^{j,2,0} + \Gamma_1^{j,0,0} \otimes \Gamma_2^{j,0,0} + 2(1-\mu) \Gamma_1^{j,1,1} \otimes \Gamma_2^{j,1,1}] \quad (2.27)$$

$$\Gamma_1^{j,2,2} = \frac{1}{l_x^3} \int_0^1 (\Phi_j'')^T \Phi_j'' d\xi = \frac{1}{l_x^3} \int_0^1 \begin{bmatrix} (\Phi_0'')^T \Phi_0'' & (\Phi_0'')^T \Psi_0'' & \cdots & (\Phi_0'')^T \Psi_{j-1}'' \\ & (\Psi_0'')^T \Psi_0'' & \cdots & (\Psi_0'')^T \Psi_{j-1}'' \\ \text{sym} & & \ddots & \vdots \\ & & & (\Psi_{j-1}'')^T \Psi_{j-1}'' \end{bmatrix} d\xi \quad (2.28)$$

$$\Gamma_1^{j,0,2} = \frac{1}{l_x} \int_0^1 \Phi_j^T \Phi_j'' d\xi = \frac{1}{l_x} \int_0^1 \begin{bmatrix} \Phi_0^T \Phi_0'' & \Phi_0^T \Psi_0'' & \cdots & \Phi_0^T \Psi_{j-1}'' \\ & \Psi_0^T \Psi_0'' & \cdots & \Psi_0^T \Psi_{j-1}'' \\ \text{sym} & & \ddots & \vdots \\ & & & \Psi_{j-1}^T \Psi_{j-1}'' \end{bmatrix} d\xi \quad (2.29)$$

$$\Gamma_1^{j,2,0} = (\Gamma_1^{j,0,2})^T \quad (2.30)$$

$$\Gamma_1^{j,1,1} = \frac{1}{l_x} \int_0^1 (\Phi_j')^T \Phi_j' d\xi = \frac{1}{l_x} \int_0^1 \begin{bmatrix} (\Phi_0')^T \Phi_0' & (\Phi_0')^T \Psi_0' & \cdots & (\Phi_0')^T \Psi_{j-1}' \\ & (\Psi_0')^T \Psi_0' & \cdots & (\Psi_0')^T \Psi_{j-1}' \\ \text{sym} & & \ddots & \vdots \\ & & & (\Psi_{j-1}')^T \Psi_{j-1}' \end{bmatrix} d\xi \quad (2.31)$$

$$\Gamma_1^{j,0,0} = l_x \int_0^1 \Phi_j^T \Phi_j d\xi = l_x \int_0^1 \begin{bmatrix} \Phi_0^T \Phi_0 & \Phi_0^T \Psi_0 & \cdots & \Phi_0^T \Psi_{j-1} \\ & \Psi_0^T \Psi_0 & \cdots & \Psi_0^T \Psi_{j-1} \\ \text{sym} & & \ddots & \vdots \\ & & & \Psi_{j-1}^T \Psi_{j-1} \end{bmatrix} d\xi \quad (2.32)$$

where Φ_j' and Φ_j'' represent the first and second derivatives with respect to the local coordinate ξ , respectively. The integrals $\Gamma_2^{j,f,g}$ ($f, g=0, 1, 2$) are similar to $\Gamma_1^{j,f,g}$ ($f, g=0, 1, 2$) with only l_x and $d\xi$ replaced by l_y and $d\eta$, respectively.

Similar to the beam structures, in the lifting or lowering procedure between scales, the sub-matrices in Equations (2.28) to (2.32) at the current scale can be retained, and only a few rows and columns need to be added or deleted. Notably, the support region of the 2D wavelet at scale $j + 1$ is only a quarter of scale j . This favorable localization characteristic helps develop the progressive damage detection approach. In the multi-scale model, the original region can be refined to four equal sub-regions by adding a new scale, but such a refinement process avoids the hanging node problems mentioned in Chapter 1.

The scaling functions of the cubic Hermite multi-wavelets at scale 0 (Figure 2.1) are the same as the polynomial shape function adopted in the traditional finite element (Zienkiewicz and Taylor 1961; Bogner et al. 1965). Therefore, the presented cubic Hermite WFEM can seamlessly connect to the traditional finite element or even refine elements in TFEM. Considering the fact that most existing structural models are built using TFEM, this feature of cubic Hermite WFEM is a prominent advantage that makes the proposed multi-scale damage detection method more acceptable.

2.5 Summary

This chapter establishes the theoretical basis for multi-scale dynamic analysis and damage detection methods. The principles of selecting appropriate wavelet element and the basic concept of cubic Hermite multi-wavelet are introduced briefly, and multi-scale dynamic formulations together with the corresponding lifting schemes for beam and plate structures are derived. In particular, a multi-scale formulation of beam structures subjected to moving load excitation is presented.

Chapter 3 Progressive Damage Detection Based on Modal Strain Energy

3.1 Introduction

Based on the WFEM concept in Chapter 2, this chapter presents a multi-scale damage detection method in which structural modeling resolutions are not only spatially varying but also dynamically changing according to actual needs. MSE is utilized to detect sub-element damage in beam and thin plate structures in a progressive manner. The suspected region is first identified with a low-scale WFEM model. Then, the more accurate damage location and severity are estimated with multi-scale WFEM with local refinement. Although this strategy can be implemented via TFEM, the multi-scale and localization properties of WFEM can considerably facilitate the adaptive change in modeling resolutions. For plate structures in particular, problems associated with hanging nodes can be avoided. Numerical studies are conducted to verify the effectiveness and advantages of the proposed WFEM- and MSE-based multi-scale damage detection strategy. This strategy can operate efficiently in terms of DOFs in WFEM and sensors in the vibration test.

3.2 Progressive Damage Detection

Damage detection methods based on MSE have been extensively explored in the context of TFEM (e.g., Shi and Law 1998; Cornwell et al. 1999; Shi et al. 2000a; 2000b; 2002; Guan and Karbhari 2008; Yan et al. 2010). A similar method is adopted for WFEM in this chapter. Given that the strategy described in this chapter aims to identify damages smaller than an element, the strategy employs MSE in a sub-element. In addition, in WFEM, the MSE of a given sub-element cannot be calculated as the direct

combination of mode shape vector and element stiffness matrix unlike in TFEM. Thus, the sub-element partial differential equations that govern the free vibration of a beam and thin plate are utilized in the formulation of the damage quantification matrix via modal perturbation.

In damage detection studies, a common assumption is that no mass change occurs after damage. Damage causes perturbations, which are typically small, in the i^{th} eigenvalue and in the i^{th} mode shape of the beam or thin plate compared with an undamaged one (Shi et al. 2000b; Fox and Kapoor 1968)

$$\lambda_i^d = \lambda_i + \Delta\lambda_i \quad (3.1)$$

$$\varphi_i^d = \varphi_i + \Delta\varphi_i = \varphi_i + \sum_{s \neq i} p_{is} \varphi_s \quad (3.2)$$

where λ_i and λ_i^d are the i^{th} eigenvalue before and after damage, respectively. φ_i and φ_i^d are the i^{th} mode shape before and after damage, respectively. The change in the i^{th} mode shape $\Delta\varphi_i$ is expressed as a linear combination of mode shapes other than the present one. In WFEM, eigenvalue λ_i and eigenvector φ_i can be obtained directly from Equations (2.14) and (2.25) for beams and plates, respectively.

3.2.1 Beam Structure

3.2.1.1 Damage Localization

The MSE of the r^{th} sub-element L_r associated with the i^{th} mode of a Bernoulli–Euler beam ($MSEB_{i,r}$) before and after damage are expressed as (Cornwell et al. 1999)

$$MSEB_{i,r} = \frac{1}{2} \int_{L_r} EI(x) \cdot \left(\frac{\partial^2 \varphi_i}{\partial x^2} \right)^2 dx \quad (3.3a)$$

$$MSEB_{i,r}^d = \frac{1}{2} \int_{L_r} EI^d(x) \cdot \left(\frac{\partial^2 \varphi_i^d}{\partial x^2} \right)^2 dx \quad (3.3b)$$

where superscript d denotes damage and $EI(x)$ is the flexural rigidity of the sub-element. Given that flexural rigidity after damage $EI^d(x)$ is unpredictable, the original flexural rigidity $EI(x)$ can be utilized instead as an approximation in Equation (3.3b). In accordance with Shi and Law (1998), a normalized change ratio of $MSEB$ is regarded as the damage location indicator.

$$NMSECR_{i,r} = \frac{|MSEB_{i,r}^d - MSEB_{i,r}|}{MSEB_{i,r}} / \max\left(\frac{|MSEB_{i,r}^d - MSEB_{i,r}|}{MSEB_{i,r}}\right) \quad (3.4)$$

If more than one vibration modes are considered, the damage location indicator in the r^{th} sub-element is defined as the average of $NMSECR_{i,r}^i$ for all the concerned modes.

$$NMSECR_r = \frac{1}{m} \sum_{i=1}^m NMSECR_{i,r} \quad (3.5)$$

3.2.1.2 Damage Quantification

The occurrence of damage in a beam can be represented by a change in flexural rigidity as follows:

$$EI^d(x) = EI(x) + \Delta EI(x) = EI(x) + \sum_r \alpha_r EI(x) \quad (-1 \leq \alpha_r \leq 0) \quad (3.6)$$

where α_r is the flexural rigidity reduction factor of the r^{th} sub-element (L_r).

The damage-induced change in $MSEB_{i,r}$ can then be expressed in two ways.

$$\begin{aligned} \Delta MSEB_{i,r} &= MSEB_{i,r}^d - MSEB_{i,r} \\ &= \frac{1}{2} \int_{L_r} [EI(x) + \Delta EI(x)] \cdot \left(\frac{\partial^2 \varphi_i}{\partial x^2} + \frac{\partial^2 \Delta \varphi_i}{\partial x^2}\right)^2 dx - \frac{1}{2} \int_{L_r} EI(x) \cdot \left(\frac{\partial^2 \varphi_i}{\partial x^2}\right)^2 dx \quad (3.7) \\ &= \int_{L_r} [EI(x) \left(\frac{\partial^2 \varphi_i}{\partial x^2}\right) \left(\frac{\partial^2 \Delta \varphi_i}{\partial x^2}\right)] dx + \frac{1}{2} \int_{L_r} \Delta EI(x) \cdot \left(\frac{\partial^2 \varphi_i}{\partial x^2}\right)^2 dx \end{aligned}$$

$$\begin{aligned}
\Delta MSEB_{i,r} &= MSEB_{i,r}^d - MSEB_{i,r} \\
&= \frac{1}{2} \int_{L_r} [EI(x) + \sum_r \alpha_r EI(x)] \cdot \left(\frac{\partial^2 \varphi_i^d}{\partial x^2}\right)^2 dx - \frac{1}{2} \int_{L_r} EI(x) \cdot \left(\frac{\partial^2 \varphi_i}{\partial x^2}\right)^2 dx \\
&= \frac{1}{2} \int_{L_r} EI(x) \left(\frac{\partial^2 \varphi_i^d}{\partial x^2}\right)^2 dx + \frac{1}{2} \int_{L_r} \sum_r \alpha_r EI(x) \left(\frac{\partial^2 \varphi_i^d}{\partial x^2}\right)^2 dx - \frac{1}{2} \int_{L_r} EI(x) \left(\frac{\partial^2 \varphi_i}{\partial x^2}\right)^2 dx
\end{aligned} \tag{3.8}$$

In Equation (3.7), the flexural rigidities and mode shapes in the damaged state are represented by $EI(x) + \Delta EI(x)$ and $\varphi_i + \Delta \varphi_i$, respectively; in Equation (3.8), they are represented by $EI(x) + \sum_r \alpha_r EI(x)$ and φ_i^d , respectively.

According to the dynamics of the beam (Clough and Penzien 1993), the partial differential equation that defines the eigensolutions is

$$\frac{\partial^2}{\partial x^2} [EI(x) \frac{\partial^2 \varphi_i}{\partial x^2}] - \lambda_i m(x) \varphi_i = 0 \tag{3.9}$$

When the beam is subject to damage, the above equation with a small perturbation becomes

$$\frac{\partial^2}{\partial x^2} \{ [EI(x) + \Delta EI(x)] \cdot \frac{\partial^2 (\varphi_i + \Delta \varphi_i)}{\partial x^2} \} - (\lambda_i + \Delta \lambda_i) m(x) (\varphi_i + \Delta \varphi_i) = 0 \tag{3.10}$$

Substituting Equations (3.1), (3.2), and (3.6) into Equation (3.10) and neglecting small terms lead to

$$\frac{\partial^2}{\partial x^2} [EI(x) \sum_{s \neq i} p_{is} \frac{\partial^2 \varphi_s}{\partial x^2} + \Delta EI(x) \frac{\partial^2 \varphi_i}{\partial x^2}] - \lambda_i m(x) \sum_{s \neq i} p_{is} \varphi_s - \Delta \lambda_i m(x) \varphi_i = 0 \tag{3.11}$$

By pre-multiplying φ_s and computing the integral along the interval $[0, L_i]$ on both sides of Equation (3.11), where L_i is the total length of the beam, and considering the orthogonal condition

$$\int_L \varphi_s m(x) \varphi_i dx = 0 \quad (s \neq i) \tag{3.12}$$

the coefficient p_{is} for a beam can be computed as

$$p_{is} = \frac{1}{\lambda_i - \lambda_s} \int_L [\Delta EI(x) \frac{\partial^2 \varphi_s}{\partial x^2} \frac{\partial^2 \varphi_i}{\partial x^2}] dx \quad (3.13)$$

Supposing k sub-elements are damaged, the following damage equation can be obtained from Equations (3.7), (3.8), and (3.13).

$$\begin{bmatrix} \chi_{11} & \chi_{12} & \cdots & \chi_{1k} \\ \chi_{21} & \chi_{22} & \cdots & \chi_{2k} \\ \vdots & \vdots & & \vdots \\ \chi_{k1} & \chi_{k2} & \cdots & \chi_{kk} \end{bmatrix} \begin{Bmatrix} \alpha_1 \\ \alpha_2 \\ \vdots \\ \alpha_k \end{Bmatrix} = \begin{Bmatrix} \Delta EB_{i,1} \\ \Delta EB_{i,2} \\ \vdots \\ \Delta EB_{i,k} \end{Bmatrix} \quad (3.14)$$

where

$$\begin{aligned} \chi_{mm} = & \sum_{s \neq i} p_{is} [\int_{L_m} EI(x) \frac{\partial^2 \varphi_s}{\partial x} \frac{\partial^2 \varphi_i}{\partial x} dx] \\ & + \frac{1}{2} \int_{L_m} EI(x) \left(\frac{\partial^2 \varphi_i^d}{\partial x} \right)^2 dx - \frac{1}{2} \int_{L_m} EI(x) \left(\frac{\partial^2 \varphi_i}{\partial x} \right)^2 dx \end{aligned} \quad (3.15)$$

$$\chi_{mn} = \sum_{s \neq i} p_{is} [\int_{L_m} EI(x) \frac{\partial^2 \varphi_s}{\partial x} \frac{\partial^2 \varphi_i}{\partial x} dx] \quad (3.16)$$

$$\Delta EB_{i,m} = \frac{1}{2} \int_{L_m} EI(x) \cdot \left(\frac{\partial^2 \varphi_i^d}{\partial x^2} \right)^2 dx - \frac{1}{2} \int_{L_m} EI(x) \cdot \left(\frac{\partial^2 \varphi_i}{\partial x^2} \right)^2 dx \quad (3.17)$$

where ($1 \leq m \leq k, 1 \leq n \leq k$). After the damages are localized using the method described in Section 3.2.1.1, the severities of the damages can be qualified by solving the above described damage matrix equation [Equation (3.14)]. The two-stage process, that is, localization and quantification, can effectively reduce the matrix size and minimize the computation cost. Notably, unlike in damage localization, $[EI(x) + \Delta EI(x)]$ rather than $[EI(x)]$ is used as the flexural rigidity after damage in the damage matrix equation. Therefore, the iteration computation adopted in Shi et al. (2002b) is not required, which helps enhance detection efficiency.

3.2.2 Plate Structure

Damage localization and quantification for thin plate structures are similar to those for

beam structures. The meanings of the symbols are the same as those in Section 3.2.1, unless otherwise specified.

3.2.2.1 Damage Localization

According to Cornwell et al. (1999), the MSE of a sub-element A_r associated with the i^{th} mode shape of a plate is

$$MSEP_{i,r} = \frac{1}{2} \iint_{A_r} D(x, y) \left[\left(\frac{\partial^2 \phi_i}{\partial x^2} \right)^2 + \left(\frac{\partial^2 \phi_i}{\partial y^2} \right)^2 + 2\nu \left(\frac{\partial^2 \phi_i}{\partial x^2} \right) \left(\frac{\partial^2 \phi_i}{\partial y^2} \right) + 2(1-\nu) \left(\frac{\partial^2 \phi_i}{\partial x \partial y} \right)^2 \right] dx dy \quad (3.18a)$$

$$MSEP_{i,r}^d = \frac{1}{2} \iint_{A_r} D^d(x, y) \left[\left(\frac{\partial^2 \phi_i^d}{\partial x^2} \right)^2 + \left(\frac{\partial^2 \phi_i^d}{\partial y^2} \right)^2 + 2\nu \left(\frac{\partial^2 \phi_i^d}{\partial x^2} \right) \left(\frac{\partial^2 \phi_i^d}{\partial y^2} \right) + 2(1-\nu) \left(\frac{\partial^2 \phi_i^d}{\partial x \partial y} \right)^2 \right] dx dy \quad (3.18b)$$

where A_r represents the r^{th} sub-element with damage; $MSEP_{i,r}$ and $MSEP_{i,r}^d$ represent the MSE before and after damage of the sub-element, respectively; and $D(x, y)$ denotes the sub-element flexural rigidity. The intact $D(x, y)$ is employed as an approximation in Equation (3.18b) when flexural rigidity after damage $D^d(x, y)$ is unknown. $NMSECR_i^d$ in Equation (3.4) and $NMSECR_r$ in Equation (3.5) can still be utilized to localize damage in plate structures with $MSEP$ instead of $MSEB$.

3.2.2.2 Damage Quantification

Assuming that the plate damage is represented by a change in flexural rigidity,

$$D^d(x, y) = D(x, y) + \Delta D(x, y) = D(x, y) + \sum_r \beta_r D(x, y) \quad (-1 \leq \beta_r \leq 0) \quad (3.19)$$

where β_r is the damage index of sub-element A_r .

According to Clough and Penzien (1993), the partial differential equation that defines the eigensolutions of an undamaged plate is

$$D\left[\frac{\partial^4 \varphi_i}{\partial x^4} + 2\frac{\partial^4 \varphi_i}{\partial x^2 \partial y^2} + \frac{\partial^4 \varphi_i}{\partial y^4}\right] - \lambda_i m(x, y) \varphi_i = 0 \quad (3.20)$$

When the plate is subjected to damage, Equation (3.20) with a small perturbation becomes

$$[D + \Delta D]\left[\frac{\partial^4 (\varphi_i + \Delta \varphi_i)}{\partial x^4} + 2\frac{\partial^4 (\varphi_i + \Delta \varphi_i)}{\partial x^2 \partial y^2} + \frac{\partial^4 (\varphi_i + \Delta \varphi_i)}{\partial y^4}\right] - (\lambda_i + \Delta \lambda_i) m(\varphi_i + \Delta \varphi_i) = 0 \quad (3.21)$$

Substituting Equation (3.20) into Equation (3.21) and neglecting the small terms lead to

$$D\left[\frac{\partial^4 \Delta \varphi_i}{\partial x^4} + 2\frac{\partial^4 \Delta \varphi_i}{\partial x^2 \partial y^2} + \frac{\partial^4 \Delta \varphi_i}{\partial y^4}\right] + \Delta D\left[\frac{\partial^4 \varphi_i}{\partial x^4} + 2\frac{\partial^4 \varphi_i}{\partial x^2 \partial y^2} + \frac{\partial^4 \varphi_i}{\partial y^4}\right] - \lambda_i m \Delta \varphi_i - \Delta \lambda_i m \varphi_i = 0 \quad (3.22)$$

By pre-multiplying $\varphi_s (s \neq i)$, computing the integral along the solving domain on both sides of Equation (3.22), and considering orthogonal conditions, the coefficient p_{is} for a plate is computed as

$$p_{is} = \frac{1}{\lambda_i - \lambda_s} \iint_{\Omega} \Delta D \left(\frac{\partial^4 \varphi_i}{\partial x^4} + 2\frac{\partial^4 \varphi_i}{\partial x^2 \partial y^2} + \frac{\partial^4 \varphi_i}{\partial y^4} \right) \varphi_s dx dy \quad (3.23)$$

Damage-induced changes in $MSEP_{i,r}$ can be expressed in two ways as follows:

$$\begin{aligned}
\Delta MSEP_{i,r} &= MSEP_{i,r}^d - MSEP_{i,r} \\
&= \frac{1}{2} \iint_{A_r} (D + \Delta D) \left[\left(\frac{\partial^2 \varphi_i}{\partial x^2} + \frac{\partial^2 \Delta \varphi_i}{\partial x^2} \right)^2 + \left(\frac{\partial^2 \varphi_i}{\partial y^2} + \frac{\partial^2 \Delta \varphi_i}{\partial y^2} \right)^2 + 2\nu \left(\frac{\partial^2 \varphi_i}{\partial x^2} + \frac{\partial^2 \Delta \varphi_i}{\partial x^2} \right) \left(\frac{\partial^2 \varphi_i}{\partial y^2} + \frac{\partial^2 \Delta \varphi_i}{\partial y^2} \right) + 2(1-\nu) \left(\frac{\partial^2 \varphi_i}{\partial x \partial y} + \frac{\partial^2 \Delta \varphi_i}{\partial x \partial y} \right)^2 \right] dx dy \\
&\quad - \frac{1}{2} \iint_{A_r} D \left[\left(\frac{\partial^2 \varphi_i}{\partial x^2} \right)^2 + \left(\frac{\partial^2 \varphi_i}{\partial y^2} \right)^2 + 2\nu \left(\frac{\partial^2 \varphi_i}{\partial x^2} \right) \left(\frac{\partial^2 \varphi_i}{\partial y^2} \right) + 2(1-\nu) \left(\frac{\partial^2 \varphi_i}{\partial x \partial y} \right)^2 \right] dx dy \\
&= \iint_{A_r} D \left[\frac{\partial^2 \varphi_i}{\partial x^2} \cdot \frac{\partial^2 \Delta \varphi_i}{\partial x^2} + \frac{\partial^2 \varphi_i}{\partial y^2} \cdot \frac{\partial^2 \Delta \varphi_i}{\partial y^2} + 2\nu \left(\frac{\partial^2 \varphi_i}{\partial x^2} \cdot \frac{\partial^2 \Delta \varphi_i}{\partial y^2} + \frac{\partial^2 \varphi_i}{\partial y^2} \cdot \frac{\partial^2 \Delta \varphi_i}{\partial x^2} \right) + 2(1-\nu) \frac{\partial^2 \varphi_i}{\partial x \partial y} \cdot \frac{\partial^2 \Delta \varphi_i}{\partial x \partial y} \right] dx dy \\
&\quad + \frac{1}{2} \iint_{A_r} \Delta D \left[\left(\frac{\partial^2 \varphi_i}{\partial x^2} \right)^2 + \left(\frac{\partial^2 \varphi_i}{\partial y^2} \right)^2 + 2\nu \frac{\partial^2 \varphi_i}{\partial x^2} \cdot \frac{\partial^2 \varphi_i}{\partial y^2} + 2(1-\nu) \left(\frac{\partial^2 \varphi_i}{\partial x \partial y} \right)^2 \right] dx dy
\end{aligned} \tag{3.24}$$

$$\begin{aligned}
\Delta MSEP_{i,r} &= MSEP_{i,r}^d - MSEP_{i,r} \\
&= \frac{1}{2} \iint_{A_r} (D + \sum_r \beta_r D) \left[\left(\frac{\partial^2 \varphi_i^d}{\partial x^2} \right)^2 + \left(\frac{\partial^2 \varphi_i^d}{\partial y^2} \right)^2 + 2\nu \left(\frac{\partial^2 \varphi_i^d}{\partial x^2} \right) \left(\frac{\partial^2 \varphi_i^d}{\partial y^2} \right) + 2(1-\nu) \left(\frac{\partial^2 \varphi_i^d}{\partial x \partial y} \right)^2 \right] dx dy \\
&\quad - \frac{1}{2} \iint_{A_r} D \left[\left(\frac{\partial^2 \varphi_i}{\partial x^2} \right)^2 + \left(\frac{\partial^2 \varphi_i}{\partial y^2} \right)^2 + 2\nu \left(\frac{\partial^2 \varphi_i}{\partial x^2} \right) \left(\frac{\partial^2 \varphi_i}{\partial y^2} \right) + 2(1-\nu) \left(\frac{\partial^2 \varphi_i}{\partial x \partial y} \right)^2 \right] dx dy \\
&= \frac{1}{2} \iint_{A_r} D \left[\left(\frac{\partial^2 \varphi_i^d}{\partial x^2} \right)^2 + \left(\frac{\partial^2 \varphi_i^d}{\partial y^2} \right)^2 + 2\nu \left(\frac{\partial^2 \varphi_i^d}{\partial x^2} \right) \left(\frac{\partial^2 \varphi_i^d}{\partial y^2} \right) + 2(1-\nu) \left(\frac{\partial^2 \varphi_i^d}{\partial x \partial y} \right)^2 \right] dx dy \\
&\quad + \frac{1}{2} \iint_{A_r} \sum_r \beta_r D \left[\left(\frac{\partial^2 \varphi_i^d}{\partial x^2} \right)^2 + \left(\frac{\partial^2 \varphi_i^d}{\partial y^2} \right)^2 + 2\nu \left(\frac{\partial^2 \varphi_i^d}{\partial x^2} \right) \left(\frac{\partial^2 \varphi_i^d}{\partial y^2} \right) + 2(1-\nu) \left(\frac{\partial^2 \varphi_i^d}{\partial x \partial y} \right)^2 \right] dx dy \\
&\quad - \frac{1}{2} \iint_{A_r} D \left[\left(\frac{\partial^2 \varphi_i}{\partial x^2} \right)^2 + \left(\frac{\partial^2 \varphi_i}{\partial y^2} \right)^2 + 2\nu \left(\frac{\partial^2 \varphi_i}{\partial x^2} \right) \left(\frac{\partial^2 \varphi_i}{\partial y^2} \right) + 2(1-\nu) \left(\frac{\partial^2 \varphi_i}{\partial x \partial y} \right)^2 \right] dx dy
\end{aligned} \tag{3.25}$$

In Equation (3.24), the flexural rigidity and mode shapes in the damage state are represented by $D+\Delta D$ and $\varphi_i+\Delta\varphi_i$, respectively; in Equation (3.25), they are represented by $D+\sum_r\beta_r D$ and φ_i^d , respectively.

Supposing that k sub-elements existing in a plate are identified as possible damaged regions by *NCRMSE* as described in Section 3.2.2.1, the following damage quantification equation is obtained from Equations (3.23), (3.24), and (3.25).

$$\begin{bmatrix} \gamma_{11} & \gamma_{12} & \cdots & \gamma_{1k} \\ \gamma_{21} & \gamma_{22} & \cdots & \gamma_{2k} \\ \vdots & \vdots & & \vdots \\ \gamma_{k1} & \gamma_{k2} & \cdots & \gamma_{kk} \end{bmatrix} \begin{Bmatrix} \beta_1 \\ \beta_2 \\ \vdots \\ \beta_k \end{Bmatrix} = \begin{Bmatrix} \Delta EP_{i,1} \\ \Delta EP_{i,2} \\ \vdots \\ \Delta EP_{i,k} \end{Bmatrix} \quad (3.26)$$

where

$$\begin{aligned}
\gamma_{mm} = & \sum_{s \neq i} p_{is} \iint_{A_m} \left[\frac{\partial^2 \varphi_i}{\partial x^2} \frac{\partial^2 \varphi_s}{\partial x^2} + \frac{\partial^2 \varphi_i}{\partial y^2} \frac{\partial^2 \varphi_s}{\partial y^2} + 2\nu \left(\frac{\partial^2 \varphi_i}{\partial x^2} \frac{\partial^2 \varphi_s}{\partial y^2} + \frac{\partial^2 \varphi_i}{\partial y^2} \frac{\partial^2 \varphi_s}{\partial x^2} \right) + 2(1-\nu) \frac{\partial^2 \varphi_i}{\partial x \partial y} \frac{\partial^2 \varphi_s}{\partial x \partial y} \right] dx dy \\
& + \frac{1}{2} \iint_{A_m} D_0 \left[\left(\frac{\partial^2 \varphi_i}{\partial x^2} \right)^2 + \left(\frac{\partial^2 \varphi_i}{\partial y^2} \right)^2 + 2\nu \left(\frac{\partial^2 \varphi_i}{\partial x^2} \right) \left(\frac{\partial^2 \varphi_i}{\partial y^2} \right) + 2(1-\nu) \left(\frac{\partial^2 \varphi_i}{\partial x \partial y} \right)^2 \right] dx dy \\
& - \frac{1}{2} \iint_{A_m} D \left[\left(\frac{\partial^2 \varphi_i^d}{\partial x^2} \right)^2 + \left(\frac{\partial^2 \varphi_i^d}{\partial y^2} \right)^2 + 2\nu \left(\frac{\partial^2 \varphi_i^d}{\partial x^2} \right) \left(\frac{\partial^2 \varphi_i^d}{\partial y^2} \right) + 2(1-\nu) \left(\frac{\partial^2 \varphi_i^d}{\partial x \partial y} \right)^2 \right] dx dy
\end{aligned} \tag{3.27}$$

$$\gamma_{mm} = \sum_{i \neq s} p_{is} \iint_{A_m} \left[\frac{\partial^2 \varphi_i}{\partial x^2} \frac{\partial^2 \varphi_s}{\partial x^2} + \frac{\partial^2 \varphi_i}{\partial y^2} \frac{\partial^2 \varphi_s}{\partial y^2} + 2\nu \left(\frac{\partial^2 \varphi_i}{\partial x^2} \frac{\partial^2 \varphi_s}{\partial y^2} + \frac{\partial^2 \varphi_i}{\partial y^2} \frac{\partial^2 \varphi_s}{\partial x^2} \right) + 2(1-\nu) \frac{\partial^2 \varphi_i}{\partial x \partial y} \frac{\partial^2 \varphi_s}{\partial x \partial y} \right] dx dy \tag{3.28}$$

$$\begin{aligned}
\Delta EP_{i,m} = & \frac{1}{2} \iint_{A_m} D_0 \left[\left(\frac{\partial^2 \varphi_i^d}{\partial x^2} \right)^2 + \left(\frac{\partial^2 \varphi_i^d}{\partial y^2} \right)^2 + 2\nu \left(\frac{\partial^2 \varphi_i^d}{\partial x^2} \right) \left(\frac{\partial^2 \varphi_i^d}{\partial y^2} \right) + 2(1-\nu) \left(\frac{\partial^2 \varphi_i^d}{\partial x \partial y} \right)^2 \right] dx dy \\
& - \frac{1}{2} \iint_{A_m} D_0 \left[\left(\frac{\partial^2 \varphi_i}{\partial x^2} \right)^2 + \left(\frac{\partial^2 \varphi_i}{\partial y^2} \right)^2 + 2\nu \left(\frac{\partial^2 \varphi_i}{\partial x^2} \right) \left(\frac{\partial^2 \varphi_i}{\partial y^2} \right) + 2(1-\nu) \left(\frac{\partial^2 \varphi_i}{\partial x \partial y} \right)^2 \right] dx dy
\end{aligned} \tag{3.29}$$

where $(1 \leq m \leq k, 1 \leq n \leq k)$. Once the damages are localized using the damage localization indicator [Equations (3.4) and (3.5)], they can be qualified by solving the damage quantification equation [Equation (3.26)].

3.2.3 Damage Detection Procedure

A progressive damage detection strategy is adopted in this section. A low-resolution structure model is utilized to acquire the potential location and severity of damage, and a multi-resolution model with refinement in the suspected regions is used to obtain a more accurate estimation of the damage. Although this adaptive-scale strategy can theoretically be realized in the context of TFEM with an effort to re-mesh the models and reconstruct the matrices, the novel WFEM provides considerable convenience and freedom to dynamically change the modeling scale according to the requirements of each step. A flowchart of the progressive damage detection process is shown in Figure 3.1. The process consists of the following main steps.

- Step 1: Arrange the sensors in the tested beam or plate structure, measure the mode shapes, and calculate the MSE in each region.
- Step 2: Analyze the modal properties of the undamaged beam or plate using multi-scale WFEM and then compute the MSE in the corresponding regions.
- Step 3: Locate the suspected region by comparing the analytical and measured MSE, and then quantify the damage severity. However, damage quantification is not optional in this step. To reduce the computation cost, damage quantification can be performed in Step 6 after the damage is properly localized.
- Step 4: Refine WFEM by adding high-scale wavelet terms in the suspected damage regions. Add more sensors in the corresponding regions of the tested beam or plate.
- Step 5: Repeat Steps 1–4 until accurate estimations of the location and severity of the damage are achieved. If the new sub-regions with equal size obtained after refinement are all located as damage regions, this iterative process can be stopped.
- Step 6: Quantify the damage severity using the damage quantification Equation (3.14) or (3.26) for beam or plate structures, respectively.

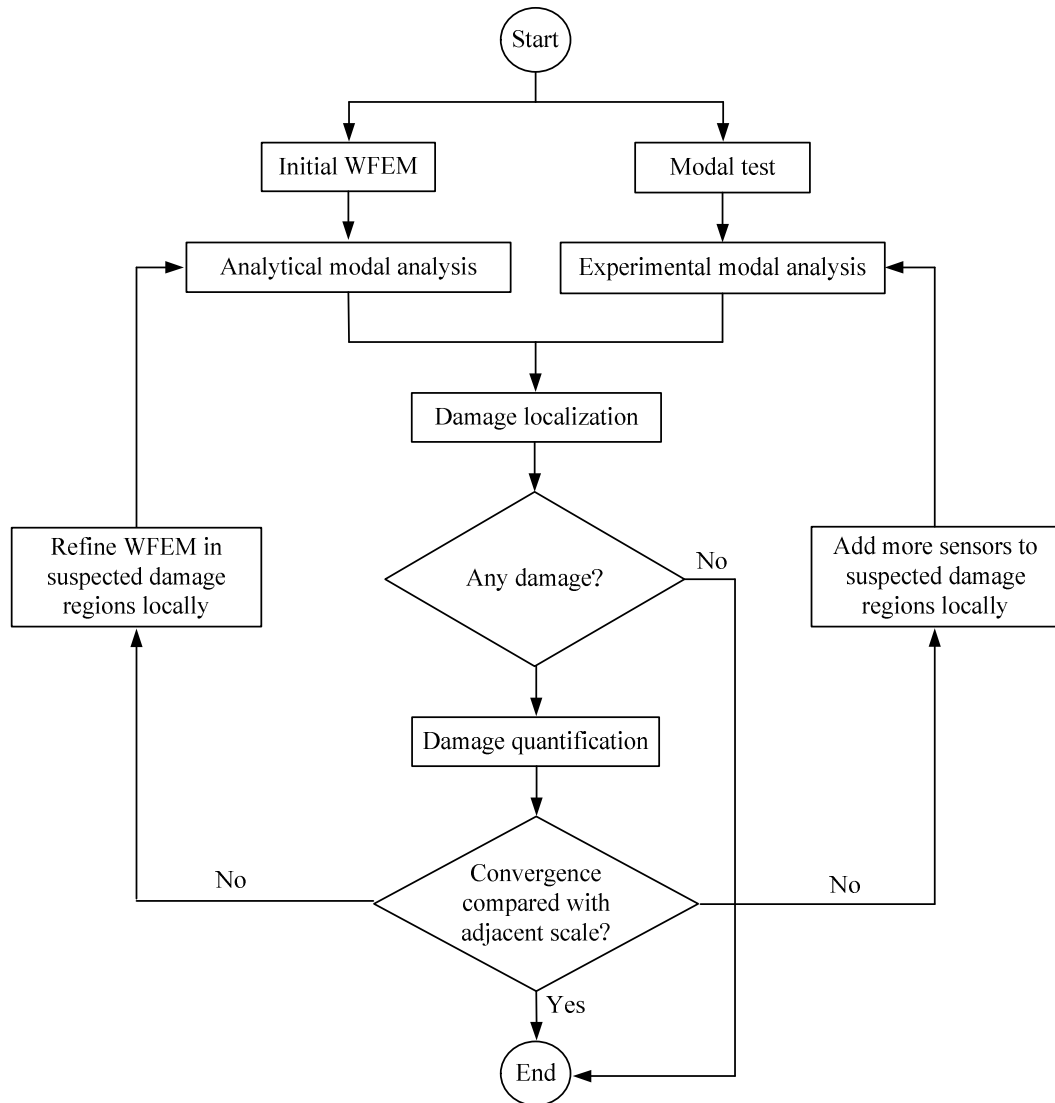


Figure 3.1. Flowchart of the adaptive-scale damage detection scheme

This progressive damage detection strategy is efficient in terms of computation and testing, given the following: (1) the structural model is refined only in the key regions, (2) the refinement process is convenient because of the salient features of WFEM, and (3) only a limited number of sensors need to be added in the critical regions.

3.3 Numerical Study

Numerical examples of a simply supported beam, a two-span continuous beam, and a thin plate simply supported on four corners are provided to demonstrate the effectiveness of the progressive damage detection strategy in consideration of different

damage scenarios. In the numerical simulations, the modal properties in damaged state obtained from very densely meshed TFEMs are regarded as "measured" results. Considering that only the lower mode shapes can be measured in actual field testing, only the first mode shape is used in the examples without noise (Sections 3.3.1 and 3.3.2); the first four mode shapes are used in the examples with noise (Section 3.3.3).

3.3.1 Beam Structure

Table 3.1 provides a summary of the three damage cases of the beams investigated in this section. The first two cases involve a simply supported beam, and the third one involves a two-span continuous beam. The material and section properties of the beams are as follows: elastic modulus $E = 2 \text{ Gpa}$, density $\rho = 2500 \text{ Kg/m}^3$, cross-sectional area $A = 0.005 \text{ m}^2$, and moment of inertia $I = 1.667 \times 10^{-4} \text{ m}^4$. Different locations and severity of the damage are assumed in the three cases, where location refers to the damage interval and severity refers to the loss of flexural rigidity in the damage interval.

Case B-1 involves a simply supported beam structure subjected to a single damage in the interval of [5.25, 5.5] with 20% severity. Figure 3.2 shows the model refinement process, and Figure 3.3 shows the damage detection results in each stage.

Table 3.1. Damage scenarios considered in the numerical simulations of the beam

Structure	Damage Scenarios		Damage	
			Location(m)	Severity (%)
Simply-supported beam	Case B-1	Single damage	[5.25, 5.5]	20
	Case B-2	Double damage	[1,1.5]	20
			[6.25,6.5]	20
Two-span continuous beam	Case B-3	Double damage	[3.25,3.5]	20
			[12.5,12.75]	20

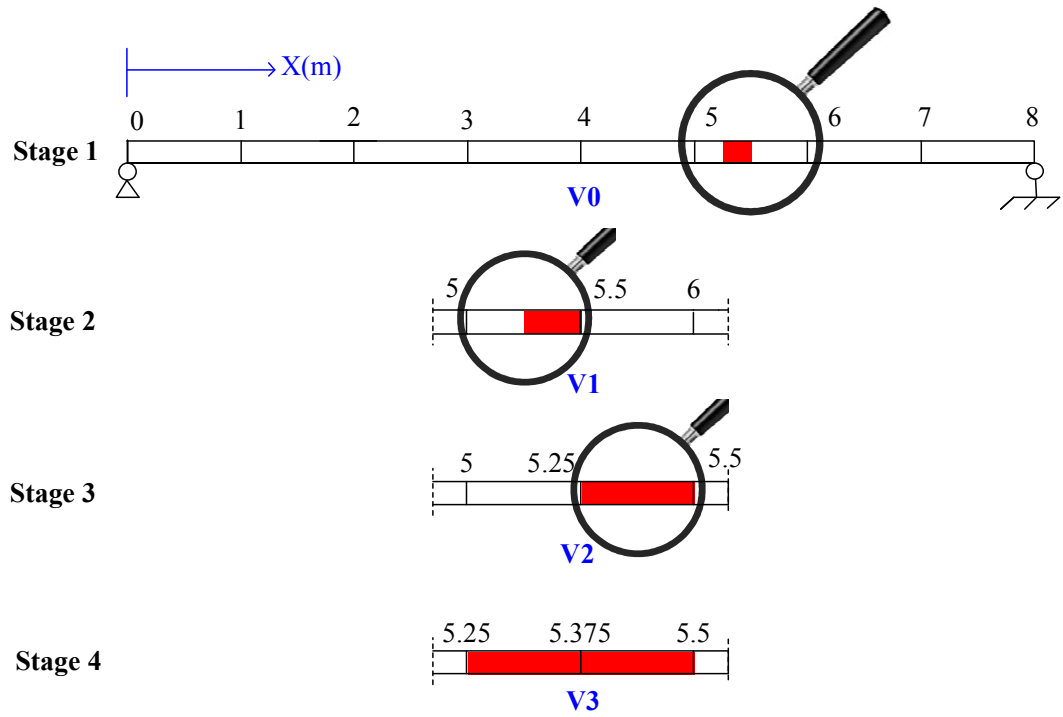
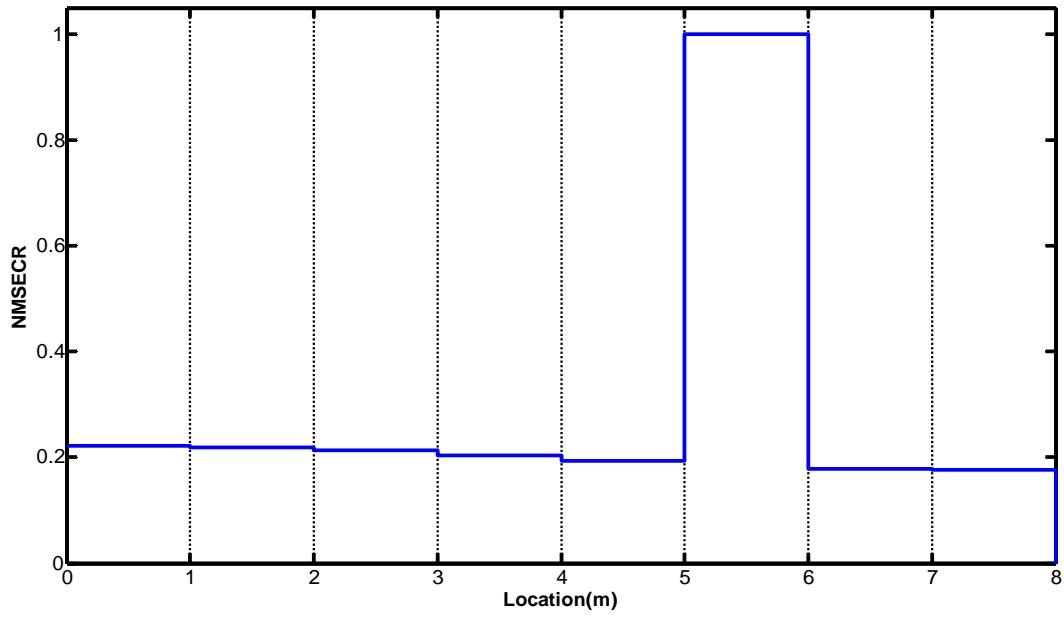
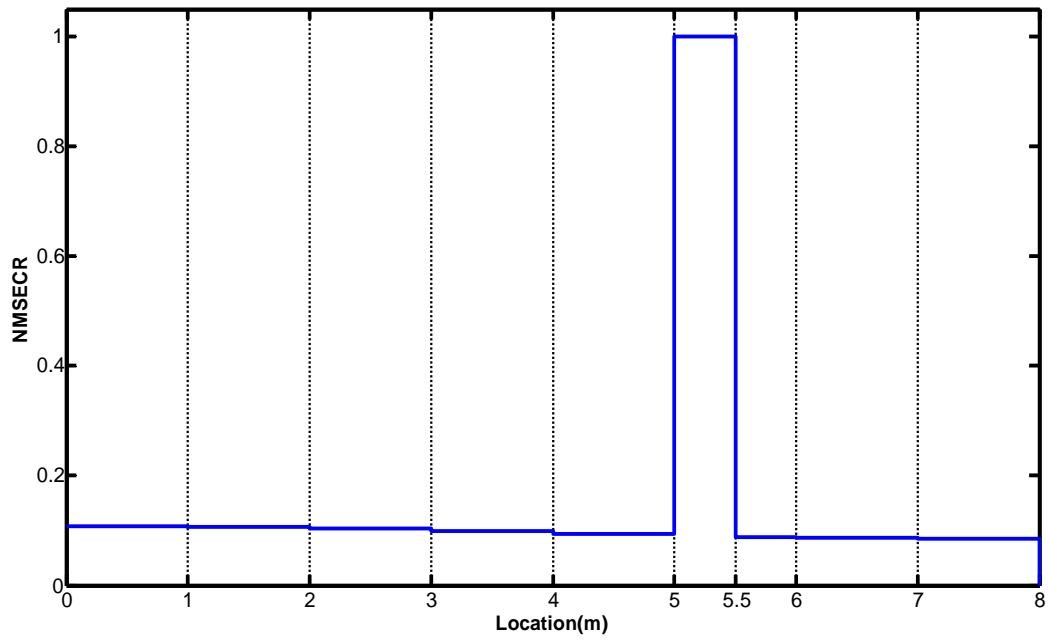


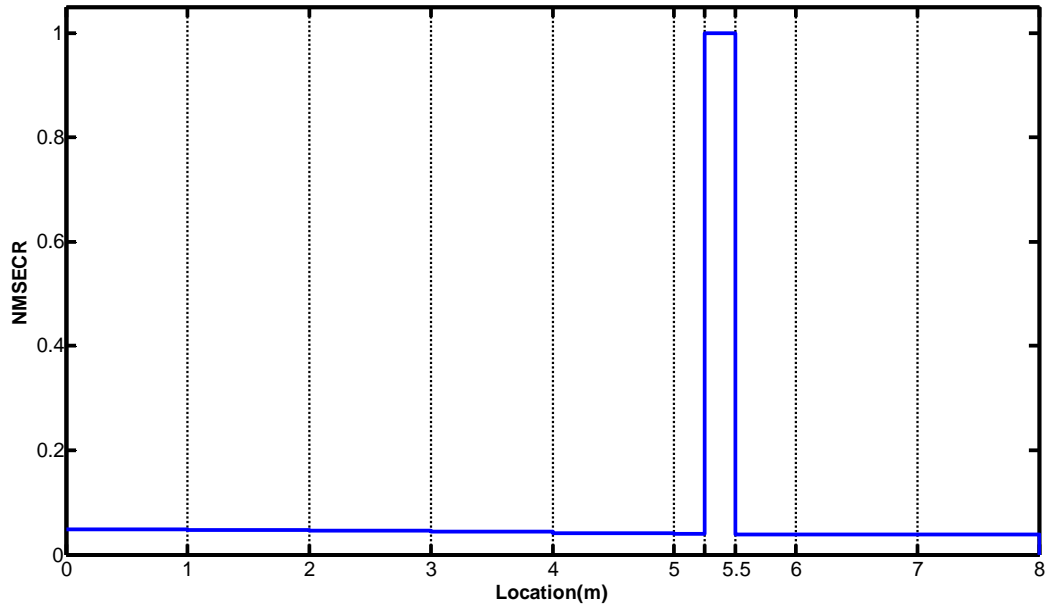
Figure 3.2. Model refinement process for Case B-1



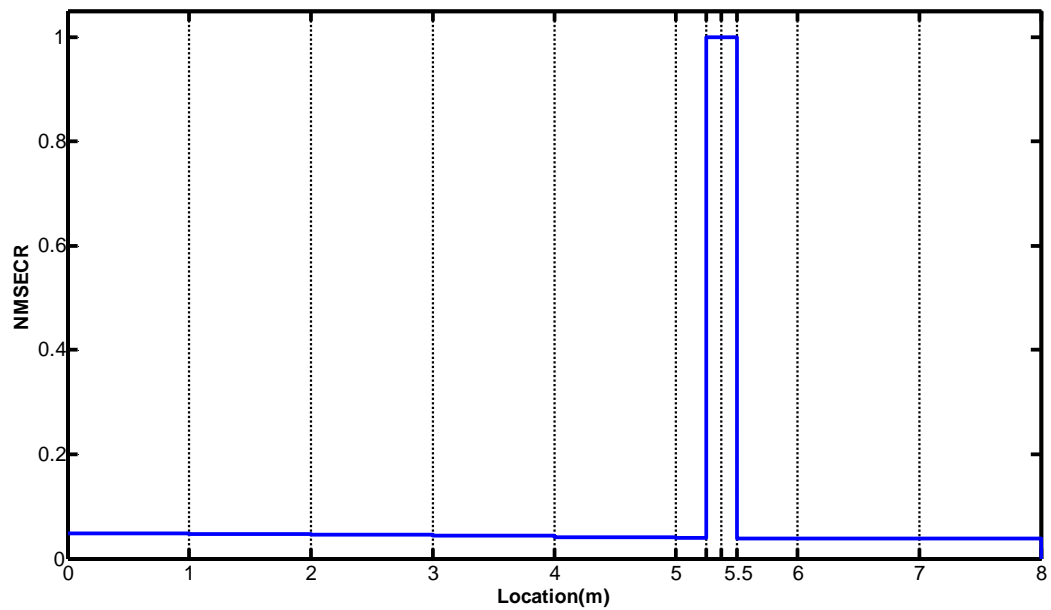
(a) Stage 1, $\beta = -0.064$ in $[5, 6]$



(b) Stage 2, $\beta = -0.115$ in $[5, 6]$



(c) Stage 3, $\beta = -0.217$ in $[5.25, 5.5]$



(d) Stage 4, $\beta = -0.210$ on $[5.25, 5.375]$, $\beta = -0.209$ in $[5.375, 5.5]$

Figure 3.3. Adaptive-scale damage identification results for Case B-1

In the adaptive-scale damage detection process, a low-scale WFEM is used to simulate the original beam structure. In stage 1, the beam is modeled by eight cubic Hermite

wavelet elements at scale 0, that is, the shape functions of each element are approximated in wavelet space V_0 . In this stage, the damage size is actually smaller than that of each element. The corresponding number of DOFs at scale 0 is 18. The MSEB associated with the first mode shape is computed for eight beam elements, as shown in Figure 3.2. By comparing the difference between the simulated and "measured" results, the location and severity of damage are estimated using the method described in Sections 3.2.1.1 and 3.2.1.2, as shown in Figure 3.3a. Although accurate damage severity cannot be obtained because of the low-scale model, the suspected damage region, that is, interval [5, 6], can be successfully identified at scale V_0 . Subsequently, in Stage 2, the WFEM is refined on interval [5, 6] by lifting the wavelet scale; that is, the shape function of the wavelet is represented by the wavelet approximation in space V_1 . Meanwhile, one more measurement point at $x = 5.5$ is added in the modal test. Thus, the resolution of the measured mode shapes is also refined in this region. As shown in Figure 3.3b, the damage can be localized in a smaller sub-element region in Stage 2. Repeating the refinement and detection process allows for a more accurate estimation of damage location and severity through iteration. The results in Stages 3 and 4 show almost the same damage severity, implying that the estimation converges and no further refinement is necessary. The quantification results of the damage severity in each stage are also shown in Figure 3.3. The relatively inaccurate estimation of damage severity in the low-scale model is expected because of the inaccurate assumption of damage location. However, quantification accuracy is effectively improved with the progressive refinement of the model, and the accuracy finally converges toward the real value in Stages 3 and 4. The damage quantification results in Figures 3.3a, 3.3b, and 3.3c are for illustration only. According to the procedure described in Section 3.2.3, damage severity may be quantified only when the damage location is best identified, that is, in the last stage (Figure 3.3d) in this case.

Considering that the damage location is always unpredictable, TFEM should be uniformly meshed without the adaptive-scale technique. A total of 32 beam elements with 66 DOFs are required to accurately capture the damage in Case 1, where a single

damage region consists of $1/32$ of the entire beam. However, with the proposed adaptive-scale strategy, only 24 DOFs in Stage 4 are utilized in WFEM. Furthermore, specifying the required model scale in advance is not required, and the damage is localized and quantified progressively.

Case B-2 involves a beam subjected to double damages with 20% severity. The damage locations and severities are described in Table 3.1, and the corresponding refinement process and damage detection results are presented in Figure 3.4 and Table 3.2, respectively. Following a similar process, the locations and severities of the damage can be identified with progressively improved accuracy. Given that the left-hand damage consists of $1/16$ of the entire beam, a good estimation is obtained in Stage 2 and verified in Stage 3. Thus, no further refinement is conducted in this region in the last stage. In comparison, the right-hand damage is $1/32$ of the beam length, and the relevant region is gradually refined until Stage 4. These findings demonstrate that the model scale can be adaptively adjusted according to the actual damage scenarios. Such adaptability of the proposed strategy can help achieve accurate results with reduced number of DOFs, sensors, and computation cost in applications.

Figure 3.5 shows the dimension and damage locations of a two-span continuous beam. The severity of two damages is also 20%, with one in the interval of $[3.25, 3.5]$ and the other in the interval of $[12.5, 12.75]$. The corresponding damage identification results are summarized in Table 3.2. Again, both the locations and severities of the damages can be identified with progressively improved accuracy.

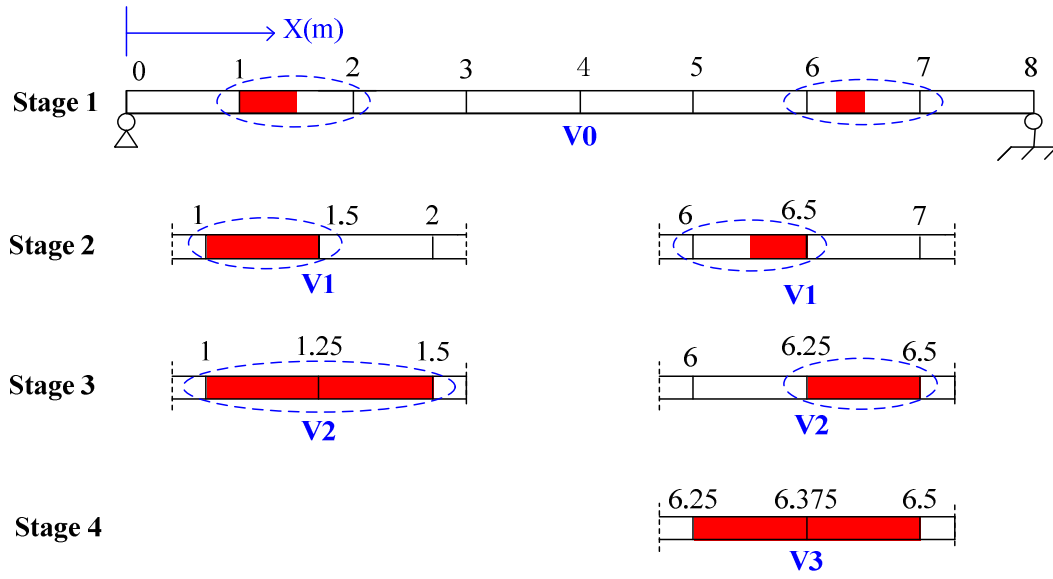


Figure 3.4. Model refinement process for Case B-2

Table 3.2. Adaptive-scale location and quantification of damage using WFEM

Stage	Case B-1		Case B-2		Case B-3	
	Location(m)	Severity (%)	Location(m)	Severity (%)	Location(m)	Severity (%)
1	[5, 6]	6.4	[1, 2]	7.8	[3, 4]	5.4
			[6, 7]	5.2	[12, 13]	5.4
2	[5, 5.5]	11.5	[1, 1.5]	21.7	[3, 3.5]	9.0
			[6, 6.5]	9.5	[12.5, 13]	9.0
3	[5.25, 5.5]	21.7	[1, 1.25]	20.4	[3.25, 3.5]	21.2
			[1.25, 1.5]	20.5	[12.5, 12.75]	21.2
			[6.25, 6.5]	20.5		
4	[5.25, 5.375]	21.0	[1, 1.25]	20.4	[3.25, 3.375]	20.6
	[5.375, 5.5]	20.9	[1.25, 1.5]	20.4	[3.375, 3.5]	20.1
			[6.25, 6.375]	20.3	[12.5, 12.625]	20.1
			[6.375, 6.5]	20.2	[12.625, 12.75]	20.6

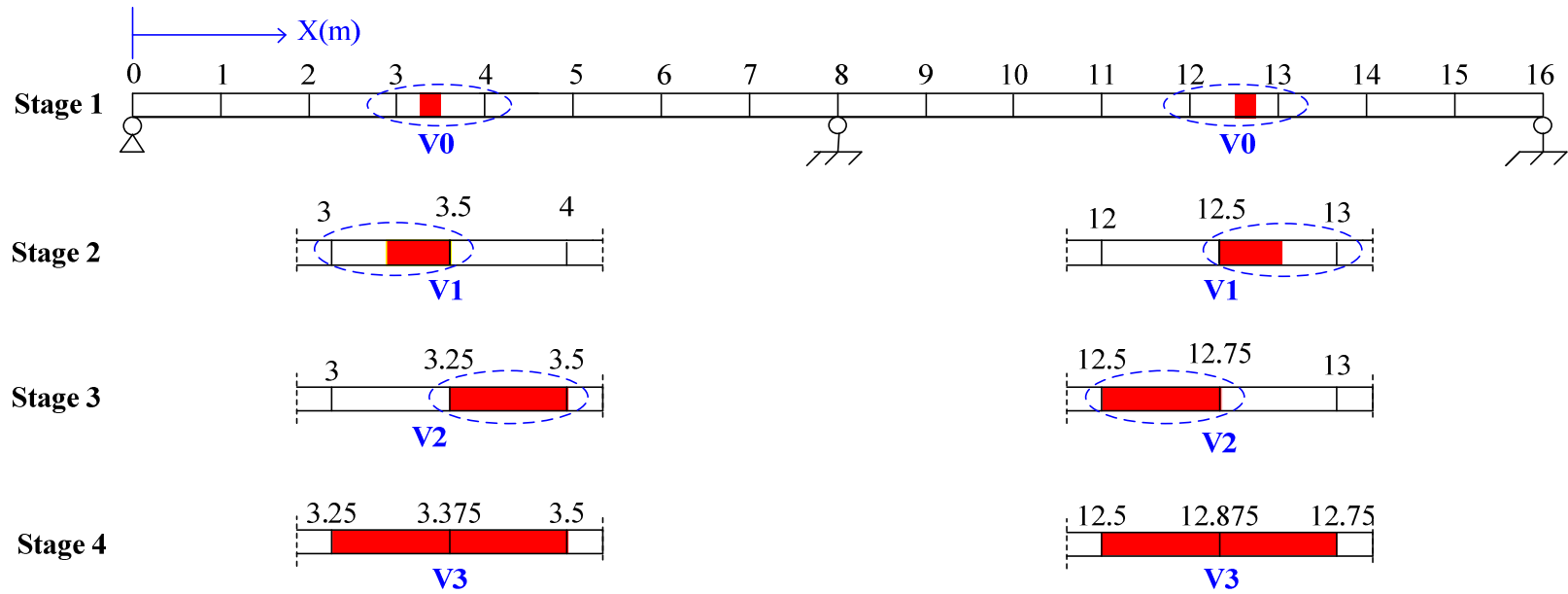


Figure 3.5. Model refinement process for Case B-3

3.3.2 Plate Structure

Figure 3.6 shows a thin plate with dimensions of 600 mm \times 700 mm \times 3 mm. The material of the plate has the following properties: elastic modulus $E = 68.9$ Gpa , density $\rho = 2700$ Kg/m³ , and Poisson's ratio $\mu = 0.27$. Table 3.3 shows the two damage cases considered in this section: single- and double-damage cases.

Case P-1 involves a single damage (Damage I) in the rectangle $[0.2, 0.25] \times [0.375, 0.4]$ with 20% damage severity. Figures 3.7 and 3.8 show the adaptive-scale model refinement process and corresponding damage localization results, respectively.

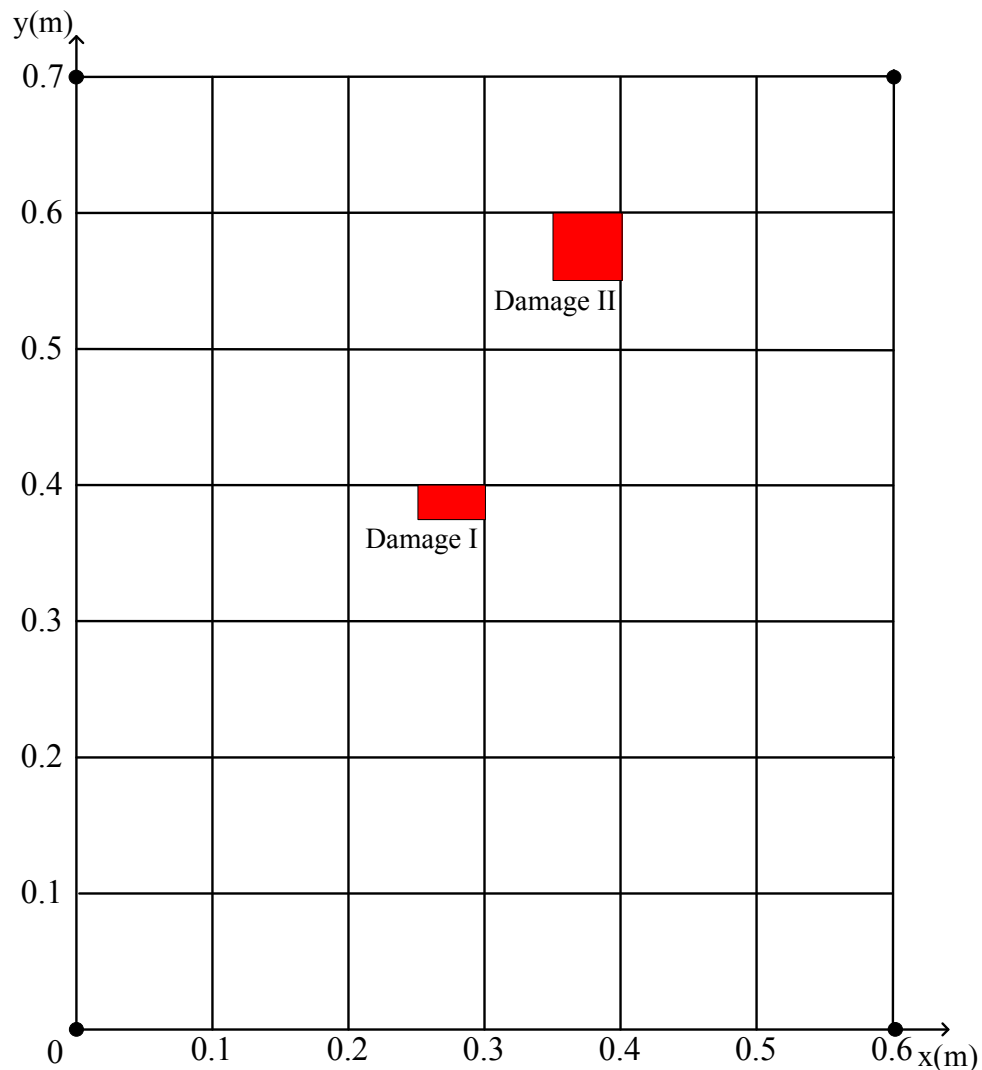


Figure 3.6. Thin plate in numerical study

Table 3.3. Damage scenarios considered in the numerical simulations of the plate

Damage scenarios	Damage		
	Region	Severity (%)	
Case P-1	Damage I	$[0.25, 0.3] \times [0.375, 0.4]$	20
Case P-2	Damage I	$[0.25, 0.3] \times [0.375, 0.4]$	20
	Damage II	$[0.35, 0.4] \times [0.55, 0.6]$	10

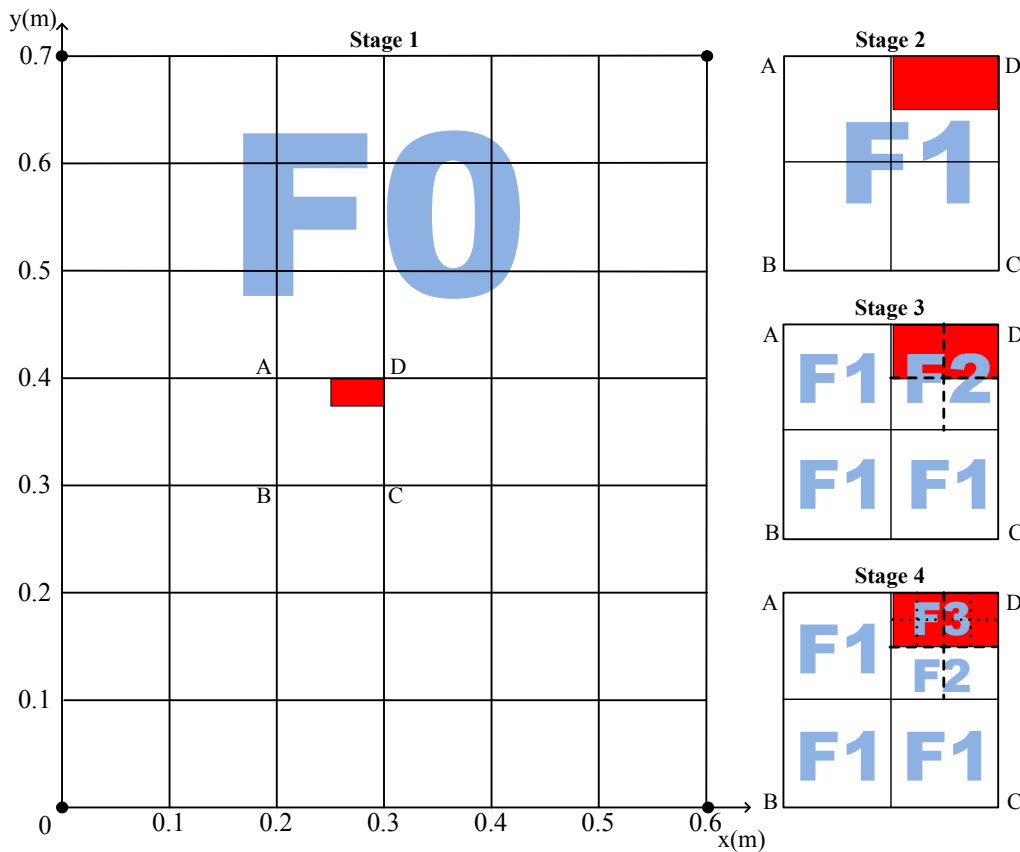


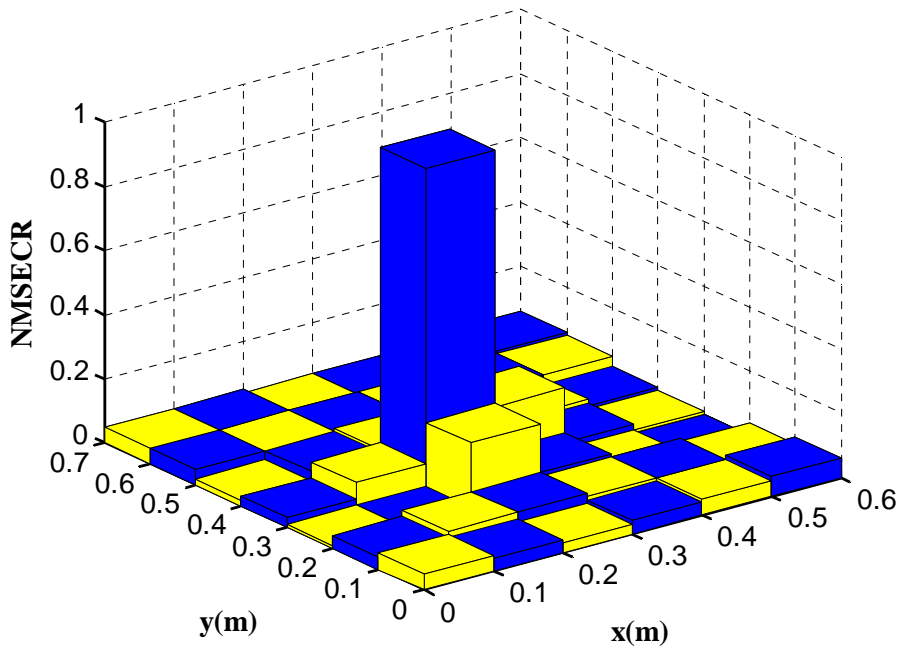
Figure 3.7. Model refinement process for Case P-1

In Stage 1, the plate is first modeled by 6×7 wavelet plate elements at scale 0, that is, the displacement field function of each element is approximated in wavelet space F_0 . The corresponding number of DOFs at this stage is 220. Figure 3.8 shows the damage location indicators associated with the first mode shape for each region. Figure 3.8a indicates that the region $[0.2, 0.3] \times [0.3, 0.4]$ (ABCD) is an identified suspected

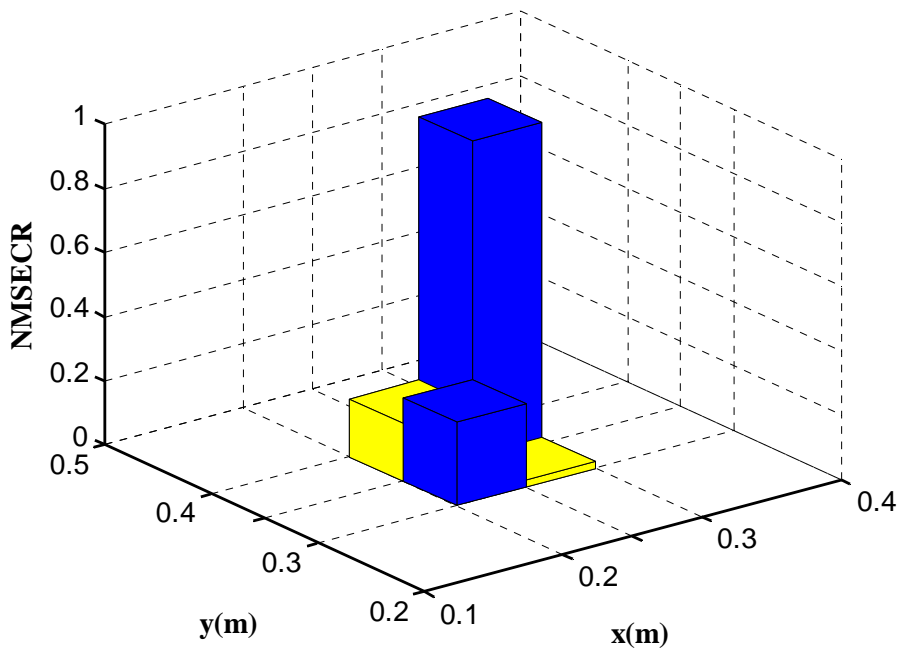
damage region. Table 3.4 describes the damage severity estimated by using the damage quantification equation [Equation (3.26)]. Subsequently, WFEM is refined in region ABCD by adding scale 0 wavelets in Stage 2. In this stage, the wavelet approximation space is lifted to F1. One more measurement point at interval (0.25, 0.35) is added to increase the resolution of the measured mode shape in region ABCD in the vibration test. Only the MSE in the suspected region ABCD is calculated. Figure 3.8b shows the damage location identified in a smaller region ($[0.25, 0.3] \times [0.35, 0.4]$) with improved estimation accuracy. Further refinement and identification processes are performed for accurate detection results. In Stage 3, the wavelet approximation space in the suspected region is lifted to F2. Consequently, the suspected damage regions are further reduced to $[0.25, 0.275] \times [0.375, 0.4]$ and $[0.275, 0.3] \times [0.375, 0.4]$, which are identical to the actual damage regions in Figure 3.8c. The refinement process is continued in Stage 4 by lifting the wavelet approximation space to F3 in the suspected regions. Two more measurement points at (0.2625, 0.3875) and (0.2875, 0.3875) are added in the modal test. The suspected damage regions are not reduced further as Stages 3 and 4 provide the same results (Figures 3.8c and 3.8d). Table 3.4 shows the corresponding damage quantification results. The accuracy of damage severity quantification is effectively improved with the progressive refinement of WFEM. This case requires at least 24×28 plate elements with 2,896 DOFs to capture the damage location and severity accurately if TFEM with uniform meshing is used. However, only 236 DOFs are used in Stage 4 through multi-scale WFEM.

Table 3.3 and Figure 3.6 show the double damages in Case P-2: the first region $[0.2, 0.25] \times [0.375, 0.4]$ with 20% severity (Damage I) and the second region $[0.35, 0.4] \times [0.55, 0.6]$ with 10% severity (Damage II). Following the same process employed in Case P-1, damage is progressively identified with improved accuracy. Figures 3.9 and 3.10 and Table 3.4 present the WFEM refinement process, damage localization, and quantification results, respectively. Given that Damage II consists of $1/168$ ($1/12 \times 1/16$) of the entire plate, a good estimation of damage location and severity are obtained in Stage 2 and confirmed in Stage 3. Therefore, the wavelet approximation space is

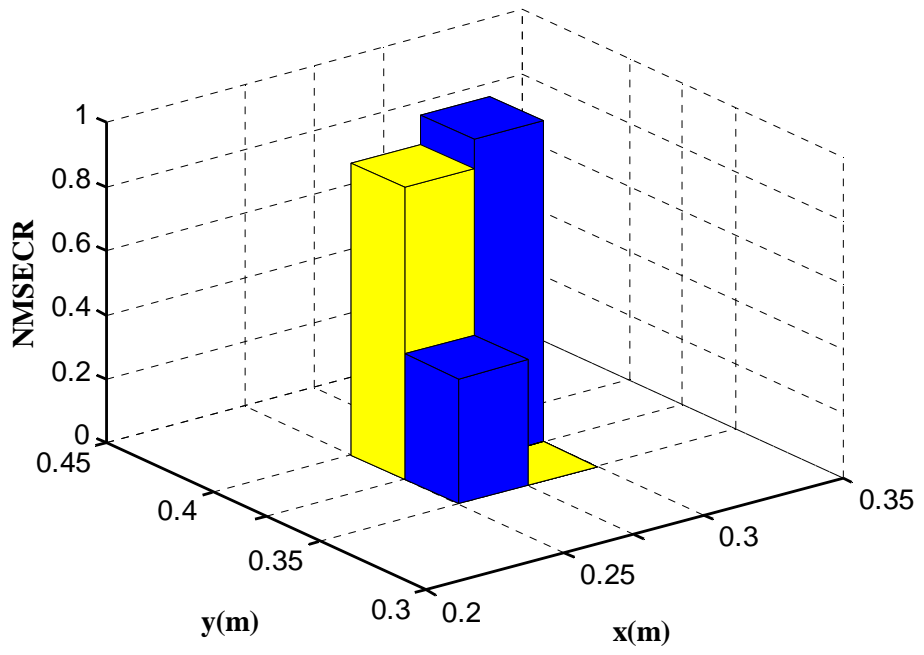
recovered to F1 in the Damage II region in Stage 4. By contrast, Damage I consists of $1/336$ ($1/12 \times 1/32$) of the plate. The relevant region is gradually refined until Stage 4.



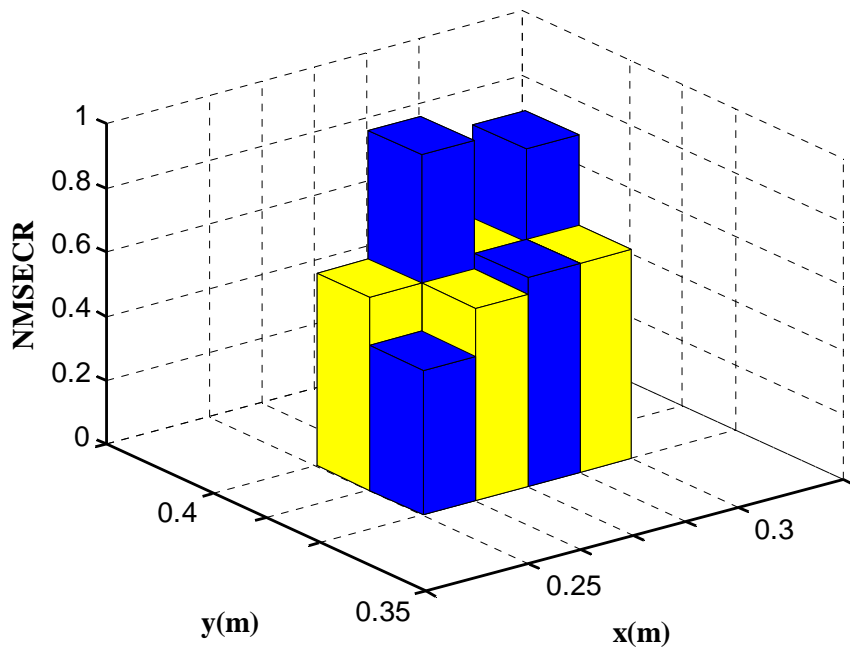
(a) Stage 1



(b) Stage 2



(c) Stage 3



(d) Stage 4

Figure 3.8. Adaptive-scale damage identification results for Case P-1

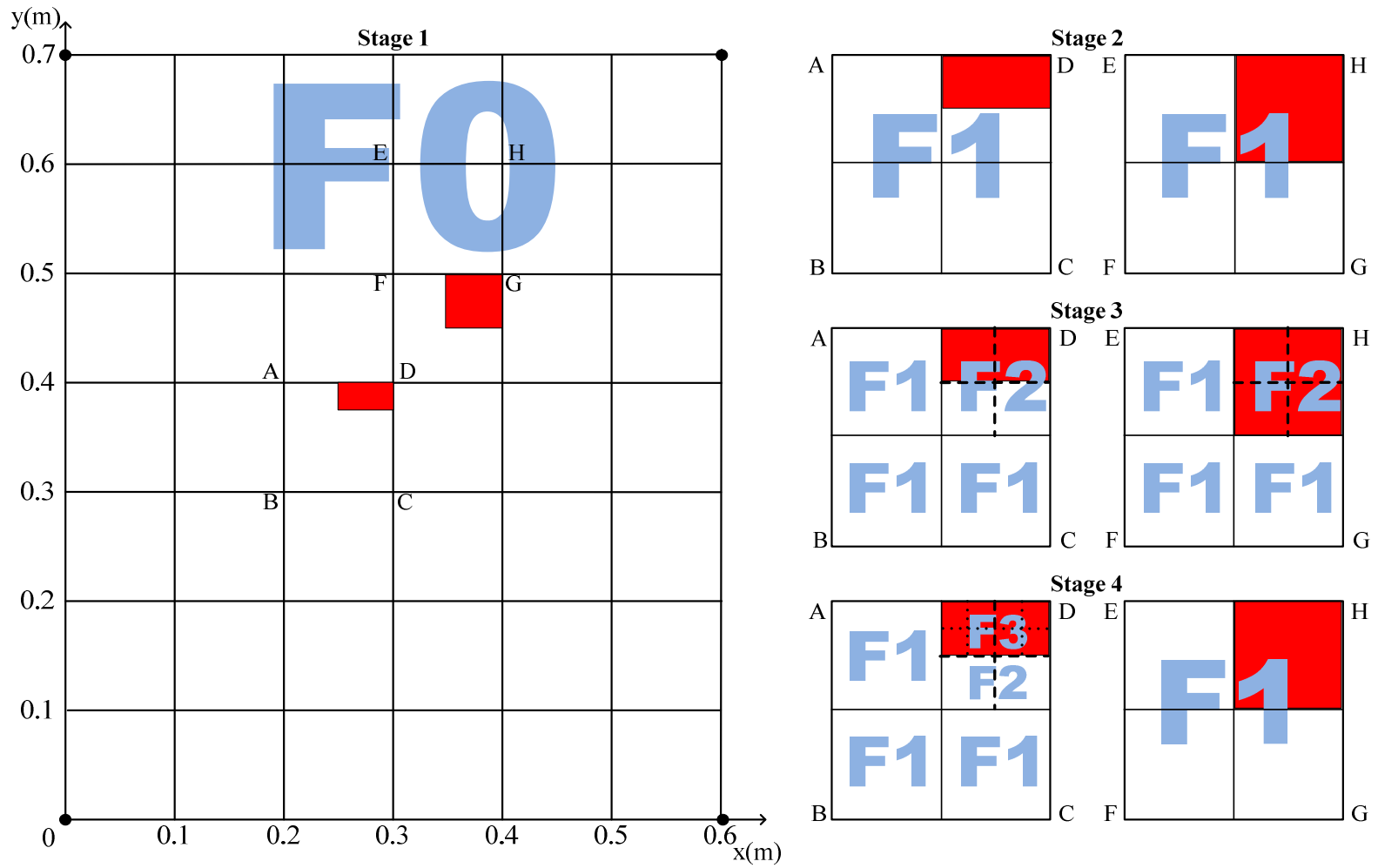
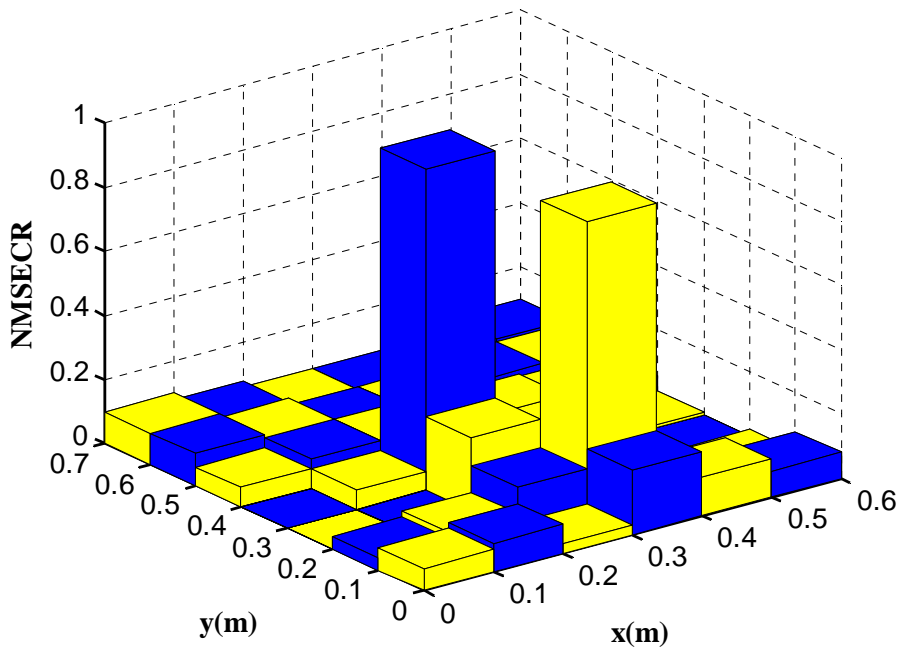


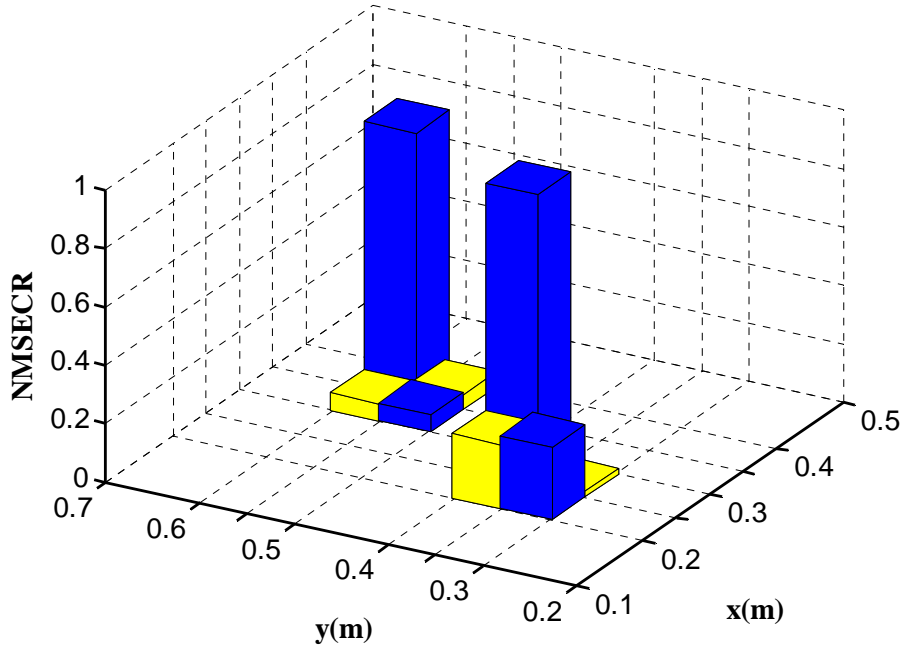
Figure 3.9. Model refinement process for Case P-2

Table 3.4. Damage severity quantification results

Case	Stage 1	Stage 2	Stage 3	Stage 4
Case P-1	$[0.2, 0.3] \times [0.3, 0.4]$, 2.8%	$[0.25, 0.3] \times [0.35, 0.4]$, 10.4%	$[0.25, 0.275] \times [0.375, 0.4]$, 19.1%	$[0.2500, 0.2625] \times [0.3750, 0.3875]$, 18.4%
				$[0.2500, 0.2625] \times [0.3875, 0.4000]$, 18.7%
				$[0.2625, 0.2750] \times [0.3750, 0.3875]$, 20.0%
				$[0.2625, 0.2750] \times [0.3875, 0.4000]$, 18.8%
				$[0.2750, 0.2850] \times [0.3750, 0.3875]$, 18.8%
				$[0.2750, 0.2850] \times [0.3875, 0.4000]$, 19.8%
				$[0.2850, 0.3000] \times [0.3750, 0.3875]$, 18.2%
				$[0.2850, 0.3000] \times [0.3875, 0.4000]$, 18.4%
			$[0.35, 0.375] \times [0.55, 0.575]$, 9.8%	
			$[0.35, 0.375] \times [0.575, 0.6]$, 10.0%	/
$[0.3, 0.4] \times [0.5, 0.6]$, 2.8%	$[0.35, 0.4] \times [0.55, 0.6]$, 9.9%	$[0.375, 0.4] \times [0.55, 0.575]$, 9.8%		
		$[0.375, 0.4] \times [0.575, 0.6]$, 9.9%		
Case P-2	$[0.2, 0.3] \times [0.3, 0.4]$, 2.5%	$[0.25, 0.3] \times [0.35, 0.4]$, 10.9%	$[0.25, 0.275] \times [0.375, 0.4]$, 19.1%	$[0.2500, 0.2625] \times [0.3750, 0.3875]$, 19.5%
				$[0.2500, 0.2625] \times [0.3875, 0.4000]$, 18.4%
				$[0.2625, 0.2750] \times [0.3750, 0.3875]$, 19.8%
				$[0.2625, 0.2750] \times [0.3875, 0.4000]$, 18.2%
				$[0.2750, 0.2850] \times [0.3750, 0.3875]$, 18.2%
				$[0.2750, 0.2850] \times [0.3875, 0.4000]$, 19.6%
				$[0.2850, 0.3000] \times [0.3750, 0.3875]$, 17.6%
			$[0.275, 0.3] \times [0.375, 0.4]$, 18.9%	$[0.2850, 0.3000] \times [0.3875, 0.4000]$, 19.5%



(a) Stage 1



(b) Stage 2

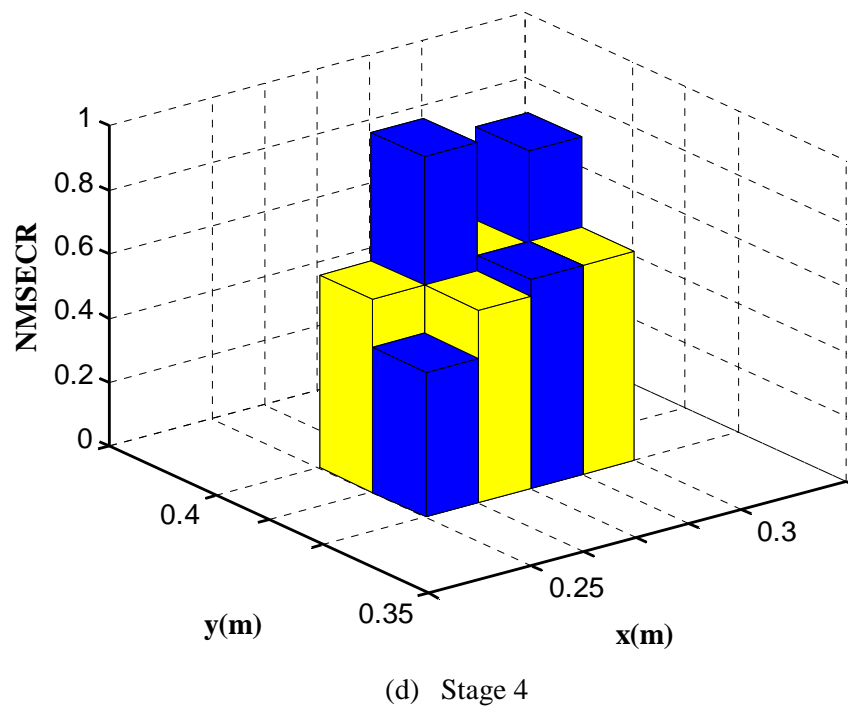
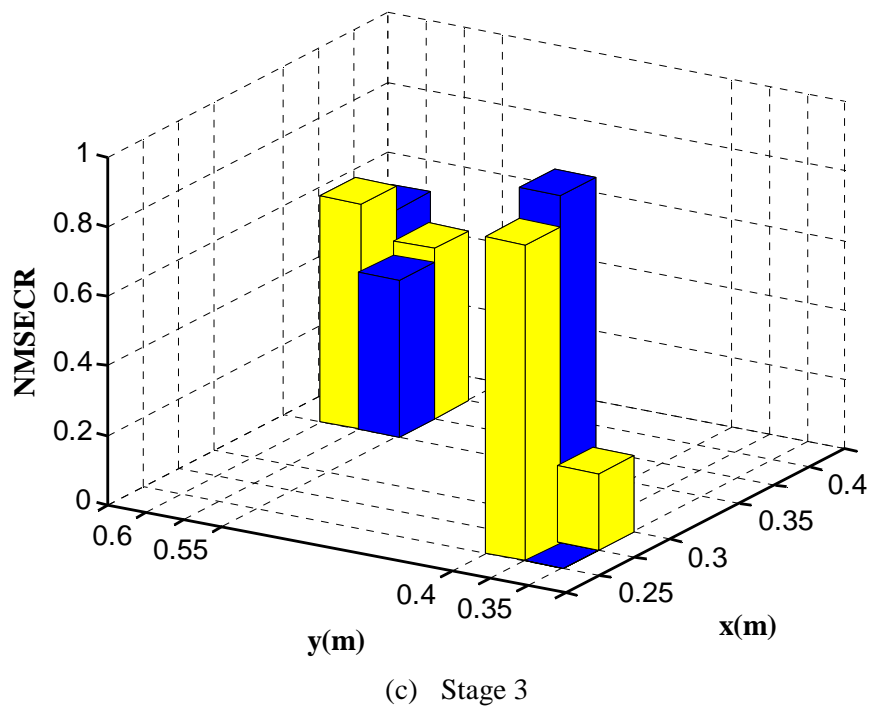


Figure 3.10. Adaptive-scale damage identification results for Case P-2

3.3.3 Noise Effects

In the actual modal test, the collected data are inevitably contaminated by measurement noise. Therefore, the sensitivity of the proposed damage detection strategy to the error or uncertainty in the measured modal properties is examined.

The mode shape with measurement error is expressed by (Yan et al. 2010)

$$\tilde{\varphi}_{ir} = \varphi_{ir}(1 + \eta\zeta_{ir}) \quad (3.30)$$

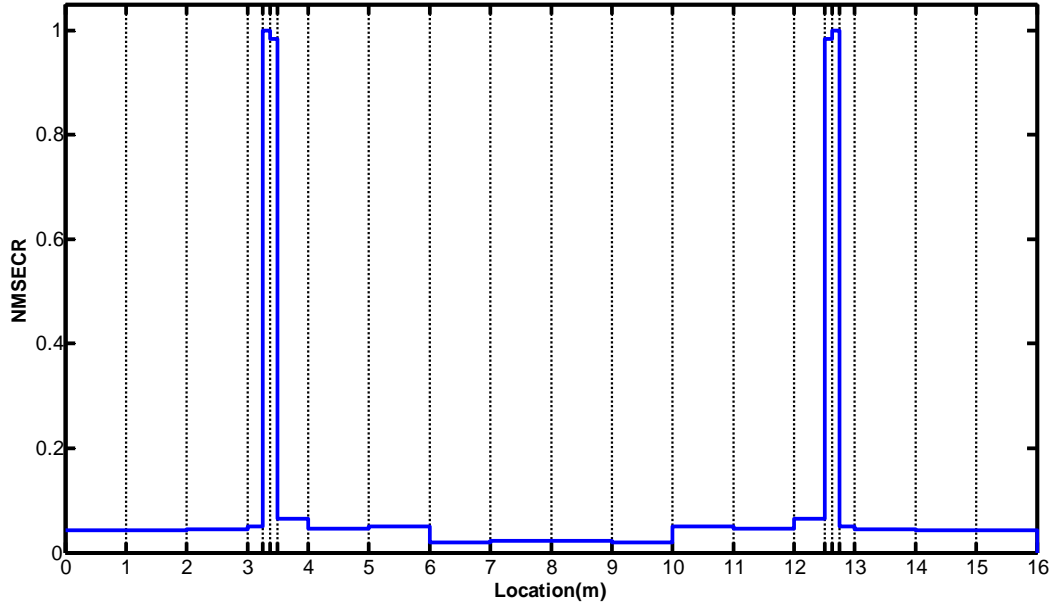
where $\tilde{\varphi}_{ir}$ and φ_{ir} are the "measured" and accurate mode shape components of the i^{th} mode at the r^{th} DOF, respectively; η is the measurement error level considered in the "measured" mode shapes; and ζ_{ir} is the zero-mean Gaussian random variables. The random measurement error is simulated through the Monte Carlo method, and each level of measurement error consists of 1,000 Monte Carlo simulations. The statistical characteristics of the damage detection results, such as the coefficient of variance (COV) of the estimated damage location and severity, are examined.

$$COV = \frac{\sigma_a}{\bar{a}} \quad (3.31)$$

where \bar{a} and σ_a represent the mean and standard deviation of the damage index (location or severity), respectively. Five different levels of measurement error in mode shapes are considered: 1%, 2%, 3%, 4%, and 5%.

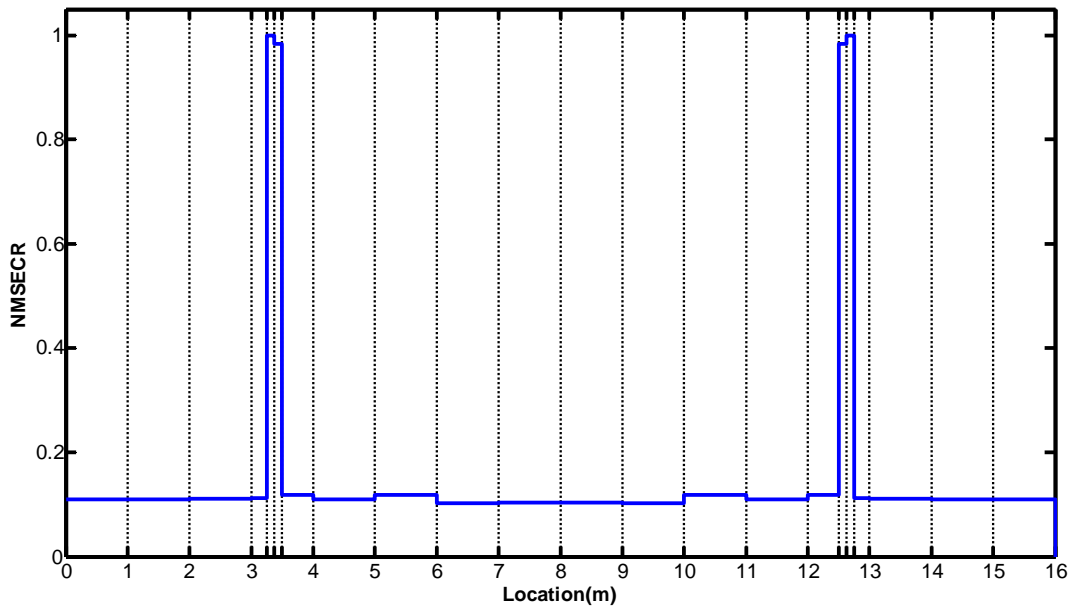
Figure 3.11 shows the damage localization and quantification results in the last stage (Stage 4) of Case B-3 with different levels of measurement error. The *NMSECRs* and the estimated damage severities are the ensemble average of 1,000 samples. The average results can well reflect the locations and severities of the double damages, but the presence of measurement error affects the average *NMSECR* of undamaged regions, which increases with the measurement error level. In general, no significant changes can be observed among three measurement error levels, implying that the effect of random measurement error can be minimized by averaging the results from a sufficient

number of measurements. However, apparent changes in COV can be observed with the increase in the measurement error level.



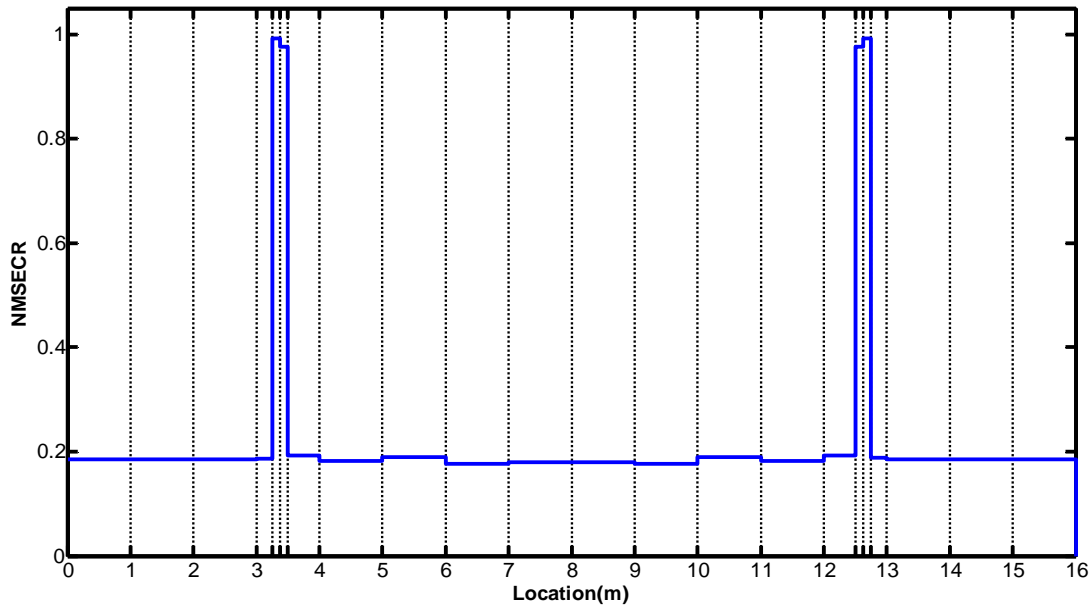
(a) No error

$\beta = -0.206$ in $[3.25, 3.375]$, $\beta = -0.201$ in $[3.375, 3.5]$
 $\beta = -0.201$ in $[12.5, 12.625]$, $\beta = -0.206$ in $[12.625, 12.75]$



(b) 3% error

$\beta = -0.205$ in $[3.25, 3.375]$, $\beta = -0.200$ in $[3.375, 3.5]$
 $\beta = -0.200$ in $[12.5, 12.625]$, $\beta = -0.205$ in $[12.625, 12.75]$



(c) 5% error

$\beta = -0.205$ in $[3.25, 3.375]$, $\beta = -0.200$ in $[3.375, 3.5]$
 $\beta = -0.200$ in $[12.5, 12.625]$, $\beta = -0.205$ in $[12.625, 12.75]$

Figure 3.11. Damage detection results under different noise levels in Stage 4 of Case B-3

Figures 3.12 and 3.13 show the COVs of the estimated damage indices (location and severity) at different scales in Case B-1 and Case B-3. Figures 3.14 and 3.15 show the COVs of the estimated damage indices (location and severity) at different scales in Case P-1. A high COV in the results implies a high level of uncertainty in a single sample or more samples are required to obtain accurate estimation. In general, the uncertainty in the detection results increases with the measurement error level. The same error level results have high COV at a high wavelet scale, indicating that a high-scale WFEM is sensitive to measurement noise. Measurement noise affects the detection results of plate structures more than that of beam structures.

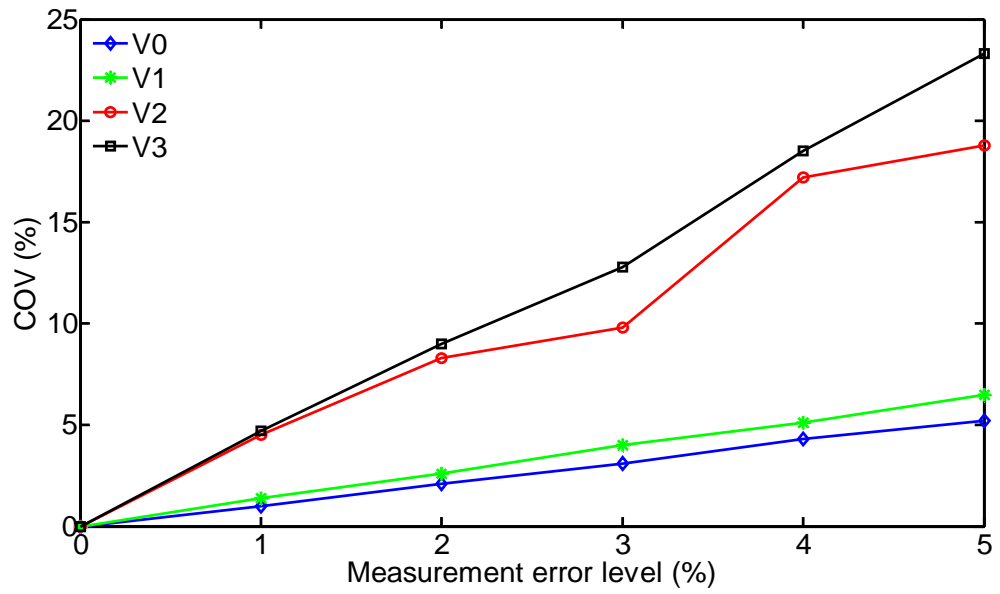


Figure 3.12. COV of the estimated damage localization index in Case B-1

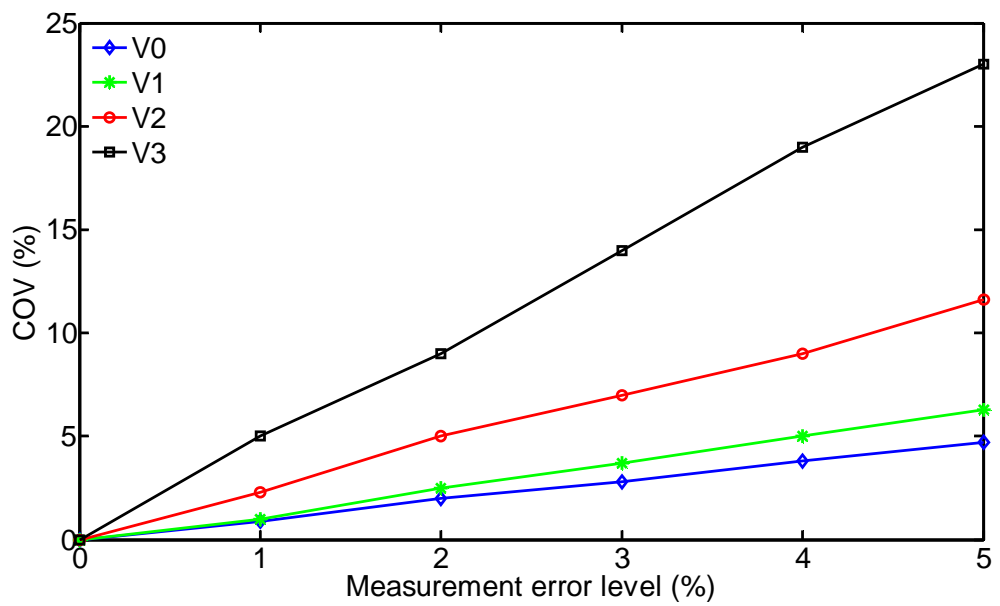


Figure 3.13. COV of the estimated damage severity index in Case B-3

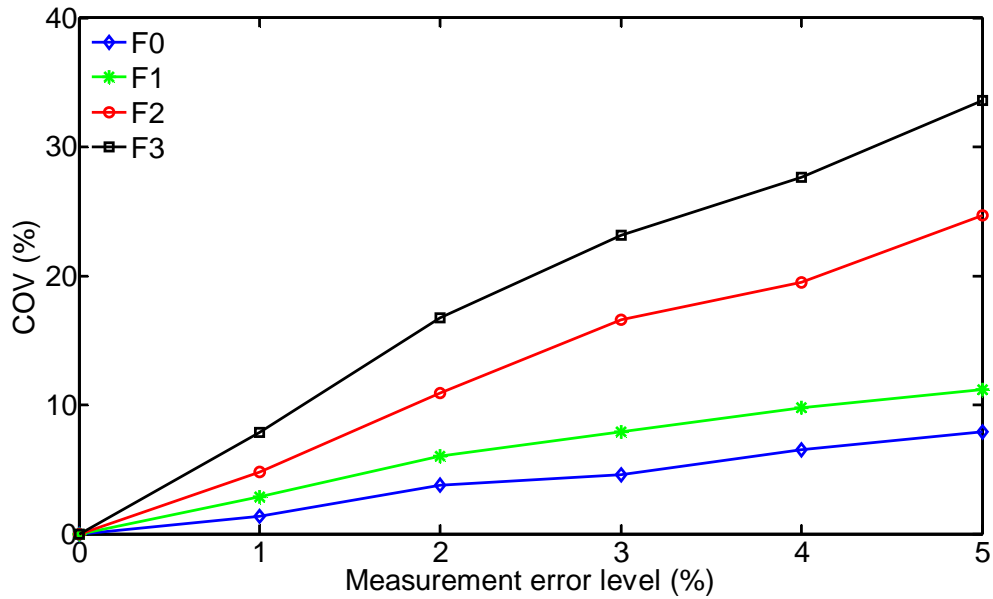


Figure 3.14. COV of the estimated damage localization index in Case P-1

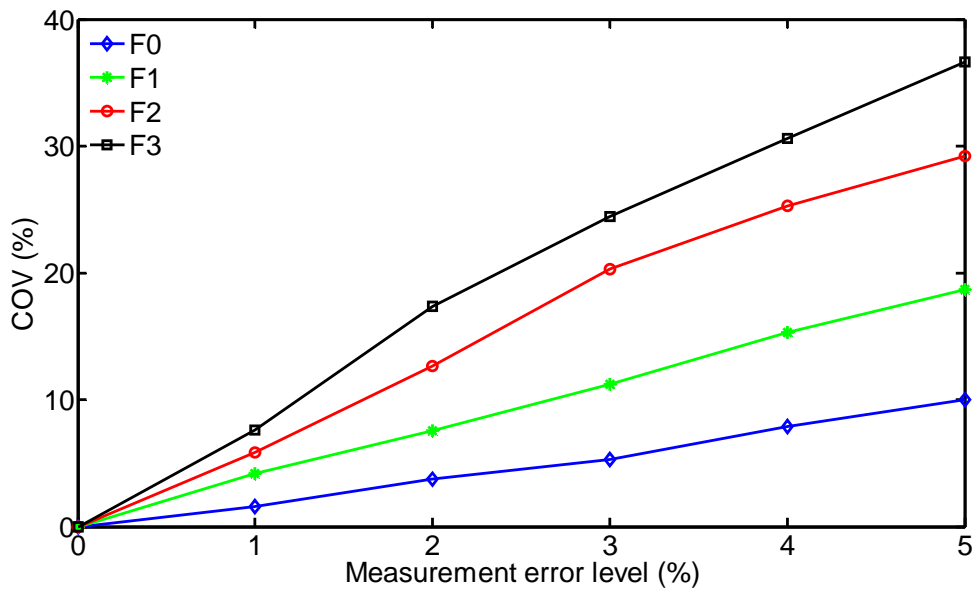


Figure 3.15. COV of the estimated damage severity index in Case P-1

3.4 Summary

A progressive damage detection strategy is proposed for beam and thin plate structures through the use of wavelet finite beam and plate elements, respectively. By using MSE as a damage indicator, structural damage is localized and quantified progressively. A coarse WFEM is used to identify the likely damaged region, and gradually lifted

WFEMs with local refinement are used to estimate the accurate location and severity of the damage. The superior multi-resolution and localization properties of WFEM allow for a flexible and convenient change in modeling scales in the damage detection process. WFEM is gradually refined from low to high resolution in critical regions. Therefore, the WFEM-based progressive damage detection strategy achieves a desirable tradeoff between modeling details and entirety. Moreover, it allows for the arrangement of sensors in the most likely damaged regions, which does not only reduce the number of required sensors but also enhances the damage detection capability. The two-step detection process (i.e., localization and quantification) also improves the efficiency and accuracy of damage detection.

Numerical examples of a simply supported beam, a two-span continuous beam, and a thin plate simply supported on four corners are analyzed under different damage scenarios. The results demonstrate that the proposed strategy can progressively and accurately locate and quantify sub-element damages. The proposed strategy is efficient in terms of DOFs, sensors, and computation effort because the wavelet scale can be adaptively enhanced and reduced according to actual needs. The effect of measurement noise on the detection results is also assessed via Monte Carlo simulations. Detection accuracy at a relatively higher scale is more sensitive to noise. Measurement noise affects the detection results of plate structures more than that of beam structures.

Chapter 4 Progressive Damage Detection Based on Model Updating

4.1 Introduction

FEM updating is a commonly employed structural damage detection tool. It aims to achieve a high level of agreement between numerical results and test data by modifying structural mass, stiffness, and damping parameters in numerical models. Following the same strategy as in Chapter 3, a progressive damage detection method based on WFEM updating for beam and plate structures is proposed in this chapter. Sub-element damage can be gradually identified through the multi-scale model updating process according to the measured modal properties. The scale of the wavelet elements in the regions of concern is adaptively enhanced or reduced to remain compatible with the gradually identified damage regions during the process; the test modal information remains the same, i.e., no sensors replacement or new sensors are needed. The proposed method can effectively minimize the number of DOFs in WFEM as well as the number of unknown variables to be updated. Thus, computation efficiency can be considerably enhanced. Numerical and experimental examples are provided to validate the proposed multi-scale WFEM updating-based damage detection method.

4.2 Progressive Updating of WFEM

FEM updating aims to minimize the error between certain quantities obtained from the measurement data and model simulation. Selecting updating parameters and formulating an objective function are two critical components during the FEM updating procedure.

4.2.1 WFEM Updating

Damage detection studies often assume that no mass alteration occurs before and after damage, which is acceptable in most situations. Damage indexes BD_s for beam and PD_s for plate are represented by the relative variation of flexural rigidity as follows:

$$BD_s = 1 - \frac{EI_d^s}{EI_u^s} \quad (4.1a)$$

$$PD_s = 1 - \frac{D_d^s}{D_u^s} \quad (4.1b)$$

where EI and D are the flexural rigidity of the beam and plate, respectively. Subscripts u and d denote the undamaged and damaged states, respectively. Given that damage is assumed to be the reduction in flexural rigidity in a sub-element region, that is, the damage size is only part of an element rather than an entire element, the primary multi-scale and localization characteristics of WFEM can be fully maximized. The identification of the damage index for each sub-element region allows one to estimate not only the damage location but also the damage severity.

The optimization problem involves minimizing the difference between experimental and numerical modal properties by updating sub-element flexural rigidity. The measured natural frequency and MAC, which are commonly adopted in model updating, are also utilized in this chapter in the objective function.

$$\min J(\mathbf{p}) = \sum_{i=1}^n \alpha_i \left[\left(\frac{\lambda_{ni}(\mathbf{p}) - \lambda_{ni}^0}{\lambda_{ni}^0} \right) - \left(\frac{\lambda_{ei}^d - \lambda_{ei}^u}{\lambda_{ei}^u} \right) \right]^2 + \sum_{i=1}^n \beta_i \left[\text{sqrt}(MAC_{ni}(\mathbf{p})) - \text{sqrt}(MAC_{ei}) \right]^2 \quad (4.2)$$

$$\lambda_{ni} = (2\pi f_{ni})^2 \quad (4.3a)$$

$$\lambda_{ei} = (2\pi f_{ei})^2 \quad (4.3b)$$

$$MAC_{ni} = \frac{[\phi_{ni}^T(\mathbf{p})\phi_{ni}^0]^2}{[\phi_{ni}^T(\mathbf{p})\phi_{ni}(\mathbf{p})][(\phi_{ni}^0)^T\phi_{ni}^0]} \quad (4.4a)$$

$$MAC_{ei} = \frac{[(\phi_{ei}^u)^T \phi_{ei}^d]^2}{[(\phi_{ei}^u)^T \phi_{ei}^d][(\phi_{ei}^u)^T \phi_{ei}^d]} \quad (4.4b)$$

where the vector $\mathbf{p} \in R^n$ represents the set of updating parameters; superscript 0, u , and d denote the initial, undamaged, and damaged states, respectively; f_{ni} and f_{ei} are the numerical and experimental natural frequency of the i^{th} mode, respectively; ϕ_{ni} and ϕ_{ei} are the numerical and measured mode shape of the i^{th} mode; and α_i and β_i are the weighting factors of the i^{th} mode (usually assigned according to their importance and measurement accuracy in experiment). In the following numerical and experimental study, they are all set to 1.

For the numerical study, considering that the initial state (denoted by 0) of the WFEM is assumed to be the same as the undamaged state (denoted by u), the objective function can be simplified as

$$\min J(\mathbf{p}) = \sum_{i=1}^n \alpha_i \left[\frac{\lambda_{ni}(\mathbf{p}) - \lambda_{ei}}{\lambda_{ei}} \right]^2 + \sum_{i=1}^n \beta_i [sqrt(MAC_i) - 1]^2 \quad (4.5)$$

$$MAC_i = \frac{(\phi_{ni}^T \phi_{ni})^2}{(\phi_{ni}^T \phi_{ni})(\phi_{ei}^T \phi_{ei})} \quad (4.6)$$

4.2.2 Damage Detection Procedure

By using the salient multi-scale characteristics of WFEM, a progressive damage detection strategy is developed for beam and plate structures. Figure 4.1 presents the flowchart of this damage detection scheme. The detailed procedure is described as follows.

Step 1: Install sensors on the concerned structure and measure its dynamic parameters (i.e., frequencies and mode shapes), and then calculate the MACs. Only the magnitudes of the mode shapes at DOFs coincident with sensor locations are

adopted.

Step 2: Select and initialize updating parameters, update a relatively low-scale WFEM, and estimate the occurrence and rough location of the structural damage (if any).

Step 3: Refine the WFEM in the suspected region accordingly by adding high-scale wavelet terms. Select the updating parameters in the suspected region only, and update the lift WFEM by iteration, with the initial values being the damage severities obtained in the last step. Consequently, the damage can be localized in a smaller region, and the damage severity can be quantified more accurately.

Step 4: Check the convergence of the results, and stop if the difference is smaller than a prescribed threshold. Otherwise, repeat Step 3.

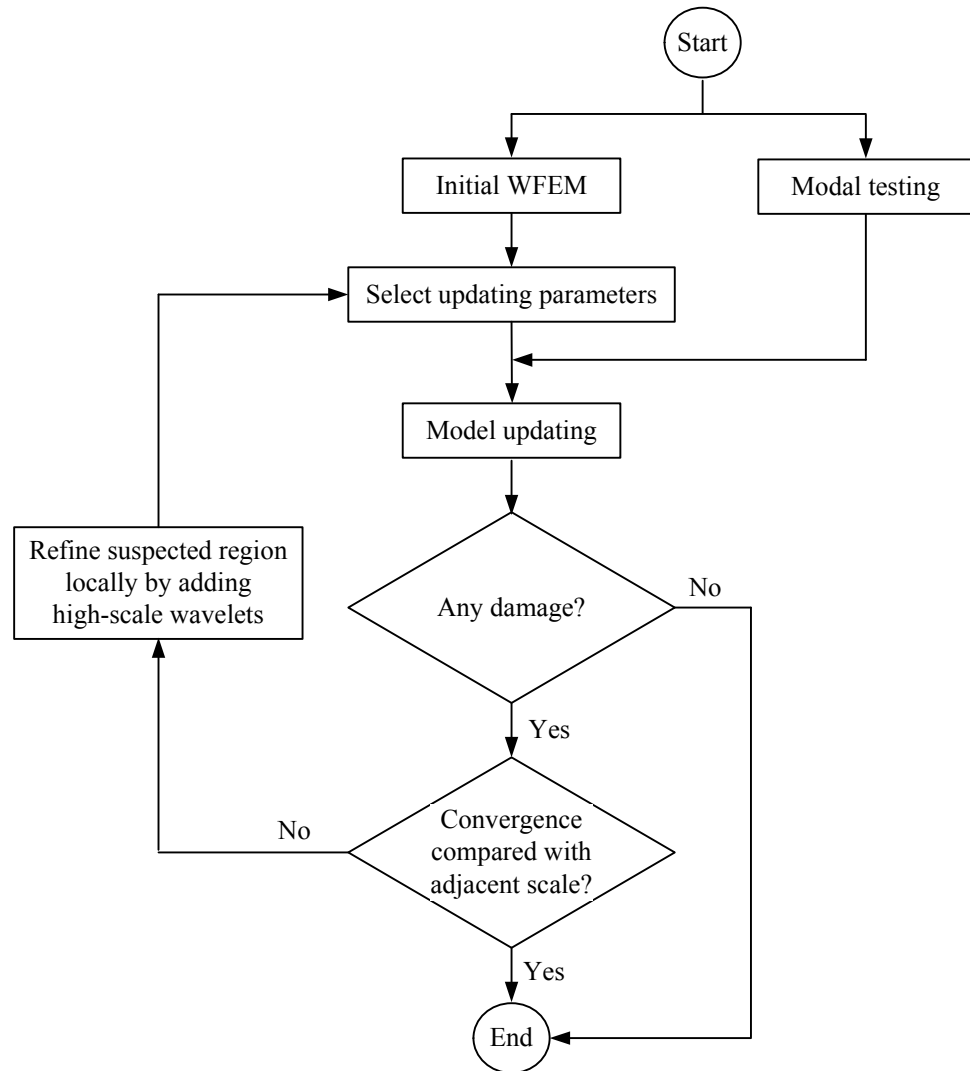


Figure 4.1. Diagram of the multi-scale WFEM updating scheme

During the damage detection process, the updating parameters are adaptively selected according to the gradually identified damage scenarios and limited to the suspected regions only. Thus, the computation cost in the optimization process can be reduced considerably. Furthermore, only WFEM is adaptively changed, and no additional requirements, such as installing more sensors in the suspected damage regions, are required in the modal test.

4.2.3 Effect of Sub-Element Damage

The impact of sub-element damage on the beam element stiffness matrix is illustrated by the following example. Figure 4.2 shows a wavelet beam element with a localized damage within the interval of [0.25, 0.5]. The damage severity is 80%. The change percentage of each element in the stiffness of the damaged wavelet finite element compared with the undamaged one is

$$\Delta = \begin{bmatrix} \begin{array}{cccc|c} \hline 0.05 & 0.10 & 0.05 & 0.00 & \\ \hline 0.10 & 0.16 & 0.10 & 0.03 & \\ \hline 0.05 & 0.10 & 0.05 & 0.00 & \\ \hline 0.00 & 0.03 & 0.00 & 0.01 & \\ \hline \end{array} \left. \begin{array}{l} [-1,1] \\ [0,2] \end{array} \right\} \begin{array}{l} V_0 \\ \\ \\ \end{array} \\ \begin{array}{c} \\ \\ \\ \end{array} \left. \begin{array}{l} 0.20 \\ 0.35 \end{array} \right\} [0,1] \\ \begin{array}{c} \\ \\ \\ \end{array} \left. \begin{array}{l} 0.40 \\ 0.40 \\ 0 \end{array} \right\} \begin{array}{l} [0,0.5] \\ [0.5,1] \end{array} \\ \begin{array}{c} \\ \\ \\ \end{array} \left. \begin{array}{l} 0 \\ 0 \\ 0.8 \end{array} \right\} \begin{array}{l} [0,0.25] \\ [0.25,0.5] \end{array} \\ \begin{array}{c} \\ \\ \\ \end{array} \left. \begin{array}{l} 0.8 \\ 0.8 \end{array} \right\} \end{bmatrix} \quad (4.7)$$

in which V_0 denotes the part constructed based on the scaling function at scale 0; W_0 , W_1 , and W_2 denote the parts constructed based on the wavelet functions at scale 0, 1, and 2, respectively. The support regions corresponding to each scale are also shown in the equation. At scale 0, although the non-zero elements in the sub-matrix W_0 indicate the likely change in this element, its change percentage is much less than 0.8. With the increase in scale, the values in W_2 not only indicate the location of the sub-element damage [0.25, 0.5], but also accurately represent the damage severity index equal to 0.8.

This is due to the different support regions of the wavelets at different scales. The support length is equal to 2 for scaling functions at scale 0 and equal to 1, 0.5, and 0.25 for wavelet functions at scale 0, 1, and 2, respectively. The elements in sub-matrix W_2 corresponding to the wavelets with the support regions in the interval $[0, 0.25]$ are equal to 0, whereas the matrix elements whose support regions are in the interval $[0.25, 0.5]$ are 0.8, equal to the damage severity.



Figure 4.2. Local damage in a wavelet beam element

In the progressive damage detection process, the damage index that reflects sub-region flexural rigidity can be selected as the parameter to be updated, where the length of the sub-region corresponds to the support length of the current scale. In the aforementioned example, the damage index of interval $[0, 1]$ is selected as the updating parameter for scale 0, the damage indices of intervals $[0, 0.5]$ and $[0.5, 1]$ are selected for scale 1, and the damage indices of intervals $[0, 0.25]$ and $[0.25, 0.5]$ are selected for scale 2. As shown in Equation (4.7), the stiffness matrix of the presented beam WFEM is fully scale-decoupled, which greatly reduces the computation cost. The progressive method performs efficiently because in each refinement stage, only higher scales of wavelets are added in the suspected region to achieve more precise results. The effect of sub-region damage on the plate element is similar.

4.3 Numerical Study

Numerical examples of a simply supported beam and a thin plate simply supported on four corners are employed again to demonstrate the effectiveness of the proposed progressive damage detection method.

Densely-meshed TFEMs are used to simulate the damaged structures and extract modal properties. The noise effect is considered in the numerical simulations using the same

method described in Section 3.3. In this section (Section 4.3), 0.5% artificial random noise is introduced in the frequencies and mode shapes. Only the first four frequencies and mode shapes are utilized because only the lower modes can be measured in real modal tests. Considering the difficulty in measuring rotational DOFs, only vertical DOFs in mode shapes are used. The modal information used in different stages is the same, and no new sensors are added during the WFEM refinement process.

4.3.1 Beam Structure

Figure 4.3 shows a simply supported beam with a length of $L = 8$ m, elastic modulus of 2.0×10^{11} N/m², density of 7.6×10^3 Kg/m³, cross-sectional area of $A = 0.08 \times 0.08$ m², and moment of inertia of $I = 3.4133 \times 10^{-6}$ m⁴. As shown in Table 4.1, two damage scenarios with different damage locations and severities are considered. In both cases, the assumption is that only vertical DOFs of mode shapes are measured at points ($x = 1, 2, \dots, 7$ m).

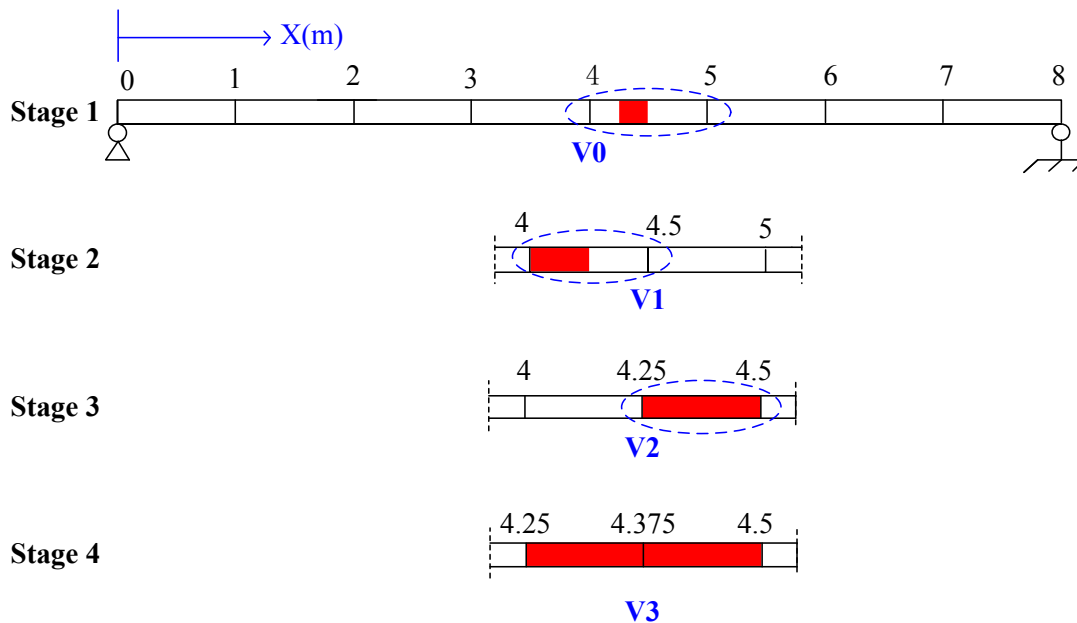


Figure 4.3. Model refinement process in Case B1

Table 4.1. Damage scenarios considered in the numerical simulations of the beam

	Damage scenario	Damage location	Damage severity (%)
Case B1	Single damage	[4.25, 4.5]	20
Case B2	Multiple damage	[2.75, 3]	20
		[4.5, 5]	10

Figure 4.3 illustrates the process of progressive damage detection in Case B1. The beam was modelled by eight equal-length wavelet elements. In Stage 1, the damage indices of the eight elements are updated via the optimization process with the objective function defined in Equation (4.5). The updating results are represented by Stage 1 in Figure 4.4, which implies that the interval [4, 5] is a possible damage region. In Stage 2, the suspected element is refined by adding wavelets of scale 0 (Figure 4.3). Meanwhile, the damage indices of intervals [4.0, 4.5] and [4.5, 5] are selected as the updating parameters. Thus, the number of parameters to be updated and the corresponding computation effort are significantly reduced. The damage severities estimated in Stage 1 are regarded as initial values, and optimal estimation of the parameters can be obtained by iteration with the same objective function as that in Stage 1. The corresponding updating results are shown in Figure 4.4. Apparently, the interval [4, 4.5] is likely to be a damaged region. Hence, the location of the damage is estimated with a high spatial resolution. By refining the suspected region further, a more accurate estimation of damage location and severity can be achieved. Stages 3 and 4 provide almost the same damage detection results (Figure 4.4), implying that the estimation converges and no further refinement are necessary.

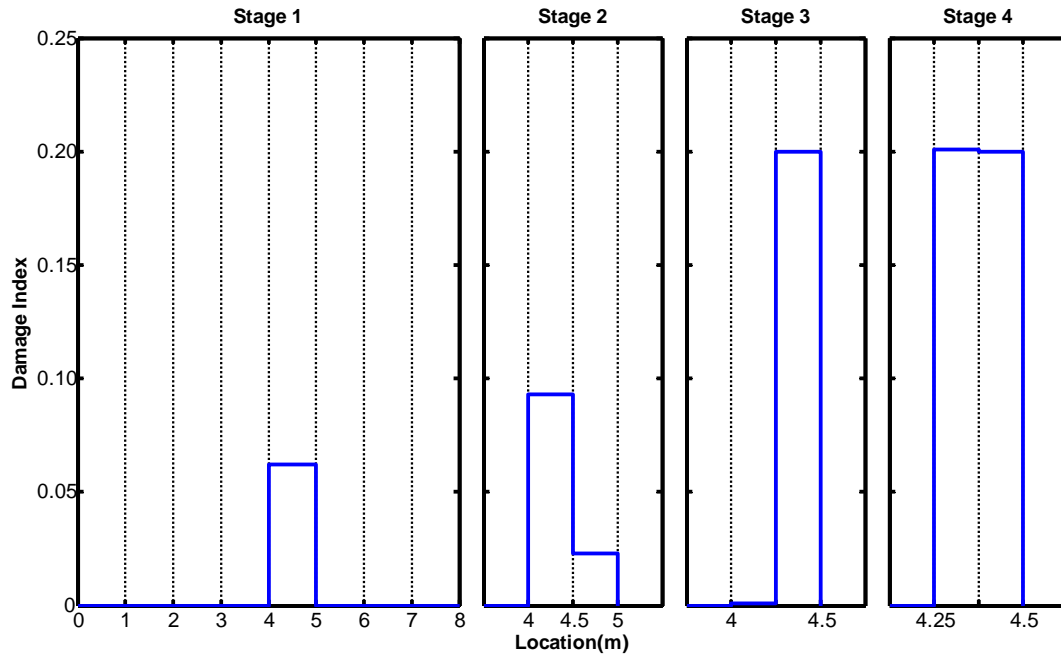


Figure 4.4. Progressive damage identification results in Case B1

For model updating-based damage detection, a large number of DOFs and updating parameters would increase the computation amount and even make the solutions non-unique and ill-conditioned. Given that the WFEM scale can be adaptively adjusted according to actual needs, structural damage can be identified with satisfactory accuracy at the cost of minimized number of DOFs in the model and updating parameters in optimization. In Case B1, the damage region length is $1/32$ of the total length of the beam. Using traditional finite elements, 32 beam elements and 66 DOFs in FEM and 32 updating parameters are generally needed to accurately capture the damage location and severity. With WFEM, only 24 DOFs (Stage 4), 8 updating variables (Stage 1), and 2 updating variables (Stages 2, 3, and 4) are used.

Figure 4.5 shows the model refinement and parameter updating process in Case B2, in which the beam structure is subjected to double damages with different locations and severities (Table 4.1). Different from Case B1, a false alarm of damage locations occurred in the first stage because of the relatively low resolution of the WFEM and low number of updating parameters. As shown in Figure 4.6, in Stage 1 of Case B2, intervals $[0, 1]$, $[2, 3]$, and $[4, 5]$ are identified as probable damage regions, but the first

one is actually a false alarm. However, after refining the model in the three concerned intervals in Stage 2, the updating results suggest that intervals [2, 3] and [4, 5] are probable damage regions and interval [0, 1] is not. Therefore, in Stage 3, the suspected intervals [2, 3] and [4, 5] are further refined by adding wavelets of scale 1. Interval [0, 1] is reverted to the state in Stage 1.

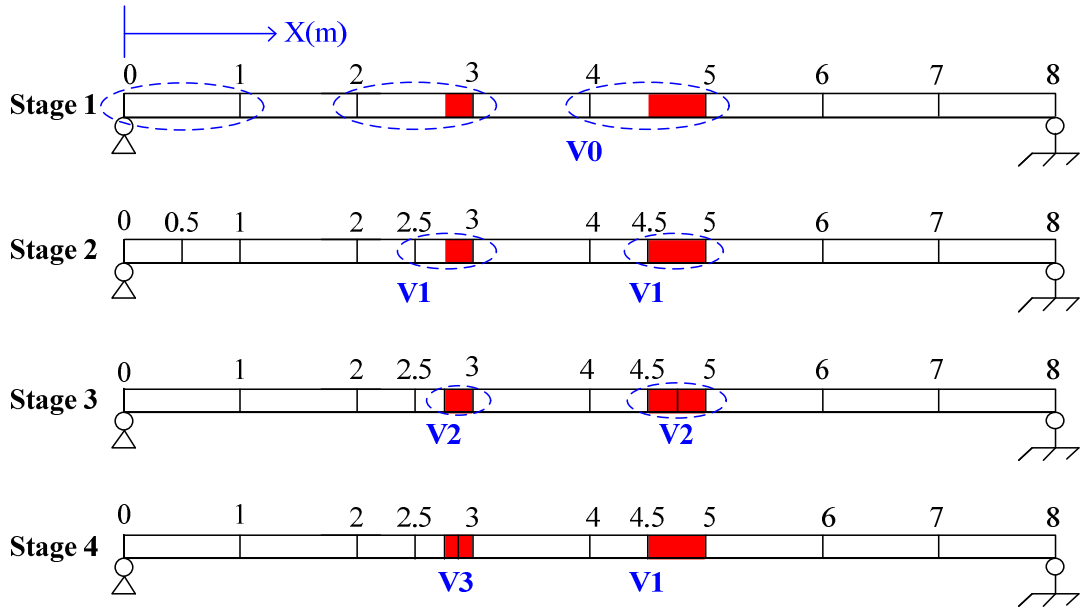


Figure 4.5. Model refinement process in Case B2

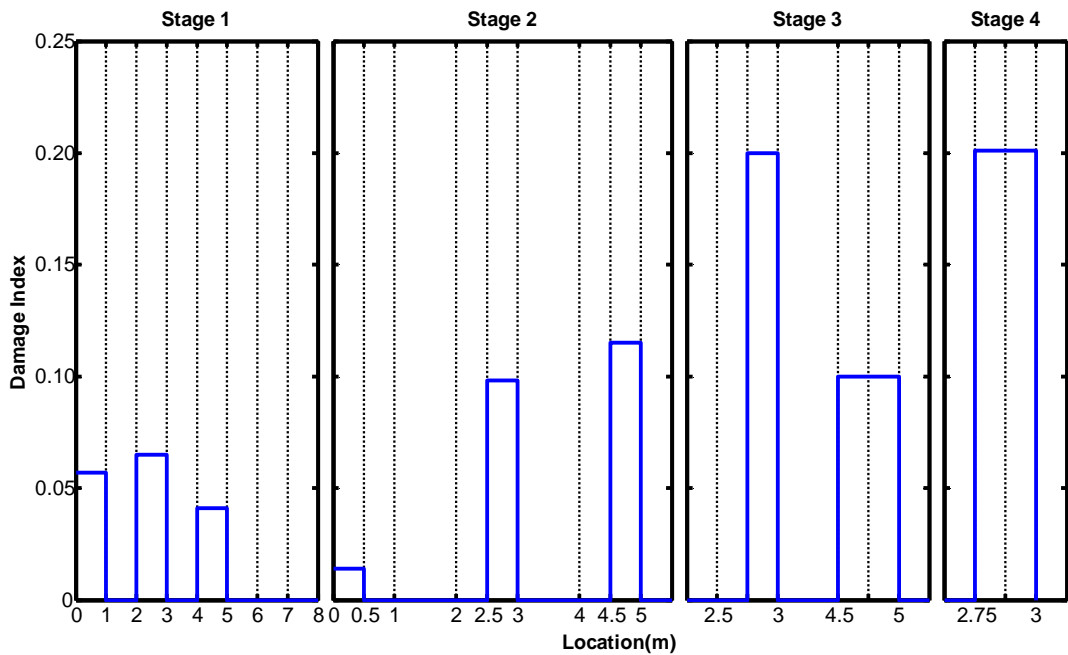


Figure 4.6. Progressive damage identification results in Case B2

The right-hand damage region consists of 1/16 of the entire beam, whereas the left-hand damage region consists of 1/32. The resolutions of the structural model of these two regions are enhanced or reduced according to actual needs during the damage detection process. This adaptability of structural model scales will efficiently minimize the computation cost.

4.3.2 Plate Structure

Figure 4.7 shows a numerical example of a thin plate simply supported on four corners under different damage scenarios (as summarized in Table 4.2). The physical material properties are dimensions of 700 mm × 500 mm × 3 mm, elastic modulus $E = 68.9 \text{ Gpa}$, Poisson's ratio $\mu = 0.27$, and density $\rho = 2700 \text{ Kg/m}^3$. Only vertical DOFs in the mode shapes at the 44 sensor locations (Figure 4.7) are used during the entire damage detection process.

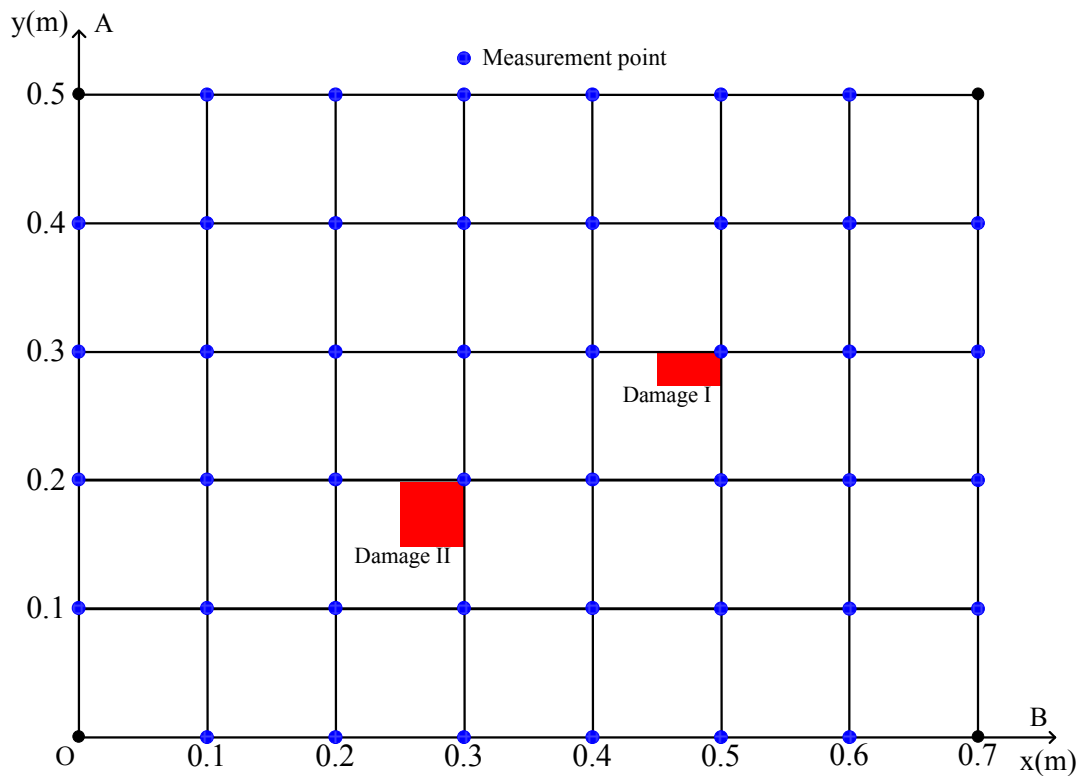


Figure 4.7. Thin plate in the numerical study

Table 4.2. Damage scenarios considered in the numerical simulations of the plate

Damage Scenarios	Damage		
	Region (m)	Severity (%)	
Case P1	Damage I	[0.45, 0.5]×[0.275, 0.3]	30
Case P2	Damage I	[0.45, 0.5]×[0.275, 0.3]	30
	Damage II	[0.25, 0.3]×[0.15, 0.2]	20

Case P1 involves a single damage in the region $[0.45, 0.5] \times [0.275, 0.3]$ with 30% severity. Figures 4.8 and 4.9 show the identification process and the corresponding results, respectively. The entire damage detection process of Case P1 consists four stages. In Stage 1, the plate is divided into 35 (7×5) wavelet plate elements at scale 0, that is, the displacement is approximated in wavelet space F0. The corresponding number of DOFs at this stage is 176. The damage indices of the 35 elements are obtained by minimizing the objective function as defined in Equation (4.5); the results are plotted in Figure 4.9a. The region $[0.4, 0.5] \times [0.2, 0.3]$ (denoted as ABCD) is a potential damage region, although the damage severity is not estimated accurately because of the low-scale model. In Stage 2, wavelets of scale 0 are added to the potential damage region (ABCD) of WFEM to expand the approximation space from F0 to F1. Four damage indices associated with the four equal sub-regions divided from region ABCD (Figure 4.8) are regarded as updating parameters. The significantly reduced number of updating parameters greatly minimizes the corresponding computation amount. With the estimated damage severities in Stage 1 as initial values, the optimization process is implemented again to acquire more precise results. The results shown in Figure 4.9b indicate that the region $[0.45, 0.5] \times [0.25, 0.3]$ is more likely to be a damaged region than the other three, which means the damage is localized in a small region. Similar refinements are applied in the progressively identified potential damage regions, and optimization processes are implemented accordingly. Hence, gradually accurate estimations of the damage location and severity are obtained (Figures 4.9c and 4.9d). Stages 3 and 4 present almost the same damage identification

results that are close to the real value. For example, the damage region of $[0.45, 0.5] \times [0.4275, 0.3]$ is identified in both Stages 3 and 4, with the average damage severity equal to 29.6% and 30.1%, respectively.

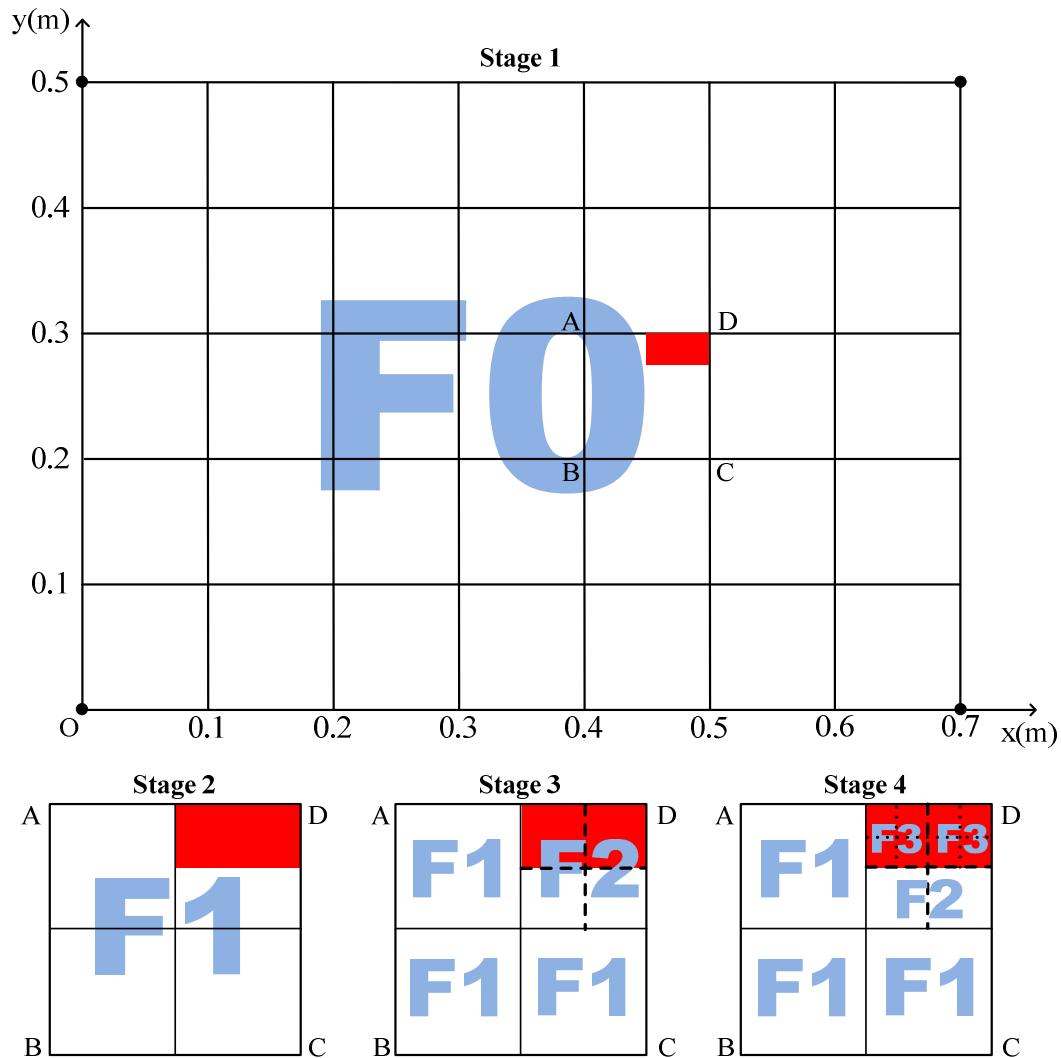
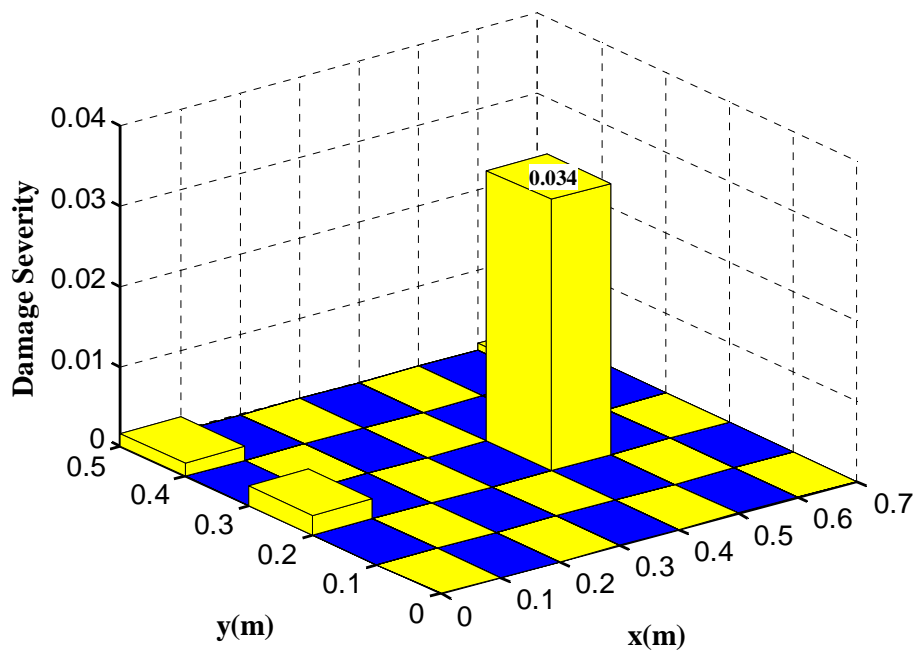
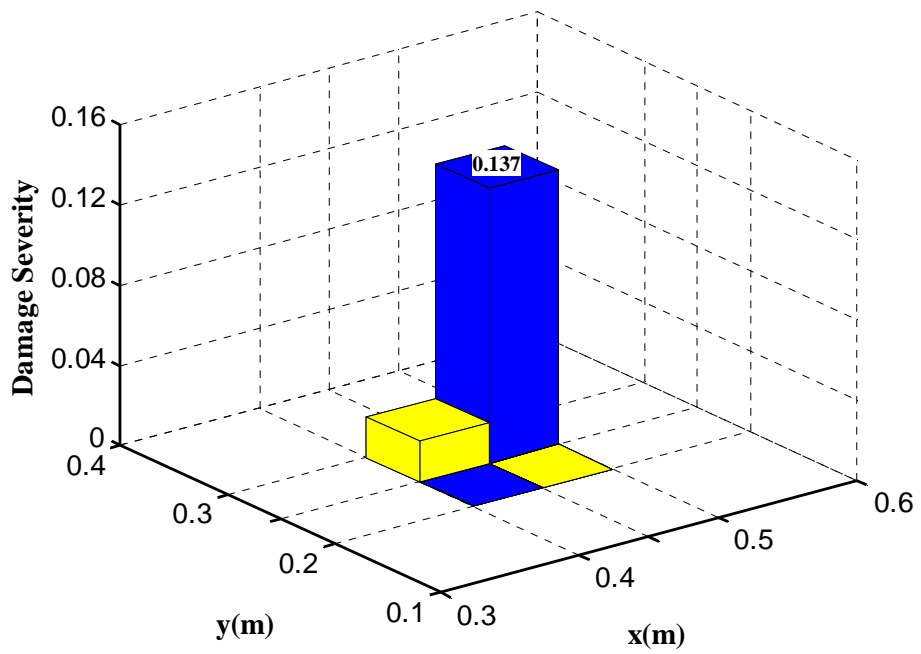


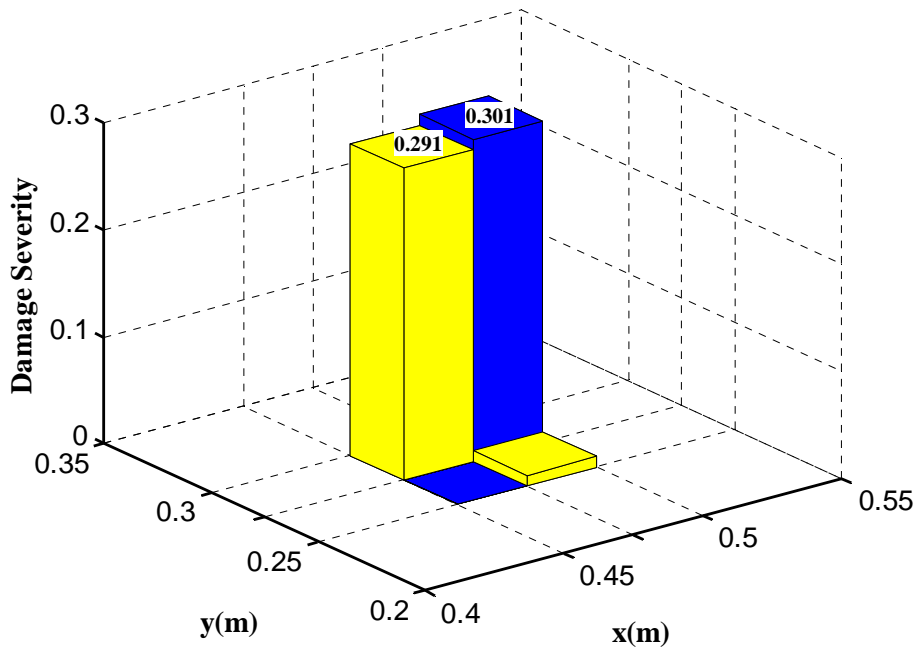
Figure 4.8. Model refinement process in Case P1



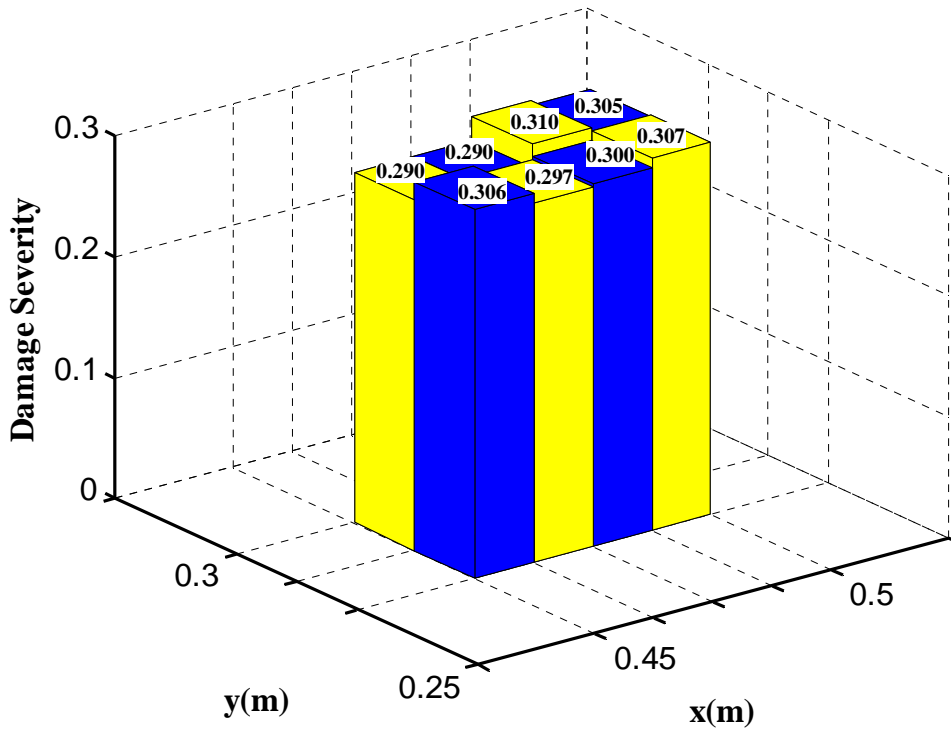
(a) Stage 1



(b) Stage 2



(c) Stage 3



(d) Stage 4

Figure 4.9. Progressive damage identification results in Case P1

The numbers of DOFs in Stages 1 to 4 are 176, 180, 184, and 192, respectively; the corresponding numbers of updating parameters are 35, 4, 4, and 8, respectively. However, if TFEM is adopted, uniformly meshed 28×20 (at least 14×20) plate elements are required to accurately identify the damage because it consists of $1/280$ ($1/14 \times 1/20$) of the entire plate and cannot be known in advance. The numbers of DOFs and updating parameters are 2,420 (at least 1,244) and 560 (at least 280), respectively. Thus, the optimization process would be impractical and time consuming, if not impossible. With the proposed approach, damage detection becomes very efficient because only WFEM is refined in probable damage regions and no sensors are replaced or no new sensors are needed.

Figure 4.10 shows the model refinement and updating process in Case P2, in which the plate is subjected to double damages, that is, Damage I in $[0.45, 0.5] \times [0.275, 0.3]$ with 30% severity and Damage II in $[0.35, 0.4] \times [0.55, 0.6]$ with 20% severity, as listed in Table 4.2. Given that the extent of the two damages is not the same, this case will highlight the flexibility characteristic of WFEM in damage detection more clearly. The WFEM refinement process and damage detection results are presented in Figures 4.10 and 4.11, respectively. Detection accuracy is effectively improved with the progressive refinement of WFEM.

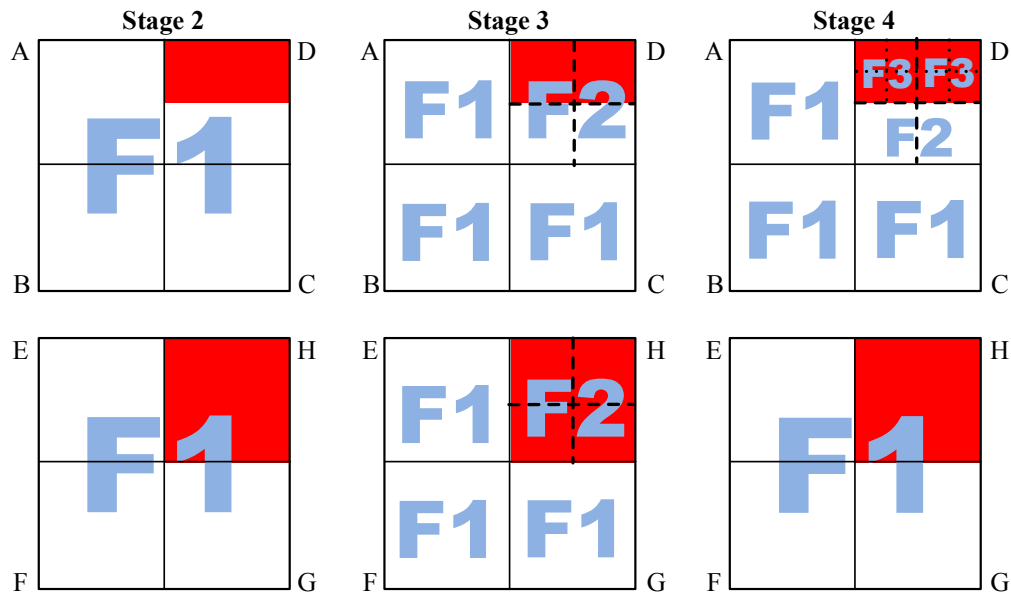
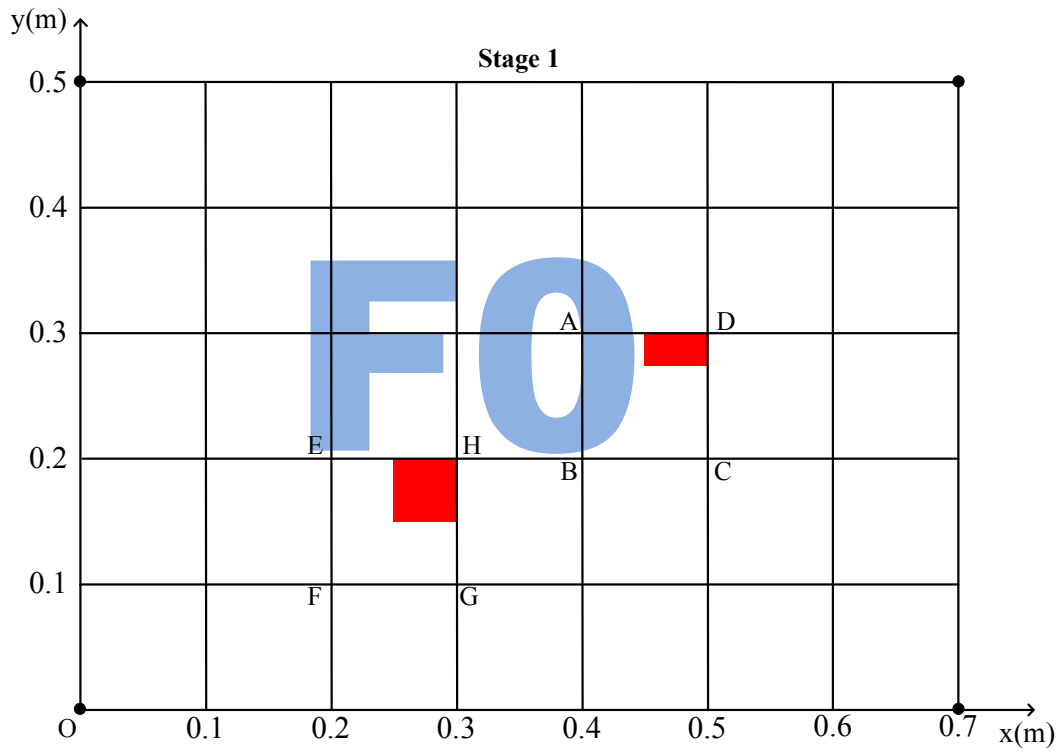
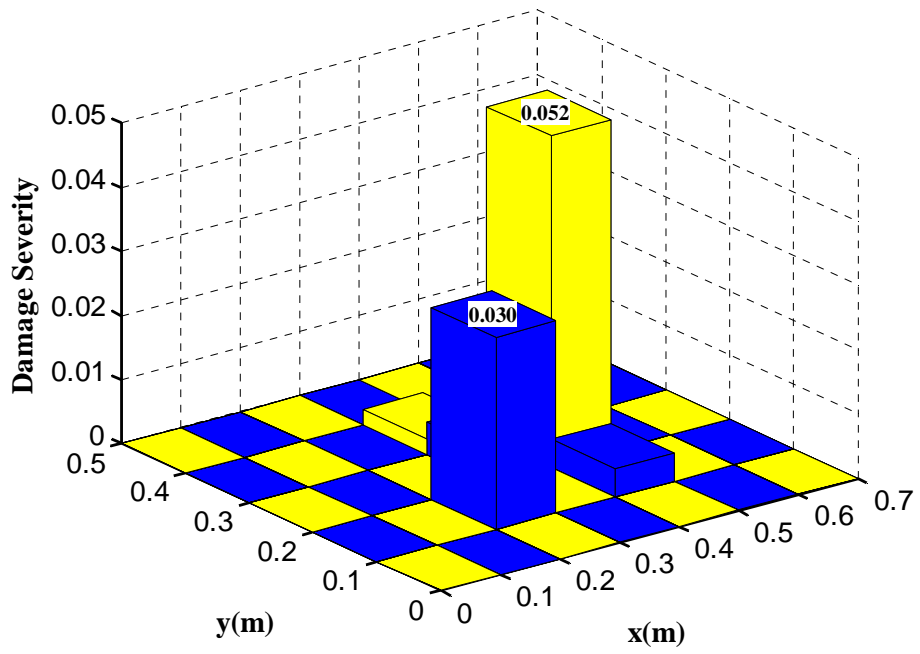
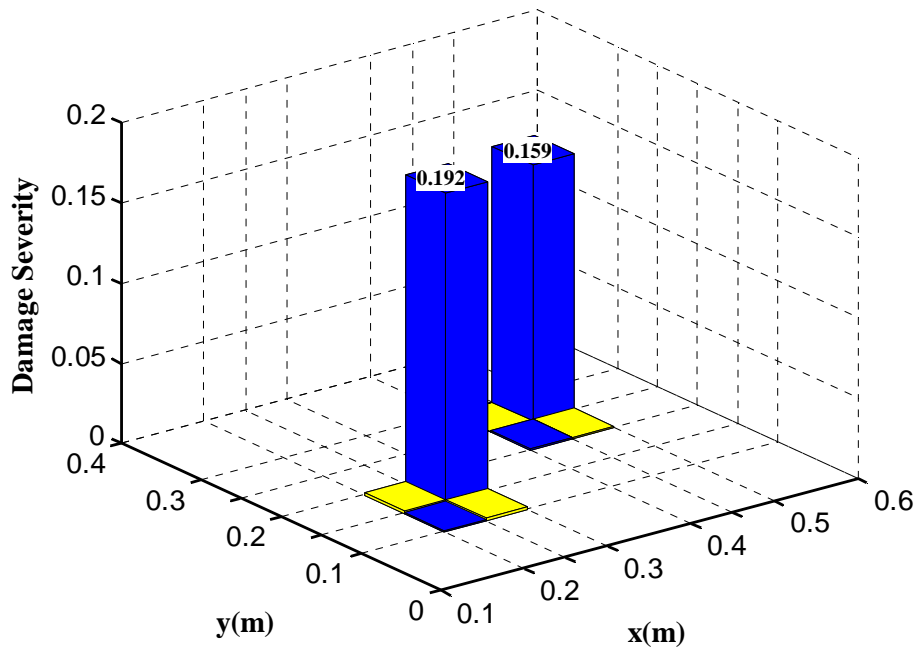


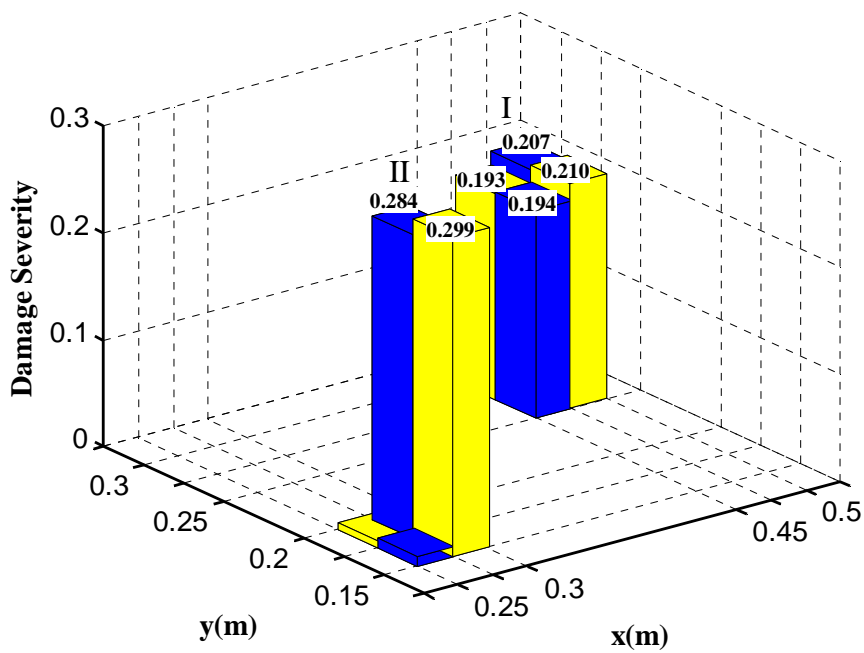
Figure 4.10. Model refinement process in Case P2



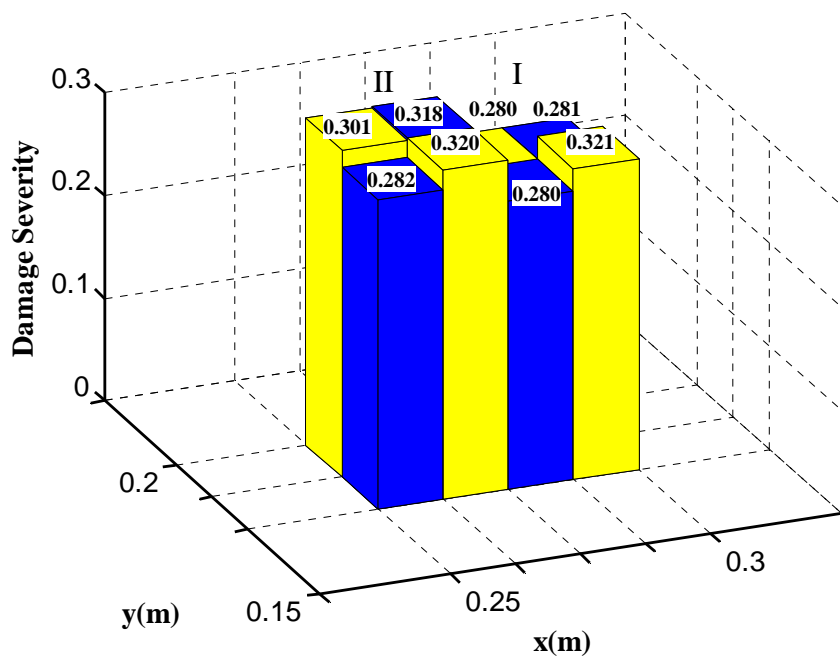
(a) Stage 1



(b) Stage 2



(c) Stage 3 II



(d) Stage 4

Figure 4.11. Progressive damage identification results in Case P2

4.4 Experimental Verification

Two experimental studies, namely, a single-bay single-story steel portal frame and an aluminum plate fixed-supported on two adjacent sides, are conducted to examine the effectiveness of the proposed progressive damage detection method in actual testing environment.

4.4.1 Frame Structure

4.4.1.1 Experimental Description

Figure 4.12 shows the single-bay single-story steel portal frame investigated in this section. The experiment was initially reported by Hao and Xia (2002). The Young's modulus and density of the steel material are 2.0×10^{11} N/m² and 7.67×10^3 Kg/m³, respectively. The cross sections are 40.5×6.0 mm² and 50.5×6.0 mm² for the beam and columns, respectively. The vibrations of the undamaged and damaged frames are measured with accelerometers in a series of hammer impact tests, and their modal properties are obtained through frequency response function analyses. Four saw cuts are created to represent multiple damages in the frame, with their locations shown in Figure 4.12. Sequential cases representing different damage severities are tested in the laboratory. The case corresponding to saw cut depth $d = 40\%$ of the section width [Case F4 in Hao and Xia (2002)] is employed in this section to validate the progressive damage detection strategy. Table 4.3 presents the first 12 in-plane vibration frequencies of the frame in undamaged and damaged states. Figure 4.13 shows the first 12 in-plane mode shapes of the steel frame for the undamaged state. Although the mode shapes are measured at 29 equally spaced points in the tests, only the DOFs at 14 points (i.e., $x = 0.2, 0.4, \dots, 0.28$ m) are considered in each mode shape in the WFEM-based progressive damage detection method presented in this chapter.

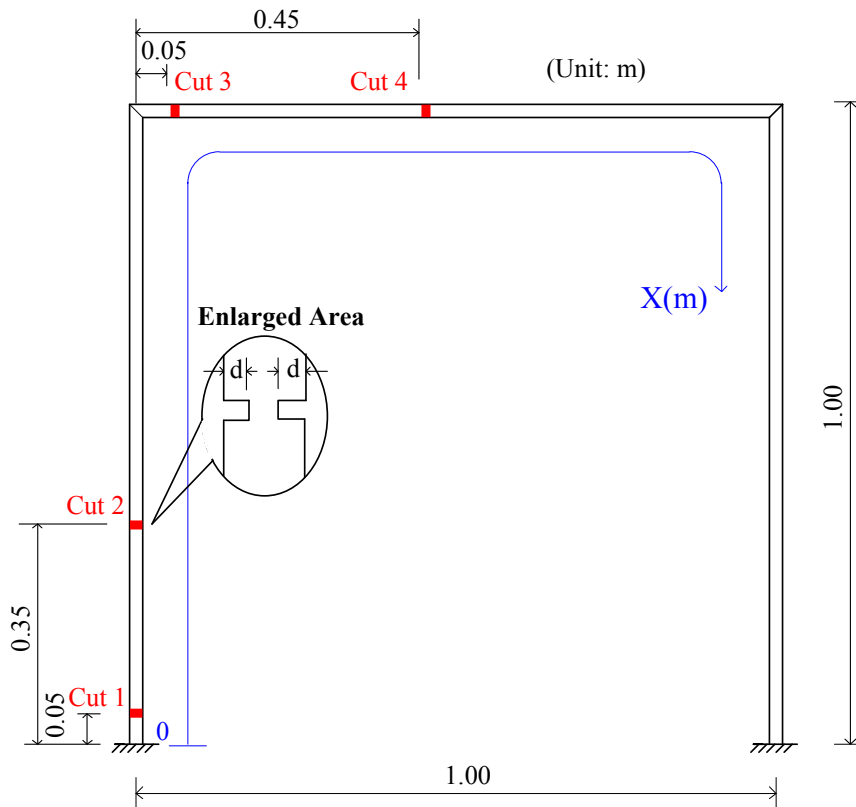


Figure 4.12. Configuration of the frame specimen (Hao and Xia 2002)

Table 4.3. Modal frequencies of the tested frames (Hz) (Hao and Xia 2002)

Mode	Undamaged	Damaged	Mode	Undamaged	Damaged
1	4.49	4.31	7	87.79	85.91
2	17.41	16.90	8	132.99	129.95
3	27.99	26.68	9	155.42	152.57
4	30.89	29.76	10	165.67	162.92
5	61.84	60.80	11	228.70	225.30
6	74.41	71.14	12	255.30	248.51

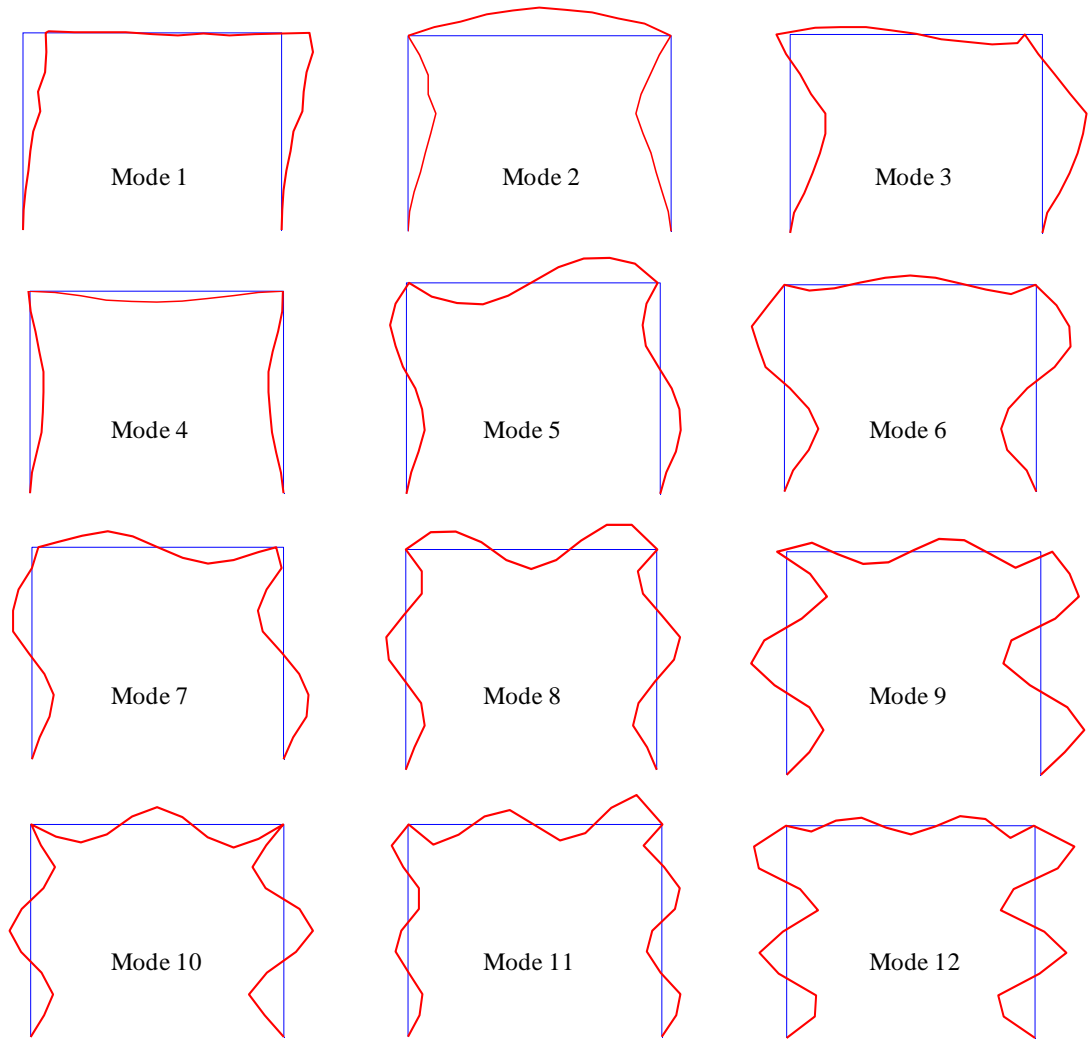
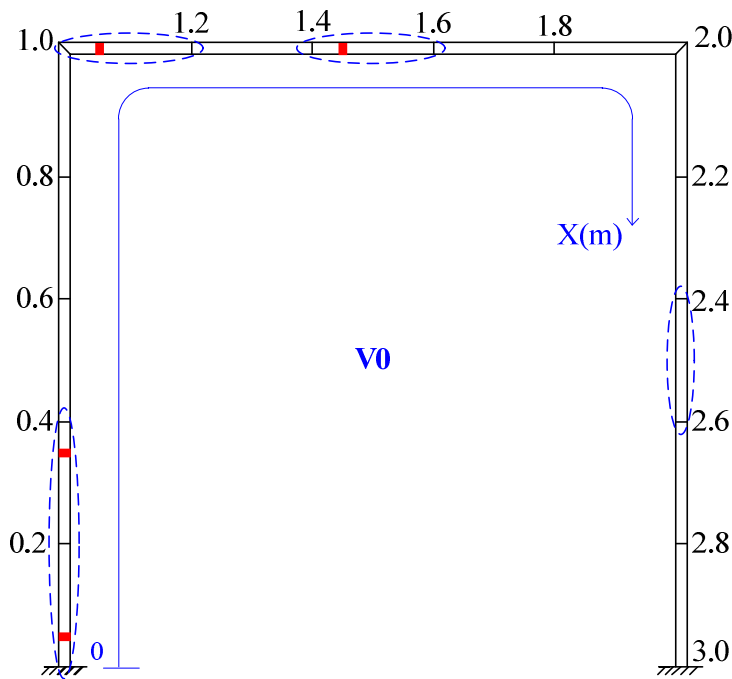


Figure 4.13. Experimental mode shapes of the undamaged frame

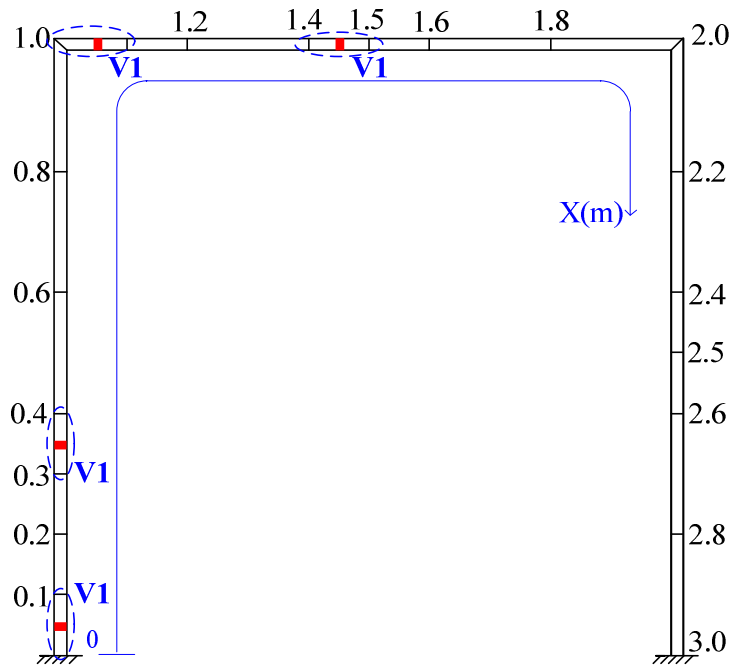
4.4.1.2 Damage Detection Process and Results

Figure 4.14 illustrates the damage detection process. The frame was initially modelled by 15 equal-length plane beam-type wavelet finite elements described in Chapter 2. The numbers in the figure stands for the nodal coordinates x measured from the left column base toward the right column base (Figure 4.12). In Stage 1, the damage indices of the 15 elements were optimized with the objective function defined in Equation (4.2). Owing to the relatively low resolution of the WFEM and signal noise, misjudgment of damage locations occurs in the first stage. As shown in Figure 4.14a, five intervals, namely, $[0, 0.2]$, $[0.2, 0.4]$, $[1.0, 1.2]$, $[1.4, 1.6]$, and $[2.4, 2.6]$, are possible damage regions, where the last one is actually a false alarm. In Stage 2, the suspected regions

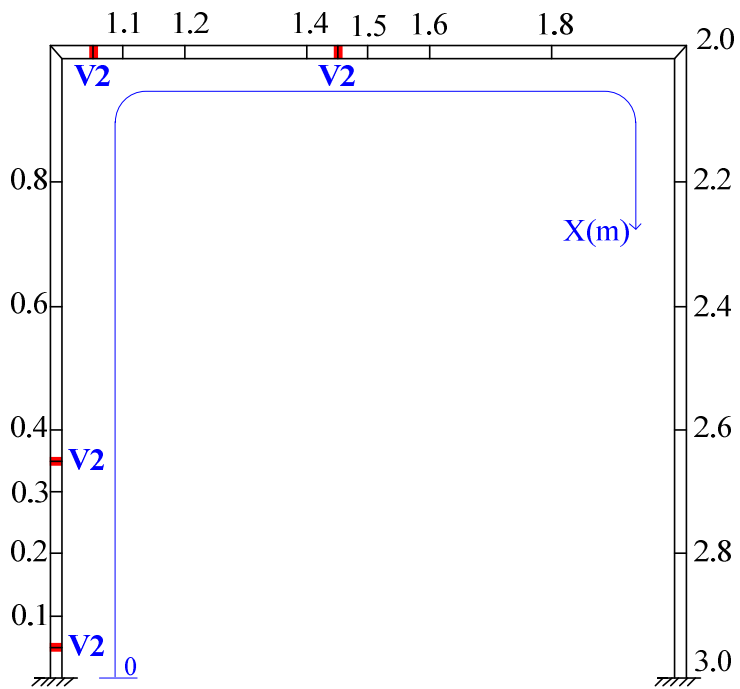
are further refined by adding wavelets of scale 0 (Figure 4.14b). Meanwhile, the damage indices corresponding to intervals $[0, 0.1]$, $[0.1, 0.2]$, $[0.2, 0.3]$, $[0.3, 0.4]$, $[1.0, 1.1]$, $[1.1, 1.2]$, $[1.4, 1.5]$, $[1.5, 1.6]$, $[2.4, 2.5]$, and $[2.5, 2.6]$ are selected as updating parameters. Optimization of the updating parameters can be obtained via iteration, with the initial values equal to the damage severities estimated in Stage 1. The optimization results suggest that only the first four intervals are probable damage regions. The false alarm in interval $[2.4, 2.6]$ is successfully removed, so the probable damage regions are reduced to smaller intervals where the saw cuts are located. As indicated in Figure 4.15, by further refinement of the suspected region, the results of Stage 3 indicate that damages cannot be reduced to smaller intervals anymore, which matches the fact that the damages are located in the middle of selected intervals of Stage 2.



(a) Stage 1



(b) Stage 2



(c) Stage 3

Figure 4.14. Model refinement process

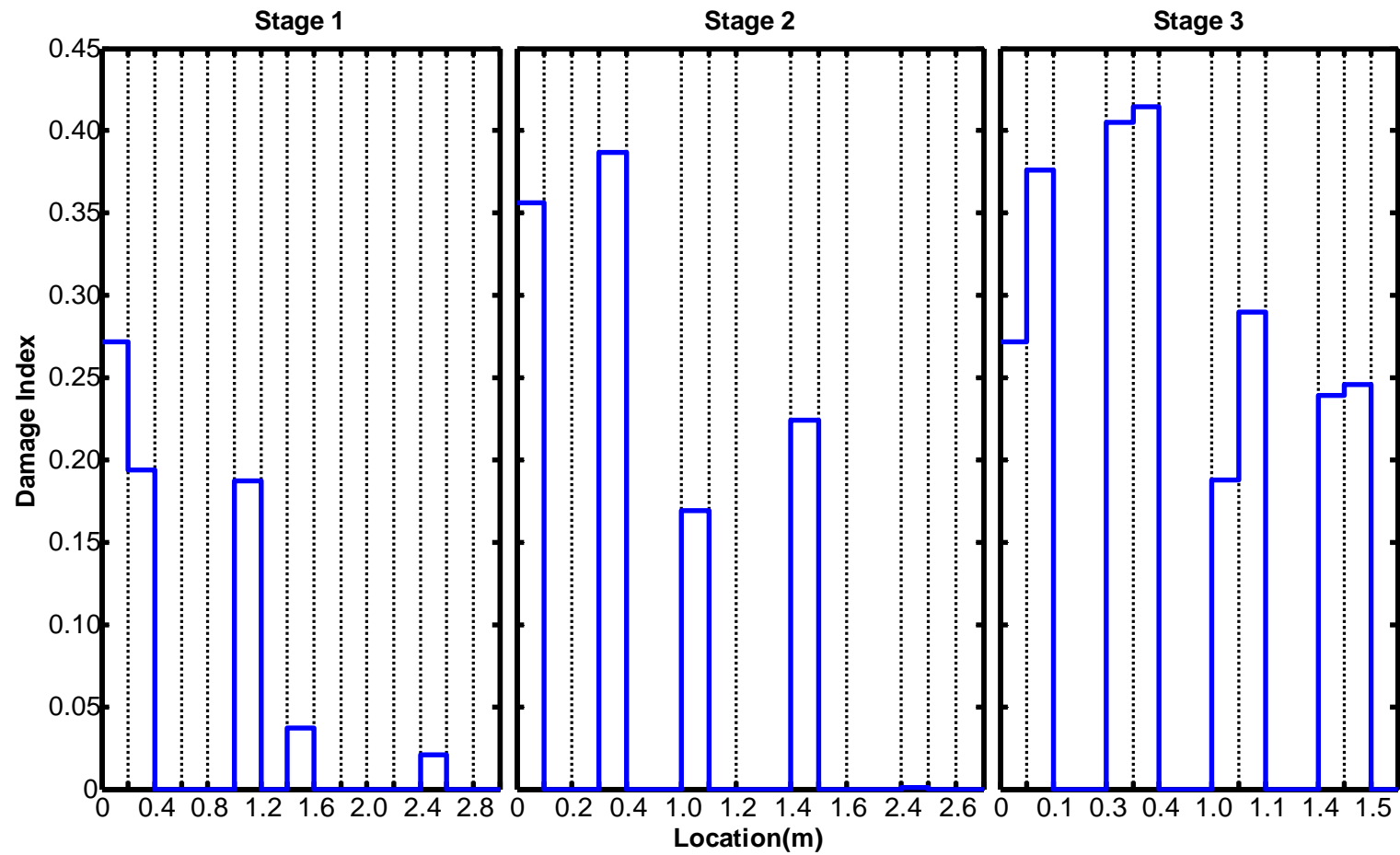


Figure 4.15. Progressive damage identification results

In the WFEM-based damage detection of the steel portal frame, only 44 DOFs are involved in Stage 3, and 14 accelerometers are used during the entire damage detection process. Experimental results were also used in the damage detection based on TFEM and genetic algorithm in the study of Hao and Xia (2002). To accurately capture the damage locations in their study, measurements at 29 DOFs were used, and the FEM included 30 equal-length beam elements and 87 DOFs. The damage localization results obtained in this section are more accurate than those of Hao and Xia (2002).

In sum, the proposed WFEM-based progressive damage detection strategy with comparatively small numbers of DOFs, sensors, and updating parameters can considerably enhance the efficiency of damage detection.

4.4.2 Plate Structure

4.4.2.1 Experimental Description

Figure 4.16 shows an aluminum plate with the dimensions of $405 \times 455 \times 3 \text{ mm}^3$. Two adjacent sides (right and lower edges) of the plate are fixed and supported on a testing table (NEWPORTs ST-UT2) through two panels. The material properties of the plate are elastic modulus $E = 68.9 \text{ Gpa}$, density $\rho = 2700 \text{ Kg/m}^3$, and Poisson's ratio $\mu = 0.27$. Figure 4.17 shows the damaged zone with the dimension of $32.7 \text{ mm} \times 18.4 \text{ mm}$. Thickness reduction of 2 mm is introduced by milling the plate. Given that the original thickness of the plate is 3 mm, damage severity can be regarded as approximately 66.7%. An electro-mechanical exciter (B&Ks 4809, Figure 4.18) is utilized to apply point-force excitation, and a scanning Doppler laser vibrometer system (Polytecs^R PSV-400) is employed to capture the out-of-plane displacements at each measurement point on the front surface of the plate.

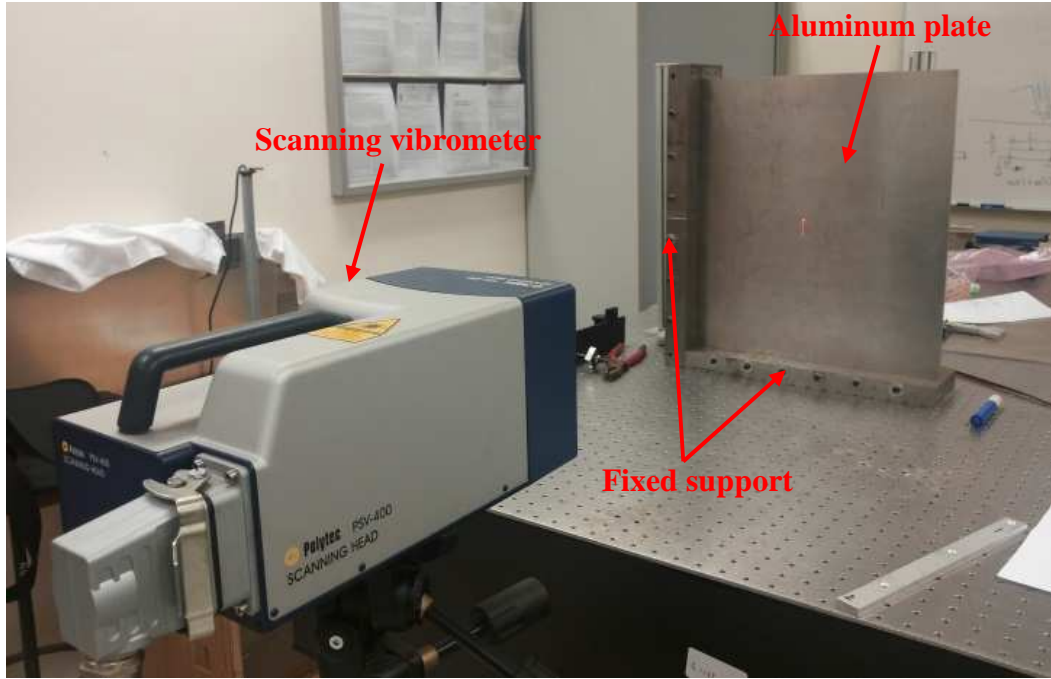


Figure 4.16. Setup of the plate experiment



Figure 4.17. Damage zone on the plate

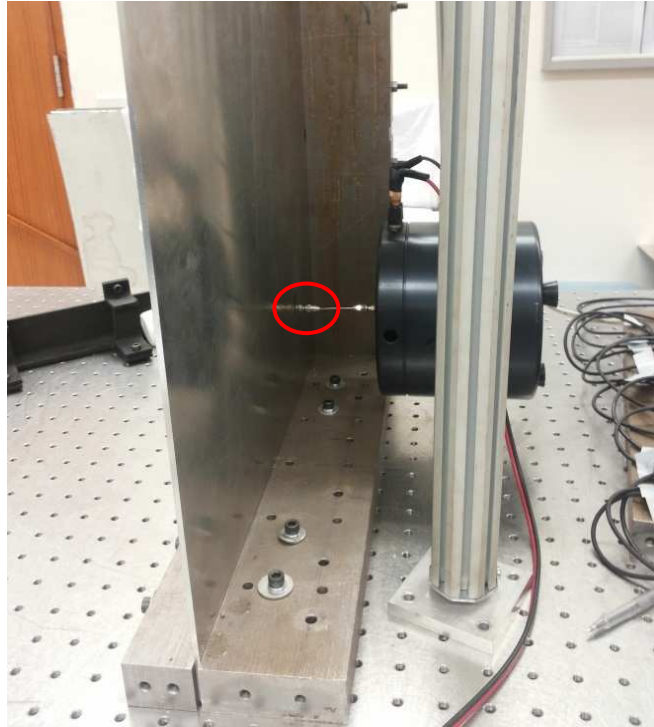


Figure 4.18. Vibration exciter

Based on the frequencies (Table 4.4) calculated from FEM of the plate in undamaged state, the excitation frequency bands in the test are determined and listed in Table 4.4. Using narrow-band random excitation helps obtain high accuracy results. Single-input-single-output (excited at single point and measured at single point) is adopted in the vibration tests, and the test is repeated three times for each mode. Then, the average of the identified frequency values are regarded as the experimental frequencies of the plate in both undamaged and damaged states. The results are listed in Table 4.4.

Table 4.4. Frequency of the plate in the experimental study (Hz)

Mode	FEM Value	Experimental Value		
	Undamaged	Excitation frequency	Undamaged	Damaged
3	109.885	[105, 115]	111.514	111.106
4	189.639	[185, 195]	189.870	189.544
5	227.818	[225, 235]	233.161	232.263
6	281.531	[275, 285]	282.359	281.232

In the following mode shape test, single-input-multi-output (excited at single point and measured at multi points) is adopted instead of single-input-single-output. Harmonic frequency excitation with a fixed frequency (e.g., 111.514 Hz for the third mode shape in the undamaged state) is used to excite the plate, and then the out-of-plane vibration displacements at the 49×49 discrete points are measured with the scanning Doppler laser vibrometer system (Figure 4.19). The displacement mode shape corresponding to this frequency is subsequently obtained. The mode shapes of the damaged plate are plotted in Figure 4.20. The first and second nature frequencies and mode shapes are not obtained because the electro-mechanical exciter is suspended and unable to reliably excite low-frequency vibration modes.



Figure 4.19. Vibration test on the plate with 49×49 measurement points

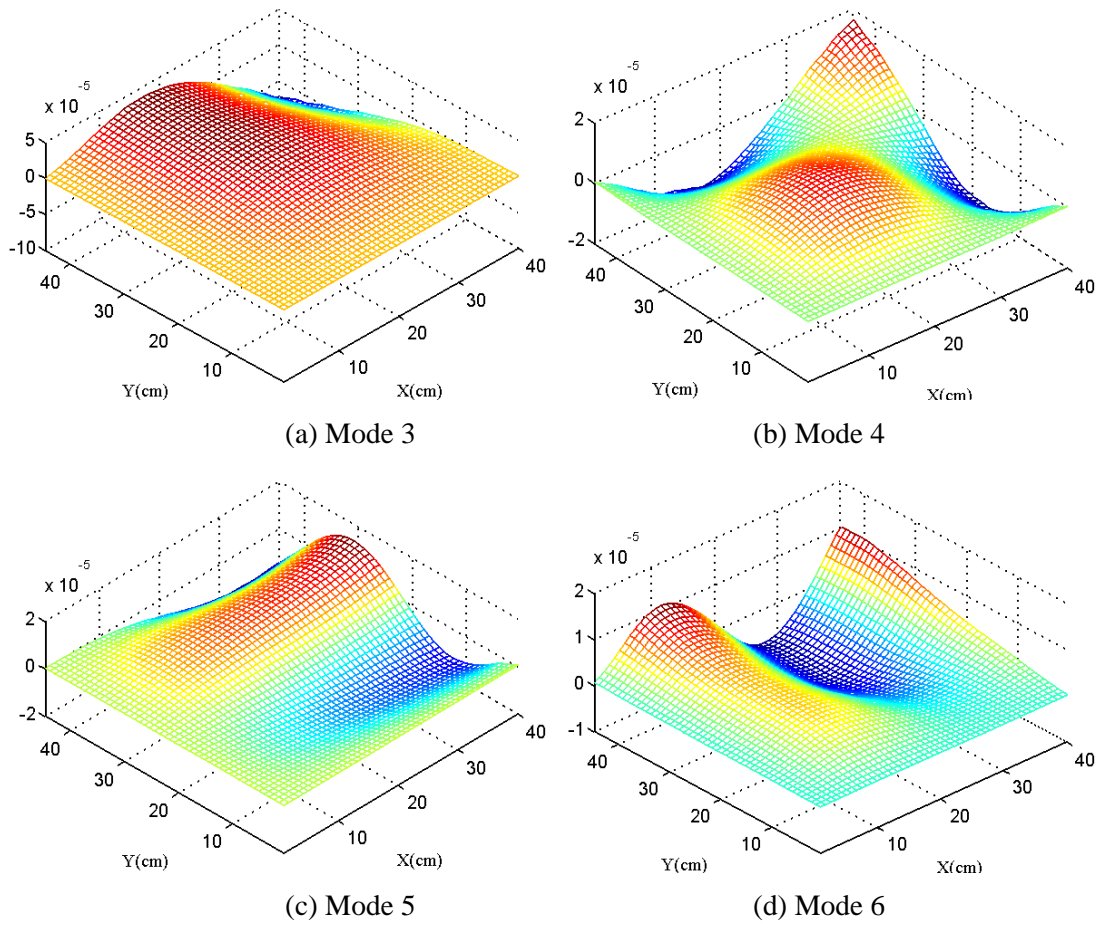


Figure 4.20. Experimental mode shapes of the damaged plate

4.4.2.2 Damage Detection Process and Results

The frequencies and MACs corresponding to the 3rd to 6th modes are used in the damage detection process. Although 49×49 spaced points are acquired in the experiment, only data at 5×5 points are used in damage detection considering the fact that too dense measurements in vibration tests require many sensors and increase the demand for signal acquisition, transmission, and processing, which may not be practical in the vibration tests of civil structures. In WFEM, the plate is initially divided into 6×6 wavelet plate elements, as shown in Figure 4.21. The original dimensions of the elements are not uniform to make the nodes of the elements consistent with the 25 measurement points. For simplicity, the dimensions of the plate are normalized to $[0, 6] \times [0, 6]$ so that all the 36 elements are square with unit dimensions, as shown in Figure 4.21.

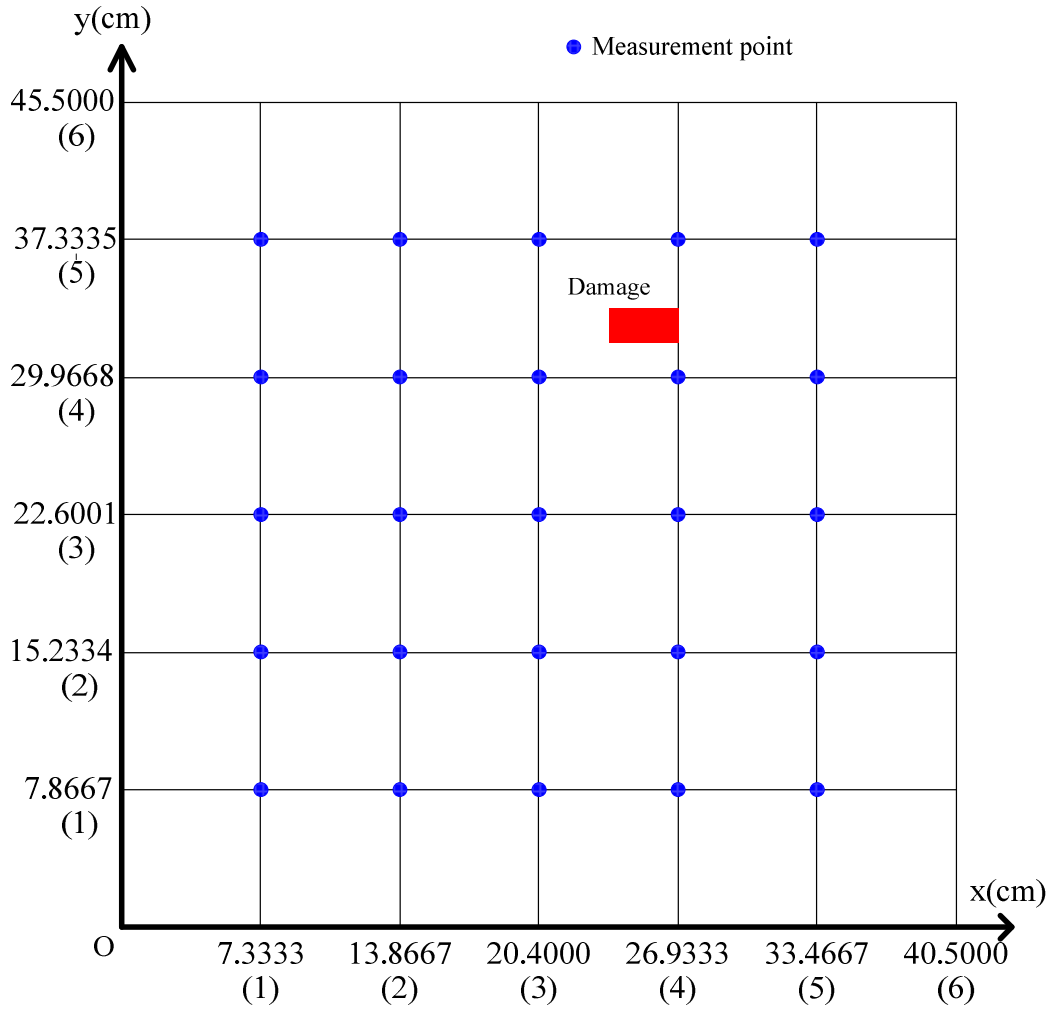
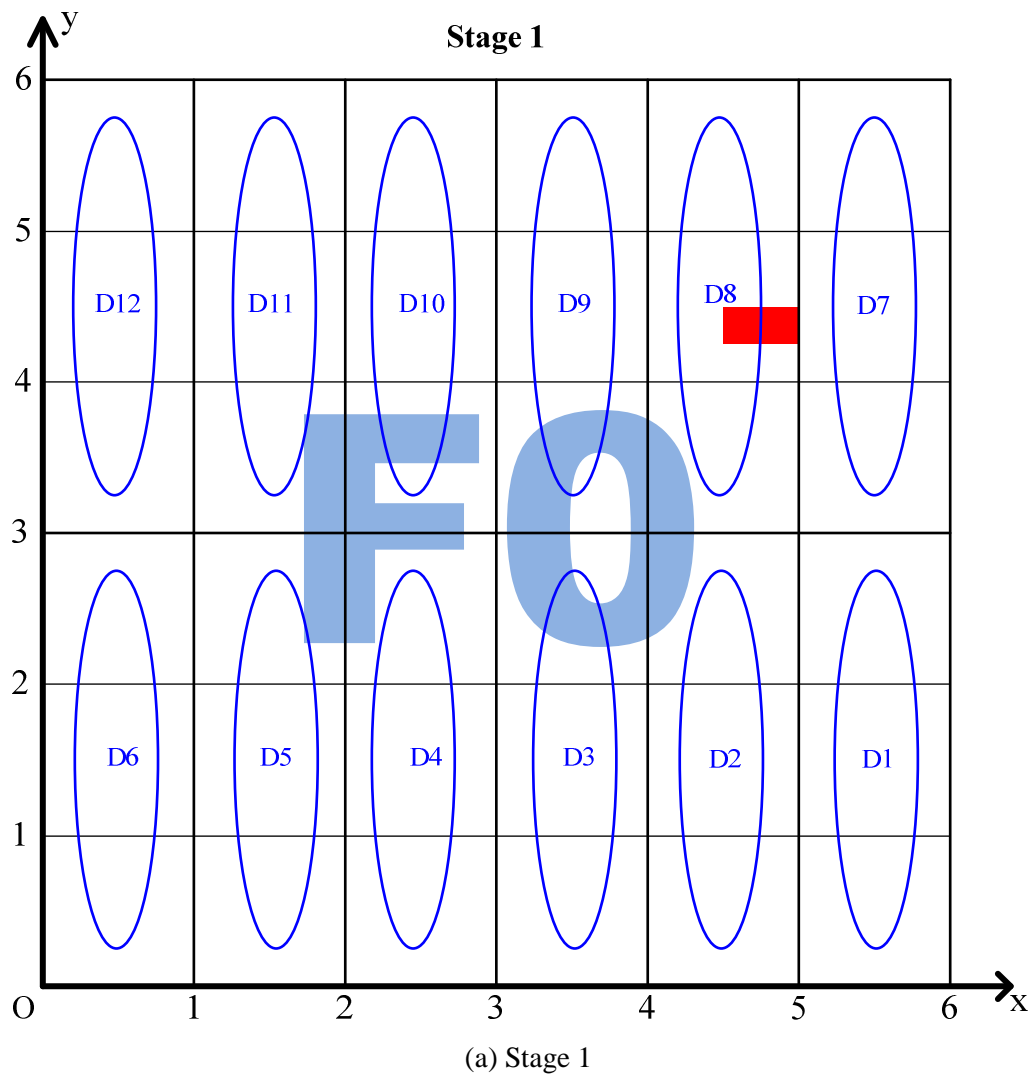
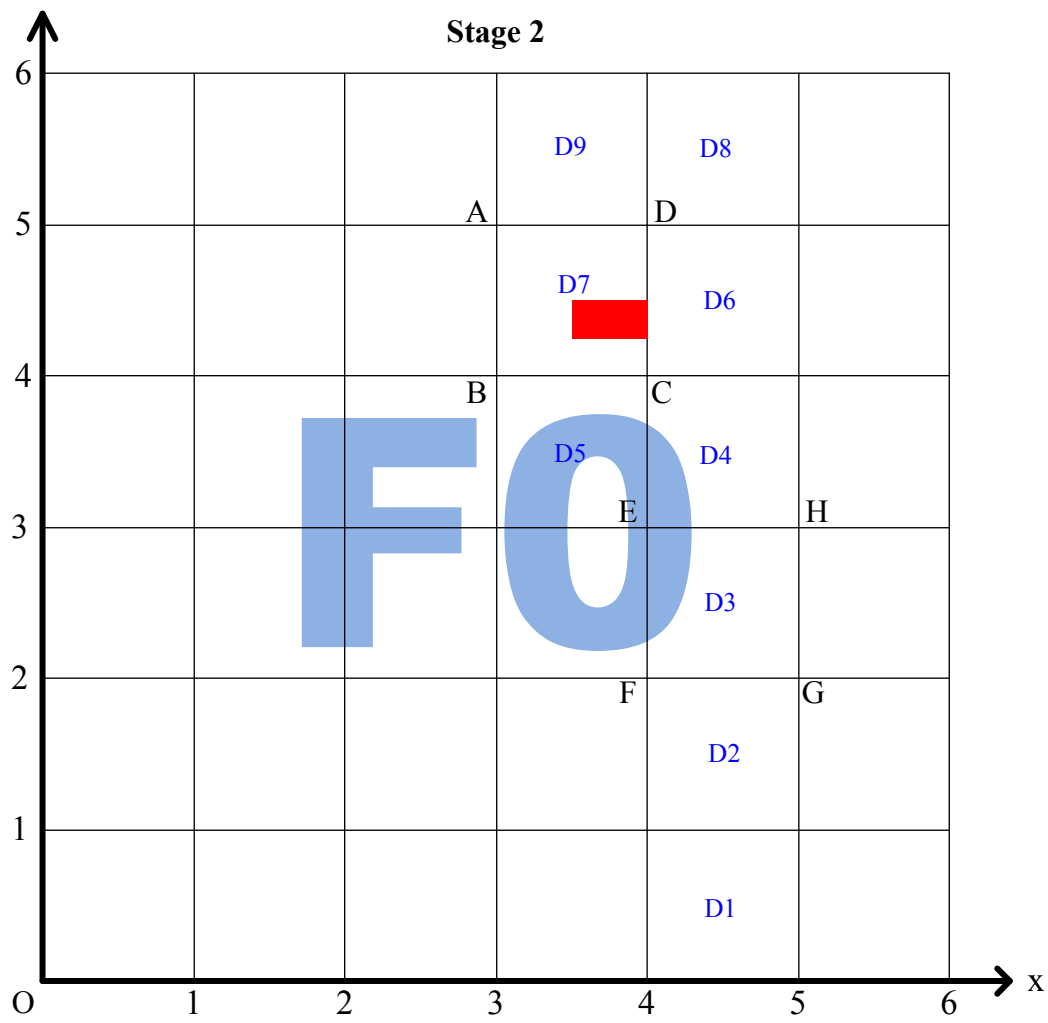


Figure 4.21. Thin plate in the experimental study

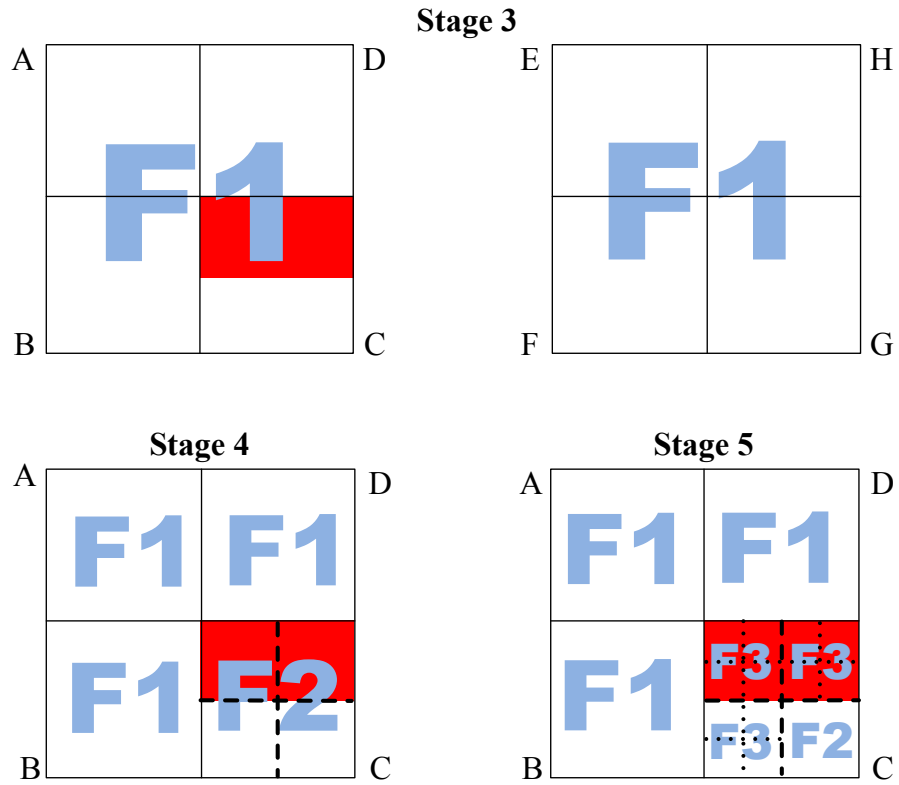
Too many updating parameters often cause difficulty in damage detection, particularly with the presence of test noise or other environmental factors. To further reduce the number of updating parameters in the initial stage, only 12 flexural rigidities (i.e., D1, D2 D12) as shown in Figure 4.22a are selected for update in Stage 1. In other words, every three elements are assumed to have a uniform parameter. The updating results are shown in Figure 4.23a. The elements related to D2, D8, and D9 are identified as possible damage regions. In Stage 2, the flexural rigidities of nine elements (Figure 4.22b) are selected as updating parameters, and the optimization process is performed again. The results show that the regions $[3, 4] \times [4, 5]$ (denoted as ABCD) and $[4, 5] \times [2, 3]$ (denoted as EFGH) are possible damage regions. Further refinements in these two regions are made in the following procedures. Figures 4.22c and 4.23 show the

damage detection process and the corresponding results, respectively. Although misjudgment occurs in the beginning stage of the damage detection process, accuracy is improved gradually with the refinement of WFEM. In Stage 4, the damages are located in three regions, namely, $[3.5, 3.75] \times [4, 4.25]$, $[3.5, 3.75] \times [4.25, 4.5]$, and $[3.75, 4] \times [4.25, 4.5]$, but the third region is a misjudgment. The damage severities are fairly satisfactory albeit different from the real value (0.66) although the third region is a misjudgment. However, further refinement in Stage 5 worsens the damage detection results in terms of damage severity. A possible reason is that high-scale WFEM is more sensitive to the error or uncertainty in the testing results, as mentioned in Section 3.3.3.



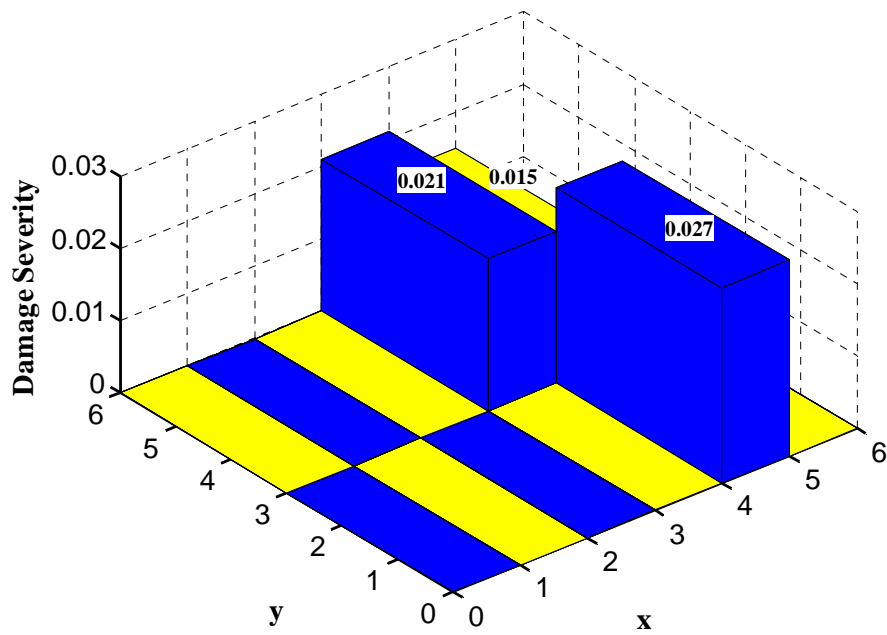


(b) Stage 2

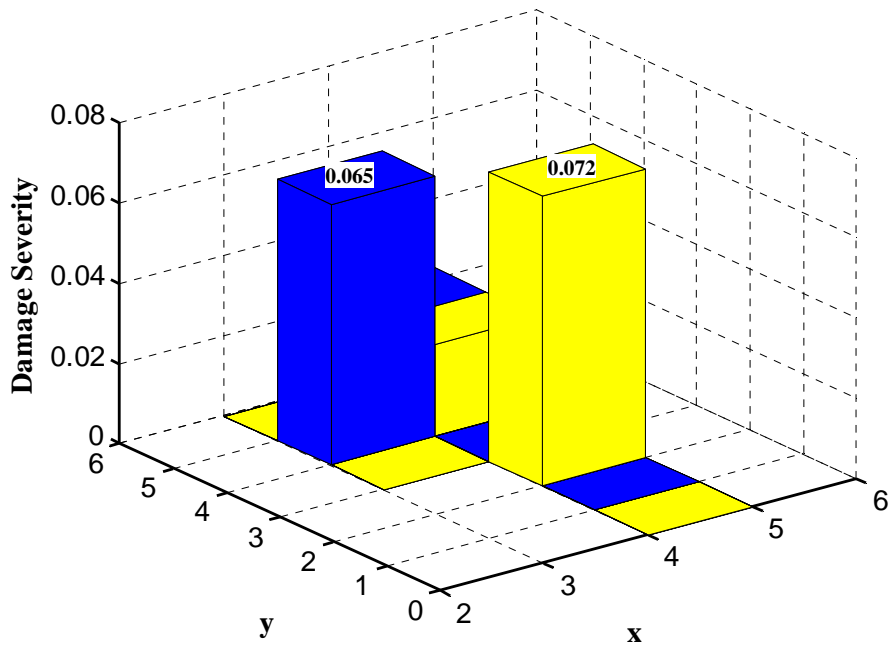


(c) Stages 3–5

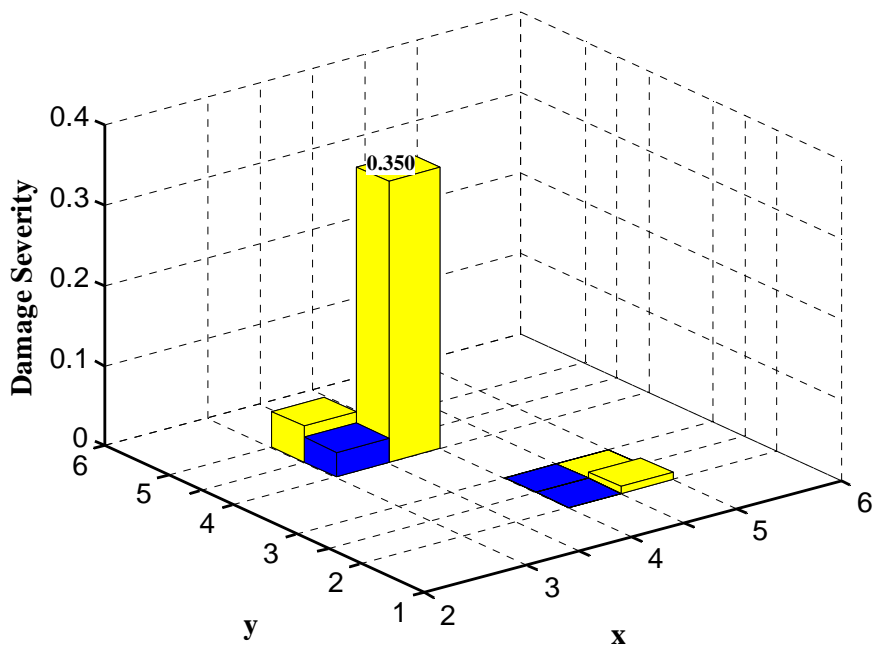
Figure 4.22. Model refinement process of the experiment



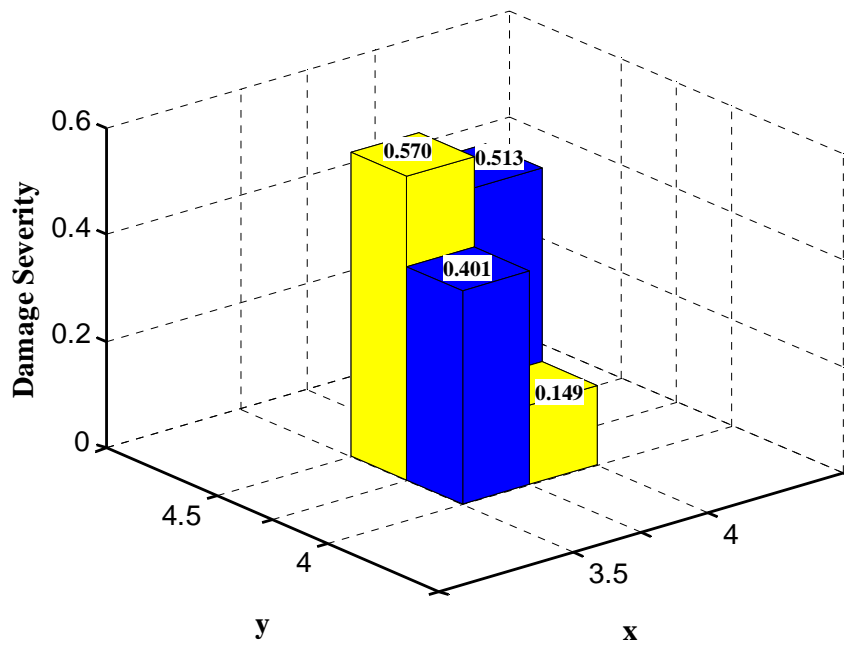
(a) Stage 1



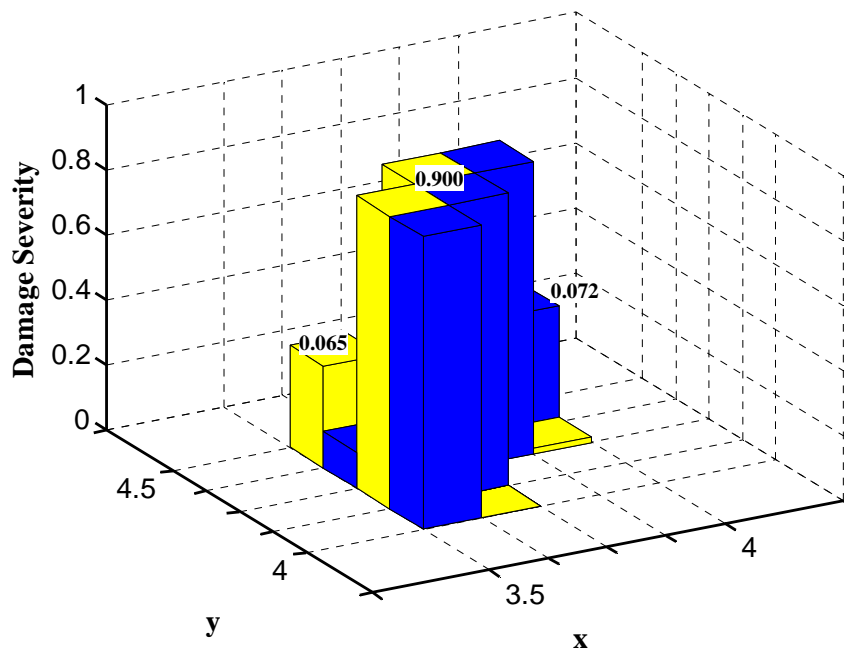
(b) Stage 2



(c) Stage 3



(d) Stage 4



(e) Stage 5

Figure 4.23. Progressive damage identification results of the plate experiment

4.5 Summary

By utilizing the unique multi-scale and localization properties of WFEM, a progressive damage detection approach with the capability to detect sub-element damage gradually by optimizing an objective function that combines frequencies and MACs is proposed for beam and plate structures. The scale of the wavelet elements in the regions of concern can be adaptively enhanced or reduced to remain compatible with gradually identified damage scenarios. The test modal information remains the same, that is, no sensors are replaced or added.

Numerical and experimental examples are investigated with different damage scenarios to demonstrate the effectiveness of the proposed method. The results demonstrated that compared with TFEM, the proposed method can identify structural damage with satisfactory accuracy and high efficiency at the cost of minimized number of DOFs in the model and updating parameters in optimization. Although sometimes misjudgments occur during the detection process, further refining the WFEM in the subsequent stages would lead to high accuracy and successfully remove the initial false alarms.

Chapters 3 and 4 present progressive damage detection based on MSE and model updating, respectively. Although the former is time efficient as it is based on analytic derivation, more sensors need to be installed in the suspected damage regions during the damage detection process. In particular, the need for the measurement of rotational DOFs in mode shapes makes the implementation of the MSE-based method very difficult, if not impossible, in real applications. Moreover, the method is highly sensitive to noise because only mode shapes are adopted. Meanwhile, model updating-based damage detection employs an optimization solution; hence, misjudgments may occur, and conducting iterative optimization becomes time consuming. In addition, determining the weighting factors is another challenging task. Nevertheless, sensors need not be added during the detection process. Therefore, model updating is the more practical method of the two.

Chapter 5 Moving Load-Induced Response of a Damaged Simply Supported Beam and Its Application in Damage Localization

5.1 Introduction

Damage detection that employs moving load-induced response time histories have received a growing amount of interest (e.g., Zhu and Law 2006; Lu and Liu 2011; Chang et al. 2014). Many moving load-based damage detection methods rely on FEM. The number of DOFs of the model and updating parameters in optimization affect not only the accuracy but also the efficiency of damage detection. As pointed out in Section 1.2.3, locating damages first by using signal processing tools (e.g., Zhu and Law 2006; Meredith et al. 2012; Khorram et al. 2013) and then selecting updating parameters in damaged regions alone can reduce the number of updating parameters effectively.

A fundamental problem that has failed to elicit adequate attention is how local damage affects the moving load-induced response. The answer to this question is essential for the development of damage localization algorithms. Yang et al. (2004a) deduced the closed-form solution of the moving load-induced dynamic response of an undamaged simply supported beam. Yang and Lin (2005) stated that the dynamic response of a damaged simply supported beam consists of two components, namely, the driving-frequency component of the moving load and the natural-frequency component of the beam. The purpose of this chapter is to investigate the effects of local damage on these two components and develop an efficient damage localization method that employs the moving load-induced response. Based on modal perturbation and modal superposition methods, the closed-form solution of the dynamic response of a damaged simply

supported beam under moving force is developed. The closed-form solution allows for the individual examination of damage-induced changes in the two components. A simple and efficient damage localization approach that employs discrete DWT and single-sensor measurement data is proposed. Numerical examples are utilized to validate the efficacy of the proposed response computation algorithm and demonstrate the effectiveness of the corresponding damage localization method.

5.2 Moving Load-Induced Response of a Simply Supported Beam

5.2.1 Undamaged Beam

Yang et al. (2004a) investigated vehicle–bridge interaction dynamics with a bridge simulated by a simply supported beam; they derived closed-form solutions for bridge and vehicle responses when a vehicle is travelling on the undamaged bridge. Furthermore, Yang and Lin (2005) stated that the dynamic response of the bridge consists of the moving-frequency component of the moving vehicle and the natural -frequency component of the bridge. The closed-form solution for the dynamic response of the bridge is briefly introduced in this subsection along with some necessary adjustments. Readers may refer to Yang et al. (2004a) and Yang and Lin (2005) for the detailed dynamic response of the moving vehicle.

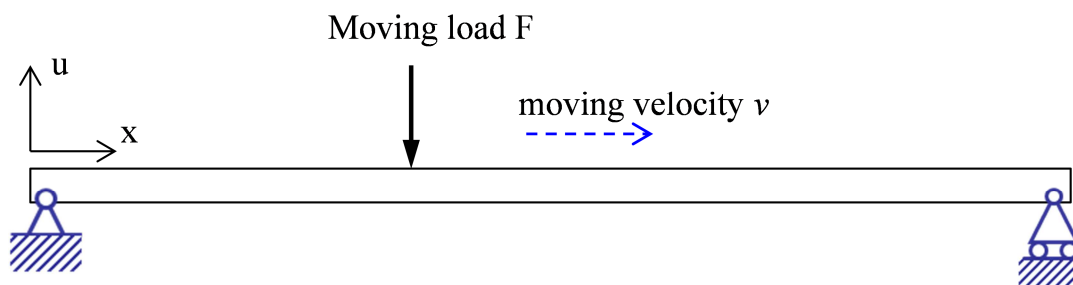


Figure 5.1. Simply supported beam subjected to moving load

By assuming that the mass of the vehicle is considerably less than that of the bridge, the moving vehicle can be approximated by a single moving load F with constant speed v (Yang et al. 2004a; Yang and Lin 2005). Figure 5.1 shows a bridge represented by a simply supported Bernoulli–Euler beam subjected to moving load F . The major parameters of the beam are as follows: beam span L , Young's modulus E , mass density ρ , cross-section area A , and moment of inertia I . For simplicity, the damping property and pavement irregularity of the bridge are ignored, so the equation of the motion governing the vertical vibration of the beam subjected to a moving load is

$$\rho A \frac{\partial^2 u(x,t)}{\partial t^2} + \frac{\partial^2}{\partial x^2} \left[EI(x) \frac{\partial^2 u(x,t)}{\partial x^2} \right] = F \delta(x - vt) \quad (5.1)$$

where x is the location in the longitudinal direction, t is time, $u(x,t)$ is the vertical displacement of the beam, v is the moving velocity of the force, and δ is the Dirac delta function. For the linearly elastic response of a simply supported beam, beam displacement $u(x,t)$ can be expressed as the superposition of mode shapes as follows:

$$u(x,t) = \sum_i q_i(t) \varphi_i(x) = \sum_i q_i(t) \sin \frac{i\pi x}{L} \quad (5.2)$$

where $\varphi_i(x) = \sin(i\pi x/L)$ is the i^{th} mode shape of the simply supported beam with a constant cross section and $q_i(t)$ is the corresponding modal coordinate. By assuming zero initial conditions, Yang et al. (2004a) derived a closed-form solution for the beam displacement response as

$$\begin{aligned} u(x,t) &= u_m(x,t) + u_n(x,t) \\ &= \frac{2F}{\rho AL} \sum_i \frac{1}{\omega_i^2(1-S_i^2)} \sin \frac{i\pi vt}{L} \sin \frac{i\pi x}{L} - \frac{2F}{\rho AL} \sum_i \frac{S_i}{\omega_i^2(1-S_i^2)} \sin(\omega_i t) \sin \frac{i\pi x}{L} \end{aligned} \quad (5.3)$$

where $i\pi v/L$ is the moving frequency of the vehicle corresponding to the i^{th} mode shape of the beam and ω_i is the i^{th} natural frequency of the beam.

$$\omega_i = \frac{i^2 \pi^2}{L^2} \sqrt{\frac{EI}{\rho A}} \quad (5.4)$$

where S_i is the ratio of moving frequency to natural frequency and is regarded as a dimensionless velocity of the moving load.

$$S_i = \frac{i\pi v}{L\omega_i} \quad (5.5)$$

As shown in Equation (5.3), the beam displacement response is expressed as the sum of two components, $u_m(x,t)$ and $u_n(x,t)$, which are governed by the moving frequencies of the load and the natural frequencies of the beam, respectively.

If the damping of the beam is considered, Equation (5.3) can be revised as (Yang and Lin 2005)

$$\begin{aligned} u(x,t) &= u_m(x,t) + u_n(x,t) \\ u_m(x,t) &= \frac{2F}{\rho AL} \sum_i \frac{1}{\omega_i^2 [(1-S_i^2)^2 + (2\zeta_i S_i)^2]} \left[(1-S_i^2) \sin \frac{i\pi vt}{L} - 2\zeta_i S_i \cos \frac{i\pi vt}{L} \right] \sin \frac{i\pi x}{L} \\ u_n(x,t) &= \frac{2F}{\rho AL} \sum_i \frac{S_i e^{-\zeta_i \omega_i t}}{\omega_i^2 [(1-S_i^2)^2 + (2\zeta_i S_i)^2]} \left[\frac{2\zeta_i^2 - (1-S_i^2)}{\sqrt{1-\zeta_i^2}} \sin(\bar{\omega}_i t) + 2\zeta_i \cos(\bar{\omega}_i t) \right] \sin \frac{i\pi x}{L} \end{aligned} \quad (5.6)$$

where ζ_i and $\bar{\omega}_i$ are the damping ratio and damped frequency of the i^{th} mode, respectively, and component $u_n(x,t)$ corresponds to a zero initial condition only.

5.2.2 Damaged Beam

The dynamic response of a damaged beam was previously studied by modeling cracks at one section with rotational springs (e.g., Zhu and Law, 2006; Roveri and Carcaterran 2012; Khorram et al. 2013). However, in this study, damage is modeled as the loss of flexural rigidity in a local region with certain length; this procedure is more commonly adopted in health monitoring of civil structures. The corresponding dynamic response of a damaged beam is derived by extending the method introduced in Section 5.2.1.

Assuming that damage leads to a local change in the flexural rigidity of the beam but not to a change in mass, damage can be represented by

$$EI^d(x) = EI(x) + \Delta EI(x) \quad (5.7)$$

where $EI(x)$ and $EI^d(x)$ are the flexural rigidities before and after damage, respectively, and $\Delta EI(x)$ is the stiffness loss resulting from the damage. The reduction in flexural rigidity causes changes, typically small perturbations, in the eigenvalues and mode shapes (Fox and Kapoor 1968; Shi et al. 2000b) as

$$\lambda_i^d = (\omega_i^d)^2 = \lambda_i + \Delta \lambda_i \quad (5.8)$$

$$\varphi_i^d(x) = \varphi_i(x) + \Delta \varphi_i(x) = \varphi_i(x) + \sum_{j=1, j \neq i}^n b_{i,j} \varphi_j(x) \quad (5.9)$$

where superscript d denotes the damage state and λ_i^d , ω_i^d , and $\varphi_i^d(x)$ are the i^{th} eigenvalue, frequency, and mode shape, respectively, of the damaged beam. The change in the i^{th} mode shape $\Delta \varphi_i(x)$ is represented by a linear combination of other modes, in which the first n modes are considered. With $b_{i,i} = 1$, Equation (5.9) can be rewritten as

$$\varphi_i^d(x) = \sum_{j=1}^n b_{i,j} \varphi_j(x) \quad (5.10)$$

The eigen solutions of a healthy beam are defined by the following partial differential equation (Clough and Penzien 1993).

$$\frac{\partial^2}{\partial x^2} \left[EI(x) \frac{\partial^2 \varphi_i(x)}{\partial x^2} \right] - \lambda_i \rho A \varphi_i(x) = 0 \quad (5.11)$$

With damage-induced perturbations, the above equation can be rewritten as

$$\frac{\partial^2}{\partial x^2} \left\{ [EI(x) + \Delta EI(x)] \cdot \frac{\partial^2 [\varphi_i(x) + \Delta \varphi_i(x)]}{\partial x^2} \right\} - (\lambda_i + \Delta \lambda_i) \rho A [\varphi_i(x) + \Delta \varphi_i(x)] = 0 \quad (5.12)$$

Substituting Equations (5.8), (5.9), and (5.11) into Equation (5.12) results in

$$\frac{\partial^2}{\partial x^2} [EI \frac{\partial^2 \Delta \varphi_i}{\partial x^2} + \Delta EI \frac{\partial^2 \varphi_i}{\partial x^2} + \Delta EI \frac{\partial^2 \Delta \varphi_i}{\partial x^2}] - \lambda_i \rho A \Delta \varphi_i - \Delta \lambda_i \rho A \varphi_i - \Delta \lambda_i \rho A \Delta \varphi_i = 0 \quad (5.13)$$

With the assumption that the perturbation terms are very small, high-order small terms

[e.g., $\Delta EI(x) \frac{\partial^2 \Delta \varphi_i(x)}{\partial x^2}$ and $\Delta \lambda_i \rho A \Delta \varphi_i(x)$] were normally neglected in previous damage detection studies (e.g., Shi et al. 2000b; Ren and Roeck 2002a; 2002b). However, these high-order terms are retained in Equation (5.13) because a noticeable error in the dynamic response induced by neglecting these terms is observed in this study.

By pre-multiplying $\varphi_s(x)$ to both sides of Equation (5.13), computing the integral in the interval $[0, L]$, and applying the orthogonal condition of mode shapes, the following equations are obtained.

$$\sum_{j=1}^n b_{i,j} \int_L \Delta EI(x) \frac{\partial^2 \varphi_i(x)}{\partial x^2} \frac{\partial^2 \varphi_j(x)}{\partial x^2} dx = \Delta \lambda_i M_i \quad (s = i) \quad (5.14a)$$

$$\sum_{j=1}^n b_{i,j} \int_L \Delta EI(x) \frac{\partial^2 \varphi_j(x)}{\partial x^2} \frac{\partial^2 \varphi_s(x)}{\partial x^2} dx = (\lambda_i + \Delta \lambda_i - \lambda_s) b_{i,s} M_s \quad (s \neq i) \quad (5.14b)$$

where

$$M_i = \rho A \int_L \varphi_i(x) \varphi_i(x) dx \quad (5.15)$$

Let $\alpha_{i,j} = \int_L \Delta EI(x) \frac{\partial^2 \varphi_i(x)}{\partial x^2} \frac{\partial^2 \varphi_j(x)}{\partial x^2} dx$. Equation (5.14) can then be expressed as the following nonlinear equation.

$$\begin{cases} \alpha_{1,1} b_{1,1} + \alpha_{1,2} b_{1,2} + \cdots + \alpha_{1,n} b_{1,n} - (\lambda_1 + \Delta \lambda_1 - \lambda_1) M_1 b_{1,1} = 0 \\ \cdots \\ \alpha_{i-1,1} b_{i-1,1} + \alpha_{i-1,2} b_{i-1,2} + \cdots + \alpha_{i-1,n} b_{i-1,n} - (\lambda_i + \Delta \lambda_i - \lambda_{i-1}) M_{i-1} b_{i-1,i-1} = 0 \\ \alpha_{i,1} b_{i,1} + \alpha_{i,2} b_{i,2} + \cdots + \alpha_{i,n} b_{i,n} - \lambda_i M_i b_{i,i} = 0 \\ \alpha_{i+1,1} b_{i+1,1} + \alpha_{i+1,2} b_{i+1,2} + \cdots + \alpha_{i+1,n} b_{i+1,n} - (\lambda_i + \Delta \lambda_i - \lambda_{i+1}) M_{i+1} b_{i+1,i+1} = 0 \\ \cdots \\ \alpha_{n,1} b_{n,1} + \alpha_{n,2} b_{n,2} + \cdots + \alpha_{n,n} b_{n,n} - (\lambda_i + \Delta \lambda_i - \lambda_n) b_{i,n} M_n = 0 \end{cases} \quad (5.16)$$

Given that $b_{i,i} = 1$ is already known, a total of n unknown coefficients (including $b_{i,j}$ and $\Delta \lambda_i$) need to be solved iteratively. Consequently, the eigenvalues λ_i^d and mode shapes $\varphi_i^d(x)$ of the damaged beam can be obtained.

Similar to the undamaged beam, the displacement response of the damaged beam can be expressed as a modal superposition.

$$u^d(x,t) = \sum_i q_i^d(t) \phi_i^d(x) = \sum_i q_i^d(t) \left[\sum_j b_{i,j} \phi_j(x) \right] = \sum_i q_i^d(t) \left[\sum_j b_{i,j} \sin \frac{j\pi x}{L} \right] \quad (5.17)$$

By substituting Equation (5.17) into Equation (5.1), multiplying both sides of the equation by $\phi_i^d(x)$, and computing the integral in the interval $[0, L]$ on both sides, the following equation can be obtained.

$$\ddot{q}_i^d(t) + (\omega_i^d)^2 q_i^d(t) = \frac{2F}{\rho AL} \sum_j b_{i,j} \sin \frac{j\pi vt}{L} \quad (5.18)$$

The loading term on the right side of the equation contains more than one periodic load. Similarly, the displacement response can be expressed as the sum of two components as follows:

$$\begin{aligned} u^d(x,t) = u_m^d(x,t) + u_n^d(x,t) = & \sum_i \left[\frac{2F}{\rho AL (\omega_i^d)^2} \sum_j \frac{b_{i,j}}{1 - (S_{i,j}^d)^2} \sin \frac{j\pi vt}{L} \right] \cdot \left(\sum_j b_{i,j} \sin \frac{j\pi x}{L} \right) \\ & - \sum_i \left[\frac{2F}{\rho AL (\omega_i^d)^2} \sum_j \frac{b_{i,j} S_{i,j}^d}{1 - (S_{i,j}^d)^2} \sin(\omega_i^d t) \right] \cdot \left(\sum_j b_{i,j} \sin \frac{j\pi x}{L} \right) \end{aligned} \quad (5.19)$$

where $S_{i,j}^d$ is the ratio of the j^{th} moving frequency to the i^{th} natural frequency.

$$S_{i,j}^d = \frac{j\pi v}{L\omega_i^d} \quad (5.20)$$

The closed-form solution in Equation (5.19) enables us to distinguish the moving- and natural-frequency components in the dynamic response of the damaged beam. These components cannot be accurately separated in the results of the FEM analysis.

5.2.3 Algorithm Verification

To verify the aforementioned algorithm for calculating the dynamic response of a damaged beam under moving force, a numerical example of a simply supported beam

with $A = 2.0 \text{ m}^2$, $L = 25 \text{ m}$, $I = 0.12 \text{ m}^4$, $E = 2.75 \times 10^{10} \text{ N/m}^2$, and $\rho = 2400 \text{ Kg/m}^3$ is studied. The beam parameters are the same as those utilized by Yang and Lin (2005). The first frequency in the undamaged state is 2.08 Hz. The beam suffers a single damage in the interval of [7.5, 8.75] with 25% severity. Four different moving velocities corresponding to $S_1 = 0.025, 0.050, 0.075,$ and 0.100 are considered. S_1 is the dimensionless moving velocity corresponding to the fundamental frequency of the undamaged beam. The sampling rate is 200 Hz.

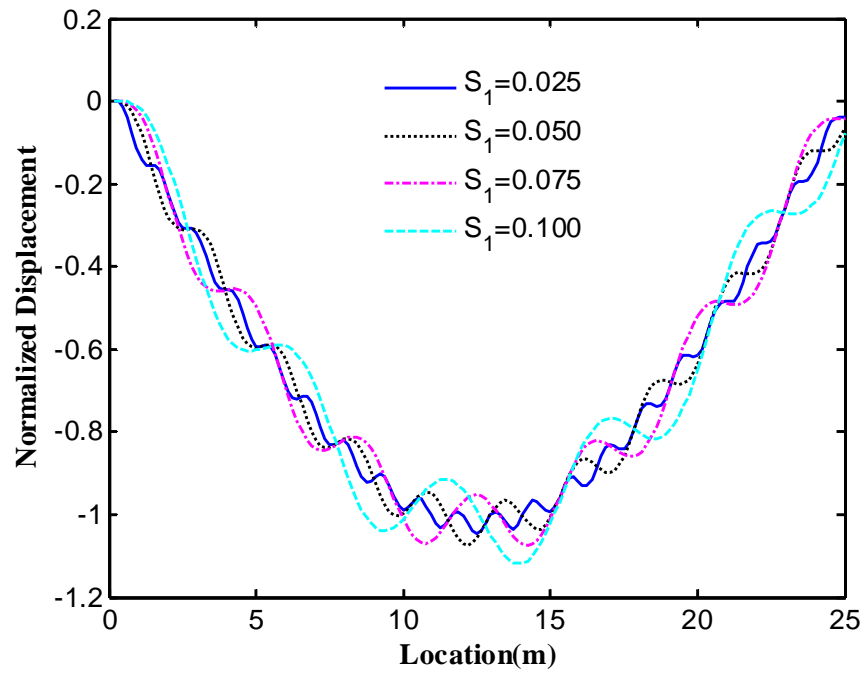
The dynamic responses of the beam with and without damage are simulated with the densely meshed TFEM and regarded as accurate reference responses. In FEM, the dynamic response of the beam is governed by the following equation of motion.

$$\mathbf{M}\ddot{\mathbf{u}}(t) + \mathbf{C}\dot{\mathbf{u}}(t) + \mathbf{K}\mathbf{u}(t) = \mathbf{f}(t) \quad (5.21)$$

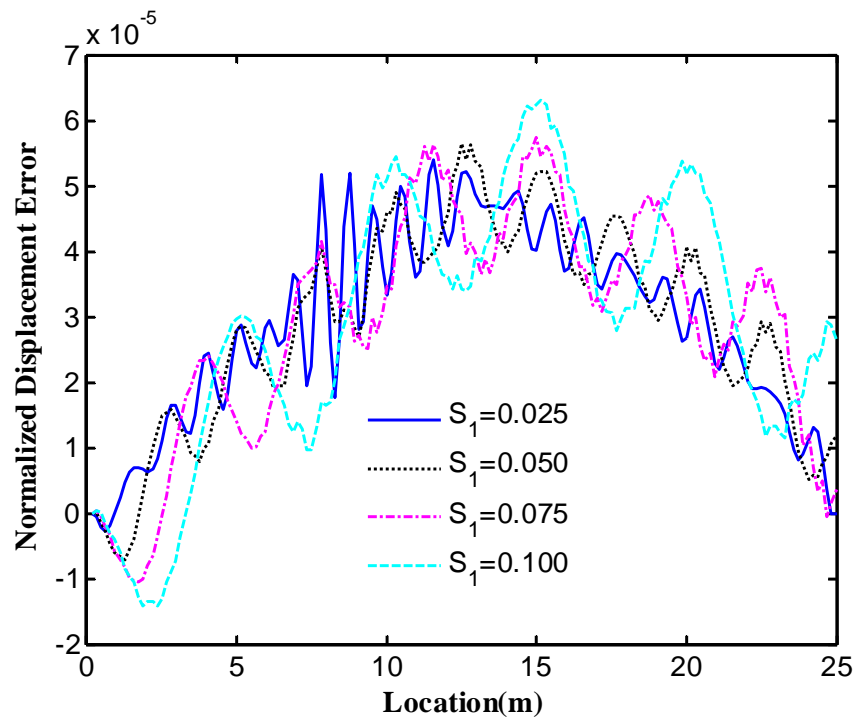
where $\mathbf{u}(t)$, $\dot{\mathbf{u}}(t)$, and $\ddot{\mathbf{u}}(t)$ are the displacement, velocity, and acceleration vectors, respectively; \mathbf{M} , \mathbf{C} , and \mathbf{K} are the global mass, damping, and stiffness matrices of the beam, respectively; and $\mathbf{f}(t)$ is the vector of applied loads calculated by applying the moving load to the corresponding nodes of the underlying element (Rowley 2007). No noise and damping are involved to ensure consistency with the proposed algorithm in Section 5.2.

Figure 5.2a shows the displacement versus the location of the moving load at the mid-span of the damaged beam calculated by the algorithm presented in Section 5.2.2. The location of the load can be easily determined from moving velocity v and time t . Unless otherwise stated, the displacements presented in this chapter are normalized to static deflection due to the load applied at the mid-span of the simply supported undamaged beam, that is, $u_{st} = FL^3 / (48EI)$. Figure 5.2b shows the errors between the displacements of the damaged beam calculated with the presented algorithm and the densely meshed TFEM. The errors are smaller than the peak displacements by four orders of magnitude. Thus, the presented algorithm can provide the moving

load-induced dynamic response of a damaged beam with sufficient accuracy.



(a) Moving load-induced displacement



(b) Computation error in the displacement response

Figure 5.2. Displacement response of the damaged beam at mid-span calculated with the presented algorithm

5.2.4 Discussion on the Undamaged Beam

Equations (5.3) and (5.19) offer deep insights into moving load-induced response-based damage detection. Usually the moving frequency of a vehicle is much lower than the natural frequency of a beam. Consequently, the moving-frequency components are dominant in the displacement response of the beam, whereas in the acceleration response, the natural-frequency components are dominant, and the contribution of the moving-frequency components is minimal and usually difficult to measure (Yang and Lin 2005; Kim and Kawatani 2008).

Paultre et al. (1992) summarized the fundamental frequencies of 898 highway bridges and concluded that the majority lies in the range of 2 Hz to 5 Hz and that fundamental frequency f_1 can be approximately estimated by the following relationship.

$$f_1 = 82L_{\max}^{-0.9} \quad (5.22)$$

where L_{\max} is the maximum span of highway bridges. Substituting Equations (5.22) and (5.4) into Equation (5.5) yields

$$S_1 = \frac{v}{164L^{0.1}} \quad (5.23)$$

Figure 5.3 shows the estimation of S_1 for three different driving speeds, namely, $v = 10$, 20, and 30 m/s. The corresponding S_1 is typically small and ranges from 0 to 0.15. Thus, the moving and natural frequencies are typically well separated, enabling the separation of the two components in Equation (5.3) by the signal processing technique described in Section 5.3.1.

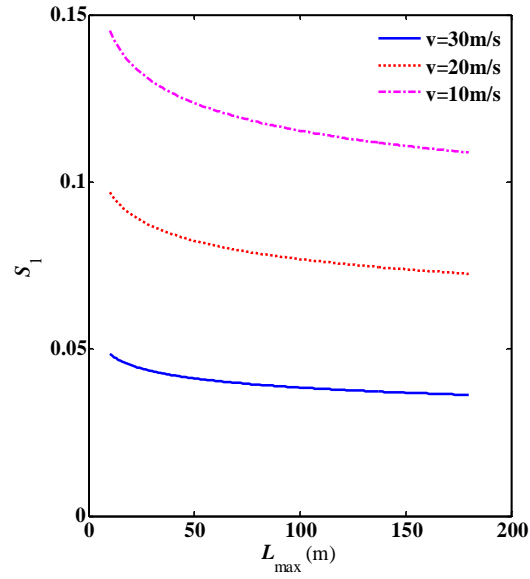


Figure 5.3. Variation in dimensionless moving velocity S_1 with the maximum span of highway bridges L_{\max}

Figure 5.4 shows the beam displacement response and contributions of different vibration modes at $S_1 = 0.1$. The moving-frequency response $u_m(x,t)$ can be regarded as the forced vibration of the beam under moving load, whereas the natural-frequency response $u_n(x,t)$ can be regarded as the free vibration response of the beam. The former is mainly contributed by the first mode and supplemented by the second and third modes; the latter is dominated by the first mode, and the contributions of the other modes are undetectable. In each mode, the response component $u_m(x,t)$ retains the mode shape information of the beam, and very high spatial resolution can be achieved with a single displacement sensor if the sampling frequency is sufficiently high. Such high spatial resolution information benefits the accuracy of damage localization. However, the component $u_m(x,t)$ vibrates at the moving frequency of the vehicle and completely loses the beam frequency information. By contrast, the response component $u_n(x,t)$ predominately vibrates at the first frequency of the beam; thus, the fundamental frequency can be easily identified from $u_n(x,t)$. However, the time history of $u_n(x,t)$ at a specific location does not represent the mode shape information. Many

displacement sensors need to be installed along the beam if the fundamental mode shape is desirable during damage detection.

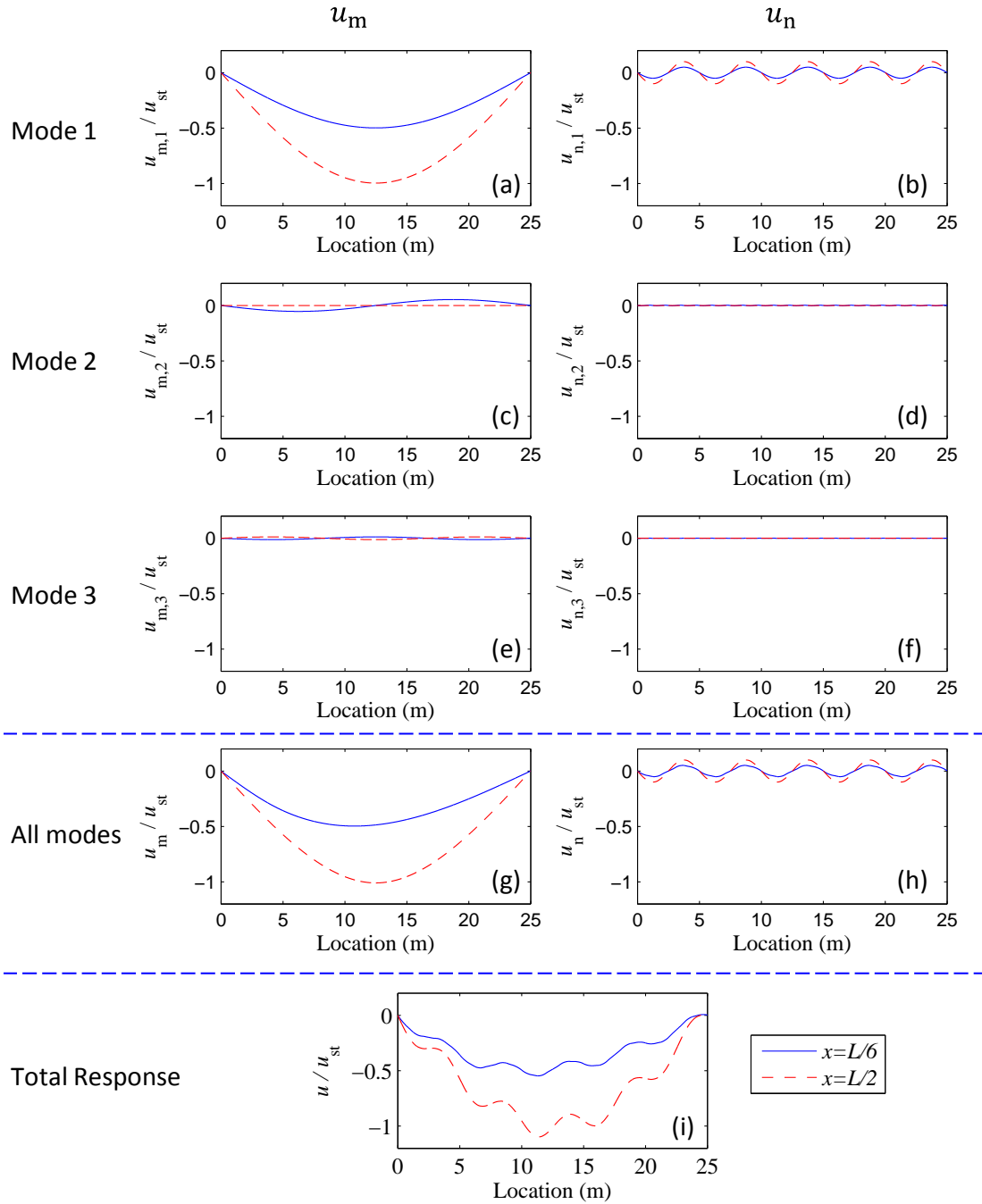


Figure 5.4. Moving load-induced displacement response of the undamaged beam ($S_1 = 0.1$)

Figure 5.5 shows the variation in the u_m and u_n components with increasing S_1 (i.e., dimensionless velocity of the moving load), where u_m and u_n are the peak dimensionless displacements measured at the mid-span ($x = L/2$). When $S_1 = 0$, $u_m(x_0, t)$ represents the static displacement influence line measured at the location of x_0 . The static influence line for damage localization is advocated by Chen et al. (2014). The moving-frequency component is generally insensitive to the increasing moving velocity. Particularly when $S_1 \leq 0.1$, the response component $u_m(x, t)$ can be regarded as a quasi-static response that is a good approximation of the static influence line. However, the amplitude of the natural-frequency component is extremely sensitive to moving velocity and increases linearly with dimensionless moving velocity S_1 .

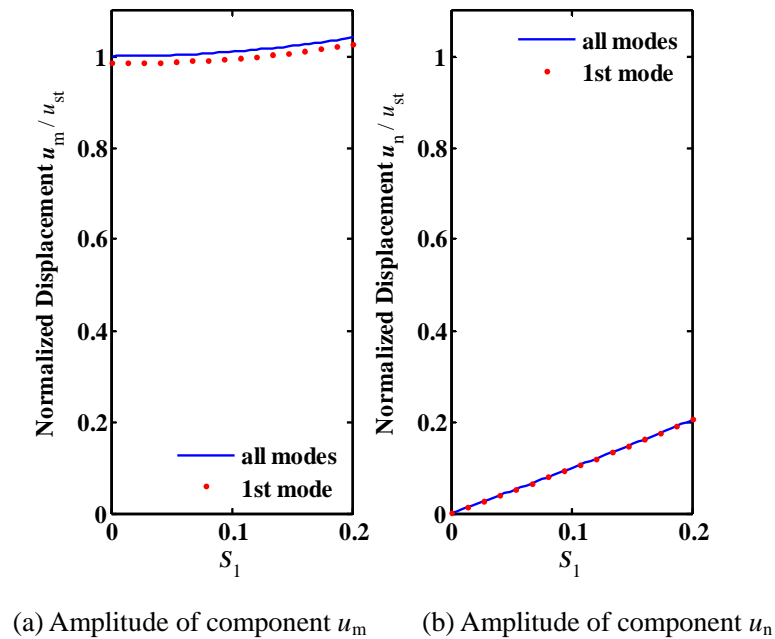


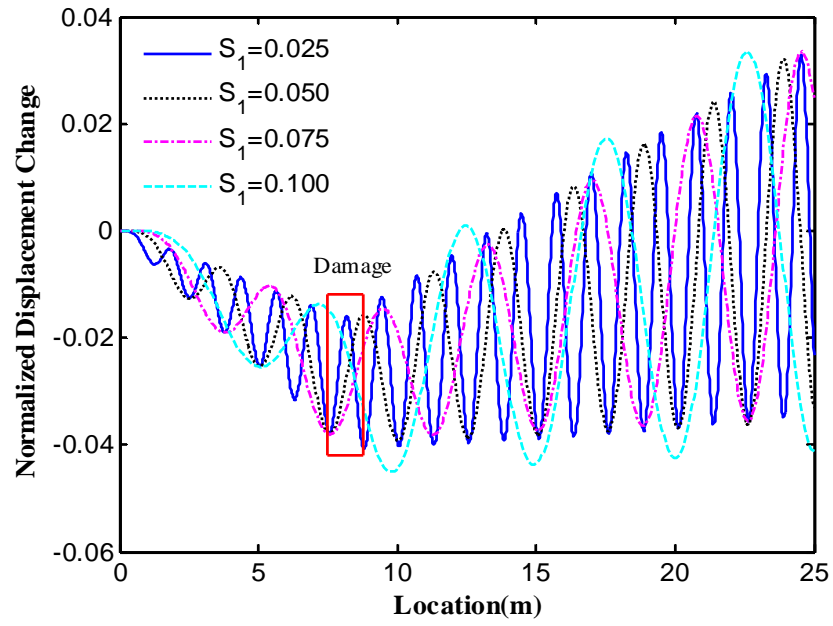
Figure 5.5. Effect of moving velocity on the displacement amplitude of the undamaged beam ($x = L/2$)

5.2.5 Discussion on the Damaged Beam

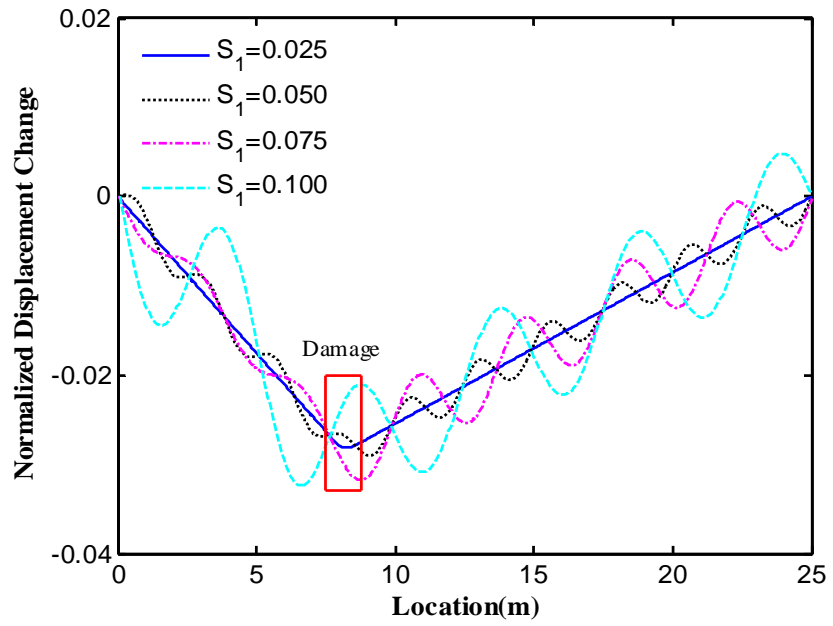
The dynamic responses of the beam with and without damage can be divided into two components, namely, the moving-frequency component related to the moving force and the natural-frequency component related to the beam. The closed-form solutions presented in Sections 5.2.1 and 5.2.2 allow for the accurate separation of these two components in the displacement and acceleration responses. This subsection investigates the local damage effect on the two different components by using the example in Section 5.2.3. This effect is very helpful in establishing a simple and effective damage localization method.

Figure 5.6 shows the damage-induced changes in the displacement time histories under moving force, including the changes in the total response and in the moving- and natural-frequency components. As shown in Figure 5.6b, the peak in the change of moving-frequency component response can apparently indicate the damage location when the moving-force velocity is relatively small; some oscillation occurs when the moving velocity increases and subsequently excites an additional dynamic effect. Therefore, the change in the moving-frequency component is a good damage indicator that enables the visualization of the damage location, especially at a low moving velocity. The damage also alters the natural-frequency component shown in Figure 5.6c. The change in Figure 5.6c is mainly due to the phase difference caused by damage-induced frequency reduction. The gradually amplified amplitude in Figure 5.6c is due to the zero damping considered in the simulation. As mentioned, the natural-frequency component is essentially free vibration under moving load. This component is significantly sensitive to moving velocity, damping ratio, and initial conditions. For example, Figure 5.7 shows the damage-induced changes in the displacement components at different damping ratios. The change in the natural-frequency component is extremely sensitive to the damping ratio, and its amplitude becomes considerably small as the damping ratio of the beam increases. By contrast, the moving-frequency component is relatively insensitive to the damping ratio, and its peak value roughly indicates the damage location

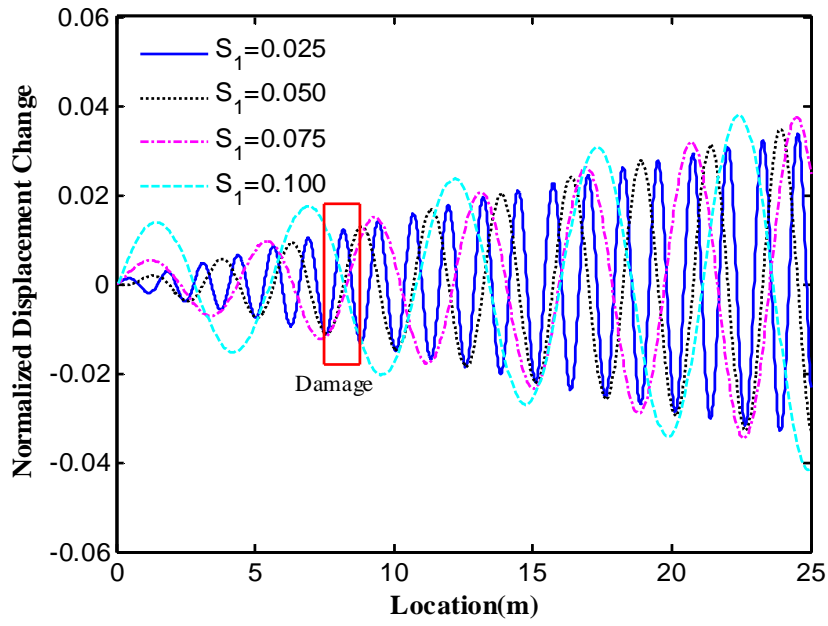
with different damping ratios.



(a) $(u^d - u) / u_{st}$

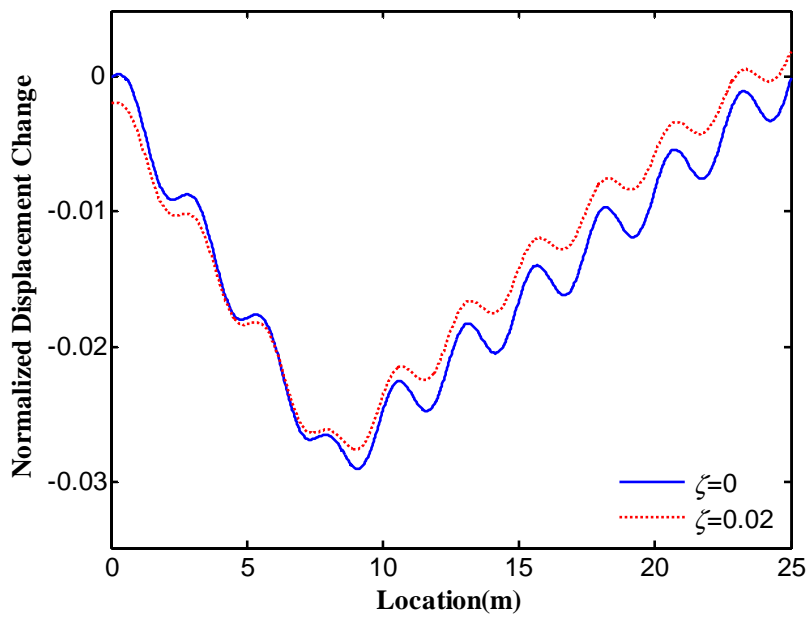


(b) $(u_m^d - u_m) / u_{st}$

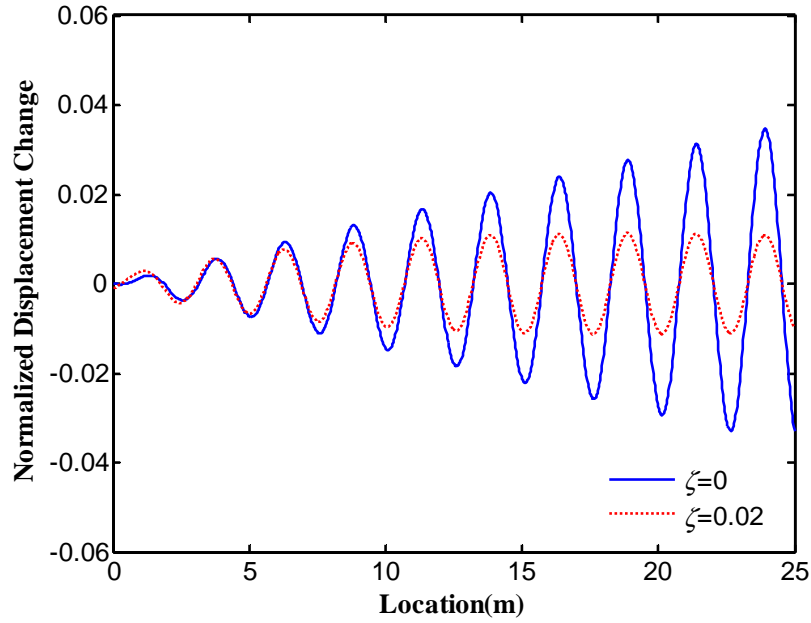


(c) $(u_n^d - u_n) / u_{st}$

Figure 5.6. Damage-induced change in normalized displacement response at mid-span



(a) $(u_m^d - u_m) / u_{st}$



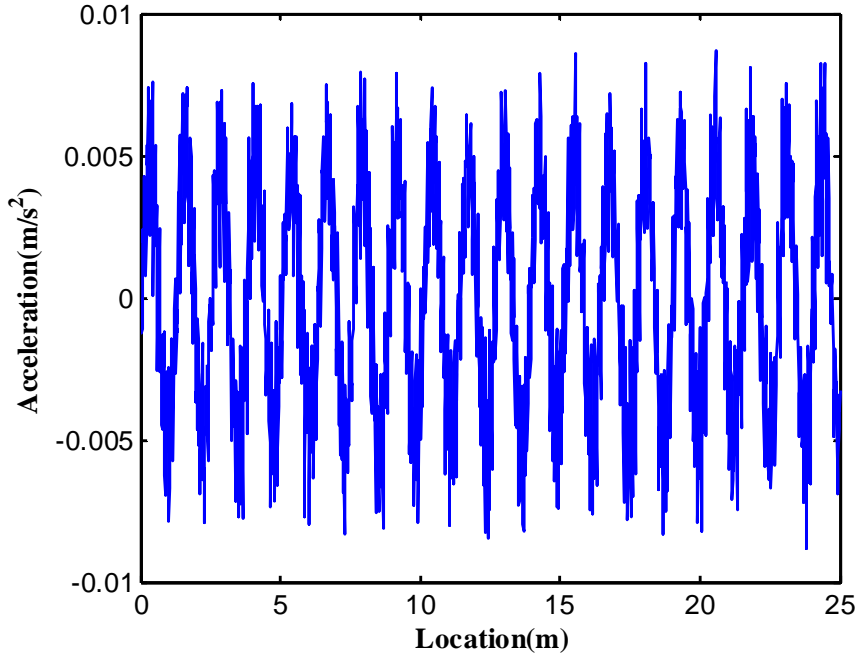
(b) $(u_n^d - u_n) / u_{st}$

Figure 5.7. Damage-induced change in normalized displacement response at mid-span for difference damping ratios ($S_1 = 0.05$)

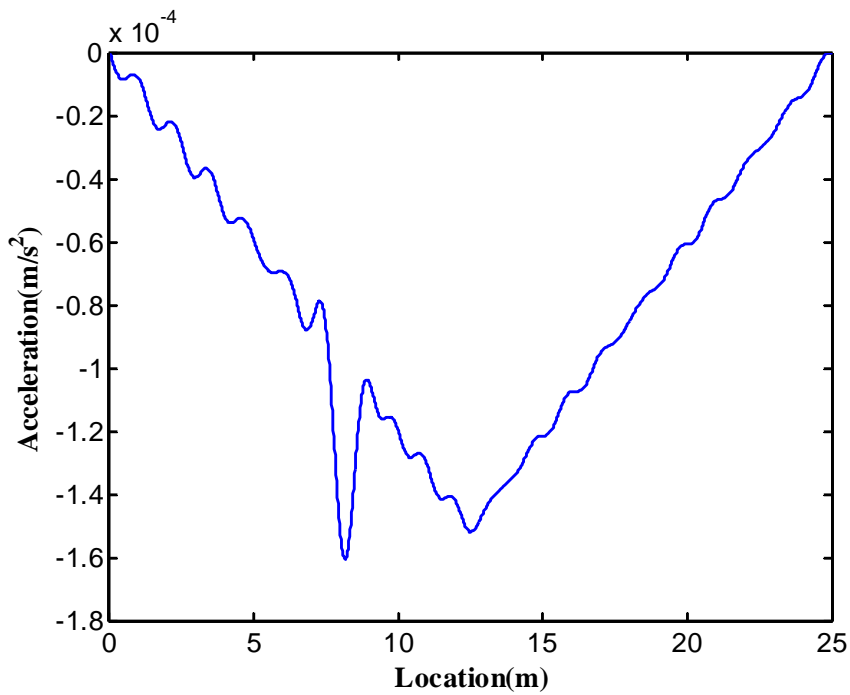
All three components shown in Figures 5.6 can be utilized for damage detection. However, the damping ratio and initial conditions can be neither maintained nor accurately measured in reality. Therefore, damage detection based on the change in the natural-frequency component in the time-domain becomes difficult, if not impossible, in engineering practice. Among the three components shown in Figure 5.6, the change in the time history of the moving-frequency component is recommended for damage detection in this study based on the above discussions.

Several studies on moving load-based damage detection methods focused on the acceleration response (Meredith et al. 2012; Gonz lez and Hester 2013). Figure 5.8 shows the acceleration responses of a damaged beam under moving load ($S_1 = 0.025$), including the total response and moving- and natural-frequency components. In the moving-frequency component, a spike can be observed at the damage location. This characteristic offers the theoretical feasibility to detect damage through proper signal processing without the need for model or baseline measurements of an undamaged beam. However, the amplitude of the spike shown in Figure 5.8b is extremely smaller (about

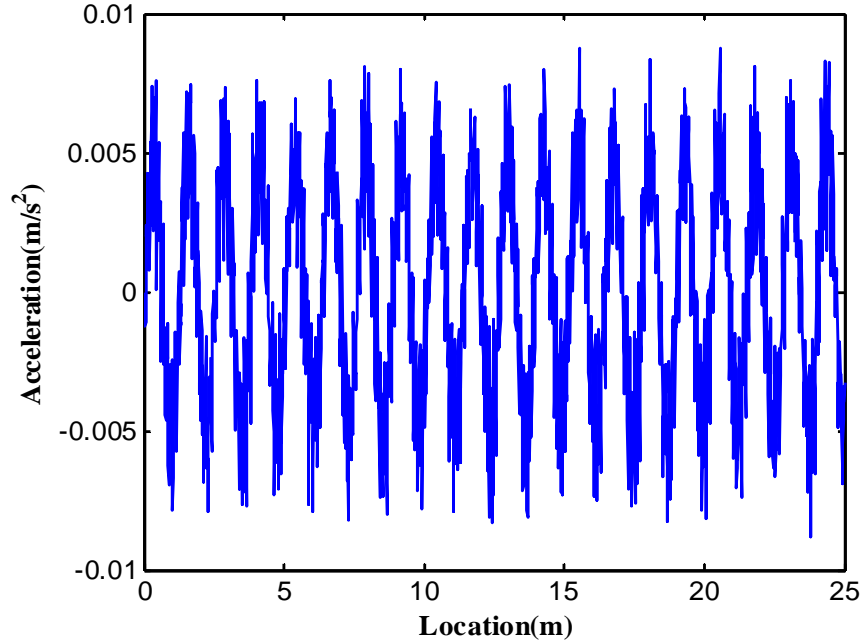
$5 \times 10^{-5} \text{ m/s}^2$) than that of the total acceleration response (about $1 \times 10^{-2} \text{ m/s}^2$). The spike is very likely to be submerged by low-level noise during measurement.



(a) Total acceleration



(b) Moving-frequency component



(c) Natural-frequency component

Figure 5.8. Acceleration response at mid-span after damage ($S_1 = 0.025$)

5.3 Wavelet-Based Damage Localization

5.3.1 Localization Procedure

Given that the change in the moving-frequency component is a good indicator of damage location, how to properly extract the moving-frequency component from the total displacement response is the key concern. Moving frequency is typically much lower than natural frequency. Hence, the two frequency components can be separated by signal processing techniques. DWT is a popular mathematical tool in signal processing. Emphasized as the main merit of wavelet, the multi-scale feature enables the analysis of signals at different scales in the time-frequency domain (Mallat 1988; Chui 2009; Brousseau 2009). As illustrated in Section 1.2.2.2, DWT decomposes a signal into approximation part A_i and detail part D_i , where $i = 1, 2, \dots, j$ denotes the decomposition level (Figure 1.2). The approximations correspond to the low-frequency part, whereas the details correspond to the high-frequency part (Brousseau 2009). By decomposing a signal into a specific level through DWT and

extracting the approximate band, the low-frequency components can be well separated from the original signal by removing the high-frequency components. The proposed damage localization process consists of the following steps.

Step 1: Obtain the moving load-induced dynamic responses of undamaged and damaged beams at the same location x_0 , where the dynamic response of the undamaged beam can be obtained from the baseline testing of the undamaged beam or from a reliable FEM, and calculate the difference in the total response by subtracting the dynamic responses of the undamaged and damaged beams, that is,

$$\Delta u = u(x_0, t) - u^d(x_0, t).$$

Step 2: Decompose the difference in total dynamic responses Δu through DWT to a specific level so that the part corresponding to the moving-frequency component, which is of relatively low frequency, can be well separated from the natural-frequency component and measurement noise, which is of relatively high frequency. The low- and high-frequency components are represented by approximation part A_j and detail part D_j , respectively. Decomposition should consider the frequency band corresponding to each level and the difference between the vehicle's moving frequency and structural fundamental frequency.

Step 3: Extract approximation band A_j and conduct inverse DWT to approximate the change in the moving-frequency components between the undamaged and damaged beams, that is, $\Delta u_m = u_m(x_0, t) - u_m^d(x_0, t)$.

Step 4: Determine the location of the damage, if any, based on the peaks of the change in the moving-frequency component Δu_m .

5.3.2 Numerical Study

The abovementioned simply supported beam is employed in the numerical study to demonstrate the effectiveness of the proposed damage localization method. Three damage scenarios with different damage locations are listed in Table 5.1.

Table 5.1. Damage scenarios of the simply supported beam

Damage scenario	Damage location	Damage severity (%)
Case 1 Single damage	[7.5, 8.75]	25
Case 2 Double damage	[8.75, 10], [16.25, 17.5]	25
Case 3 Triple damage	[6.25, 7.5], [13.75,15], [17.5,18.75]	25

Again, the accurately dynamic responses of the undamaged and damaged beams are computed through densely meshed TFEM. Although not considered in Sections 5.2.1 and 5.2.2, vibration damping universally exists in real structures and plays an important role in dynamic responses. Rayleigh damping is considered in the numerical simulation, in which the damping matrix is constructed as a combination of mass and stiffness matrices as follows:

$$[\mathbf{C}] = a_1[\mathbf{M}] + a_2[\mathbf{K}] \quad (5.24)$$

where a_1 and a_2 are two coefficients to be determined according to the target damping ratio. Given that only the first two vibration modes are significant in moving load-induced response (Yang et al. 2004b), a damping ratio of $\zeta = 0.02$ is assigned to these two modes. Considering that measured data are inevitably contaminated by measurement noise in dynamic tests, the noise effect is considered by adding zero-mean Gaussian noise to the accurate dynamic response as follows (Zhu and Law 2006):

$$\mathbf{u} = \mathbf{u}_{cal} + E_p N_{noise} \times \sigma(\mathbf{u}_{cal}) \quad (5.25)$$

where \mathbf{u} is the noisy displacement response, E_p is the noise level, N_{noise} is a vector of independent random variables following a standard normal distribution, \mathbf{u}_{cal} is the vector of the displacement response, and $\sigma(\mathbf{u}_{cal})$ is the standard deviation of the response. A single displacement transducer is assumed to be installed at the mid-span to measure the vertical flexural displacement.

Figure 5.9 shows a representative damage-induced change in the total displacement response at the mid-span with and without noise in Case 1 ($S_1 = 0.025$). The noise level is equal to 5% of the total displacement response. Without noise, the change in the total displacement can roughly indicate the damage location (as shown by the bold line). However, the presence of noise makes directly visualizing the damage location by subtracting the total responses before and after the damage difficult. The oscillation in the total response also results in multiple peaks, which also hinder accurate damage localization.

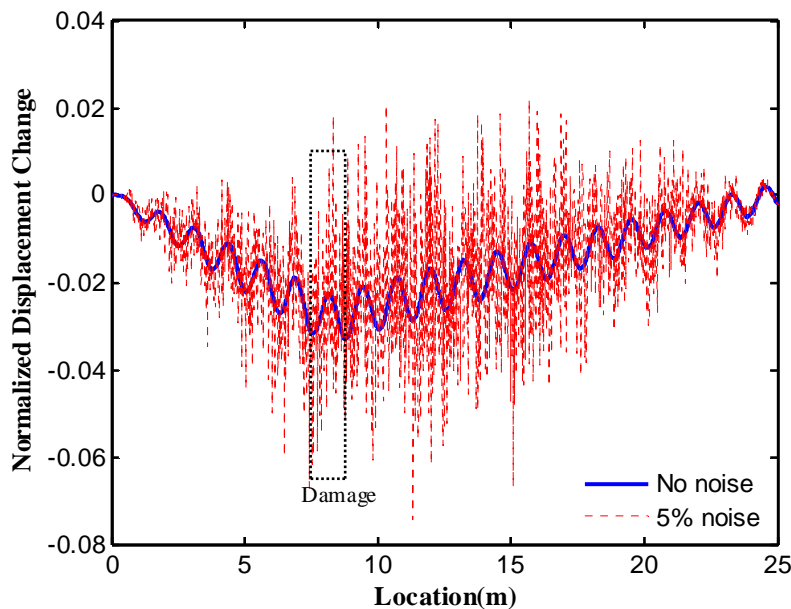


Figure 5.9. Damage-induced total displacement change at mid-span in Case 1 with and without noise ($S_1 = 0.025$)

DWT of the signal shown in Figure 5.9 should be performed subsequently for signal separation and denoising purposes. A type of widely used Daubechies wavelet, wavelet "db30" is employed in this study. The fundamental frequency of the beam is approximately 2.08 Hz, and the moving frequency is typically lower than 0.5 Hz in the numerical study. Hence, the change in the total displacement is decomposed to scale 7, and the corresponding lowest frequency band is [0, 1.5625] Hz, which can properly remove the natural-frequency component, undesirable noise, and oscillations in the dynamic response.

5.3.3 Discussion

Figures 5.10 and 5.11 show the damage localization results in Case 1 at four different moving velocities, namely, $S_1 = 0.025, 0.050, 0.075,$ and 0.1 . Five percent noise level is considered in Figure 5.10, whereas various noise levels are considered in Figure 5.11. When the travelling velocity is relatively low, the peak of the filtered curve can satisfactorily locate the damage with only a slight shift (Figure 5.10). However, high moving velocity causes large oscillations in both moving- and natural-frequency components (Figure 5.6). Thus, when dimensionless velocity S_1 increases to 0.1 , the localization results become unacceptable, and a noticeable shift in the peaks from the actual damage location can be observed (Figure 5.11). High moving load velocity reduces the accuracy of damage localization based on moving load-induced responses. This conclusion is consistent with the findings in previous studies (e.g., Nguyen and Tran 2010; González and Hester 2013).

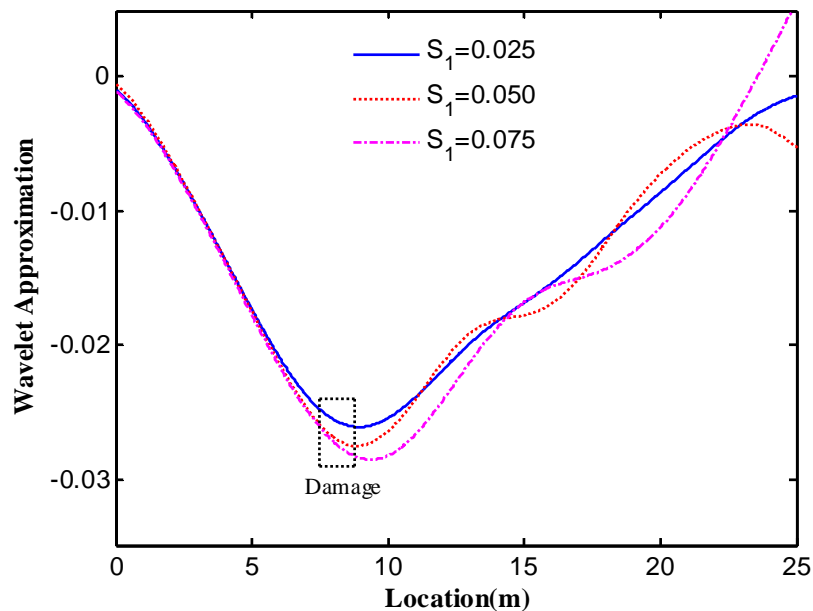


Figure 5.10. DWT results of displacement change with 5% noise in Case 1

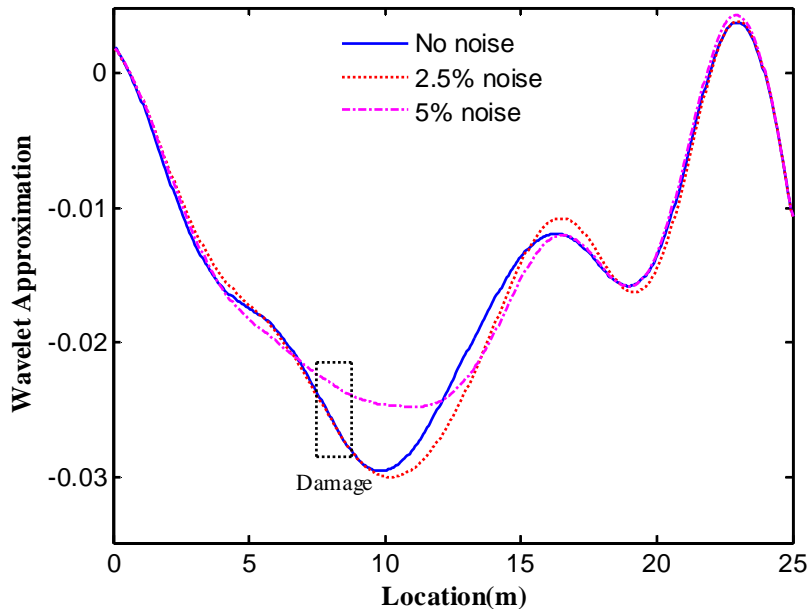


Figure 5.11. DWT results of displacement change under different noise levels in Case 1 ($S_1 = 0.1$)

Similar damage localization results in Cases 2 (double damages) and 3 (triple damages) are shown in Figures 5.12 and 5.13, respectively. Approximately five percent noise and three different moving velocities ($S_1 = 0.025, 0.050,$ and 0.075) are considered in the simulations, and the effect of multiple damage locations on the proposed method is examined. In Case 2 (i.e., Figure 5.12), the two damages can be located fairly well when $S_1 = 0.025$ and 0.050 , but localization becomes difficult when $S_1 = 0.075$. This finding implies that the case with more than one damage is more sensitive to the influence of increasing moving velocity. In Case 3 (i.e., Figure 5.13), the satisfactory localization results of the triple damages are difficult to achieve by direct visual inspection. In summary, the proposed damage localization method can work effectively in cases with relatively low moving velocity and few damages.

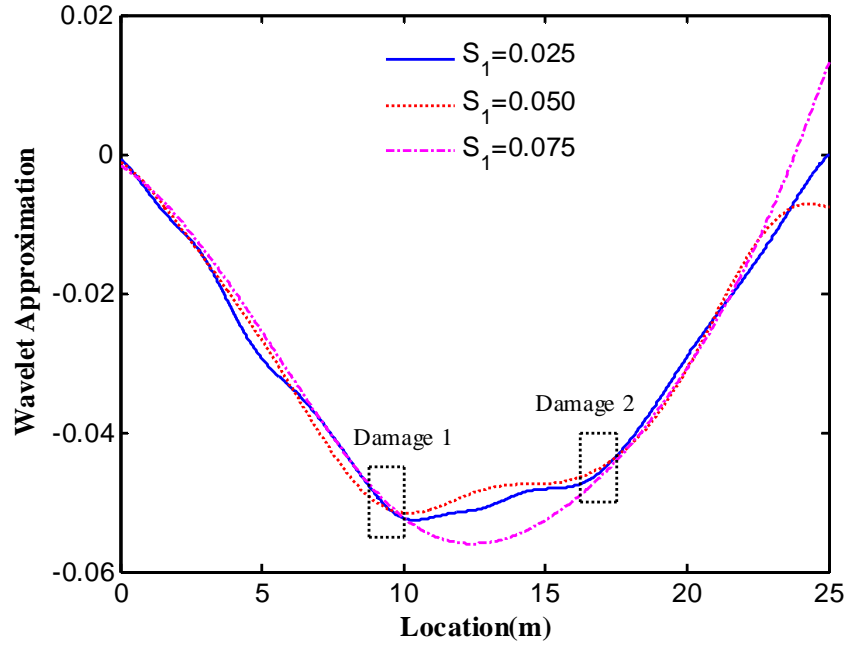


Figure 5.12. DWT results of displacement change with 5% noise in Case 2

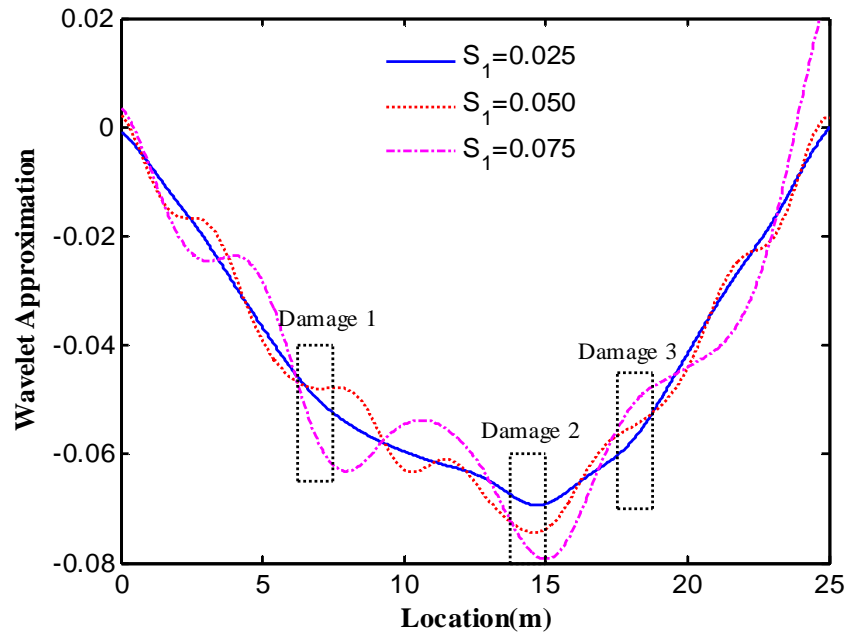


Figure 5.13. DWT results of displacement change with 5% noise in Case 3

As mentioned previously, maintaining the consistency and equality of moving velocities of vehicles is difficult in the two moving load tests. Therefore, the effect of unstable and unequal moving velocities is also investigated. The following velocity time histories are assumed.

$$V_u = 2.605 \times 1.04 \times (1 + 0.05 \times \sin(2\pi t) + 0.1 \times \sin(5\pi t)) \quad (5.26a)$$

$$V_d = 2.605 \times (1 + 0.1 \times \sin(2\pi t) + 0.05 \times \sin(5\pi t)) \quad (5.26b)$$

where V_u and V_d are the moving velocities of the load in the tests on the undamaged and damaged beams, respectively. Figure 5.14 shows a comparison of the time histories of moving velocities before and after damage occurs. The mean velocity in the undamaged state is 4% higher than that in the damaged state. The mean velocity of 2.605 m/s corresponds to $S_1 = 0.025$. The harmonic terms in Equation (5.26) simulate the fluctuations in moving velocity. The damaged beam corresponding to Case 1 with 5% noise in the displacement response is analyzed again under the assumed varying velocity.

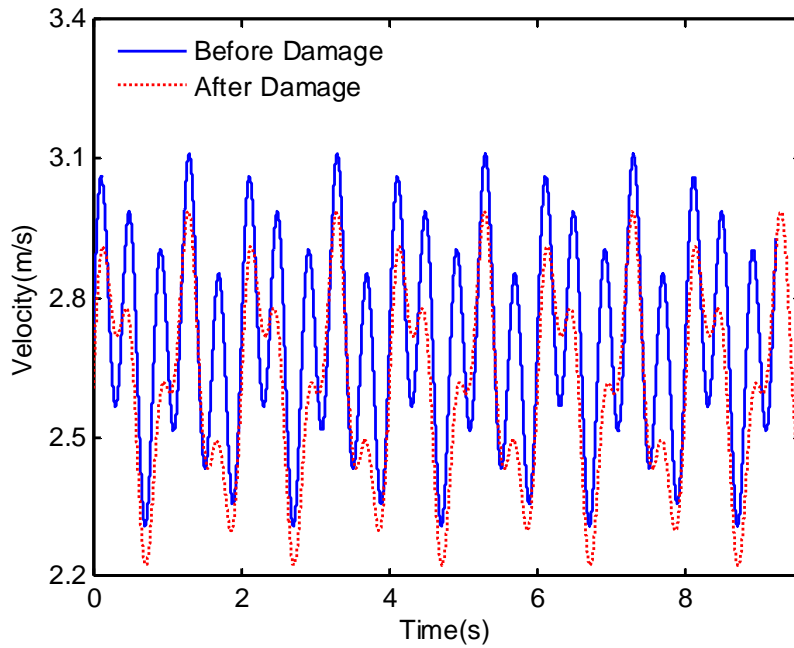


Figure 5.14. Velocity time history of the force before and after damage

With the same time interval and different moving velocities, the location intervals in the undamaged and damaged states are unequal. Thus, direct subtraction of displacement responses before and after damage is prohibited. Given the knowledge of location series in the two states, the displacement responses of the undamaged and damaged beams can be easily interpolated to obtain a consistent location interval. Subsequently, the damage

localization process described in Section 5.3.1 can be implemented. As shown in Figure 5.15, the single damage in Case 1 can still be successfully located. This finding indicates that the presented damage localization method is still effective despite slightly unstable and unequal moving velocities. Notably, the end effect that occurs in the DWT result makes damage detection close to the ends very challenging.

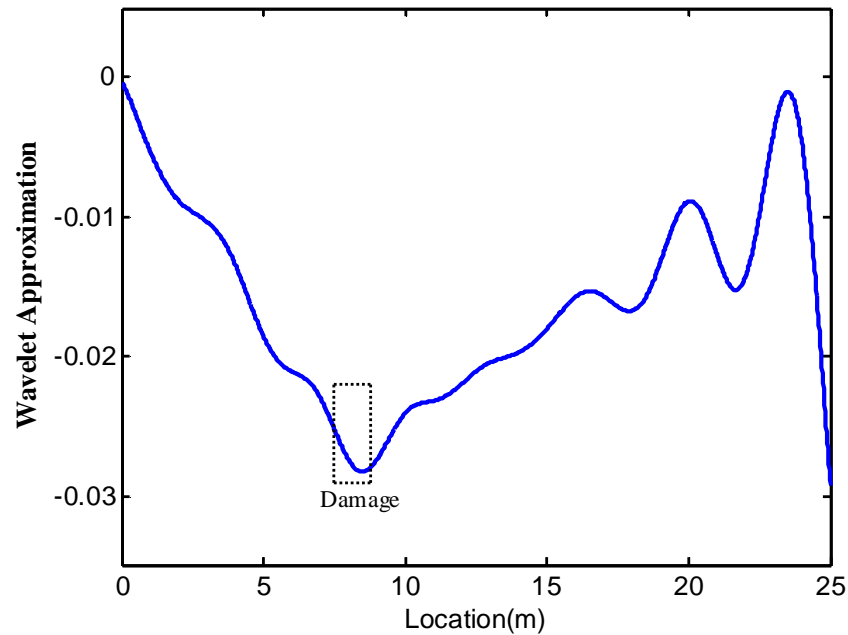


Figure 5.15. DWT results of the displacement change under varying velocity

A constant moving load, which essentially ignores the dynamics of moving vehicles, is considered in the above theoretical derivation and numerical examples. Although Yang and Lin (2005) assumed that vehicle mass is considerably less than bridge mass and thus, a moving vehicle may be approximated by a moving force, the potential effect of vehicular dynamics on bridge response is still examined by adopting a vehicle model, as shown in Figure 5.16. Lu and Liu (2011) proposed the use of this three-parameter mass–spring–damper model to simulate a moving vehicle. The same parameters from Lu and Liu (2011) are adopted in this study: $m_v = 4.0 \times 10^3$ Kg, $c_v = 1.0 \times 10^3$ Ns/m, $k_v = 6.0 \times 10^5$ N/m. Road surface roughness should also be considered in the actual vibration test. The random road surface roughness of a beam can be assumed as a kind of zero-mean, real-valued, stationary Gaussian process as follows (Yang et al. 2012; Li

and Au 2015):

$$r(x) = \sum_{m=1}^N 2\sqrt{S_m(\omega_m)\Delta\omega} \cos(2\pi\omega_m x + \theta_m) \quad (5.27)$$

where

$$\omega_m = \omega_l + (m - 1/2)\Delta\omega \quad (m = 1, 2, \dots, N) \quad (5.28a)$$

$$\Delta\omega = (\omega_u - \omega_l) / N \quad (5.28b)$$

in which ω_u and ω_l are the upper and lower cut-off spatial frequencies, respectively.

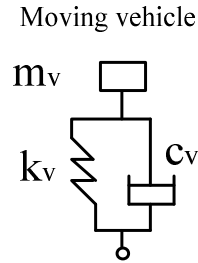


Figure 5.16. Moving vehicle model

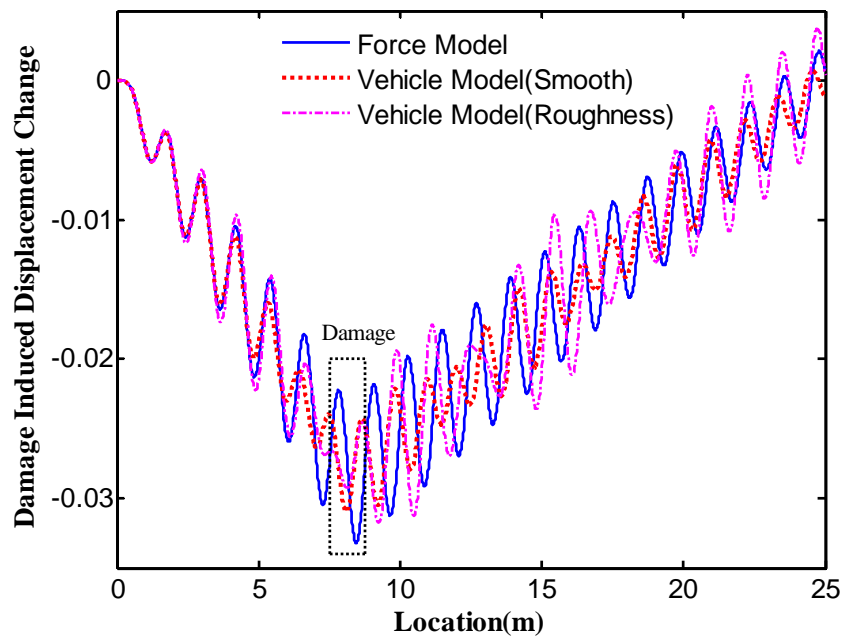
The power spectral density function $S_m(\omega_m)$ can be expressed in terms of the spatial frequency ω_m of road surface roughness as follows (Yang et al. 2012; Li and Au 2015):

$$S_m(\omega_m) = \vartheta\omega_m^{-2} \quad (\omega_l < \omega_m < \omega_u) \quad (5.29)$$

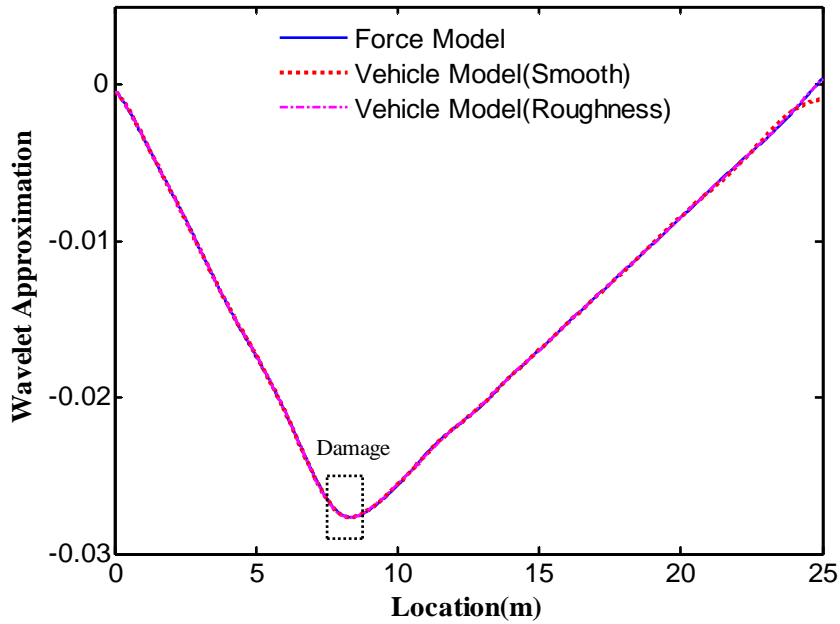
The values of ϑ , ω_l , ω_u , and N can be determined according to ISO specification (ISO8608:1995). In this study, the values of ϑ , ω_l , ω_u , and N are set to $1 \times 10^{-8} \text{ m}^2$ (m/cycle), 0.05 cycle/m, 2 cycle/m, and 1,024, respectively (Li and Au 2015).

To examine the effectiveness and robustness of the proposed damage localization method, Case 1 in Section 5.3.2 is re-analyzed in consideration of the vehicular dynamic model and road roughness. Figure 5.17a shows the damage-induced

displacement changes at mid-span with $S_1 = 0.025$ in Case 1. The bridge responses are calculated individually with the moving-force and moving-vehicle models (with and without road roughness). Given the influence of vehicular dynamics and road roughness, apparent differences are observed among the results from different models. However, the response changes extracted using DWT are nearly identical (Figure 5.17b). This result clearly indicates that the moving-frequency component of the bridge response is insensitive to the introduction of vehicular dynamics and road roughness, although the total response is significantly affected. It can be explained by the fact that the typical moving frequency of a vehicle is considerably lower than the natural frequency. This result does not only justify the use of the moving-force model in the previous section but also demonstrates the advantage of using the moving-frequency component in damage detection. A slight discrepancy can be observed at the right end in Figure 5.17b. This discrepancy is mainly caused by the end effects of DWT.



(a) Displacement change



(b) DWT disposed displacement change

Figure 5.17. Comparison of the results calculated using different models (Case 1)

5.4 Summary

This chapter investigates the effects of local stiffness reduction on the dynamic response of a simply supported beam subjected to moving load. A simple and effective damage localization method is developed accordingly through DWT. A computation algorithm based on modal perturbation and superposition method is proposed and verified. The proposed algorithm enables the accurate separation of the dynamic response of a damaged beam under moving load into two components: moving- and natural-frequency components. In the time-domain, the damage-induced change in the moving-frequency component has a relatively low frequency and is relatively insensitive to the variations in moving velocity, damping ratios, and initial conditions. By contrast, the change in the natural-frequency component has a relatively high frequency, and the time history of this component is very sensitive to variations in damping ratios, initial conditions, and vehicular dynamics. Therefore, a change in the moving-frequency component is regarded as a promising indicator of damage location, particularly when the moving velocity of the load is low and the number of damage

locations is limited. As a frequency separating and denoising tool, multi-scale DWT is conducted to extract the moving-frequency component from the total displacement response induced by a moving load. Subsequently, the likely damage location can be efficiently identified via measurement with a single displacement sensor.

Numerical examples at different moving load velocities, noise levels, and numbers of damage locations are presented to verify the efficacy and robustness of the proposed damage localization method. Single and double damages can generally be located with satisfactory accuracy. However, detecting several damage locations is difficult. High moving velocity of the load reduces the accuracy of damage localization, especially in cases of multiple damages. The investigation conducted in this chapter indicates that the proposed damage localization method is insensitive to vehicular dynamics and road surface roughness.

Chapter 6 Two-Phase Damage Detection of Beam Structures Subjected to a Moving Vehicle

6.1 Introduction

FEM updating under moving load is a popular damage detection method for beam structures (e.g., Majumder and Manohar 2002; Lu and Law 2007a; 2007b; Lu and Liu 2011; Li and Law 2012). The numbers of model DOFs and updating parameters in model updating affect the computation cost and accuracy of damage detection. The damage localization method that employs DWT introduced in Chapter 5 can help reduce the number of updating parameters by limiting the updating parameters in the identified damage regions only. Furthermore, a multi-scale FEM whose resolution is compatible with load conditions and damage scenarios can help reduce the total number of DOFs.

- (1) In terms of compatibility with loading conditions, an ideal option is to use multi-scale mesh generation with a dense mesh in regions near the load–beam contact positions and a coarse mesh in other regions so that sufficient modeling accuracy can be achieved with a reduced number of DOFs (Rieker et al. 1996). Consequently, the regions with a fine mesh resolution should be adaptively changed according to the contact point when the load moves over time.
- (2) In terms of compatibility with damage scenarios, the previous chapters presented a promising scheme in which coarse and fine meshes are utilized for undamaged and damaged regions, respectively. Consequently, the mesh resolution should be progressively changed. A coarse FEM is used to identify the likely damage region first; subsequently, local refinement in the likely damaged regions is conducted to estimate the accurate damage location and severity.

In both schemes, the mesh resolution should be adaptively changed during damage detection. The implementation of a dynamically changed meshing scheme in the context of TFEM is difficult. WFEM provides a more convenient alternative to solve this problem, given that it enables convenient changes in the spatial resolution of wavelet elements according to actual needs.

This chapter presents a WFEM-based adaptive-scale analysis strategy for beam structures subjected to moving load. In the strategy, the scales of wavelet elements can be conveniently changed according to the time-varying load–beam contact position. Subsequently, a two-phase damage detection method, that is, localization and then quantification, is developed by combining adaptive-scale analysis strategy, DWT-based damage localization (presented in Chapter 5), and progressive damage detection (presented in Chapter 4). The damage-induced displacement changes are decomposed by DWT to locate damages and then employed to quantify the damages in a progressive manner via multi-scale WFEM updating technique, with updating parameters limited to suspected damage regions only. The elemental scales of WFEM change dynamically not only according to the moving vehicle–beam contact positions but also to the identified damage regions. As a result, the number of DOFs and updating parameters and the corresponding computation effort are significantly reduced. A laboratory experiment is conducted to verify the feasibility and efficiency of the proposed two-phase damage detection method for beam structures under a moving load.

6.2 WFEM-Based Modeling Strategy

6.2.1 Adaptive-Scale Analysis Strategy

This section presents an adaptive-scale analysis strategy for beam structures subjected to a moving load (Figure 6.1). The beam is divided into N segments, each of which may contain one or more wavelet elements. The main strategy is to utilize an adaptive-scale WFEM, in which the element scales change according to the load–beam contact

positions. For instance, high-scale elements are utilized in the moving load–beam contact region and low-scale elements in the other regions. As the load–beam contact position moves over time, the element scales in each region are dynamically lifted and lowered during the process, thereby reducing the number of DOFs and the computation cost.

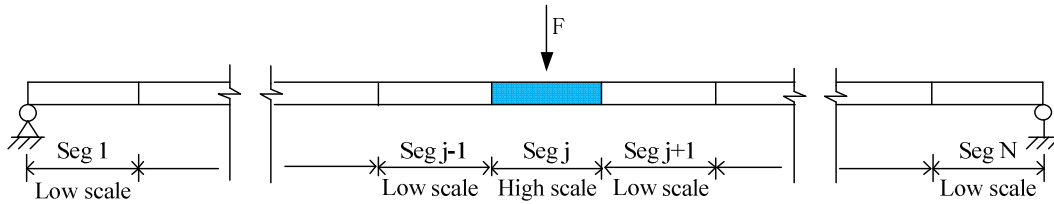


Figure 6.1. Adaptive-scale analysis strategy

6.2.2 Numerical Study

A simply-supported beam under a moving force (Figure 6.2) is simulated to demonstrate the efficacy of the adaptive-scale moving-load analysis strategy. The physical parameters of the beam are as follows: cross section $A = 1 \text{ m} \times 0.6 \text{ m}$, Young's modulus $E = 33 \text{ Gpa}$, mass density $\rho = 2.5 \times 10^3 \text{ Kg/m}^3$, and length $L = 16 \text{ m}$. The velocity of the moving force is 10 m/s . The beam is subjected to double damages in the intervals of $[3, 3.5]$ and $[9, 9.5]$ with 20% and 25% severity, respectively.

Initially, the beam is divided into eight equal segments, with each segment containing two wavelet beam elements (Figure 6.2). The scales of the wavelet elements are equal to 1 and 0 in the contact region and other regions, respectively. The total number of DOFs in the multi-scale WFEM is 38. For comparison, a TFEM with 16 beam elements (34 DOFs) is also used to model this problem. In addition, very densely meshed TFEMs of the undamaged and damaged beams are employed to simulate accurate dynamic responses induced by moving force, which are used as a reference.

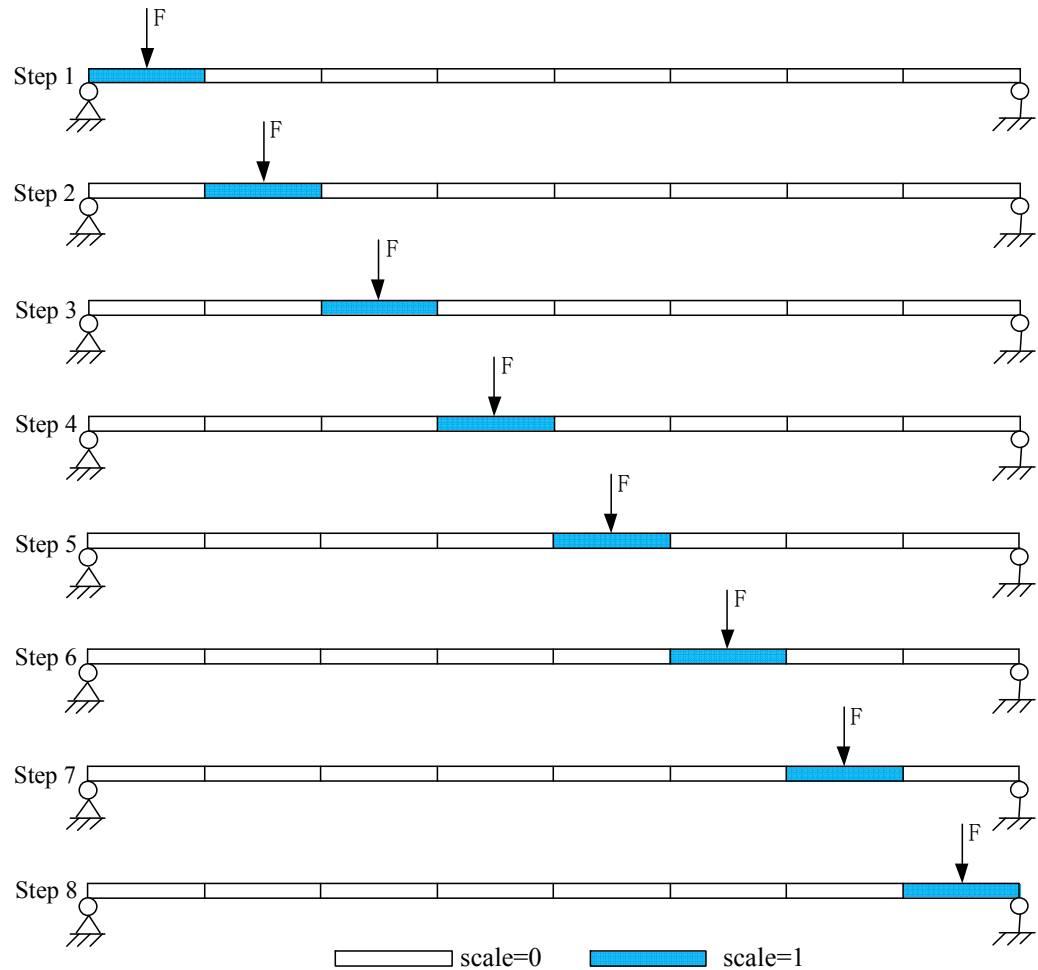


Figure 6.2. Adaptive wavelet element scale strategy during the moving process

The accurate displacement time histories at locations $\frac{1}{4}L$, $\frac{1}{2}L$, and $\frac{3}{4}L$ of the undamaged beam are shown in Figure 6.3. The corresponding displacement errors calculated with WFEM and TFEM are shown in Figure 6.4. The WFEM results have a very minimal error, and the computation error of WFEM is generally smaller than that of TFEM by two orders of magnitude. This comparison clearly indicates that WFEM with similar number of elements can achieve better accuracy. In other words, WFEM can considerably reduce the total DOFs and enhance computation efficiency. Figure 6.5 shows the accurate displacement change induced by the damage at the locations of $\frac{1}{4}L$, $\frac{1}{2}L$, and $\frac{3}{4}L$. The computation error from TFEM is comparable to the displacement change induced by the damage in this example. This observation implies that TFEM with such spatial resolution would compromise the damage detection results if used.

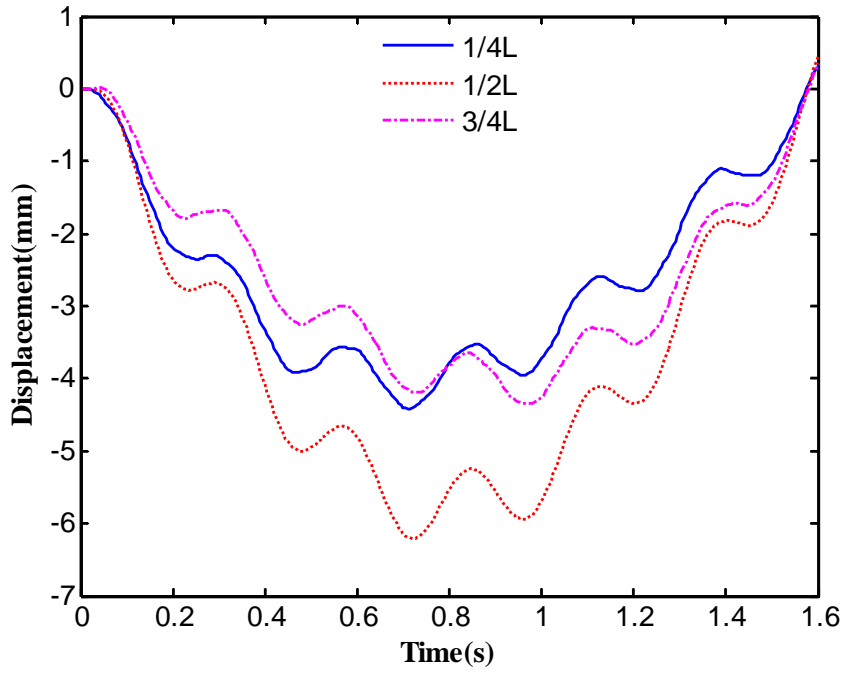
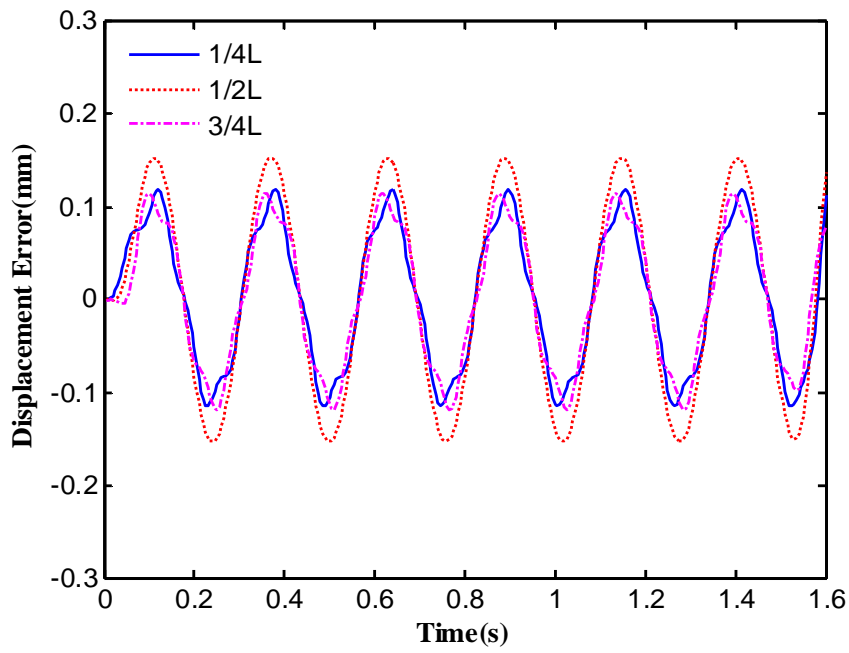
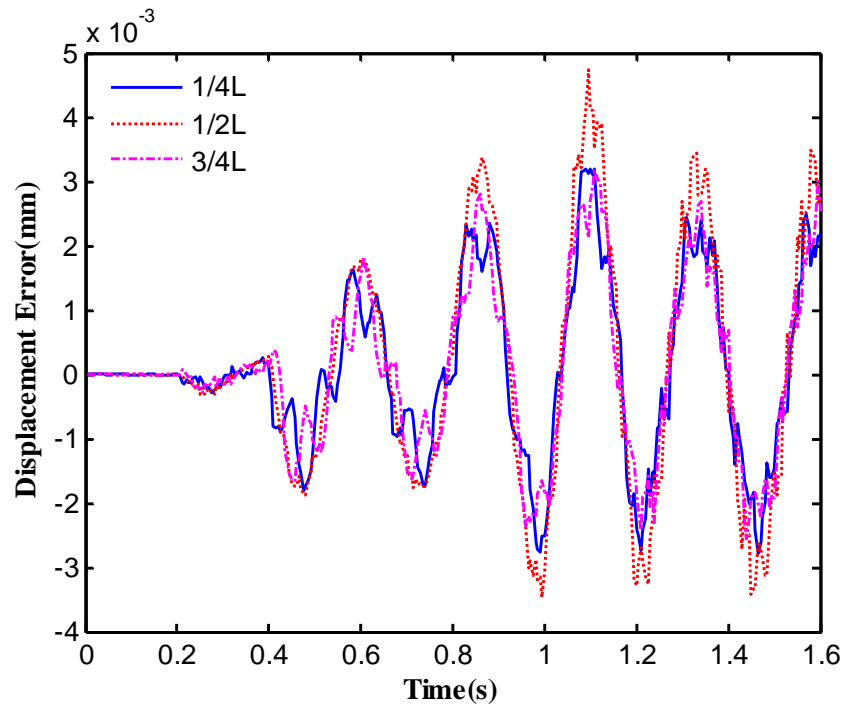


Figure 6.3. The accurate displacement time history



(a) TFEM (16elements)



(b) WFEM (16elements)

Figure 6.4. Displacement error calculated by different models

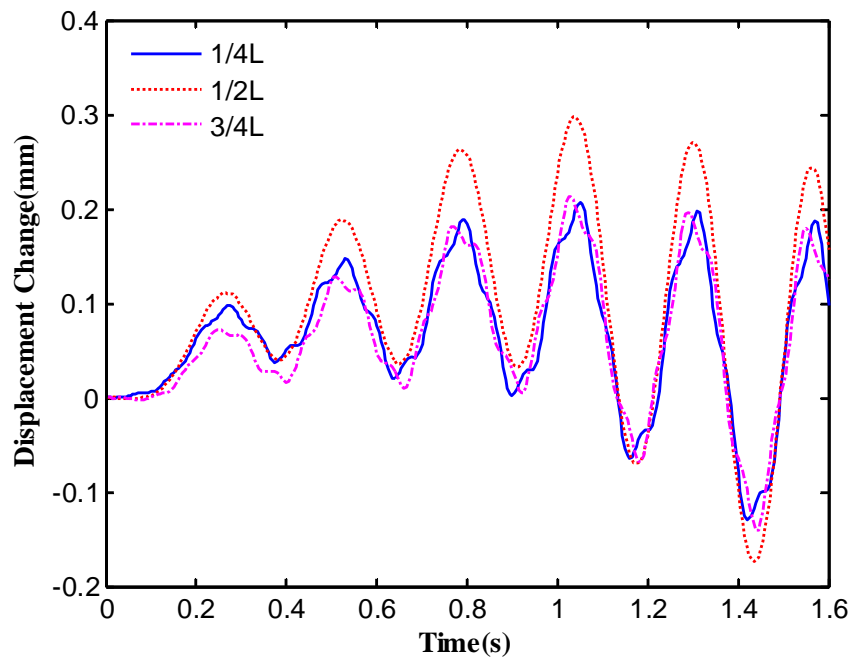


Figure 6.5. Damage-induced displacement change of the beam

6.2.3 Discussion

The example in Section 6.2.2 demonstrates the efficacy of the proposed WFEM-based adaptive-scale analysis strategy for a beam under moving load excitation. In the implementation of this strategy, two parameters should be determined: the length and scale of localized wavelet element refinement. Generally, a large refinement length (RL) improves accuracy and requires less frequent changes of the model in the moving process. However, it also corresponds to a large number of DOFs in FEM. RL, that is, the length of the segment in contact with the moving load, is equal to 1/8 of the total beam length in the numerical example. To examine the effect of different RLs, Figure 6.6 shows the computation errors in the displacement response at the mid-span location when $RL = 1/4$, $1/8$, and $1/16$ are used individually in WFEM. Although increasing RL can generally improve the accuracy of the dynamic analysis, such an improvement is insignificant in moving load problems. Similarly, lifting the wavelet elements to a scale higher than 1 results in very limited accuracy improvement and is regarded as unnecessary in this study. It verifies that the current selection of RL and scale in WFEM can provide sufficient computation accuracy.

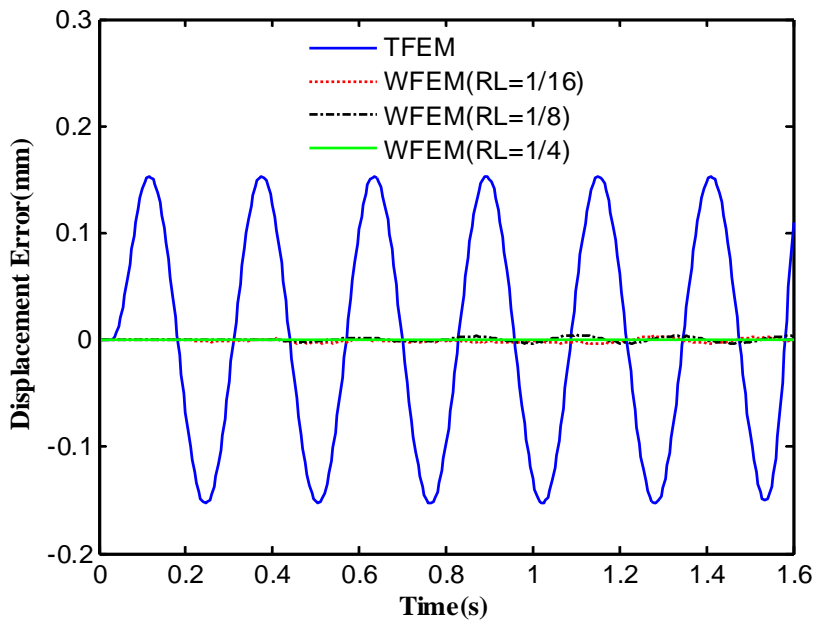


Figure 6.6. Effects of RL

6.3 Two-Phase Damage Detection Method

To achieve an optimal tradeoff between damage detection accuracy and efficiency, a two-phase (localization and then quantification) damage detection method is developed in this section for beam structures under a moving vehicle by combining the adaptive-scale moving-loading analysis strategy, DWT-based damage localization (Chapter 5), and progressive damage detection (Chapter 4). The corresponding flowchart is shown in Figure 6.7.

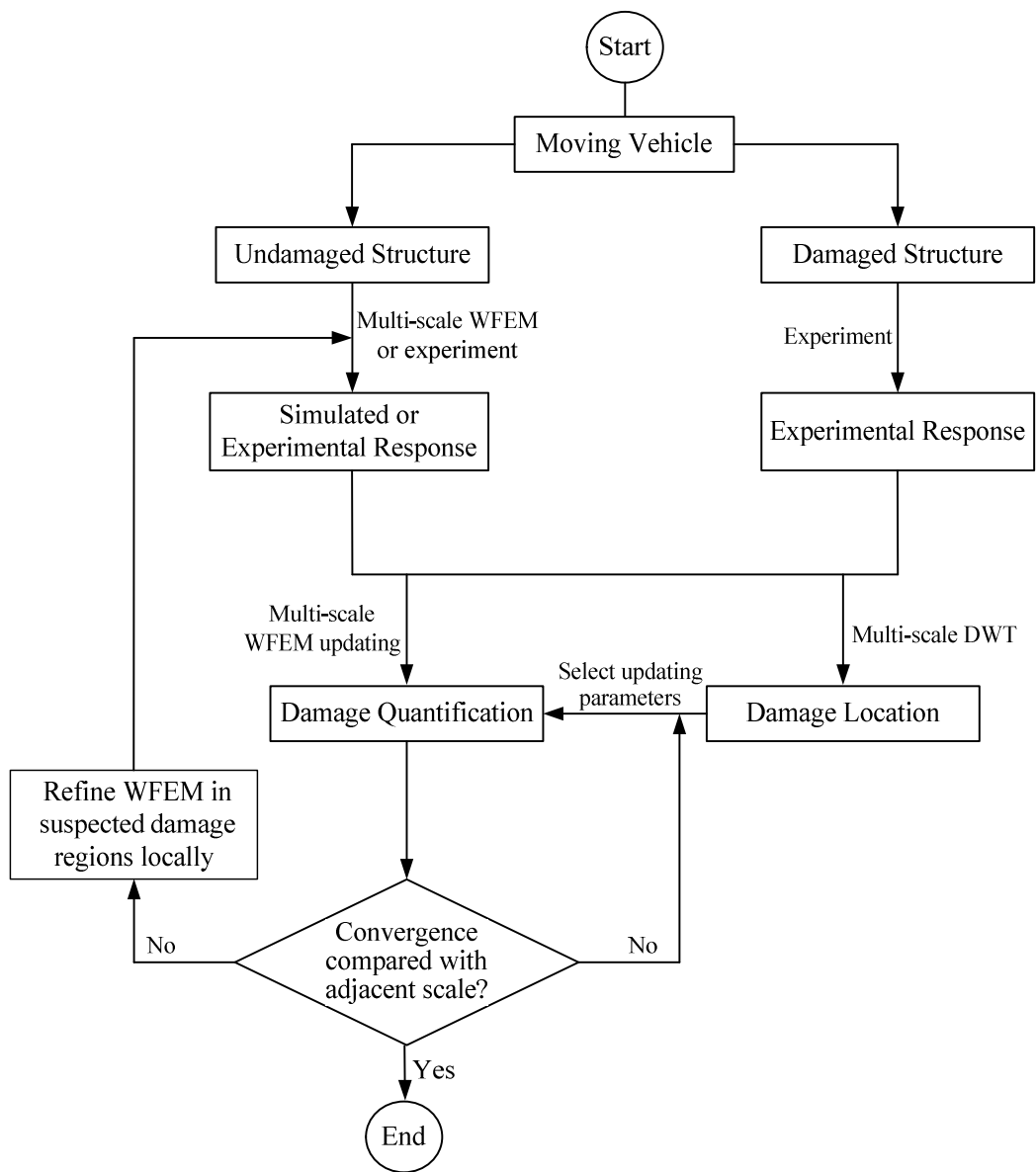


Figure 6.7. Diagram of multi-scale damage detection

The structural dynamic response in the undamaged state is obtained through simulations or field tests. Damages are located by separating the dynamic response change via DWT and quantified by progressive WFEM updating. DWT separates different dynamic response components effectively and reduces the noise effect. Multi-scale WFEM minimizes the number of DOFs in the model. Given that the updating parameters are only limited to the suspected damage regions with the initial damage localization in the first phase, the computation cost in the model updating process is considerably reduced. The details of damage localization and quantification are presented in Sections 6.3.1 and 6.3.2, respectively.

6.3.1 Damage Localization

Chapter 5 examines the effects of local stiffness loss on the two different components in the beam response induced by moving load. A simple and intuitive damage localization method is developed by decomposing the original dynamic response into a specific level through DWT. Although only the case of a single-moving force is studied, the analysis can also be applied to cases of multi-axle vehicles provided that the axle distance is relatively small compared with the bridge length.

6.3.2 Damage Quantification

To achieve an optimal tradeoff between damage detection accuracy and efficiency, the wavelet element scales change adaptively not only according to the moving load–beam contact positions but also to the suspected damage scenarios identified. Therefore, (1) high- and low-scale wavelet beam elements are used in the vehicle–beam contact regions and in other regions, respectively, and (2) once the suspected damage regions are identified, local refinement is subsequently conducted to estimate more accurate results.

The model updating technique combined with WFEM enables damage detection under moving load in a progressive manner. Although damage was represented by stiffness

loss without mass change in the previous chapters, damage in the following experiment is introduced by drilling holes on a beam and is associated with both stiffness and mass loss in a local segment. As shown in Section 6.4, this mass loss cannot be ignored. The damage index is represented by the relative reduction in local flexural rigidity as follows:

$$d_r = \frac{EI_r^u - EI_r^d}{EI_r^u} \quad (6.1)$$

where EI_r^u and EI_r^d are the segmental flexural rigidity before and after damage, respectively. This index is also utilized to approximate the mass loss in the same region; thus, it does not introduce new updating parameters. As a result, the damage leads to the modification of structural stiffness and mass matrices during updating.

The objective function of the damage detection algorithm is defined as

$$f_{obj} = \sum_n \left\{ \frac{[\mathbf{q}_n^{u,f}(t) - \mathbf{q}_n^{u,e}(t)]^2}{N_u} - \frac{[\mathbf{q}_n^{d,f}(t) - \mathbf{q}_n^{d,e}(t)]^2}{N_d} \right\}^2 \quad (6.2)$$

where superscripts f and e denote the FEM simulation and experimental results, respectively; superscripts u and d denote the dynamic response of the undamaged and damage states, respectively; N denotes the number of data points in response time history that depends on moving velocity; n denotes the displacement transducer number; and \mathbf{q} denotes the moving-frequency component extracted from the total dynamic displacement response induced by a moving vehicle. In the displacement response from each sensor, the data points close to both ends are excluded in the objective function to avoid the end effect of DWT. By including four series of displacement responses in the objective function, damage detection can tolerate a slight modeling error between the initial FEM and the physical structure in the undamaged state. The detailed damage quantification procedure is described as follows.

Step 1: Select updating parameters related to the suspected damage regions identified through the damage localization results using DWT in Phase 1.

Step 2: Detect the severity of the suspected damages by using a low-scale WFEM

model and the adaptive moving-load analysis strategy by minimizing the objective function.

Step 3: Lift the wavelet element scale in the identified damage regions but maintain the scale of other regions as in the last step. Select and update damage indexes in the reduced damage regions only. Consequently, the damage can be detected more accurately.

Step 4: Check the convergence of the results, and stop if the difference is smaller than a prescribed threshold. Otherwise, repeat Step 3.

6.4 Experimental Verification

6.4.1 Experiment Description

An experiment on a beam with a moving vehicle (Figure 6.8) is conducted to investigate the effectiveness and efficiency of the proposed two-phase damage detection method. The beam is made of a steel plate with uniform thickness. The beam is divided into three individual spans: a leading span for initial acceleration of the vehicle, a main span, and a trailing span for vehicle deceleration. The main span is well separated from the two side spans and can be regarded as an independent simply supported beam. The plane view, cross section, and dimensions of the steel beam are shown in Figure 6.8. The beam has a cross section of 150 mm \times 15.8 mm (width \times thickness), modulus of elasticity of $2.05 \text{ N/m}^2 \times 10^{11} \text{ N/m}^2$, and density of $7,780 \text{ kg/m}^3$. The vehicle has two axles (four wheels), and the distance between the two vehicle axles is 16.1 cm (Figure 6.9). The total weight of the vehicle is 10.53 Kg. An electric motor (Figure 6.10) is employed to pull the vehicle to move along the center line of the beam. With a variable resistor, the velocity of the vehicle is controlled via the voltage input to the motor.

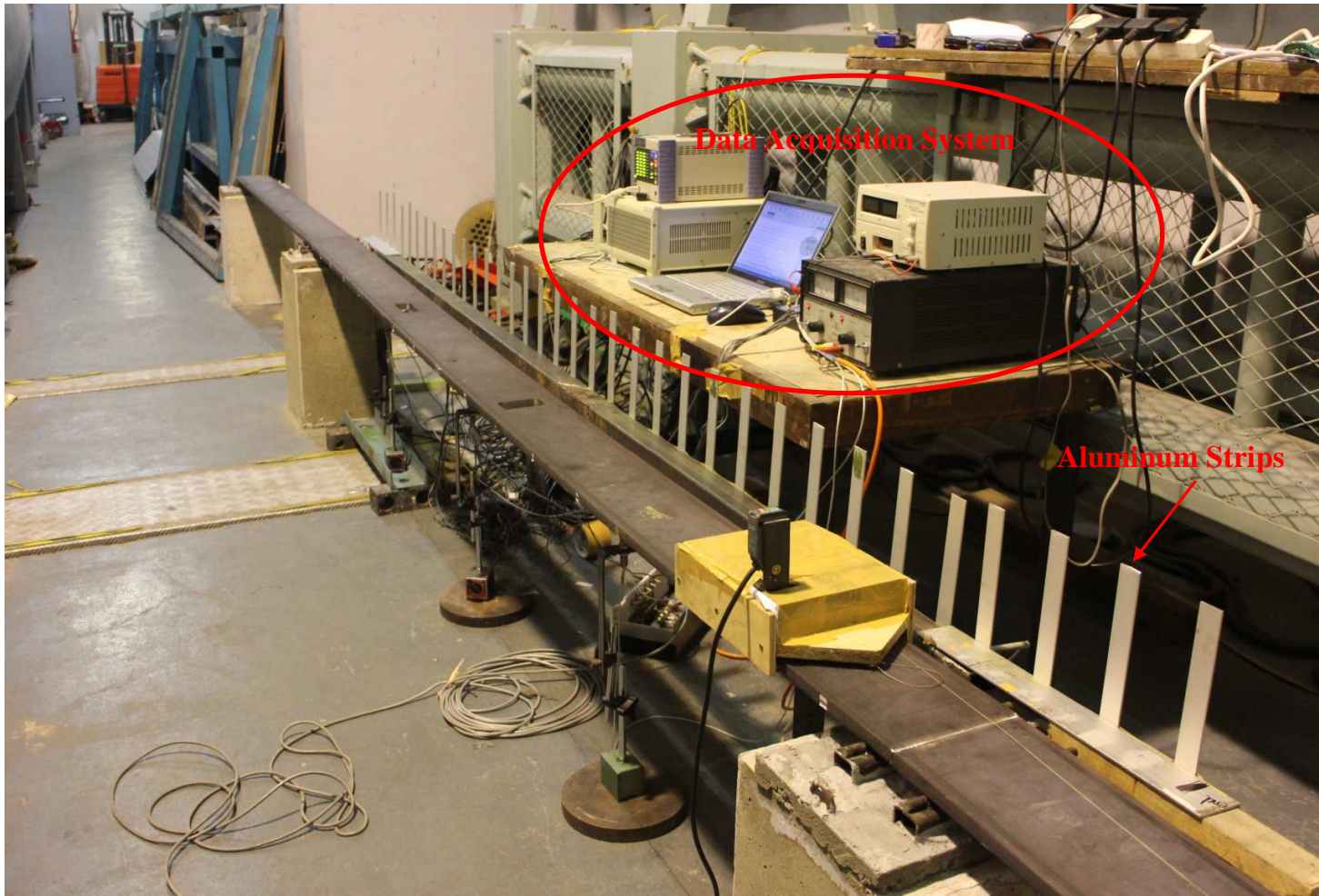
As shown in Figure 6.8b, three eddy current displacement sensors (Figure 6.11) are installed in three sections of the beam: 0.825 m from the left end, on the mid-span, and 0.825 m from the right end. These three sections are hereinafter referred to as $\frac{1}{4} L$, $\frac{1}{2} L$, and $\frac{3}{4} L$ for simplicity. As pointed out in previous studies (e.g., Nguyen and Tran 2010;

Hester and González 2012), the velocity of a moving vehicle affects the damage detection results. Given that velocity cannot be maintained perfectly constant in the experiment, 35 aluminum strips are placed in an array beside the beam to obtain more accurate location and velocity information. When the vehicle moves along the beam, the photoelectric sensor installed on the vehicle can detect the moment of passing each strip. The average velocity can be estimated based on the interval length and the consumed time in each interval. Subsequently, in the following damage quantification process, the same velocity record is used in the WFEM-based dynamic analysis.

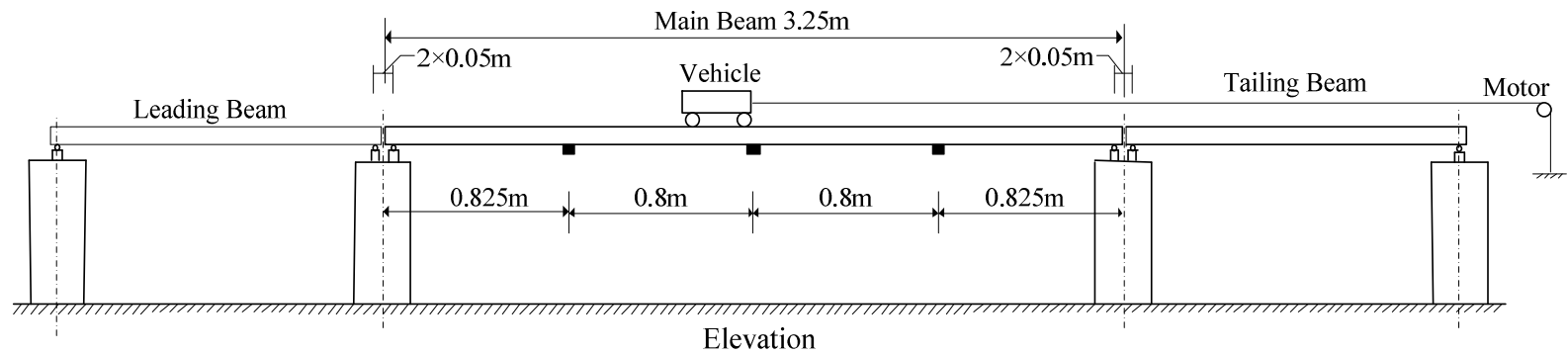
In this chapter, two damage cases are introduced through saw cuts at different locations, as shown in Table 6.1 and Figure 6.12. The dimensions of the damages are approximately 5 mm × 8 mm (length × width) for Damage I and approximately 10 mm × 4 mm (length × width) for Damage II. Given that the total width of the beam section is 150 mm, the damage severities corresponding to Damages I and II are approximately 53% and 27%, respectively. Case 1 involves Damage I only, and Case 2 involves both Damages I and II.

Table 6.1. Damage scenarios of the simply supported beam

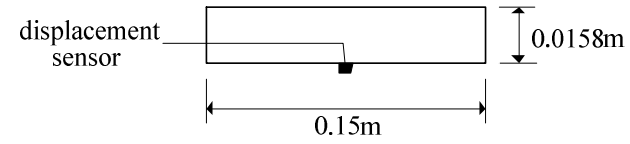
Scenario	Location	Severity (%)	Combination	
Case 1	Single damage	[1.925, 1.975]	53%	Damage I
Case 2	Double damage	[1.925, 1.975]	53%	Damage I
		[1.025, 1.125]	27%	Damage II



(a) Experimental arrangement



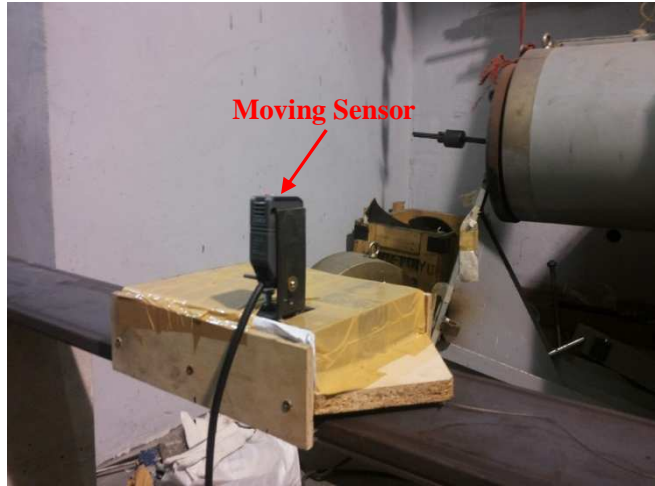
Elevation



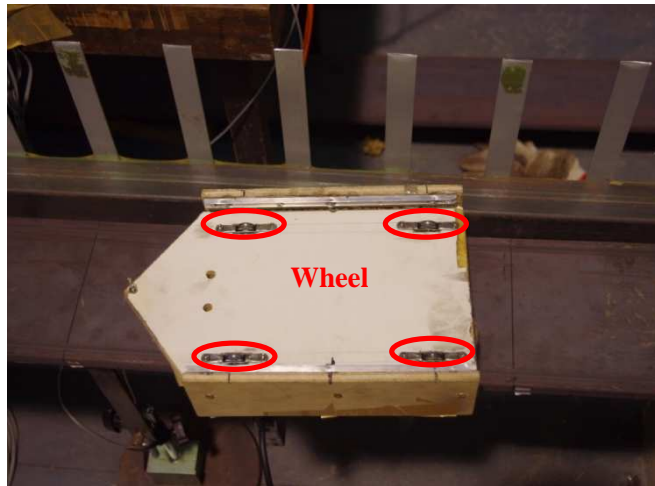
Cross Section of the Beam

(b) Configuration of the beam

Figure 6.8. Experimental arrangement and configuration of the beam



(a)

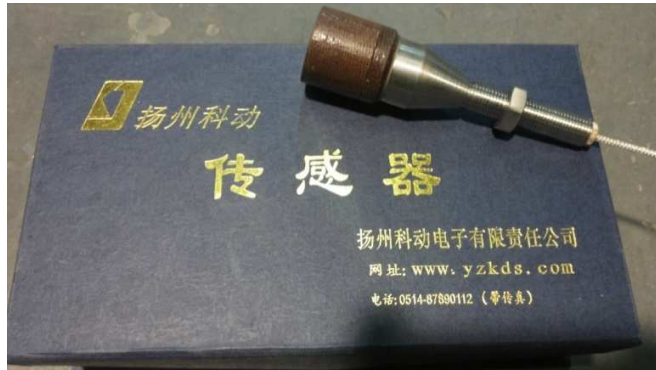


(b)

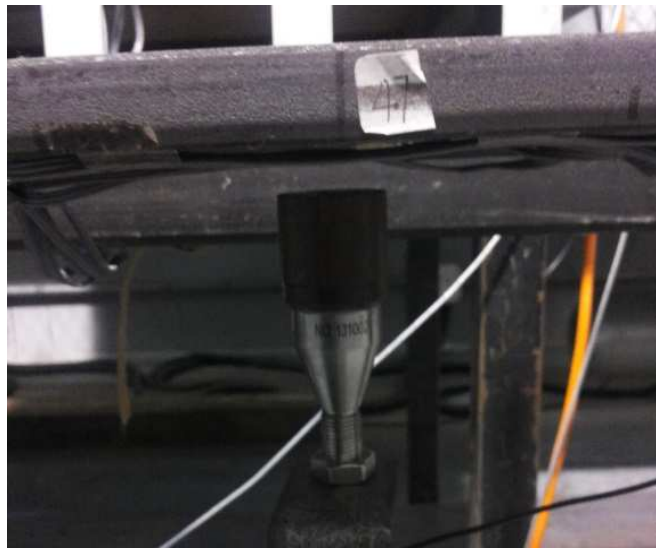
Figure 6.9. Moving vehicle



Figure 6.10. Electric motor

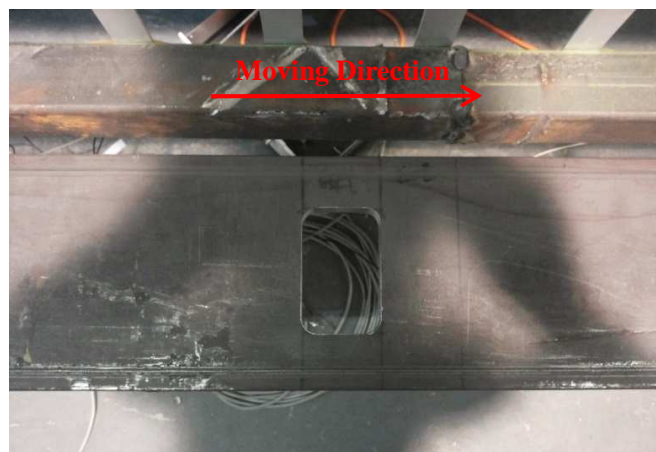


(a)

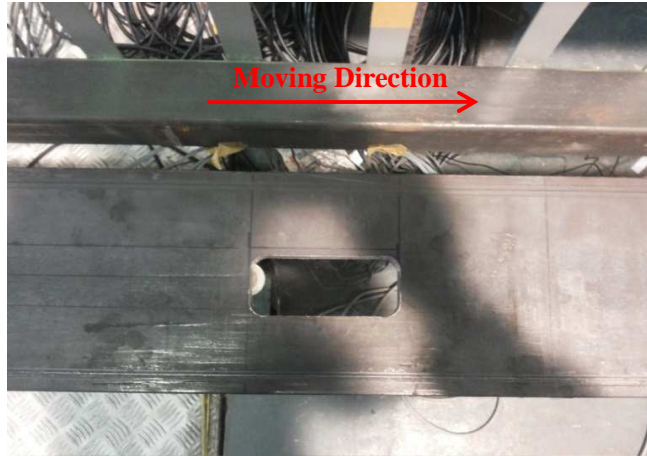


(b)

Figure 6.11. Displacement transducers



(a) Damage I



(b) Damage II

Figure 6.12. Beam damages

The moving load experiments on the beam without damage and with single or double damage are conducted under four moving velocities, namely, 0.6, 1.15, 1.65, and 2.1 m/s. These moving velocities are referred to in this chapter as Velocity-1, -2, -3 and -4. The velocity information is summarized in Table 6.2, where S_1 is the dimensionless moving velocity defined in Equation (5.5). To ensure the accuracy of the velocity information obtained by the moving photoelectric sensor on the vehicle, experimental data are recorded with a high sampling frequency of 2,000 Hz. However, the displacement time histories are resampled to 200 Hz because high sampling frequency is unnecessary for the displacement response. Figure 6.13 shows a typical record of dynamic displacement responses at Velocity-1. Figure 6.14 shows the corresponding velocities estimated in the 34 intervals and the average velocity across the entire beam. Compared with the average velocity, the deviations in the interval velocities are less than $\pm 15\%$, which implies that the moving velocity is relatively smooth and steady.

In Chapter 5, the vehicle was represented by moving force and moving mass–spring–dashpot single-DOF systems individually. The former is much simpler than the latter because only the load vector in the finite element formulation needs to be changed during each time step in the time-integration procedure; the system mass and stiffness matrices can remain the same. However, only the weight of the vehicle is considered, and the dynamics of the vehicle is actually ignored in the moving force representation. The

single-DOF model that consists of mass, spring, and dashpot can better represent the dynamics of the vehicle provided that its parameters can be accurately determined. Section 5.3.3 examined the effects of different moving vehicle models. The results indicated that the moving-frequency component extracted using DWT is insensitive to vehicle dynamics, and the corresponding damage-induced changes are nearly the same except for the end parts. For better computation efficiency, a simpler moving force model, in which two moving forces are used to represent two axles, is adopted in the following study.

Table 6.2. Velocity parameters

Item	Velocity (m/s)	S_1
Velocity-1	0.60	0.0258
Velocity-2	1.15	0.0494
Velocity-3	1.65	0.0709
Velocity-4	2.10	0.0902

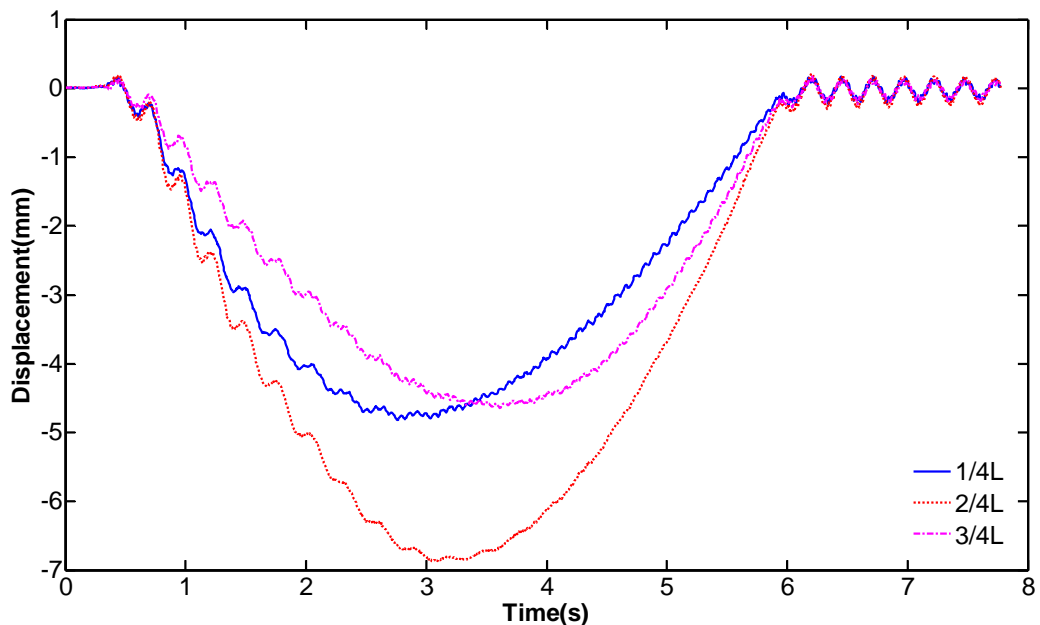


Figure 6.13. Typical displacement time history of the undamaged beam

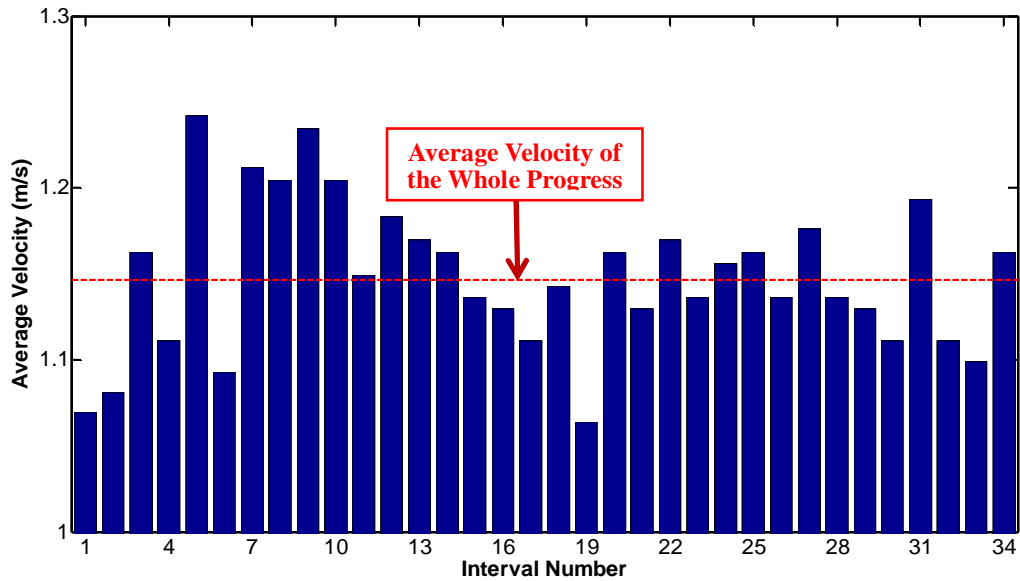


Figure 6.14. Typical velocity information of the moving vehicle

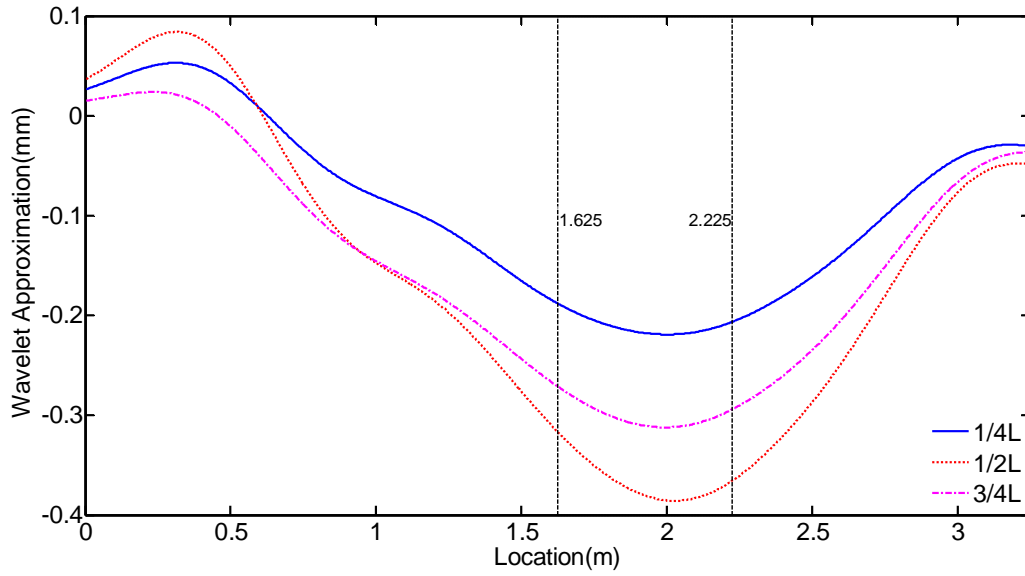
6.4.2 Damage Detection

6.4.2.1 Single Damage

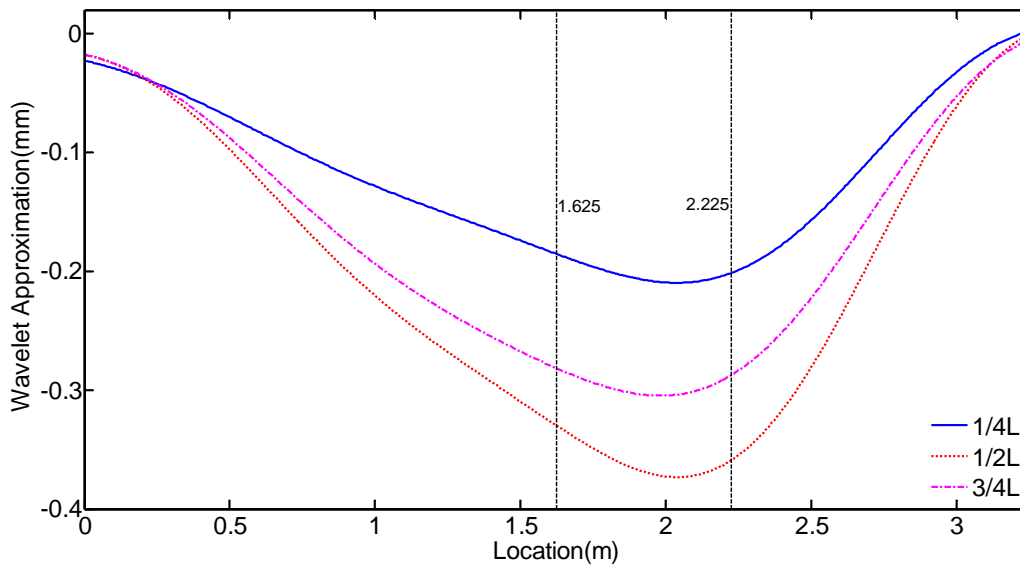
As shown in Table 6.1, Case 1 involves a single damage in the interval of [1.925, 1.975] with 53% severity (Damage I). First, the dynamic displacement response is decomposed through the method described in Section 6.3.1. The results are shown in Figure 6.15. The “location” in the figure refers to the coordinate of the mid-point of the two axles of the vehicle model. In the first phase, the damage is approximated to be located around 2.0 m from the left end in Velocity-1, -2, and -3 cases. The results of Velocity-4 ($S_1 = 0.09$) are not shown here because they can hardly indicate the damage location. This observation is consistent with the observation in Section 5.3.3 that damage localization becomes more difficult when S_1 is larger than 0.075. All the three displacement sensors installed at different locations provide similar results regarding the possible damage location. Thus, one displacement sensor is theoretically sufficient to determine the damage location. However, in practical applications, more than one sensor can provide some redundancy and avoid misjudgment through cross validation when one of the sensors does not work properly.

In the second phase, multi-scale WFEM updating is employed to quantify the damage severity. Figure 6.16 shows the initial finite element mesh, including 20 elements. The elemental length is 0.05 m for elements 1, 2, 19, and 20; 0.075 m for elements 3 and 18; and 0.1 m for the others. Different elemental lengths are utilized to make the nodes consistent with the locations of supports and sensors. The scale of the wavelet elements employed in wheel–beam contact elements and in the other elements are 1 and 0, respectively. The wavelet element scales change continuously when the wheel–beam contact positions move over time. The scales of the elements at the two ends (element 1, 2, 3, 18, 19, and 20) remain unchanged during the entire process because their elemental lengths are relatively short. The total number of DOFs is 46 (when the two axles are located in different elements) or 44 (when the two axles are located in the same element). Figure 6.17 shows the strategy of the adaptive wavelet element scale during damage quantification. With the suspected damage interval [1.625, 2.225] identified in Phase 1, the damage indices of elements 11, 12, and 13, instead of all the elements, are selected as updating parameters in the first stage of Phase 2. The three damage indices are updated by minimizing the objective function defined in Equation (6.2), and the updating results are shown in Figure 6.18. The estimated velocity using the information from the photoelectric sensor on the vehicle is utilized in the WFEM simulations. The first and last 50 data points in the DWT-decomposed displacement time history are excluded in the objective function. The optimization value of [1.825, 2.025] is much larger than that of intervals [1.625, 1.825] and [2.025, 2.225]. Therefore, interval [1.825, 2.025] is identified as a probable damage interval. In Stage 2, the wavelet element scale in this interval is lifted from 0 to 1, but the other regions and adaptive-scale changing strategy remain the same as in Stage 1, as shown in Figure 6.17. The damage indices of elements 11 and 13 are not considered updating parameters because they are relatively small in the first quantification stage. In the following stages, the flexural rigidities are selected with a similar strategy. With the scale lifting in element 12, two updating parameters corresponding to intervals [1.825, 1.925] and [1.925, 2.025] are selected; subsequently, the latter is detected as the more likely damage interval. Repeating the refinement and updating process allows for more accurate estimations of the damage. Stages 3 and 4 show almost the same results, implying that the estimation converges and no further refinement is necessary. The quantification results of

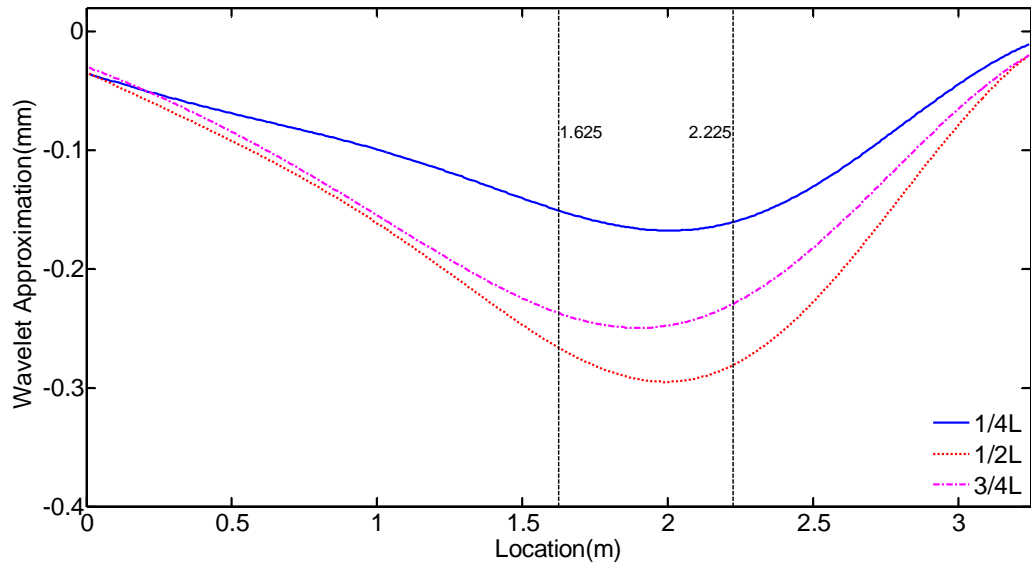
the damage severity in each stage are shown in Figure 6.18.



(a) Velocity-1



(b) Velocity-2



(c) Velocity-3

Figure 6.15. Damage localization results for Case 1

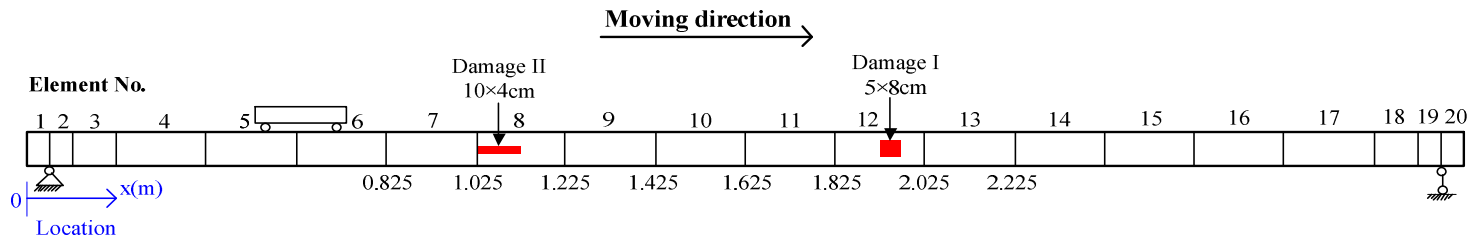


Figure 6.16. Finite element mesh of the beam

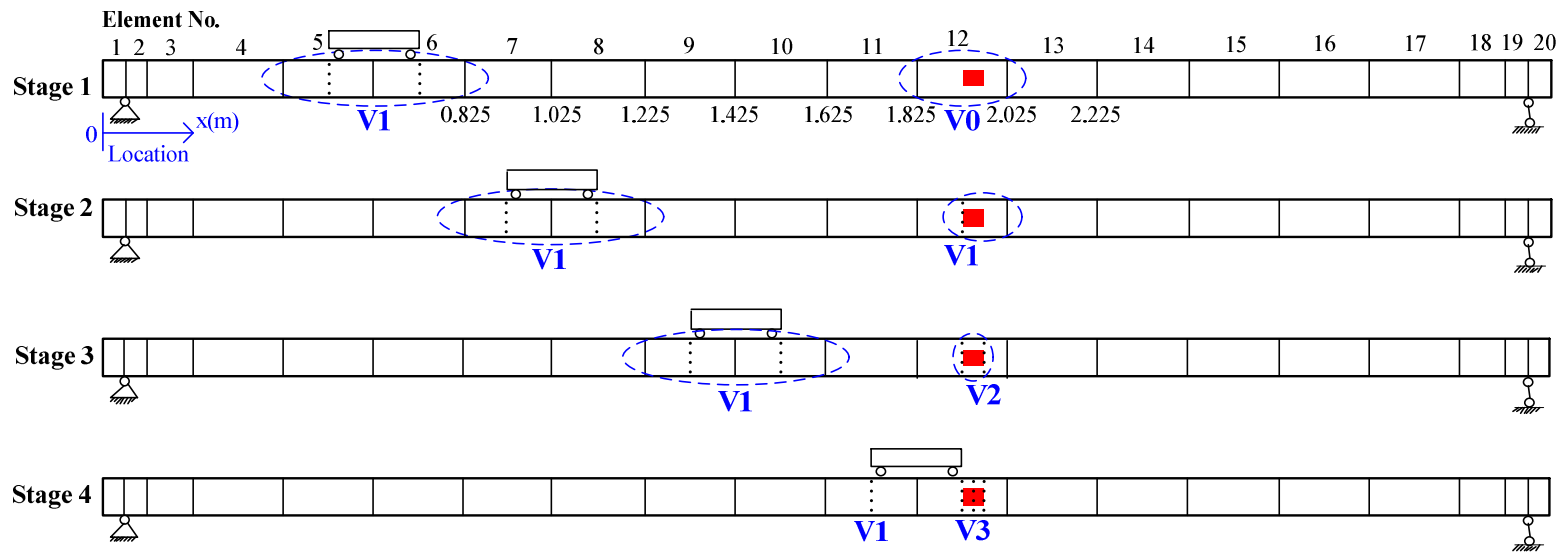
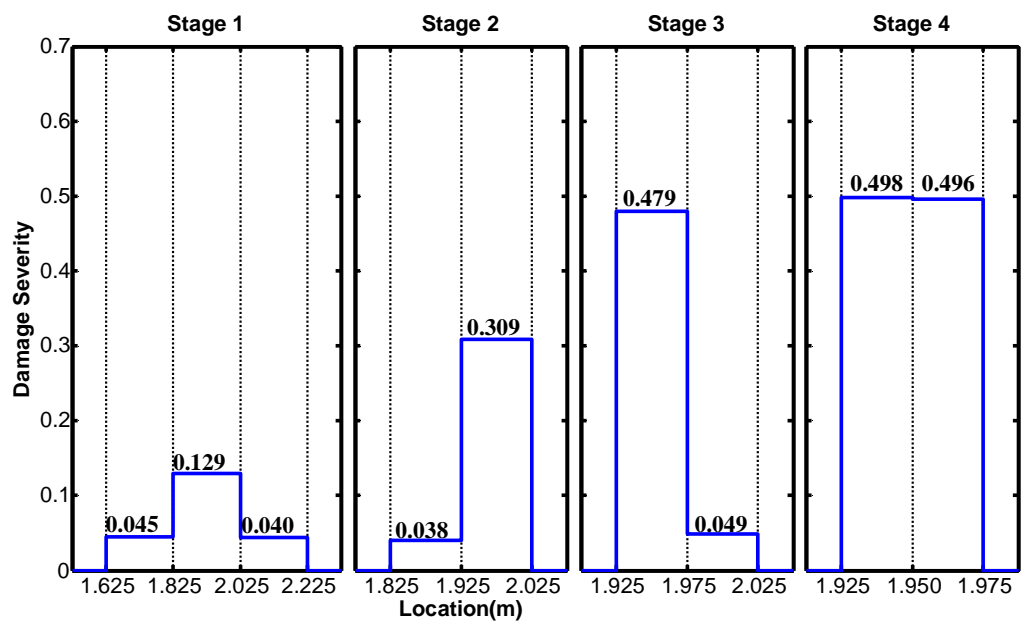
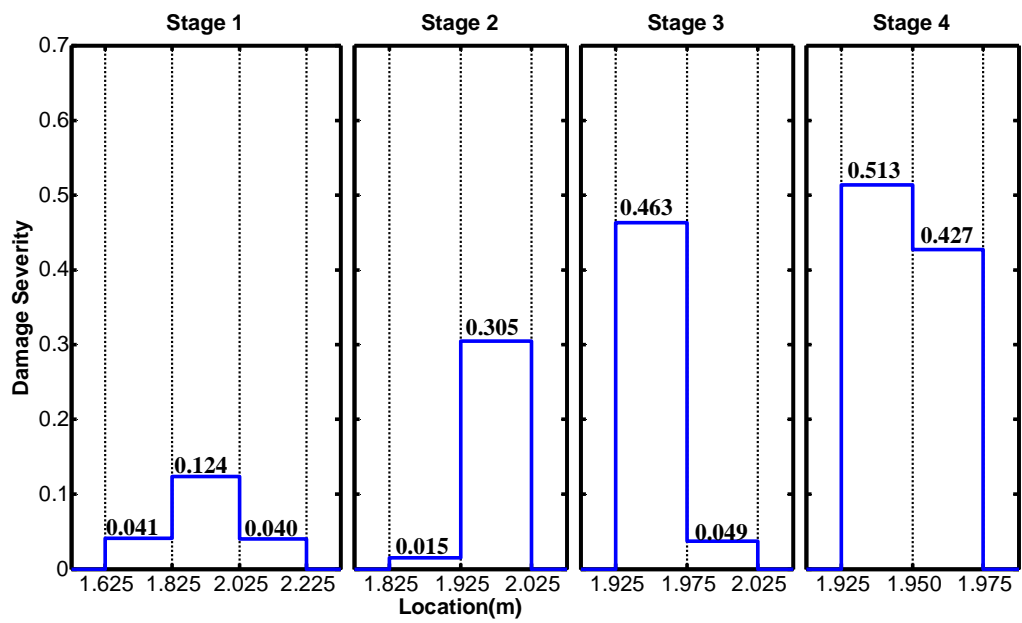


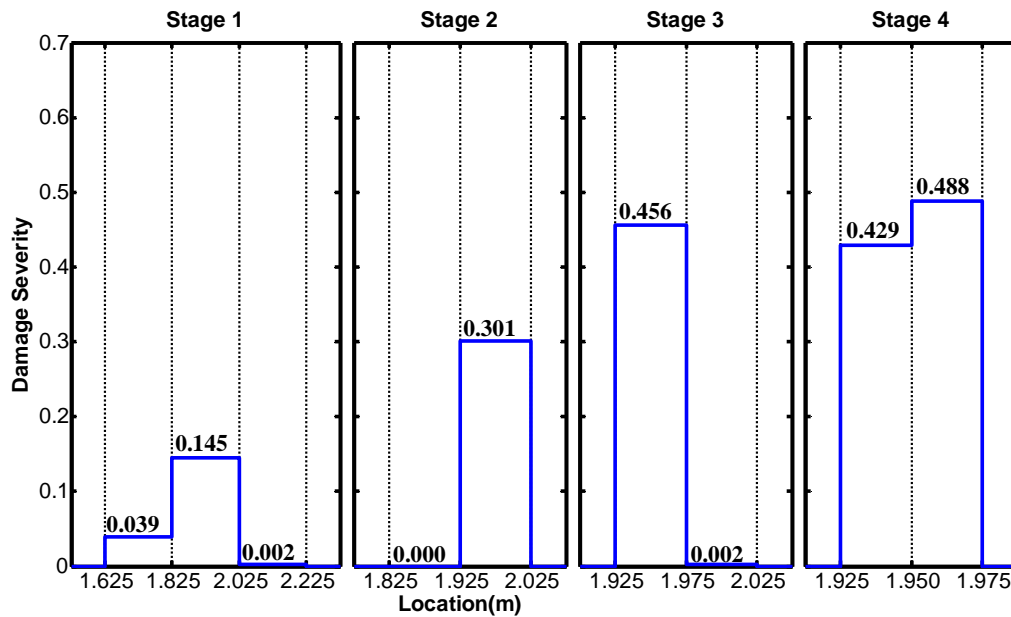
Figure 6.17. Adaptive wavelet element scale strategy during the quantification process in Case 1



(a) Velocity-1



(b) Velocity-2



(c) Velocity-3

Figure 6.18. Damage quantification results for Case 1

The relatively inaccurate estimation of damage severity in a low-scale model is expected given the inaccurate assumption of the damage size. However, the quantification accuracy is effectively improved with the progressive refinement of the model, and quantification finally converges toward the actual value in Stages 3 and 4. The procedure and adaptive wavelet finite element strategy employed in Velocity-2 and Velocity-3 are similar to those adopted in Velocity-1; the corresponding damage location and quantification results are shown in Figure 6.17 and Figure 6.18, respectively. Although the results for Velocity-3 are not as favorable as those for Velocity-1 and Velocity-2, the damage localization results for Velocity-3 are still acceptable. As shown in Figure 6.17, the DWT-decomposed displacement responses exhibit slight shifts from the actual damage location. Consequently, the damage quantification results in Stage 4 for Velocity-2 and Velocity-3 slightly deviate from the actual damage severity (53%).

Considering that actual damage locations are always unpredictable, TFEM updating, if employed in this case, should be uniformly meshed without the adaptive-scale analysis strategy. Consequently, 62 (the 4th to 17th elements should be divided into 4 elements individually) beam elements with 126 DOFs are required to accurately capture the damage

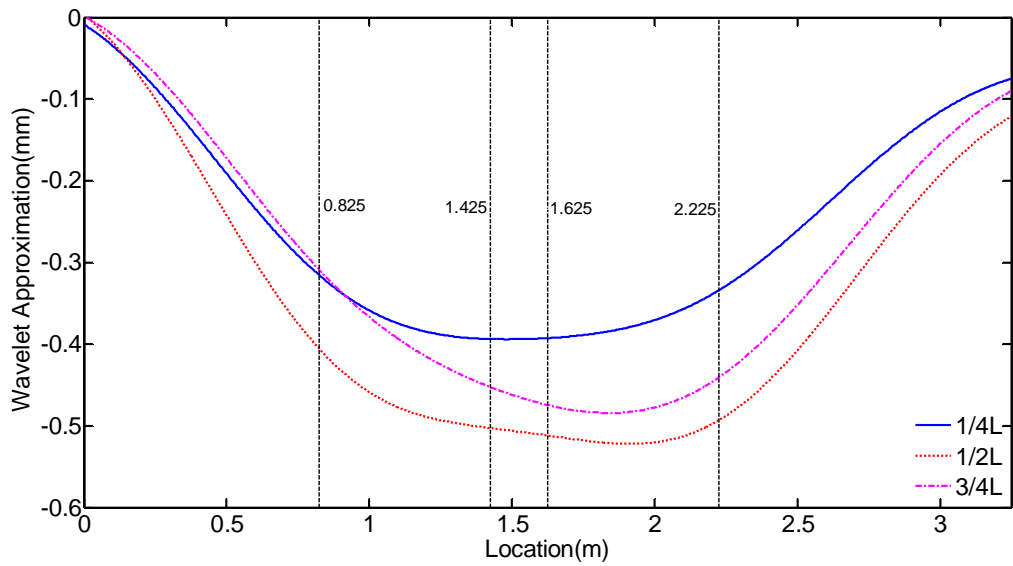
in Case 1, where the single damage region consists of about 1/4 of one wavelet element. Moreover, without the preliminary damage localization in the first phase, a large element number may lead to too many updating parameters, which make optimization time consuming and challenging, if not impossible. However, with the proposed adaptive-scale strategy, only 52 DOFs in Stage 4 are used in WFEM to achieve the same accuracy level of damage detection. Furthermore, specifying the required model scale in advance is not required because the model scale is adaptively refined in a progressive manner.

6.4.2.2 Double Damages

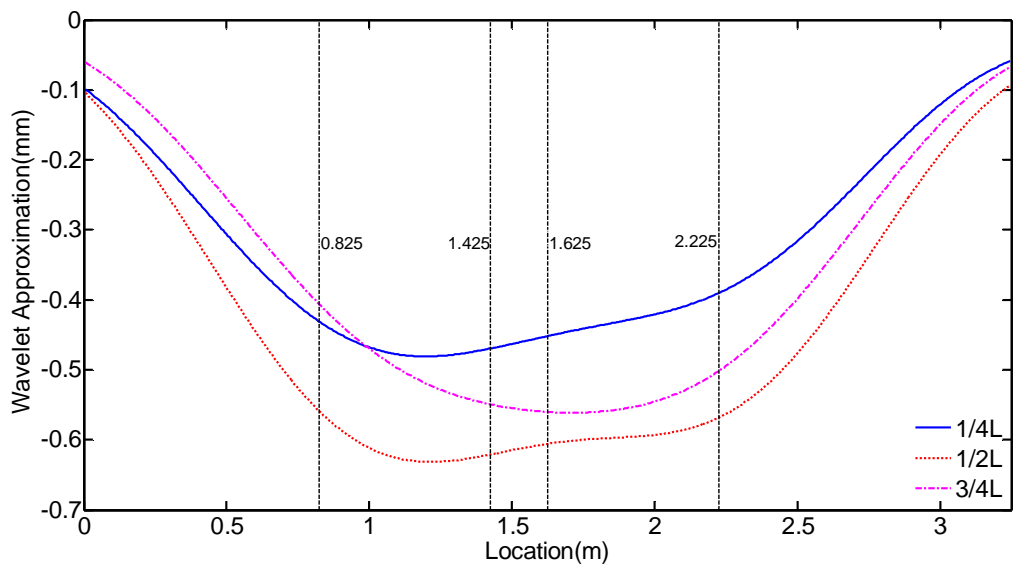
As shown in Table 6.1, Case 2 involves a beam subjected to double damages: one in the interval of [1.925, 1.975] with 53% severity (Damage I) and the other in the interval of [1.025, 1.125] with 27% severity (Damage II). The DWT-decomposed changes in the dynamic displacement response are shown in Figure 6.19. The damages are initially located around 1.0 and 2.0 m from the left support in Velocity-1 and -2, respectively. The results for Velocity-3 and -4 are not shown here because the damage locations can be hardly visualized, which is also consistent with the observation in Section 5.3.3 that double damages cannot be localized when $S_1 > 0.05$. The following damage quantification process is similar to that in Case 1. The strategy of adaptive wavelet element scale during the damage quantification process is shown in Figure 6.20. In Stage 1 of the quantification phase, the damage indexes of elements 7 to 9 and 11 to 13 (corresponding to the suspected damage regions [0.825, 1.425] and [1.625, 2.225]) are selected as updating parameters. Following the same process, the locations and severities of the damage can be identified with progressively improved accuracy, as shown in Figure 6.21. Given that the left-hand damage consists of 1/2 of an element, a good estimation is obtained in Stage 2. No further improvement can be achieved in Stage 3, so no further refinement is conducted in this region in Stage 4. By contrast, the right-hand damage is 1/4 of an element's length, and the relevant region is gradually refined until Stage 4. The wavelet scale of the left-hand damage remains the same as in Stage 3, and the corresponding damage severities in the two sub-intervals identified in Stage 3 are used without further updating in Stage 4. The quantification results of the right damage are approximately 0.55 and 0.6 in Velocity-1 and -2, respectively, both of which are slightly higher than the real value. Compared with Case

1, the quantification results slightly worsened.

Case 2 demonstrates that the model scale can be adaptively adjusted according to the actual damage scenarios. This adaptability of the proposed method can help achieve accurate results with minimal DOFs, updating parameters, and computation cost.

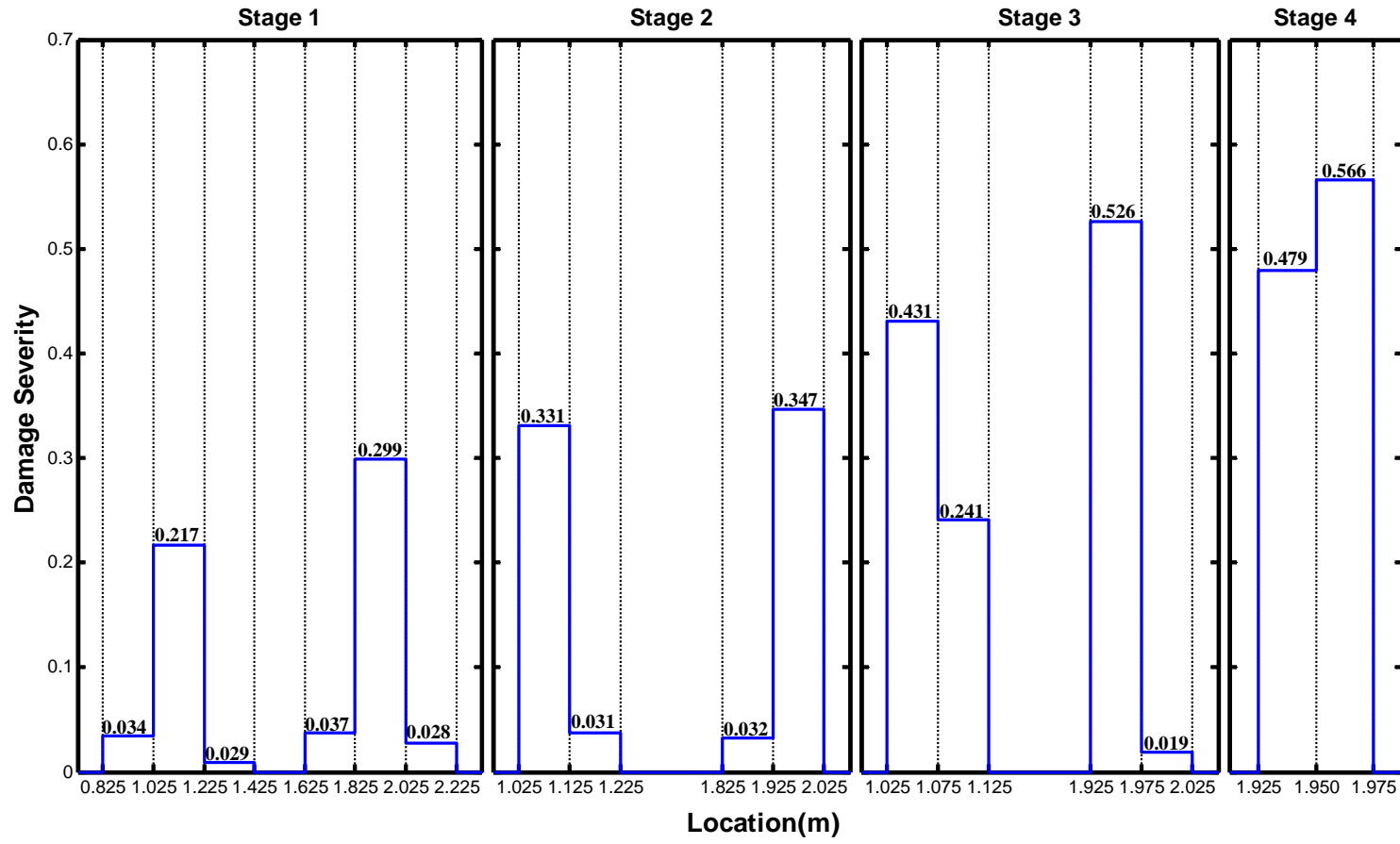


(a) Velocity-1

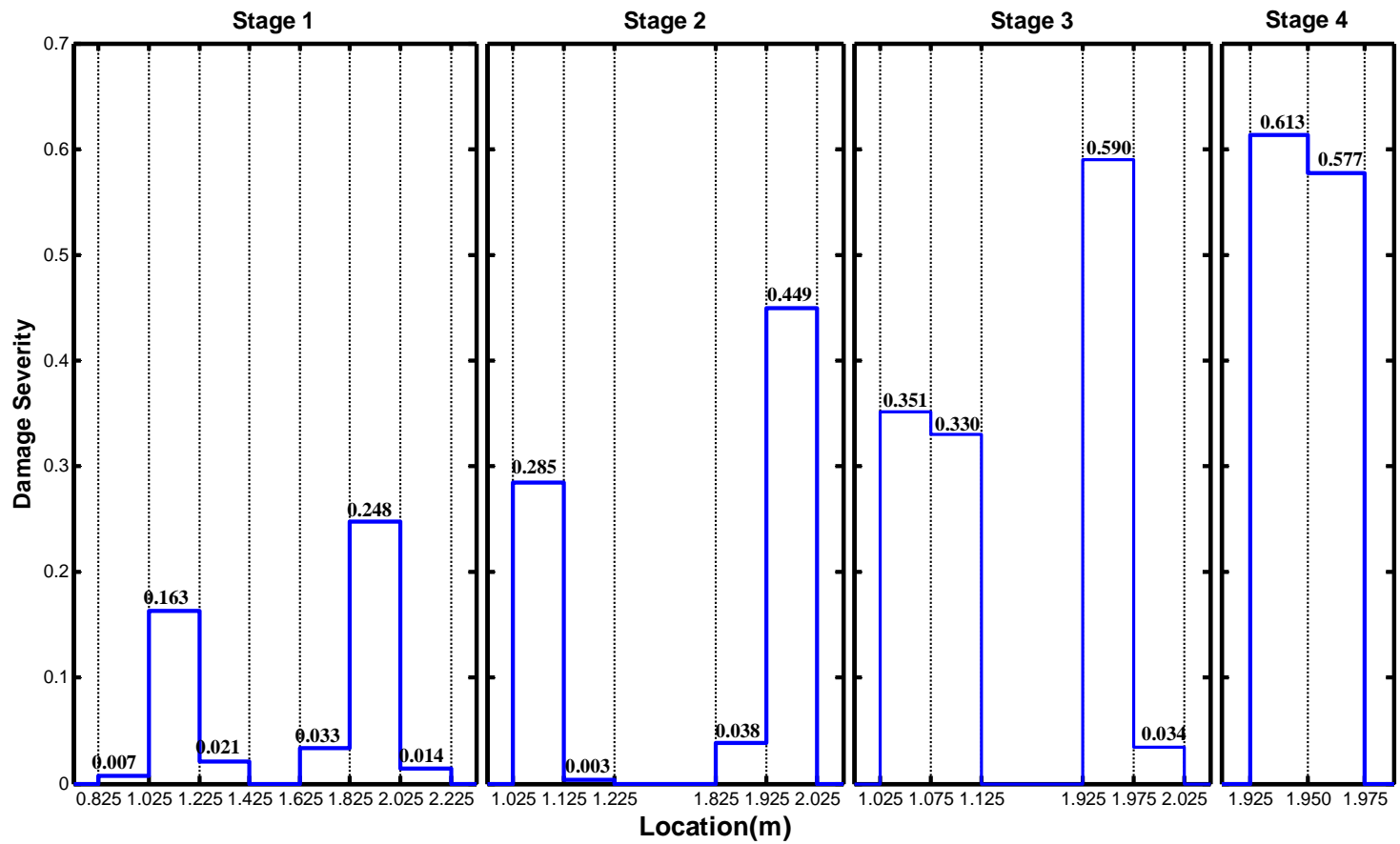


(b) Velocity-2

Figure 6.19. Damage localization results for Case 2



(a) Velocity-1



(b) Velocity-2

Figure 6. 21. Damage quantification results for Case 2

6.4.3 Discussion

The damage localization and quantification results of the experiment generally agree well with the actual damage scenarios. This good agreement can be attributed to the four main factors: (1) Two-phase damage detection strategy. Given the initial damage localization in the first phase, only a small number of updating parameters in the suspected regions are selected in the second phase, which improves both optimization efficiency and accuracy. If the damage indexes of all the elements are selected as updating parameters, the damage detection performance would degrade. (2) Accurate velocity information. With the on-vehicle moving photoelectric sensor, the average velocities in the intervals can be calculated and employed in the WFEM simulation. (3) Use of the moving-frequency component. The component that is sensitive to the uncertainties in damping, noise, vehicle model, and velocity is removed from the total dynamic displacement response via DWT decomposition. (4) Relatively large damage extent. In the experiment, the severities are 27% and 53% for Damages I and II, respectively, and the damage length is 0.1 and 0.05 m for Damages I and II, respectively.

The FEMs of both the beam and vehicle affect the accuracy of dynamic analysis of the moving vehicle-induced response and the corresponding damage detection. Given the lack of vehicle parameters in common situations, identifying the vehicle-beam interaction force has been regarded as an alternative in previous studies. However, the error in the identified interaction force may considerably limit the accuracy of damage detection. Road roughness is another factor that cannot be either ignored or accurately modelled as far as the total dynamic response of beam structures subjected to a moving load is concerned. Fortunately, the low-frequency component separated from the total displacement through DWT decomposition is insensitive to the aforementioned uncertain factors, which considerably improves the applicability of the proposed damage detection method for moving load excited beam structures. In actual implementations of the proposed methodology, a slow vehicle moving velocity is

always favorable because the damage detection performance of the proposed method degrades with increase in moving velocity, particularly in the presence of multiple damage locations.

6.5 Summary

To balance the modeling fidelity and computation amount in the dynamic analysis of beam structures under moving load, a WFEM-based adaptive-scale moving-load analysis strategy is proposed in this chapter. In the strategy, the scales of wavelet elements change dynamically according to the moving load–structure contact point. The simulated simply supported beam reveals that the strategy can effectively minimize the number of DOFs in dynamic analysis and enhance computation efficiency and accuracy compared with TFEM with a fixed uniform mesh.

A two-phase damage detection approach that consists of localization and quantification phases is subsequently proposed. The approach combines DWT-based damage localization, progressive damage detection, and adaptive-scale moving-load analysis. In the first phase, DWT is employed to decompose the change in the moving-load frequency component from the change in the total dynamic displacement response and localize the possible damage regions. In the second phase, WFEM is updated with the updating parameters limited to the suspected damage regions only to estimate damage severity in a progressive manner. The elemental scales of WFEM change dynamically not only according to the moving load-beam contact points but also to the progressively identified damage results. This two-phase method can achieve efficient consistency among FEM resolution, damage scenarios, and load conditions as well as an optimal tradeoff between the accuracy and efficiency of damage detection.

A laboratory experiment is conducted at different moving velocities to investigate the feasibility and efficiency of the proposed two-phase damage detection method. Both single and double damages can be localized and quantified with satisfactory accuracy when the moving vehicle velocity is low. A high moving vehicle velocity degrades the

accuracy of the damage localization method, especially in cases with multiple damages. Compared with traditional moving load-based damage detection methods in literature, the approach proposed in this chapter is more practical because of its insensitivity to damping, vehicle model, and road roughness. The proposed approach exhibits a great potential for future damage detection in actual beam structures.

Chapter 7 Conclusions and Recommendations

7.1 Conclusions

Damage localization and quantification of civil infrastructures using damage-induced changes in dynamic characteristics or responses have been receiving worldwide interest in the past two decades. This dissertation focused on the development of a multi-scale structural damage detection strategy for beam and plate structures through the use of WFEM. This novel strategy achieves desirable consistency among structural modeling, damage scenarios, and external load conditions and demonstrates high efficiency in both frequency- and time-domain damage detection examples with respect to the number of DOFs in structural models and number of sensors in vibration tests. The main contributions and conclusions of this thesis are summarized as follows.

- (1) The basic concept of multi-scale wavelet finite element was introduced, with emphasis on cubic Hermite wavelet elements with high computational performance, superior localization character, and favorable compatibility with TFEM. Multi-scale dynamic formulations and corresponding lifting schemes were derived for wavelet beam and plate structures by using cubic Hermite multi-wavelets. In particular, multi-scale dynamic equations of beam structures modeled by WFEM were formulated under moving load excitation. These dynamic formulations formed the theoretical basis of the multi-scale dynamic analysis and damage detection methods based on WFEM. The advantages of WFEM over TFEM were likewise discussed.
- (2) Progressive damage detection methods based on multi-scale WFEM was proposed in the frequency-domain to detect sub-element damage in beam and thin plate structures. WFEM, which was used together with MSE or model updating technique in this study, allows one to adaptively change the modeling scale according to actual

needs. For instance, a coarse WFEM was used to identify the possible damage region first, and then gradually refined WFEMs with local refinement (i.e., scale lifting) were used to estimate a more accurate damage location and severity. This progressive strategy ensures that structural models remain compatible with actual identified damage scenarios during the detection process. Thus, WFEM is computationally efficient because of the reduced number of DOFs in the model and operationally convenient because of the reduced number of sensors in the vibration test.

- (3) When used with MSE, the WFEM-based damage detection method requires more sensors to be installed in the damaged regions in the subsequent stages once the most likely damage regions are identified in the initial stage. Given that only mode shapes are considered, the method is sensitive to measurement noise. However, this method is time efficient because it is based on analytic derivation.

Numerical examples of simply supported and continuous beams and a simply supported thin plate were provided and analyzed under different damage scenarios. The results demonstrated that the multi-scale strategy can progressively and accurately locate and quantify structural damages. The impact of measurement noise on damage detection was assessed via Monte Carlo simulations. Detection accuracy with a high-scale model is sensitive to noise. The detection accuracy of plate structures is more sensitive to measurement noise than that of beam structures.

- (4) When used with model updating technique, the WFEM damage detection method considers an objective function that combines frequencies and MAC. The experimental modal information remains the same during the detection process, and no sensor movement or addition is required. However, this method is time consuming because the optimization process involves iterations.

Numerical examples (including that of a simply supported beam and plate) and experimental examples (including that of a single-bay single-story frame and a thin

plate fixed-supported on two adjacent sides) under different damage scenarios were investigated to examine the effectiveness of the proposed method. The results demonstrated that the WFEM updating method can identify structural damage with satisfactory accuracy and with reduced numbers of DOFs in the model and updating parameters in the optimization compared with TFEM. Although misjudgments may occur in the initial stages with low-scale models, further WFEM refinement in the subsequent stages would lead to high accuracy and successfully remove the initial false alarms.

- (5) The effects of local damage on the dynamic response of a simply supported beam subjected to moving load were investigated. A computation algorithm to obtain the dynamic response of a simply supported damaged beam was developed through modal perturbation and superposition methods. This algorithm allows for the accurate separation of the dynamic response of a damaged beam under moving load into two components, namely, moving- and natural-frequency components. In the time-domain, the damage-induced change in the former component had a relatively low frequency and was relatively insensitive to the variations in damping ratios, initial conditions, vehicular dynamics, and road surface roughness. By contrast, the change in the natural-frequency component had a relatively high frequency and the time history of this component was very sensitive to the abovementioned variations. Therefore, the change in the moving-frequency component is a preferred indicator of damage location.
- (6) Through DWT decomposition, a simple and effective damage localization method was developed for beam structures subjected to moving load. As a frequency separating and denoising tool, multi-scale DWT was conducted to extract the moving-frequency component from the total displacement response induced by moving load. Subsequently, the likely damage location can be efficiently identified through measurement by a single displacement sensor.

Numerical examples with different moving load velocities, noise levels, and numbers of damage locations were analyzed to verify the efficacy and robustness of the proposed damage localization method. In general, single and double damages were located with satisfactory accuracy. However, detecting multiple damage locations was difficult. The high moving velocity of vehicle also reduced the accuracy of the damage localization method, especially in the cases with multiple damages.

- (7) An adaptive-scale analysis strategy that employs WFEM, in which the scales of wavelet elements change dynamically according to the moving load–structure contact position, was proposed to achieve balance between modeling fidelity and computation amount during the dynamic analysis of beam structures under moving load. The simulated simply supported beam revealed that this strategy can effectively minimize the number of DOFs in the model and enhance computation efficiency and accuracy compared with TFEM with a fixed uniform mesh.
- (8) A two-phase damage detection approach based on multi-scale WFEM was developed in the time domain for beam structures subjected to moving load. This approach consists of two separate phases, namely, damage localization and quantification. It combines DWT-based damage localization, adaptive-scale moving-load analysis strategy, and progressive WFEM updating in the time-domain. First, DWT is applied to separate the moving-load frequency component from the total dynamic displacement response change and locate potential structural damages. Second, with updating parameters limited to the identified damage regions only, WFEM updating is conducted in a progressive manner to estimate damage severity. The elemental scales of WFEM dynamically changed not only according to the moving load–beam contact positions but also to the progressively identified damage regions. This two-phase approach can achieve good consistency among FEM scales, damage scenarios, and load conditions as well as an optimal tradeoff between damage detection accuracy and efficiency. The proposed approach is generally

insensitive to damping, vehicle model, and roughness; therefore, it has a great potential for damage detection in actual bridges.

- (9) A laboratory experiment with different velocities of a moving vehicle and various damage scenarios was conducted to investigate the feasibility and efficiency of the proposed two-phase approach. Both single and double damages were located and quantified with satisfactory accuracy when the moving vehicle velocity was low. High moving velocity of the vehicle reduced the accuracy of damage localization, especially in the cases of double damages.

7.2 Recommendations for future work

Based on the progress and outcome of this thesis regarding the development of a WFEM-based multi-scale structural damage detection strategy in both frequency- and time-domains, several issues that warrant future investigations are highlighted as follows.

- (1) MSE was adopted to showcase the proposed WFEM-based multi-scale damage detection strategy in Chapter 3. However, several practical limitations associated with MSE-based damage detection methods have been identified by researchers. These limitations include mass normalization of measured mode shapes and ill-positioning of the sensitivity matrix. These limitations should be overcome before the proposed MSE-based damage detection method is practically implemented.
- (2) The model updating technique was widely adopted in the frequency- and time-domain in this thesis. The success of this technique depends on the accuracy of FEM, definition of the optimization problem, and selection of the optimization algorithm. Although this thesis focused on structural modeling, the latest advances in the model updating technique may be further introduced to improve the performance of the WFEM-based damage detection method.

- (3) Progressive damage detection methods for beam and plate structures were developed in this study. These two types of elements are insufficient to model large-scale complex civil structures accurately. Further investigations should be conducted to extend the current methods to other types of elements and complex structures with a combination of various element types.
- (4) The damage effect on the moving load-induced dynamic displacement response of a simply supported beam was studied, and a corresponding damage localization method was provided. This localization method needs to be further extended to other types of structures, such as continuous beams and plate structures. Moreover, accurately measuring absolute displacement is more difficult than measuring acceleration. Therefore, the proposed damage localization method should benefit from the development and application of advanced displacement measurement devices.
- (5) Another promising strategy that warrants further investigation is installing sensors on a moving vehicle instead of on structures so that the vehicle serves as an exciter and a sensory system. This strategy is more portable, convenient, and economical than the current approach that requires the permanent installation of sensors on structures.

References

- Amaratunga, K., and Sudarshan, R., (2006), "Multi-resolution modeling with operator-customized wavelets derived from finite elements", *Computer Methods in Applied Mechanics and Engineering*, 195: 2509-2532.
- Au, F.T.K., Cheng, Y.S., Tham, L.G., and Bai, Z.Z., (2003), "Structural damage detection based on a micro-genetic algorithm using incomplete and noisy modal test data", *Journal of Sound and Vibration*, 259(5): 1081-1094.
- Averbuch, A.Z., Zheludev, V.A., and Cohen, T., (2007), "Multiwavelet frames in signal space originated from Hermite splines", *IEEE Transactions on Signal Processing*, 55(3): 797-808.
- Bakhary, N., Hao, H., and Deeks, A.J., (2010), "Structure damage detection using neural network with multi-stage substructuring", *Advances in Structural Engineering*, 13(1): 95-110.
- Becker, R., and Braack, M., (2000), "Multigrid techniques for finite elements on locally refined meshes", *Numerical Linear Algebra with Applications*, 7: 363-379.
- Beheshti-Aval, S.B., Taherinasab, M., and Noori, M., (2011), "Using harmonic class loading for damage identification of plates by wavelet transformation approach", *Smart Structures and Systems*, 8(3): 253-274.
- Bernal, D., (2006), "Flexibility-based damage localization from stochastic realization results", *Journal of Engineering Mechanics*, 132(6): 651-658.
- Biboulet, N., Gravouil, A., Dureisseix, D., Lubrecht, A.A., and Combescure, A., (2013) "An efficient linear elastic FEM solver using automatic local grid refinement and accuracy control", *Finite Elements in Analysis and Design*, 68: 23-38.
- Bogner, F.K., Fox, R.L., and Schmit, L.A., (1995), "The generation of interelement, compatible displacement stiffness and mass matrices by the use of interpolation formulae", *Proceedings of the First Conference on Matrix Methods in Structural*

- Mechanics*. Air Force Flight Dynamics Laboratory, Wright Patterson Air Force Base.
- Brownjohn, J.M.W., Stefano, D.A., Xu, Y.L., Wenzel, H., and Aktan, A.E., (2011), “Vibration-based monitoring of civil infrastructure: challenges and successes”, *Journal of Civil Structural health Monitoring*, 1: 79-95.
- Bu, J.Q., Law, S.S., Zhu, X.Q., and Chan, S.L., (2006), “Vehicle condition surveillance on continuous bridges based on response sensitivity”, *Journal of Engineering Mechanics, ASCE*, 132:78-86.
- Canuto, C., Tabacco, A., and Urban, K., (1999), “The wavelet element method part I: construction and analysis”, *Applied and Computational Harmonic Analysis*, 6: 1-52.
- Canuto, C., Tabacco, A. and Urban, K., (2000), “The wavelet element method part II: Realization and additional features in 2D and 3D”, *Applied and Computational Harmonic Analysis*, 8: 123-165.
- Carden, E.P., and Fanning, P., (2004), “Vibration based condition monitoring: a review”, *Structural Health Monitoring*, 3(4): 355-377.
- Castro, L., and Freitas, J., (2001), “Wavelets in hybrid-mixed stress elements”, *Computer Methods in Applied Mechanics and Engineering*, 190: 3977-3998.
- Cattarius, J., and Inman, D.J., (1997), “Time domain analysis for damage detection in smart structures” , *Mechanical Systems and Signal Processing*, 11(3): 409-423.
- Cavadas, F., Smith, I.F.C., and Figueiras, J., (2013), “Damage detection using data-driven methods applied to moving-load responses”, *Mechanical Systems and Signal Processing*, 39(1-2): 409-425.
- Cawley, P., and Adams, R.D., (1979), “The locations of defects in structures from measurements of natural frequencies” , *Journal of Strain Analysis*, 14(2): 49-57.
- Chan, T.H.T., Li, Z.X., Yu, Y., Sun, Z.H. (2009), “Concurrent multi-scale modeling of civil infrastructures for analyses on structural deteriorating-Part II: model updating and verification”, *Finite Element in Analysis and Design*, 45(11): 795-805.
- Chan, T.H.T., Yu, Y., Wong, K.Y., Guo, L. (2007), “A multi-scale finite element model of Tsing Ma Bridge for hot spot stress analysis”, *Proceeding of International Conference on Health Monitoring of Structure, Material and Environment*, Nanjing, China

- Chang, K.C., Kim, C.W., and Kawatani, M., (2014), "Feasibility investigation for a bridge damage identification method through moving vehicle laboratory experiment", *Structure and Infrastructure Engineering*, 10(3): 328-345.
- Chen, B., and Xu, Y.L., (2007), "A new damage index for detecting sudden change of structural stiffness", *Structural Engineering and Mechanics*, 26(3):315-341.
- Chen, H.P., and Maung, T.S., (2014), "Structural damage evolution assessment using the regularised time step integration method", *Journal of Sound and Vibration*, 333(18): 4104-4122.
- Chen, W.H., and Wu, C.W., (1995), "Spline wavelets element method for frame structures vibration", *Computational Mechanics*, 16: 1-21.
- Chen, W.H., and Wu, C.W., (1996), "Adaptable spline element for membrane vibration analysis", *International Journal for Numerical Methods in Engineering*, 39: 2457-2476.
- Chen, X.F., Yang, S.J., and He, Z.J., (2004), "The construction of wavelet finite element and its application", *Finite Elements in Analysis and Design*, 40: 541-554.
- Chen, X.F., Zi, Y.Y., Li, B., and He, Z.J., (2006), "Identification of multiple cracks using a dynamic mesh-refinement method", *Journal of Strain Analysis for Engineering Design*, 41: 31-39.
- Chen, X.F., Xiang, J.W., Li, B., and He, Z.J., (2010), "A study of multiscale wavelet-based elements for adaptive finite element analysis", *Advances in Engineering Software*, 41(2): 196-205.
- Chen, Z.W., Zhu, S., Xu, Y.L., Li, Q., and Cai, Q.L., (2014), "Damage detection in long suspension bridges using stress influence lines: a case study", *Journal of Bridge Engineering, ASCE*, 16(3): 383-391.
- Choi, S., and Stubbs, N., (2004), "Damage identification in structures using the time-domain response," *Journal of Sound and Vibration*, 275(3-5): 577-590.
- Christian, B., (2009), "Application of the multi-resolution wavelet representation to no-cooperative target recognition", *Radar Conference-Surveillance for a Safer World*, Bordeaux, France
- Chui, C.K., (2009), *An Introduction to Wavelets*. Posts and Telecom Press, Beijing,

China.

- Clough, W., and Penzien, J., (1993), *Dynamics of Structures (third edition)*, McGraw-Hill, New York.
- Cornwell, P., Doebling, S.W., and Farrar, C.R., (1999), “Application of the strain energy damage detection method to plate-like structures”, *Journal of Sound and Vibration*, 224 (2): 359-374.
- Diaz, L.A., Martin, M.T., and Vampa, V., (2009), “Daubechies wavelet beam and plate finite elements”, *Finite Elements in Analysis and Design*, 45(3): 200-209.
- Ding, Y.L., Li, A.Q., Du, D.S., and Liu, T., (2010), “Multi-scale damage analysis for a steel box girder of a long-span cable-stayed bridge”, *Structure and Infrastructure Engineering*, 6(6): 725-739.
- Doebling, S.W., Farrar, C.R., and Prime, M.B., (1998), “A summary review of vibration-based damage identification methods”, *The Shock and Vibration Digest*, 30(2): 91-105.
- Doebling, S.W., Farrar, C.R., Prime, M.B., and Shevitz, D.W., (1996), *Damage Identification and Health Monitoring of Structural Mechanical Systems from Changes in Their Vibration Characteristics: A Literature Review*. Los Alamos National Laboratory, Los Alamos, NM, USA.
- Dong, H.B., Chen, X.F., Li, B., Qi, K.Y., and He, Z.J., (2009), “Rotor crack detection based on high-precision modal parameter identification method and wavelet finite element model”, *Mechanical Systems and Signal Processing*, 23(3): 869-883.
- Entezami, A., and Shariatmadar, H., (2014), “Damage detection in structural systems by improved sensitivity of modal strain energy and Tikhonov regularization method”, *International Journal of Dynamics and Control*, 2:509-520.
- Fan, W., and Qiao, P.Z., (2009), “A 2-D continuous wavelet transform of mode shape data for damage detection of plate structures”, *International Journal of Solids and Structures*, 46: 4379-4395.
- Fan, W., and Qiao, P.Z., (2011), “Vibration-based damage identification methods: a review and comparative study”, *Structural Health Monitoring*, 10(1): 83-111.
- Fan, W., and Qiao, P.Z., (2012), “A strain energy-based damage severity correction

- factor method for damage identification in plate-type structures”, *Mechanical Systems and Signal Processing*, 28: 660-678.
- Fang, S.E., Perera, R., and Roeck, G.D., (2008), “Damage identification of a reinforced concrete frame by finite element model updating using damage parameterization”, *Journal of Sound and Vibration*, 313: 544-559.
- Farrar, C.R., and Jauregui, D.A., (1998a), “Comparative study of damage identification algorithms applied to a bridge: I. Experiment”, *Smart Materials and Structures*, 7(5): 704-719.
- Farrar, C.R., and Jauregui, D.A., (1998b), “Comparative study of damage identification algorithms applied to a bridge: II. numerical study”, *Smart Materials and Structures*, 7(5): 720-731.
- Fox, C. H. J., (1992), “The location of defects in structures: a comparison of the use of natural frequency and mode shape data”, *Proceedings of the 10th International Modal Analysis Conference*.
- Fox, R.L., and Kapoor, M.P., (1968), “Rate of change of eigenvalues and eigenvectors”, *AIAA Journal*, 6(12): 2426-2429.
- Friswell, M.I., Penny, J.E.T., and Wilson, D.A.L., (1994), “Using vibration data and statistical measures to locate damage in structures”, *Modal Analysis: The International Journal of Analytical and Experimental Modal Analysis*, 9(4): 239-254.
- Fu, Y.Z., Lu, Z.R., and Liu, J.K., (2013), “Damage identification in plates using finite element model updating in time domain”, *Journal of Sound and Vibration*, 332: 7018-7032.
- Gaouda, A.M., Salama, M.M.A., Sultan, M.K., and Cliildiaoi, A.Y., (1999), “Power quality detection and classification using wavelet multi-resolution signal decomposition”, *IEEE Transactions on Power Delivery*, 14(4): 1469-1476.
- Gaouda, A.M., Salama, M.M.A., Sultan, M.R., and Chikhanim, A.Y., (2000), “Application of multi-resolution signal decomposition for monitoring short-duration variations in distribution systems”, *IEEE Transactions on Power Delivery*, 15(2): 478-785.

- Ghanem, R., and Shinozuka, M., (1995), “Structural system identification I: theory”, *Journal of Engineering Mechanics, ASCE*, 121(2): 255-264.
- González, A., and Hester, D., (2013), “An investigation into the acceleration response of a damaged beam-type structure to a moving force”, *Journal of Sound and Vibration*, 332(13): 3201-3217.
- Grande, E., and Imbimbo, M., (2014), “A multi-stage data-fusion procedure for damage detection of linear systems based on modal strain energy”, *Journal of Civil Structural Health Monitoring*, 4(2): 107-118.
- Guan H., Karbhari V.M., (2008), “Improved damage detection method based on element modal strain damage index using sparse measurement”, *Journal of Sound and Vibration*, 309(3-5): 465-494.
- Guo, H.Y., and Li, Z. L., (2014), “Structural Multi-damage identification based on modal strain energy equivalence index method”, *International Journal of Structural Stability and Dynamics*, 14(7):1450028.
- Han, J.G., Ren, W.X., and Huang, Y., (2005), “A multivariable wavelet based finite element method and its application to thick plates”, *Finite Elements in Analysis and Design*, 41:821-833.
- Han, J.G., Ren, W.X., and Huang, Y., (2006), “A spline wavelet finite-element method in structural mechanics”, *International Journal for Numerical Methods in Engineering*, 66: 166-190.
- Hao, H., and Xia, Y., (2002), “Vibration-based damage detection of structures by genetic algorithm”, *Journal of Structural Engineering-ASCE*, 7: 222-229.
- He, Y.M., Chen, X.F., Xiang, J.W., and He, Z.J., (2007a), “Adaptive multiresolution finite element method based on second generation wavelets”, *Finite Elements in Analysis and Design*, 43: 566-579.
- He, Y.M., Chen, X.F., Xiang, J.W., and He, Z.J., (2007b), “Multi-resolution analysis for finite element method using interpolating wavelet and lifting scheme”, *Communications in Numerical Methods in Engineering*, 24(11): 1045-1066.
- He, W.Y., and Ren, W.X., (2012), “Finite element analysis of beam structures based on trigonometric wavelet”, *Finite Elements in Analysis and Design*, 51: 59-66.

- He, W.Y., and Ren, W.X., (2013a), “Adaptive trigonometric hermite wavelet finite element method for structural analysis”, *International Journal of Structural Stability and Dynamics*, 1: 1350007.
- He, W.Y., and Ren, W.X., (2013b), “Trigonometric wavelet-based method for elastic thin plate analysis”, *Applied Mathematical Modelling*, 37: 1607-1617.
- He, W.Y., and Ren, W.X., (2013c), “Adaptive trigonometric wavelet composite beam element method”, *Advances in Structural Engineering*, 16(11): 1899-1910.
- He, W.Y., Ren, W.X., and Yang, Z.J., (2012), “Computation of plane crack stress intensity factors using trigonometric wavelet finite element methods”, *Fatigue and Fracture of Engineering Materials and Structures*, 35: 732-741.
- He, W.Y., and Zhu, S., (2013), “Progressive damage detection based on multi-scale wavelet finite element model: numerical study”, *Computers & Structures*, 125: 177-186.
- He, W.Y., Zhu, S., and Ren, W.X., (2014), “A wavelet finite element-based adaptive-scale damage detection strategy”, *Smart Structures and Systems*, 14(3): 285-305.
- He, Z.J., Zhao, J.Y., He, Y.B., and Meng, Q.F., (1996), “Wavelet transform and multiresolution signal decomposition for machinery monitoring and diagnosis”, *Proceedings of the IEEE International Conference on Industrial*.
- Hester, D., and González, A., (2012), “A wavelet-based damage detection algorithm based on bridge acceleration response to a vehicle”, *Mechanical Systems and Signal Processing*, 28: 145-166.
- Ho, S.L., Yang, S.Y., and Wong, H.C., (2001), “Weak formulation of finite element method using wavelet basis function”, *IEEE Transactions on Magnetics*, 37(5): 3203-3207.
- Hu, H., and Wu, C., (2009), “Development of scanning damage index for the damage detection of plate structures using modal strain energy method”, *Mechanical Systems and Signal Processing*; 23: 274-287.
- Huang, Q., Xu, Y.L., Li, J.C., Su, Z.Q. and Liu, H.J., (2012), “Structural damage detection of controlled building structures using frequency response functions”,

Journal of Sound and Vibration, 331(15): 3476-3492.

Huth, O., Feltrin, G., Maeck, J., Kilic, N., and Motavalli, M., (2005), “Damage identification using modal data: experiences on a prestressed concrete bridge”, *Journal of Structural Engineering, ASCE*, 131(12): 1898-1910.

ISO8608:1995, (1996) Mechanical Vibration. Road Surface Profiles. Reporting of Measured Data. *International Organization for Standardization (ISO)*

Jiang, S.F., Wu, S.Y., and Dong, L.Q., (2014), “Time-domain structural damage detection method based on improved multi particle swarm coevolution optimization algorithm”, *Mathematical Problems in Engineering*, Article ID 232763

Kang, J.S., Park, S.K., Shin, S., and Lee, H.S., (2005), “Structural system identification in time domain using measured acceleration”, *Journal of Sound and Vibration*, 288(1-2): 215-234.

Khorram, A., Bakhtiari-Nejad, F., and Rezaeian, M., (2012), “Comparison studies between two wavelet based crack detection methods of a beam subjected to a moving load”, *International Journal of Engineering Science*, 51: 204-215.

Khorram, A., Rezaeian, M., and Bakhtiari-Nejad, F., (2013), “Multiple cracks detection in a beam subjected to a moving load using wavelet analysis combined with factorial design”, *European Journal of Mechanics A/Solids*, 40: 97-113.

Kim, C.W., and Kawatani, M., (2008), “Pseudo-static approach for damage identification of bridges based on coupling vibration with a moving vehicle”, *Structure and Infrastructure Engineering*, 4(5): 371-379.

Kim, H.M., and Bartkowicz, T.J., (1997), “A two-step structural damage detection approach with limited instrumentation”, *Journal of Vibration and Acoustics, ASME*, 119(2): 258-264.

Kim, J.T., Park, J.H., Hong, D.S., and Park, W.S., (2010), “Hybrid health monitoring of prestressed concrete girder bridges by sequential vibration-impedance approaches”, *Engineering Structures*, 32(1): 115-128.

Ko, J., Kurdila, A.J., and Pilant, M.S., (1995), “A class of finite element methods based on orthonormal, compactly supported wavelets”, *Computational Mechanics*, 16: 235-244.

- Koc, G.K., (1994), "Complexity analysis of wavelet signal decomposition and reconstruction", *IEEE Transactions on Aerospace and Electronic Systems*, 30(3): 910-918.
- Koh, C.G., See, L.M., and Balendra, T., (1995), "Damage detection of buildings: numerical and experimental studies", *Journal of Structural Engineering, ASCE*, 121(8): 1150-1160.
- Kong, X., Cai, C.S., and Kong, B., (2014), "Damage detection based on transmissibility of a vehicle and bridge coupled system", *Journal of Engineering Mechanics, ASCE*, DOI: 10.1061/(ASCE)EM.1943-7889.0000821
- Kong, X., Wu, D. J., Cai, C. S., and Liu, Y.Q., (2012), "New strategy of substructure method to model long-span hybrid cable-stayed bridges under vehicle-induced vibration", *Engineering Structures*, 34: 421-435.
- Kosmatka, J.B., and Ricles, J.M., (1999), "Damage detection in structures by modal vibration characterization", *Journal of Structural Engineering, ASCE*, 125(12): 1384-1392.
- Law, S.S., and Li, X.Y. (2007), "Wavelet-based sensitivity analysis of the impulse response function for damage detection", *Journal of Applied Mechanics, ASME*, 74(2):375-377.
- Law, S. S., Li, X. Y., and Lu, Z. R., (2006), "Structural damage detection from wavelet coefficient sensitivity with model errors", *Journal of Engineering Mechanics, ASCE*, 132(10): 1077-1087.
- Law, S.S., Shi, Z.Y., and Zhang, L.M., (1998), "Structural damage detection from incomplete and noisy modal test data", *Journal of Engineering Mechanics, ASCE*, 124(11), 1280-1288.
- Lee, B.Y., and Tarng, Y.S., (1999), "Application of the discrete wavelet transform to the monitoring of tool failure in end milling using the spindle motor current", *The International Journal of Advanced Manufacturing Technology*, 15:238-243.
- Li, B., and Chen, X.F., (2014), "Wavelet-based numerical analysis: a review and classification", *Finite Elements in Analysis and Design*, 81:14-31.
- Li, B., Chen, X.F., Ma, J.X., and He, Z.J., (2005), "Detection of crack location and size

- in structures using wavelet finite element methods”, *Journal of Sound and Vibration*, 285: 767-782.
- Li, Z. H., and Au, F. T. K., (2011), “Feasibility of output-only damage detection method using response of a vehicle moving on a bridge” , *Proceedings of the 14th Asia Pacific Vibration Conference*, Hong Kong
- Li, Z.H., and Au, F.T.K., (2013), “Damage detection of bridge from response of a passing vehicle based on wavelet transform considering surface roughness”, *Proceedings of the 6th International Conference on Structural Health Monitoring of Intelligent Infrastructure*, Hong Kong
- Li, Z.H., and Au, F.T.K., (2014), “Damage detection of a continuous bridge from response of a moving vehicle”, *Shock and Vibration*, Article ID: 146802.
- Li, Z.H., and Au, F.T.K., (2015), “Damage detection of bridges using response of vehicle considering road surface roughness”, *International Journal of Structural Stability and Dynamics*, 15(3):1450057
- Li, Z.X., Chan, T.H.T., Yu, Y., and Sun, Z.H., (2009), “Concurrent multi-scale modeling of civil infrastructures for analyses on structural deterioration, Part I: modeling methodology and strategy”, *Finite Elements in Analysis and Design*, 45: 782-794.
- Li, J., and Law, S.S., (2012), “Damage identification of a target substructure with moving load excitation”, *Mechanical Systems and Signal Processing*, 30: 78-90.
- Li, Y., and Mau, S.T. (1991), “A case study of MIMO system identification applied to building seismic records”, *Earthquake Engineering and Structural Dynamics*, 20: 1045-1064.
- Li, J., and Zhao, X., (2006), “A super-element approach for structural identification in time domain”, *Frontiers of Mechanical Engineering in China*, 1: 215-221.
- Link, M., and Weiland, M., (2009), “Damage identification by multi-model updating in the modal and in the time domain”, *Mechanical Systems and Signal Processing*, 23(6): 1734-1746.
- Liu, F., Li, H., Li, W., and Wang, B., (2014), “Experimental study of improved modal strain energy method for damage localization in jacket-type offshore wind turbines”, *Renewable Energy*, 72:174-181.

- Lu, Z.R., and Law, S.S., (2007a), “Features of dynamic response sensitivity and its application in damage detection”, *Journal of Sound and Vibration*, 303(1-2): 305-329.
- Lu, Z.R., and Law, S.S., (2007b), “Identification of system parameters and input force from output only”, *Mechanical Systems and Signal Processing*, 21(5): 2099-2111.
- Lu, Z.R., and Liu, J.K., (2011), “Identification of both structural damages in bridge deck and vehicular parameters using measured dynamic responses”, *Computers and Structures*, 89: 1397-1405.
- Luo, S.M., (2000), “The finite element method based on interpolating with wavelet basis functions”, *Journal of Applied Mathematics and Mechanics*, 21: 1265-1270.
- Ma, J.X., Xue, J.J., and Yang, S.J., (2003), “A study of the construction and application of a Daubechies wavelet-based beam element”, *Finite Elements in Analysis and Design*, 39: 965-975.
- Majumder, L., and Manohar, C.S., (2002), “Nonlinear reduced models for beam damage detection using data on moving oscillator-beam interactions”, *Computers and Structures*, 82: 301-314.
- Mallat, S., (1988), *Multi-resolution Representation and Wavelets*, PHD Thesis, University of Pennsylvania, Philadelphia, PA.
- Mallat, S., (1989), “A theory for multiresolution signal decomposition: The wavelet representation”, *IEEE Transactions on Pattern Analysis and Machine Intelligence*, 11(7): 674-693.
- Mallat, S., (1998), *A Wavelet Tour of Signal Processing*, 2nd edition, Academic Press.
- Meredith, J., González, A., and Hester, D., (2012), “Empirical mode decomposition of the acceleration response of a prismatic beam subject to a moving load to identify multiple damage locations”, *Shock and Vibration*, 19: 845-856.
- Ndambi, J.M., Vantomme, J., and Harri, K., (2002), “Damage assessment in reinforced concrete beams using eigenfrequencies and mode shape derivatives”, *Engineering Structures*, 24(4): 501-515.
- Nguyen, K.V., and Tran, H.T., (2012), “Multi-cracks detection of a beam-like structure based on the on-vehicle vibration signal and wavelet analysis”, *Journal of Sound*

and Vibration, 329: 4455-4465.

- Ni, Y.Q., Zhou, X.T., and Ko, J.M., (2006), “Experimental investigation of seismic damage identification using PCA-compressed frequency response functions and neural networks”, *Journal of Sound and Vibration*, 290(1-2): 242-263.
- Pandey, A.K., Biswas, M., and Samman, M.M., (1991), “Damage detection from changes in curvature mode shapes”, *Journal of Sound and Vibration*, 145(2): 321-332.
- Pandey, A.K., and Biswas, M., (1994), “Damage detection in structures using changes in flexibility”, *Journal of Sound and Vibration*, 169(1): 3-17.
- Parloo, E., Guillaume, P., and Van Overmeire, M., (2003), “Damage assessment using mode shape sensitivities”, *Mechanical Systems and Signal Processing*, 17(3): 499-518.
- Patton, R.D., and Marks, P.C., (1996), “One-dimensional finite elements based on the Daubechies family of wavelets”, *AIAA*, 34:1696-1698.
- Perera, R., and Ruiz, A., (2008), “A multistage FE updating procedure for damage identification in large-scale structures based on multiobjective evolutionary optimization”, *Mechanical Systems and Signal Processing*, 22(4): 970-991.
- Peterson, L.D., Doebling, S.W., and Alvin, K.F., (1995), “Experimental determination of local structural stiffness by disassembly of measured flexibility matrices”, *Proceedings of 36th AIAA/ ASME/ ASCE/ AHS/ ASC/ Structures, Structural Dynamics, and Materials Conference*.
- Paultre, P., Chaallal, O., and Proulx, J., (1992), “Bridge dynamics and dynamic amplification factors-a review of analytical and experimental findings”, *Canadian Journal of Civil Engineering*, 19(2): 260-278.
- Quraishi, S.M., and Sandeep, K., (2013), “Multiscale modeling of beam and plates using customized second-generation wavelets”, *Journal of Engineering Mathematics*, 83:185-202.
- Ratcliffe, C.P., (1997), “Damage detection using a modified laplacian operator on mode shape data”, *Journal of Sound and Vibration*, 204(3): 505-517.

- Ren, W.X., and De Roeck, G.,(2002a), “Structural damage identification using modal data, I: simulation verification”, *Journal of Structural Engineering, ASCE*, 128(1): 87-95.
- Ren, W. X. and De Roeck, G. (2002b),“Discussion of “Structural Damage Detection from Modal Strain Energy Change” by Z.Y. Shi, S.S. Law, and L.M. Zhang”, *Journal of Engineering Mechanics, ASCE*, 128: 376-377.
- Rieker, J.R., Lin, Y.H., and Trethewey, M.W., (1996), “Discretization considerations in moving load finite element beam models”, *Finite Elements in Analysis and Design*, 21: 129-144.
- Roveri, N., and Carcaterran, A., (2012), “Damage detection in structures under traveling loads by Hilbert-Huang transform”, *Mechanical Systems and Signal Processing*, 28: 128-144.
- Rowley, C.W., (2007), “Moving Force Identification of Axle Forces on Bridges”, Ph.D. Thesis, University College Dublin, Ireland.
- Rucka, M., and Wilde, K., (2006),“Application of continuous wavelet transform in vibration based damage detection method for beams and plates”, *Journal of Sound and Vibration*, 297: 536-550.
- Salawu, O.S., (1997), “Detection of structural damage through changes in frequency: a review”, *Engineering Structures*, 19(9): 718-723.
- Shi, Z.Y., and Law, S.S., (1998), “Structural damage localization from modal strain energy change”, *Journal of Sound and Vibration*, 218(5): 825-844.
- Shi, Z.Y., Law, S.S., and Zhang, L.M., (2000a), “Damage localization by directly using incomplete mode shapes”, *Journal of Engineering Mechanics, ASCE*, 126(6): 656-660.
- Shi, Z.Y., Law S.S., and Zhang, L.M., (2000b), “Structural damage detection from modal strain energy change”, *Journal of Engineering Mechanical, ASCE*, 126 (12): 1216-1223.
- Shi, S.Y., Law, S.S., and Zhang, L.M., (2002), “Improved damage quantification from elemental modal strain energy change”, *Journal of Engineering Mechanics, ASCE*, 128(5): 521-529.

- Sohn, H., Farrar, C.R., Hemez, F.M., Shunk, D.D., Stinemates, D.W., and Nadler, B.R. (2004), *A Review of Structural Health Monitoring Literature 1996-2001*, Los Alamos National Laboratory, Los Alamos, NM, USA.
- Strintzis, M.G., (1996), "Optimal biorthogonal wavelet bases for signal decomposition", *IEEE Transactions on Signal Processing*, 44(6): 1406-1417.
- Stubbs, N., and Kim, J.T., (1996), "Damage localization in structures without baseline modal parameters", *AIAA Journal*, 34(8): 1644-1649.
- Stubbs, N., Kim, J.T., and Farrar, C.R., (1995), "Field verification of a nondestructive damage localization and severity estimation algorithm", *Proceedings of 13th International Modal Analysis Conference*.
- Stubbs, N., and Osegueda, R., (1990), "Global non-destructive damage evaluation in solids", *Modal Analysis: The International Journal of Analytical and Experimental Modal Analysis*, 5(2): 67-79.
- Sudarshan, R., Heedene, S., and Amaratunga, K., (2003), "A multiresolution finite element method using second generation Hermite multiwavelets", *Second MIT Conference on Computational Fluid and Solid Mechanics*.
- Sweldens, W., (1996), "The lifting scheme: a custom-design construction of biorthogonal wavelets", *Applied and Computational Harmonic Analysis*, 3: 186-200.
- Sweldens, W., (1997), "The lifting scheme: a construction of second generation wavelets", *SIAM Journal of Mathematical Analysis*, 29(2): 511-546.
- Teughels, A., Maeck, J., and Roeck, G.D., (2002), "Damage assessment by FE model updating using damage functions", *Computers and Structures*, 80(25): 1869-1879.
- Teughels, A., and Roeck, G.D., (2004), "Structural damage identification of the highway bridge Z24 by FE model updating", *Journal of Sound and Vibration*, 278(3): 589-610.
- Wahab, M.M.A., and De Roeck, G., (1999), "Damage detection in bridges using modal curvatures: applications to a real damage scenario", *Journal of Sound and Vibration*, 226(2): 217-235.
- Wang, S.Q., (2013), "Iterative modal strain energy method for damage severity estimation using frequency measurements", *Structural Control and Health*

- Monitoring*, 20(2): 230-240.
- Wang, Y., Li, Z.X., Wang, C.M., and Wang, H., (2013), “Concurrent multi-scale modelling and updating of long-span bridges using a multi-objective optimisation technique”, *Structure and Infrastructure Engineering*, 9(12): 1251-1266.
- Wang, Y.M., Chen, X.F., He, Y.M., and He, Z.J., (2011), “The construction of finite element multi-wavelets for adaptive structural analysis”, *International Journal for Numerical Methods in Biomedical Engineering*, 27: 562-584.
- Wang, Y.M., Chen, X.F., and He, Z.J., (2014), “Daubechies wavelet finite element method and genetic algorithm for detection of pipe crack”, *Nondestructive Testing and Evaluation*, 26(01): 87-99.
- Wang, Y.M., and Wu, Q., (2013), “Construction of operator-orthogonal wavelet-based elements for adaptive analysis of thin plate bending problems”, *Computer Modeling in Engineering & Sciences*, 93(1): 17-45.
- Xiang J.W., Chen X.F., He, Z.J., and Dong, H.B., (2007a), “The construction of 1D wavelet finite elements”, *Computational Mechanics*, 40: 325-339.
- Xiang, J.W., Chen, X.F., Mo, Q.Y., and He, Z.J., (2007b), “Identification of crack in a rotor system based on wavelet finite element method”, *Finite Elements in Analysis and Design*, 43:1068-1081.
- Xiang, J.W., Chen, X.F., and Yang, L.F. (2009), “Crack identification in short shafts using wavelet-based element and neural networks”, *Structural Engineering and Mechanics*, 33(5): 543-560.
- Xiang, J.W., and Liang, M., (2011), “Multiple damage detection method for beams based on multi-scale elements using Hermite cubic spline wavelet”, *Computer Modeling in Engineering and Sciences*, 73(3): 267-298.
- Xiang, J.W., and Liang, M. (2012), “Wavelet-based detection of beam cracks using modal shape and frequency measurements”, *Computer-Aided Civil and Infrastructure Engineering*, 27: 439-454.
- Xiang, J.W., Matsumoto, T., Wang, Y.X., and Jiang, Z.S., (2011), “A hybrid of interval wavelets and wavelet finite element model for damage detection in structures”, *Computer Modeling in Engineering and Sciences*, 81(3): 269-294.

- Xiang, J.W., Matsumoto, T., Long, J.Q., and Ma, G., (2013a), "Identification of damage locations based on operating deflection shape", *Nondestructive Testing and Evaluation*, 28(2): 166-180.
- Xiang, J.W., Matsumoto, T., Wang, Y.X., and Jiang, Z.S., (2013b), "Detect damages in conical shells using curvature mode shape and wavelet finite element method", *International Journal of Mechanical Sciences*, 66: 83-93.
- Xiao, X., Xu, Y.L., and Zhu, Q., (2014), "Multiscale modeling and model updating of a cable-stayed bridge II: model updating using modal frequencies and influence lines", *Journal of Bridge Engineering*, ASCE, DOI: 10.1061/(ASCE)BE.1943-5592.0000723
- Xu, Y.L., and Chen, J., (2004), "Structural damage detection using empirical mode decomposition: experimental investigation", *Journal of Engineering Mechanics*, ASCE, 130(11): 1279-1288.
- Yan, Y.J., Cheng, L., Wu, Z.Y., and Yam, L.H., (2007), "Development in vibration-based structural damage detection technique", *Mechanical Systems and Signal Processing*, 21: 2198-2211.
- Yan, W.J., Huang, T.L., and Ren, W.X., (2010), "Damage detection method based on element modal strain energy sensitivity", *Advances in Structural Engineering*, 13(6): 1075-1088.
- Yan, W.J., and Ren, W.X., (2012), "Statistic structural damage detection based on the closed-form of element modal strain energy sensitivity", *Mechanical System and Signal Processing*, 28: 183-194.
- Yang, Y.B., and Lin, C.W., (2005), "Vehicle-bridge interaction dynamics and potential applications", *Journal of Sound and Vibration*, 284: 205-226.
- Yang, J.N., Huang, H.W., and Lin, S., (2006a), "Sequential non-linear least-square estimation for damage identification of structures", *International Journal of Non-linear Mechanics*, 41(1): 124-140.
- Yang, J.N., Lin, S., Huang, H., Zhou, L., (2006b), "An adaptive extended Kalman filter for structural damage identification", *Structural Control and Health Monitoring*, 13(4): 849-967.

- Yang, J.N., Pan, S., and Lin, S., (2007a), “Least-squares estimation with unknown excitations for damage identification of structures”, *Journal of Engineering Mechanics, ASCE*, 133(1): 12-21.
- Yang, J.N., Pan, S., and Huang, H., (2007b), “An adaptive extended Kalman filter for structural damage identifications II: unknown inputs”, *Structural Control and Health monitoring*, 14(3): 497-521
- Yang, Y.B., Li, Y.C., and Chang, K.C., (2012) “Effect of road surface roughness on the response of a moving vehicle for identification of bridge frequencies”, *Interaction and Multiscale Mechanics*, 5(4): 347-368.
- Yang, Y.B., Lin C.W., and Yau, J.D., (2004a), “Extracting bridge frequencies from the dynamic response of a passing vehicle”, *Journal of Sound and Vibration*, 272: 471-493.
- Yang, Y.B., Yau, J.D., and Wu, Y.S., (2004b), *Vehicle-Bridge Interaction Dynamics with Applications to High Speed Railways*, World Scientific Publishing Company, Singapore.
- Ye, J.J., He, Y.M., Chen, X.F., Zhai, Z., Wang, Y.M., and He, Z.J., (2010), “Pipe crack identification based on finite element method of second generation wavelets”, *Mechanical Systems and Signal Processing*, 24(2): 379-393.
- Zhang, X.W., Chen ,X.F., Wang, X.Z., He, Z.J., (2010), “Multivariable finite elements based on B-spline wavelet on the interval for thin plate static and vibration analysis”, *Finite Elements in Analysis and Design*, 46(5): 416-427.
- Zhang, Y., Wang, L.Q., and Xiang, Z.H., (2012), “Damage detection by mode shape squares extracted from a passing vehicle”, *Journal of Sound and Vibration*, 331: 291-307.
- Zhang, Y., Lie, S.T., and Xiang, Z.H., (2013), “Damage detection method based on operating deflection shape curvature extracted from dynamic response of a passing vehicle”, *Mechanical Systems and Signal Processing*, 35: 238-254.
- Zhou, Y.H., Wang, J.Z., and Zheng, X.J., (1998), “Application of wavelet Galerkin FEM to bending of beam and plate structures”, *Journal of Applied Mathematics and Mechanics*, 19(8): 745-755.

- Zhou, Y.H., Wang, J.Z., and Zheng, X.J., (1999), “Applications of wavelet Galerkin FEM to bending of plate structure”, *Acta Mechanica Solida Sinica*, 12(2): 136-143.
- Zhou, Z.G., Wegner, L.D., and Sparling, B.F. (2007), “Vibration-based detection of small-scale damage on a bridge deck”, *Journal of Structural Engineering, ASCE*, 133(9): 1257-1267.
- Zhu, H.P., Mao, L., and Weng, S., (2014), “A sensitivity-based structural damage identification method with unknown input excitation using transmissibility concept”, *Journal of Sound and Vibration*, 2014,333(26), 7135-7150.
- Zhu, Q., Xu, Y.L., and Xiao, X., (2014), “Multiscale modeling and model updating of a cable-stayed bridge I: modeling and influence line analysis”, *Journal of Bridge Engineering, ASCE*, DOI: 10.1061/(ASCE)BE.1943-5592.0000722
- Zhu, S., He, W.Y., and Ren, W.X., (2013), “Adaptive-scale damage detection for frame structures using beam-type wavelet finite element: experimental validation”, *Journal of Earthquake and Tsunami*, 7(3):1350024.
- Zhu, X.Q., and Law, S.S., (2006), “Wavelet-based crack identification of bridge beam from operational deflection time history”, *International Journal of Solids and Structures*, 43: 2299-2317.
- Zienkiewicz, O.C., and Taylor, R.L., (1961), *The Finite Element Method (fourth edition)*, McGraw-Hill Book Company, London.